Time-Lapse Passive Seismic Velocity Tomography of Longwall Coal Mines: A Comparison of Methods

Kramer Davis Luxbacher

Dissertation submitted to the faculty of Virginia Polytechnic Institute & State University in partial fulfillment of the requirements for the degree of

Doctor of Philosophy
in
Mining Engineering

Committee Members:
Dr. Erik Westman, Chair
Dr. Anthony Iannacchione
Dr. Mario Karfakis
Dr. Tom Novak
Dr. Peter Swanson

August 19, 2008
Blacksburg, Virginia

Keywords: Longwall, Coal, Tomography, Seismic, Stress Redistribution

Time-Lapse Passive Seismic Velocity Tomography of Longwall Coal Mines: A Comparison of Methods

Kramer Davis Luxbacher

Abstract

Time-lapse passive seismic velocity tomography was conducted utilizing data from three underground longwall coal mines to produce a better understanding of the processes that lead to ground failure in mines, especially large, violent failures, such as bumps. Two of the datasets, US Western I and US Western II, were collected at bump-prone underground longwall coal mines in the Western United States using surface mounted receiver arrays, while the third data set was collected at an underground longwall coal mine in Australia utilizing an underground array. The Australian mine was experiencing problems with periodic caving and subsequent wind blasts, rather than bumps.

Seismic velocity tomography allows for non-invasive imaging of a rock mass and inference of stress redistribution from the velocity images. These tomograms are unique as they are generated using source data that was collected remotely and the sources are mining-induced. Tomograms were generated using three inversion methods: simultaneous iterative reconstructive technique (SIRT), double difference least squares event relocation, and least squares event relocation. The three methods were compared and contrasted to determine if one is superior and if event relocation improves the image. Also, the tomograms were analyzed to determine if passive seismic velocity tomography is an appropriate technology for the study of stress in mines and assistance in forecasting of bumps. The tomograms were compared with known roof events, face advance, and fall locations at the mines to establish if expected stress features can be imaged with velocity. Finally, synthetic tomograms were generated using a starting velocity model that approximates the predicted "true" model for each mine to determine if the velocity images produced correlate with the theoretical stress state at the mine.

Results indicate that high velocity zones correlating with high stress abutment regions can be imaged for the US Western I data set with all three inversion methods, but the SIRT method provided the best agreement when the synthetic tomogram was generated. Additionally,

a low velocity zone that correlates with the gob is consistently imaged. These features also redistribute with face advance.

The US Western II data set was not as densely sampled as the US Western I data set. A low velocity region was consistently present in the gob area and redistributed with face advance, but abutment stress features were not evident. Additionally an unexplained high velocity feature was evident on several of the tomograms. Synthetic tomography indicated that the double difference least squares event relocation method is most appropriate for this data set.

Finally, the Moonee Colliery results, which were also not as densely sampled as US Western I were uncertain. While velocity anomalies were often present in the vicinity of a fall, the anomalies were not reliably high or low. Again, synthetic tomography indicated that the double difference damped least squares event relocation method was most appropriate for this data set.

The tomograms presented indicate that source-receiver configuration and density and variable gridding are extremely important in the application of passive seismic velocity tomography to mines. The source-receiver configuration and density determine how well various areas of a model are constrained, and the variable gridding allows areas that are not well sampled to still be adequately constrained.

As a result of this work several things can be drawn about requirements that must be met in order to utilize seismic velocity tomography for inference of stress in underground mines. First, typical longwall stress abutment patterns can be inferred from velocity images of underground coal mines. Second, synthetic tomography and analysis of this tomography, in addition to some knowledge of the general location and frequency of microseismic events, is necessary prior to designing receiver arrays for passive seismic velocity tomography. Suboptimal source-receiver configurations may be used for passive seismic velocity tomography, but there is a minimum threshold for the number of raypaths that must be met that is unique to each site. Finally, a good understanding of the mechanics of stress and failure at the site is necessary to interpret the tomograms.

Acknowledgements

First, I would like to thank my advisor, Dr. Erik Westman for his invaluable advice and guidance. I also appreciate the encouragement and support of my committee members, Dr. Thomas Novak, Dr. Mario Karfakis, Dr. Peter Swanson, and Dr. Anthony Iannacchione. Dr. Swanson and Dr. Iannacchione, both from NIOSH, were also kind enough to provide data for this dissertation, and assistance in reducing and utilizing the data.

H. Zhang, C. Thurber, D. Eberhart-Phillips, and J.R. Evans have all developed tomography programs that are available for download that I have utilized. These programs, along with their documentation have been crucial to this research. Additionally, I sincerely appreciate Steve Schafrik, at the Virginia Center for Coal and Energy Research, taking the time to assist me with Unix. I also appreciate Michael Murphy's help in accessing the Moonee Colliery data. I would also like to express my appreciation for the opportunities afforded me by the National Science Foundation and the Department of Mining and Minerals Engineering at Virginia Tech. This project is funded by a National Science Foundation CAREER Grant (CMS-0134034).

Finally, I could not have completed this research without the support of my family, especially my husband, Mark.

Table of Contents

List of Figures

Chapter 1
Introduction

Roof control and characterization are of paramount importance to the mining industry. In 2007, 12 fatalities occurred as a result of fall of roof or rib in underground coal mines, accounting for more than a third of total coal mining fatalities. Unfortunately, six of the fatalities occurred as part of a massive failure at Crandall Canyon Mine in Utah, and an additional three occurred during rescue efforts. This event has highlighted the need for technology to improve characterization of stress in the mine roof and forecast roof fall events. Not only do falls of ground endanger the safety of miners working underground, but they can also seriously impede production and drive up operating costs.

Structural failure in mines occurs at different scales from localized falls to bumps to massive failure. Bumps are sudden and violent failure of overstressed rock. They result in a large release of energy and may cause expulsion of material or airblasts, both of which are hazardous. Seismic velocity tomography is a technology that has been implemented with limited application in underground mines. However, almost all of these studies have been localized, or short term, and seen little translation to industry. Seismic velocity tomography involves propagating seismic waves through a rock mass and measuring their velocity, and eventually generating an image of the spatial variation in velocity. Stress redistribution can be inferred from this image.

The research described here involves application of passive seismic velocity tomography to three different longwall mines using three different inversion algorithms and evaluating the results based on research in longwall stress abutment and synthetic tomography.

This dissertation consists of seven chapters. Chapter 1 is an introduction to the research. Chapter 2 is a literature review providing background and a discussion of previous work. Chapters 3 through 6 consist of 4 journal papers titled:

- *Time-lapse Passive Seismic Velocity Tomography of Longwall Coal Mines: A Comparison of Methods*
- *Synthetic Method for the Assessment of Passive Seismic Velocity Tomography*
- *Applications of Passive Seismic Velocity Tomography at Longwall Coal Mines in the Western US*

- *Passive Seismic Velocity Tomography of a Longwall Panel with Episodic Caving*

References are listed at the end of each chapter. Since the journal papers are related there is some redundancy, especially since case studies must be described in each paper. Also, to ensure that the dissertation describes all of the research undertaken all results are presented in Appendices, while the final journal papers will present a select group of figures. Finally, Chapter 7 involves a brief discussion of the conclusions drawn in the journal papers and recommendations for further research.

Chapter 2
Literature Review

2.1. Introduction

The use of seismic velocity tomography for inference of stress in underground mines requires a general understanding of several areas including rock failure forecasting, rock failure in underground mines, the relationship between rock stress and seismic velocity, methods for inverting data and generating tomographic images, microseismic monitoring, and a review of previous experimental work.

2.2. Ground Failure in Underground Mines

2.2.1. Introduction

A brief review of rock mechanics is valuable in understanding stress redistribution in underground mines. The study of rock mechanics is complex due to the highly varied nature of rocks at both microscopic and macroscopic levels. The particles, crystals, and cementing material that comprise rocks vary significantly for different rocks, and at the macroscopic level rocks contain fractures, joints, and bedding planes (Jaeger et al. 2007). These unique features may cause rocks to fail under very different conditions and contribute to widely varied experimental data even among the same type of rock.

Stress *in situ* is caused by various phenomena including surface topography, residual stress related to geologic and thermal history, fractures and discontinuities, and tectonic stress (Brady and Brown 1985; Herget 1988). Newton's first law defines force as equal to mass multiplied by acceleration, and stress is defined as force over an area. Vertical stress in a mine is usually determined by dividing overburden into columns of material and multiplying the weight of the overburden by gravitational acceleration. The vertical stress, σ_v, may be defined as follows:

$$\sigma_v = \int_0^z \rho g \, dz \ \text{(Pa)} \qquad \text{[Eq. 2.1]}$$

$\rho = \frac{\text{mass}}{\text{volume}}$ = overburden density (kg/m^3)

g = acceleration due to gravity (m/s^2)

z = depth (m)

(Herget 1988).

Determination of the horizontal stress component due to gravity is more complex. In a strictly elastic rock mass the horizontal component, σ_h, has been defined as follows:

$$\sigma_{h=\frac{\upsilon}{1-\upsilon}}\sigma_v \quad \text{(Pa)} \qquad \text{[Eq. 2.2]}$$

$\upsilon = \frac{\frac{\Delta D}{D}}{\frac{\Delta L}{L}}$ = Poisson's ratio

D= Diameter (m)

L= Length (m)

(Herget 1988).

Poisson's ratio typically ranges from 0.15 to 0.35 for rocks (Herget 1988).

Since the perfectly elastic requirement is rarely met *in situ* a factor k is often applied to the vertical stress component, σ_v, so that:

$$\sigma_h = k\sigma_v \quad \text{(Pa)} \qquad \text{[Eq. 2.3]}$$

(Herget 1988).

The factor, k, ranges from 0 to 1; at k=0 there is no horizontal stress component and at k =1 the rock is inelastic (Herget 1988).

However, Equations 2.2 and 2.3 have are now seldom used. Mark and Gadde have found that horizontal stress is generally related to regional stress trends, and increases with depth. They examined horizontal stress trends in underground mines around the world and found that this regional correlation usually shows that horizontal stress increases with depth at rates ranging from 0.8 to 2.0 times the vertical stress. They also show that the horizontal stresses found in relatively shallow underground mines are linked with those deep in the earth's crust (Mark and Gadde 2008).

Tectonic stresses, resulting from movement of plates in the earth, can also create a horizontal stress component. It is important to note that this tectonic horizontal stress component, when added to the gravitational horizontal stress component described above can exceed the vertical stress component. In many Australian coal mines, the principal horizontal stress may be as much as 2.5 times the vertical stress (Kelly 2000). Arjang and Herget compiled a database of stress measurements from 39 Canadian hardrock mines and found that horizontal stress exceeded vertical stress (1997). Similar conditions can be found in underground mines in the U.S.

Finally, in very deep mines stress may also be caused by temperature change in rock. Herget gives the linear coefficient of thermal expansion in sandstone as 10.8 x 10^{-8} m per 1°C (1988). Jaeger and others give a thorough discussion of thermoelasticity, including equations for thermal stresses (2007).

2.2.2. Behavior of Rock Under Stress

Rocks generally exhibit two distinct failure behaviors: elastic-plastic and elastic-brittle (Blès and Feuga 1986). Discussion of elastic-plastic and elastic-brittle behavior first requires definition of stress and strain. Generally, strain refers to the change in the shape of a mass as pressure is applied (Goodman 1989). For a cylindrical rock sample under uniaxial load, strain, ε, refers to the change in the length of the rock sample when pressure is applied parallel to the long axis (Peng 1986), so:

$$\varepsilon = \frac{\Delta L}{L} \qquad \text{[Eq. 2.4]}$$

ε= Strain

L= Length (m)

ΔL= Change in Length (m)

Rock stress is calculated by dividing the load by the area under load. A plot of stress versus strain allows for examination of the elastic, plastic, and brittle zones. When rocks are initially stressed they usually exhibit small amounts of strain as stress increases. This is referred to as the elastic region, because if the stress is removed the rock will regain its initial shape. When the elastic region is exceeded the rock will either fail immediately or the strain will increase with little increase in stress. The former is referred to as brittle failure and the latter is referred to as plastic strain. In either case, the initial shape of the rock cannot be recovered. There are also several types of plastic behavior – plastic with softening, plastic without work hardening, and plastic with work hardening. Plastic behavior with softening indicates that stress can actually decrease and strain will continue to increase; plastic behavior without work hardening indicates that if stress remains constant strain will continue to increase; plastic behavior with work hardening requires increasing stress for increasing strain. Since rocks are usually subjected to triaxial stress, the type of behavior is due to the relationship between the compressive stress, σ_1, and the confining stress, σ_3, as illustrated in Figure 2.1:

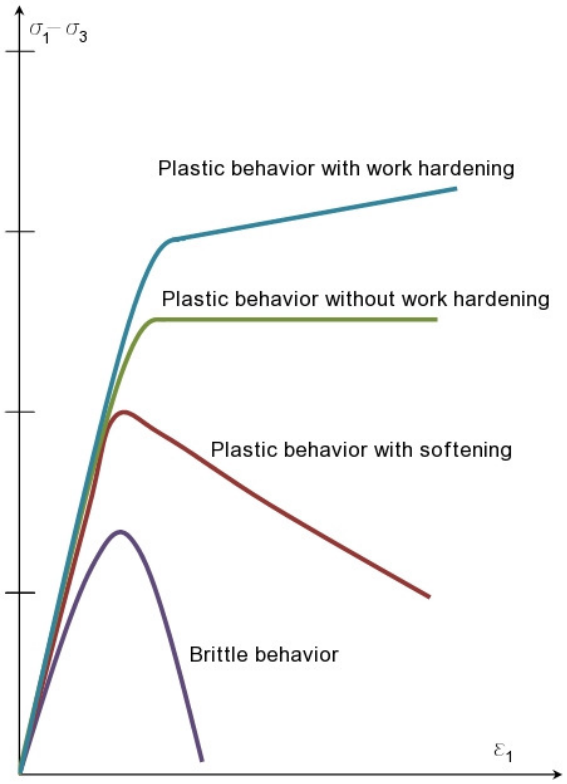

Figure 2.1. Behavior of rocks under stress (Blès and Feuga 1986).

Young's modulus, E, the slope of the stress strain curve, is often used to describe the elasticity of rocks and is equal to:

$$E = \frac{\sigma}{\varepsilon} \text{ (Pa)} \qquad \text{[Eq. 2.5]}$$

E= Young's Modulus

σ= Stress (Pa)

ε= Strain

(Goodman 1989).

Because stress-strain curves are nonlinear, Young's modulus may be measured several different ways: the tangent Young's modulus, E_t, is the slope of the curve at 50% of peak stress, the average Young's modulus, E_{av}, is the slope of the most linear portion of the curve, and the secant Young's modulus, E_s, measures the slope from 0 to some fixed percentage of peak stress (Brady and Brown 1985). The various measures are displayed in Figure 2.2:

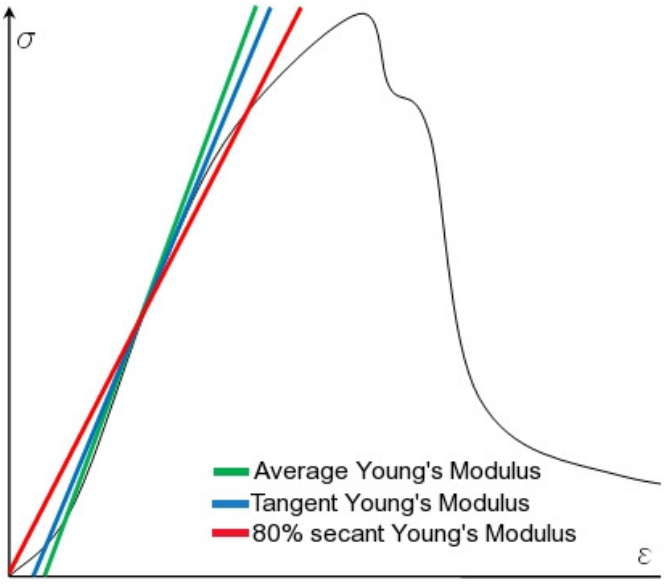

Figure 2.2. Determination of Young's Modulus.

Other measures of elasticity include the bulk modulus, K, and the shear modulus, G, also referred to as the modulus of rigidity. Equations for both moduli are displayed below (Goodman 1989):

$$K = \frac{E}{3(1-\nu)} \text{ (Pa)} \qquad \text{[Eq. 2.6]}$$

$$G = \frac{E}{2(1+\nu)} \text{ (Pa)} \qquad \text{[Eq. 2.7]}$$

ν= Poisson's Ratio

E= Young's Modulus (Pa)

(Goodman 1989).

Failure of rock occurs when stress exceeds rock strength, at the maximum point on the stress-strain curve. Mechanics of failure are dependent on the characteristics of the rock, including existing fractures. The stress-strain curve is useful in examining how rocks deform and how microfractures and pore space respond to stress and contribute to failure. Figure 2.3 relates changes taking place in the rock to the different stages of the stress-strain curve. Zone I shows seating of the rock in the testing apparatus; zone II is the elastic zone during which closure of pore space and microcracks takes place; zones III and IV are where new microcracks form and their density increases. Finally, just after the maximum stress at point D the microcracks coalesce into macrocracks (Goodman 1989).

Mechanics of failure are also highly dependent on the stiffness of the load system. Salamon determined that failure in a laboratory occurs in a violent and unstable manner when the loading machine stiffness is less steep than the post failure stiffness of the specimen. Conversely, when the loading machine stiffness is more steep than the post failure stiffness of the specimen failure occurs in a more stable manner (Salamon 1970; Swanson and Boler 1995; Maleki et al. 1999; Zipf 2001). The transfer of stored strain energy from the load system to the specimen causes the violent failure. In the case of coal bumps the loading system is the over- and under-burden while a coal pillar is being loaded.

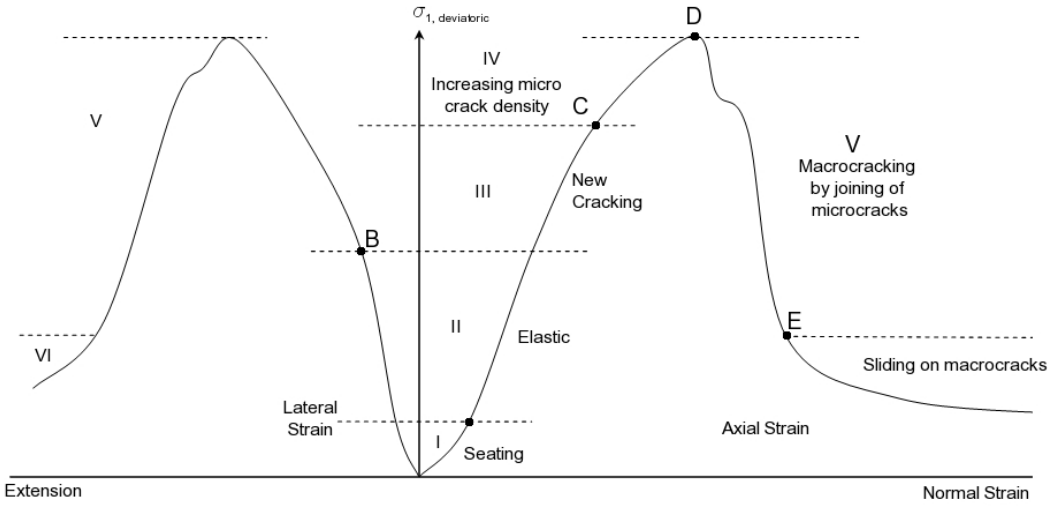

Figure 2.3. Stages of the stress-strain curve (Goodman 1989).

2.2.3. Rock Failure Criteria

The Coulomb failure criterion (1773) assumes that the force required to initiate failure along a plane is equal to the sum of two forces: a frictional force that is equal to the normal force multiplied by some constant and an internal cohesive force of the material (Jaeger et al. 2007). The Coulomb failure criterion is displayed in equation 2.7:

$$|\tau| = S_i + \sigma tan\varphi \qquad \text{[Eq. 2.8]}$$

$|\tau|$ = shear stress acting along a plane (Pa)

S_i = internal cohesive force (Pa)

φ = angle of internal friction (degrees)

σ = normal stress acting along a plane (Pa)

(Goodman 1989).

Mohr developed a graphical illustration to represent the state of stress at a point (1914). Mohr circles are displayed in Figure 2.4:

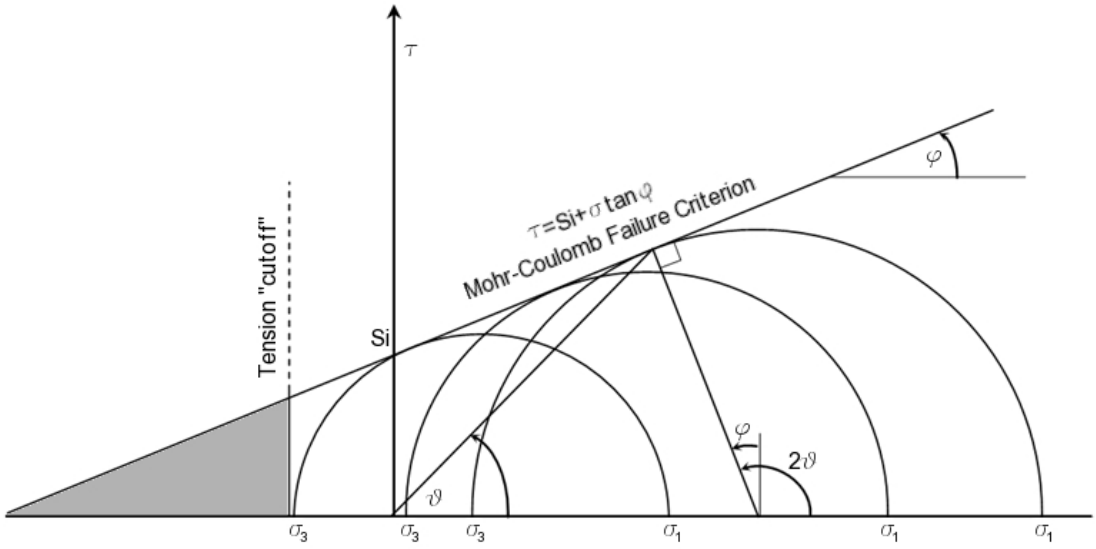

Figure 2.4. Mohr Circles and Mohr-Coulomb Failure Criterion.

Several failure parameters may be plotted and determined graphically on a Mohr circle. First, the circle is plotted between the compressive and confining stresses, σ_1 and σ_3. The angle, φ, of the failure envelope with the horizontal is the angle of internal friction. The angle, ϑ, is determined by drawing a line perpendicular to the envelope that intersects the center of the circle, and then drawing a line from the origin of the first line to the origin of the τ axis.

The Mohr-Coulomb failure criterion combines Mohr's illustration with Coulomb's equation so that Coulomb's equation creates a failure envelope tangent to Mohr's circle as displayed in Figure 2.4.

The drawback to the linear envelope that is utilized in the Mohr-Coulomb failure criterion is that experimental data show that the Coulomb failure envelope extends too far into the tensile region. Coulomb also predicted that the compressive stress, σ_1, required to produce failure increases linearly with confining stress, σ_3, while experimental data show a non-linear relationship (Jaeger et al. 2007). Mohr recommended a nonlinear failure envelope to account for this discrepancy (Mohr 1900):

$$|\tau| = f(\sigma) \text{ (Pa)} \qquad \text{[Eq. 2.9]}$$

(Jaeger et al. 2007).

The Mohr-Coulomb failure criterion is more often employed because Mohr's envelope must be determined experimentally. Pariseau contends rounding the nose of the criterion with the circle representing uniaxial tensile strength is an appropriate solution (2007).

In 1921, Griffith proposed a failure envelope for glass. This envelope has little practical application to rocks as it applies strictly to brittle materials. Griffith's criterion may underestimate stress required for a more plastic material because of the added energy expended in deforming the plastic zone at the crack tip (Dowling 1998). Griffith's criterion is:

$$T^* = \sqrt{\frac{2\gamma E_m}{\pi c}} \quad \text{(Pa)} \qquad \text{[Eq. 2.10]}$$

T^* = tensile stress at which a crack of initial length c will grow

γ = surface energy per unit area

(Jaeger et al. 2007)

Griffith's theory does explain fracture propagation in rocks; he hypothesized that fracture occurs when the maximum tangential stress near the end of a microfracture exceeds material strength (1921). Also, Brady and Brown indicate that Griffith was a pioneer in the field of fracture mechanics – one of the first scientists to use microscopic theory to predict macroscopic failure of materials (1985).

Hoek and Brown presented the following criterion for peak triaxial strength:

$$\sigma_1^{'} = \sigma_3^{'} + \sigma_{ci}\left(m\frac{\sigma_3^{'}}{\sigma_{ci}} + s\right)^{0.5} \quad \text{(Pa)} \qquad \text{[Eq. 2.11]}$$

$\sigma_1^{'}$ & $\sigma_3^{'}$ =major and minor principal effective stresses at failure (Pa)

σ_{ci} = uniaxial compressive strength of intact rock material (Pa)

m and s are material constants, where s=1 for intact rock

(1980).

The constant, m, is dependent on mineralogy, composition and grain size while the constant, s, is dependent on tensile strength and degree of fracturization. These factors were included in an attempt to present a criterion that could be used to characterize a relatively large rock mass (Hoek and Brown 1980).

2.2.4. Violent Failure in Underground Mines

Bumps, also referred to as rockbursts, mountain bumps, bounces, and bursts, are violent and sudden ground failures that cause expulsion of material into open areas. They are often accompanied by a seismic tremor and the expelled material may range from less than a ton to

hundreds of tons. It is important to note that even a very small amount of expelled material can cause serious injury to workers depending on the worker's proximity to the bump. They can also be accompanied by roof falls and floor heave (Braüner 1994).

In coal mines, bumps almost always occur where the roof or the roof and floor are massive and competent. Additionally, they generally occur at depths greater than 300 meters, although isolated bursts have been recorded in more shallow mines (Braüner 1994; Ellenberger and Heasley 2000).

Crouch describes a coal mine bump as an unstable release of energy and indicates that they occur because coal is unable to absorb all of the energy released by surround strata during yielding which explains why mines with strong and massive strata are prone to bumps (Crouch and Fairhurst 1974). Maleki and others define coal bumps as sudden failures of rock or coal near entries that result in material being ejected into the entry (Maleki et al. 1997).

Aside from the danger to miners of flying material, bumps pose other serious hazards. They may be accompanied by an airblast or windblast which can disrupt mine ventilation and has the potential to injure miners by throwing them. Additionally, violent failures may cause a large release of strata gas and propagate explosive dust into the air (Braüner 1994).

Large roof falls that are not characterized as bumps may also pose many of the same risks as bumps. Iannacchione and others indicate that non continuous caving at a longwall coal mine in Australia contributes to dangerous windblasts on the longwall face. Overburden plays a role in this case also, as the panel is overlain by a massive conglomerate, but the mining is fairly shallow with overburden ranging from 90 to 170 m. In this case the roof remains intact behind the shields for longer than is optimal with very large falls occurring periodically. Like bumps, these falls may be preceded by increased microseismic activity and pose many of the same risks (Iannacchione et al. 2007).

2.2.5. Stress Behavior in Underground Mines

As ore is extracted in underground mines the preexisting stress is redistributed around the excavated areas resulting in regions of tensile and compressive stress, with the follow parameters influencing the excavation damage zone:

- In situ stress magnitudes, orientations, and ratios
- Shape of the excavation
- The excavation method
- Geology
- Environmental factors
- Nearby excavations

(Martino and Chandler 2004).

Abutment stresses occur along or near the boundary where material has been removed (Peng and Chiang 1983). During longwall mining, coal is removed and the stress is transferred immediately in front of the face and to the sides of the longwall panel, headgate and tailgate. Failure of the strata behind the shields allows for pressure relief. Very competent strata, such as massive sandstone, may not cave immediately, contributing to extremely high abutment stresses which can result in bumps and shield damage from dynamic loading (Haramy et al. 1988). A fast retreat rate can promote caving so that time-dependent loading ahead of the face is avoided (Kneisley and Haramy 1992), and when the retreat rate is slowed this loading can lead to shield convergence and roof failure at the face (Kelly 2000).

The distribution of the abutment load is dependent on all the parameters listed above, but a widely accepted general stress abutment schematic is displayed in Figure 2.5 (Peng and Chiang 1983).

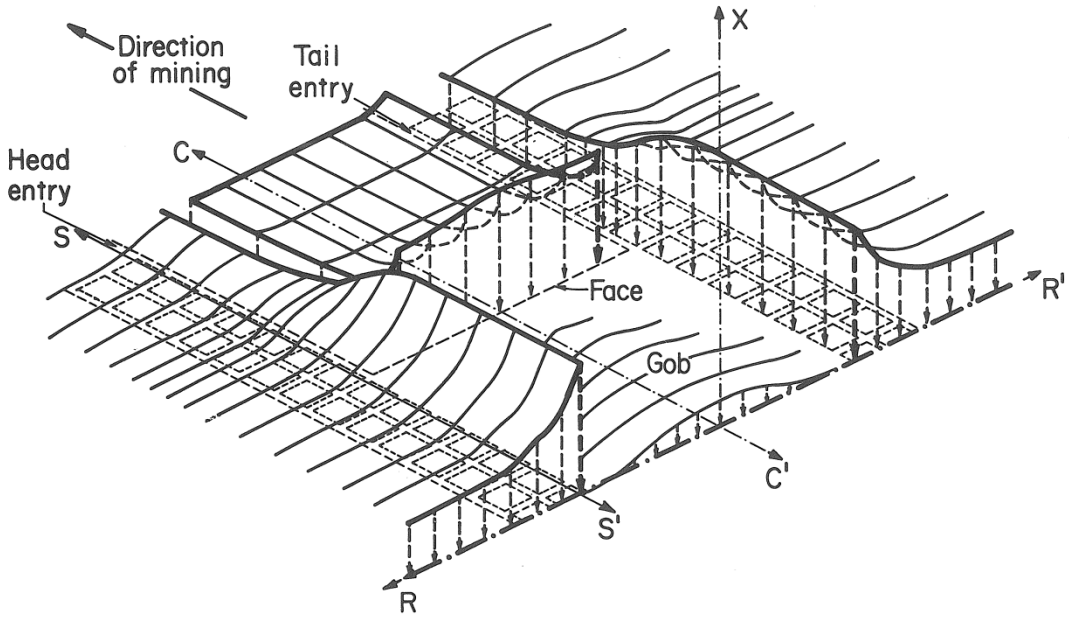

Figure 2.5. Idealized three-dimensional representation of vertical stress around longwall panel (Peng 1986).

2.2.6. Numerical Stress Analysis

Numerical stress analysis methods have found widespread application in rock mechanics and mine stress modeling. Most numerical modeling routines fit into one of the following classifications: finite element methods, boundary element methods, discrete element methods, finite difference methods, or some combination of the four.

Finite element methods are continuum methods and can be used for any process that is governed by a differential equation. The structure, a rock mass, for instance, is divided into elements that are connected at nodes. Displacement at the nodes can be calculated and related to stress and strain (Pande et al. 1990).

The finite difference method, a continuum method, divides the model into rigid blocks that interact at the edges and corners to satisfy force and displacement conditions. This method is appropriate for investigation of large deformations and allows for regular and irregular boundaries (Jeremic 1985; Barla et al. 2003).

The boundary element method is also a continuum method, but only the surface of the body is divided into elements. In a rock mass this would be the outside of the rock mass, and any interface where material properties change. This method is efficient and appropriate for homogenous and linear elastic behavior in rocks, but is not as flexible as the finite element method (Pande et al. 1990).

The discrete element method involves discretizing the body into elements of practically any shape and assigning the elements material and contact properties. The contact relationships between elements are monitored with time, and equations of dynamic equilibrium for each element are solved to meet the requirements for contact and boundary conditions. Unlike boundary element, finite element, and finite element methods, discrete element is a discontinuum method. This method can be computationally expensive and requires careful selection of material behavior (Pande et al. 1990).

Several commercial programs are used extensively for rock stress modeling in the mining industry, including LAMODEL, UDEC, FLAC^{2D}, and FLAC^{3D}. LAMODEL (Laminate Model) is a boundary element, displacement-discontinuity routine that calculates stresses and displacements in thin tabular seams (Heasley 1998). It simulates the overburden as a stack of homogenous isotropic layers with the same Poisson's ratio and Young's Modulus, and with frictionless interfaces. LAMODEL is available through the National Institute for Occupational Safety and Health (NIOSH) and has been used extensively for stress modeling (Bauer et al. 1997; Ellenberger et al. 2003; Zingano et al. 2005). UDEC, FLAC^{2D}, and FLAC^{3D} (Fast Lagrangian Continua Analysis), commercial programs available through Itasca, have also been implemented

in a number of studies (Badr et al. 2003; Gale et al. 2004; Vandergrift and Garcia 2005; Zingano et al. 2005). FLAC is a continuum code utilizing finite difference formulation. Other codes used to model mine behavior include BESOL (Karabin and Evanto 1999) , and Free Hexagonal Element Method (Procházka 2004).

In addition to numerical modeling, a number of instruments and techniques are used to measure stress in underground mines. These measurements are very useful in validating models and in providing real information for input parameters. However, they are time consuming and can generally only provide an idea of the state of stress in a localized area.

2.2.7. Microseismic Monitoring

Roof talk or rock talk, the audible noises that can be heard in the strata of a mine, have long been an indication to miners that changes are taking placing in strata. Obert and Duvall realized the importance of microseismic events in the 1930's while taking sonic measurements in an underground mine. They discovered that a rock pillar under stress was emitting microlevel sounds (Obert 1941; Obert and Duvall 1967). Numerous other researchers have verified that rocks under stress emit acoustic emissions in the laboratory and microseismic events in mines (Shah and Labuz 1995; Hardy 2003; Iannacchione et al. 2004; Filimonov et al. 2005).

Microseismic monitoring in mines allows for calculation of microseismic event source location, magnitude, and source mechanisms. Microseismic systems have been installed in many mines with a history of bumps or rockbursts. Cook utilized an array of geophones in an underground gold mine in South Africa to determine that most of the tremors experienced were mining-related (1963). In the United States much of this research was conducted by the Bureau of Mines (Blake et al. 1974). Brady describes monitoring of anomalous seismic changes that were recorded prior to 3 moderate rockbursts in the Star Mine in Idaho (1977). A mine in the Coeur D'Alene district in Idaho was instrumented to record blast signals which were analyzed in order to improve location algorithms for microseismic monitoring of mines (Swanson et al. 1992). Microseismic monitoring was implemented to investigate a rockburst at Sunshine Mine in Idaho, and seismic activity around the location of the burst indicated distressing (Scott et al. 1997).

Li and others give a thorough review of microseismic monitoring in mines in China for the prevention of rockbursts and outbursts beginning with the first microseismic system installation in 1959 (2007). Noranda's Brunswick No. 12 Mine, a zinc-lead-copper-silver mine in Canada, installed a microseismic monitoring system and developed a rockburst hazard technique based on seismic activity in the mine (Alcott et al. 1998). Microsesimic monitoring at Newstan

Colliery in Australia suggested that there is a buildup of total energy prior to windblast events (Hebblewhite and Simpson 2001). Prugger and Gendzwill correlate microseismic events with failures in Sasketchewan potash mines monitored by microseismic event arrays (1993). An MSHA fatality report from 1998 details use of a microseismic system during a microseismic event that resulted in two deaths. The microseismic system immediately alerted the operators to a problem when the event occurred, but there was no discernible warning of an imminent event (Cain et al. 2001). Microseismic systems can be useful in understanding when parts of the mining horizon are becoming unstable, but in some cases massive failure can occur with little or no warning. Microseismic systems have also been useful in locating and investigating events after they occur.

Ge lists 5 parameters for design of a successful microseismic monitoring system in a mine:

1. The monitoring volume should be surrounded in the x,y, and z directions.
2. Sensors should be located not only in the target zone, but also in the surrounding rock mass.
3. The sensors should be placed so that the array is balanced.
4. Two-dimensional arrays should be avoided as they will give poor accuracy perpendicular to the plane of sensors.
5. Frequency distributions for event signals and noise should be carefully studied, so that events may be separated from noise through appropriate filters.

(Ge 2005).

In longwall coal mines research has shown that more events are detected in the front abutment stress zones than in the gob where caving is taking place. Also, Maxwell and Young indicate that microseismic activity is highest in high velocity areas (1996). This is because the events occurring in the front abutment zones are usually compressive failures, resulting in high energy that propogate well through the intact strata. Conversely, events in the gob are more often lower energy tensile events that have a high attenuation rate as they propagate through the broken strata (Kelly 2000; Heasley et al. 2001; Iannacchione et al. 2005).

2.3. Seismic Velocity Tomography

2.3.1. Introduction

Tomography is a method for noninvasive imaging of a solid body; the body may be a manmade structure, a human body, or a geologic structure. It requires dividing the body into grid cells, or pixels, in a two-dimensional situation or cubes, or voxels, in the three-dimensional

situation, with the goal of estimating some characteristic value of the solid for each cell, so that a complete image can be generated (Cox 1999). The Radon Transform provides much of the basic framework for tomography. Radon proved that an infinite number of rays passing through a two-dimensional object at an infinite number of angles could be used to perfectly reconstruct the object (Radon 1917; Deans 1983). Tomography was first developed for use as a medical diagnostic tool and is still used extensively for this purpose. Cormack and Hounsfield developed tomography for the medical field with Cormack developing the theory in the early 1960s and Hounsfield translating it into practice in 1971 (Cormack 1992; Blahut 2004). Bracewell published research on reconstruction algorithms in 1956 for radio astronomy which were also instrumental in the development of tomography (Bracewell 1956; Blahut 2004).

Geophysical tomography, specifically seismic tomography, was realized in the early 1980s with studies examining the use of tomography for imaging of fluctuations in an ocean basin (Munk and Wunsch 1979), characterization of crystalline rock for nuclear waste depositories (Gustavsson et al. 1982), and imaging of subsurface subsidence due to mining (Albright et al. 1981).

2.3.2. Relationship between stress and velocity in rocks

Velocity tomography involves the measurement of seismic wave velocity through a medium and relies on the concept that the seismic wave velocity through a material is closely connected to the elastic constants of the material (Adams and Williamson 1923). One of the first characterizations of the Earth by examination of seismic wave velocity was by Mohorovic who identified an abrupt change in wave velocity at the boundary of the Earth's crust and mantle, now known as the Moho discontinuity (Mohorovicic 1909; Jensen and Thybo 2002; Rawlinson and Sambridge 2003). The velocity of a seismic wave is dependent on several parameters including rock type, degree of fracture, anisotropy, porosity, stress, elastic constants, and boundary conditions. While stress can be inferred from velocity measurements these other parameters also play a role.

Seismic waves can be divided into four parts: Rayleigh waves, Love waves, P-waves, and S-waves. Rayleigh waves and Love waves are surface waves; they only travel along the free surface of an elastic body (Sharma 1986). P-waves are also referred to as longitudinal or primary waves and they cause the particles of a medium to expand and contract as they travel through it. Additionally, the P-wave is the first part of the wave form to arrive. S-waves, also known as shear waves, cause particles to move perpendicular to the direction of wave travel. P- and S-

wave velocity equations are displayed below in equations 2.12 and 2.13, respectively (Sharma 1986).

$$V_p = \sqrt{\frac{(1-\upsilon)Eg}{(1+\upsilon)(1-2\upsilon)\gamma}} \quad \text{(m/s)} \qquad \text{[Eq. 2.12]}$$

$$V_s = \sqrt{\frac{Eg}{2(1+\upsilon)\gamma}} \quad \text{(m/s)} \qquad \text{[Eq. 2.13]}$$

E = Young's Modulus (Pa)

g =graviational acceleration (m/s^2)

υ = Poisson's ratio (unitless)

γ = Density (kg/m^3)

Figure 2.6 displays particle motion for P- and S- waves.

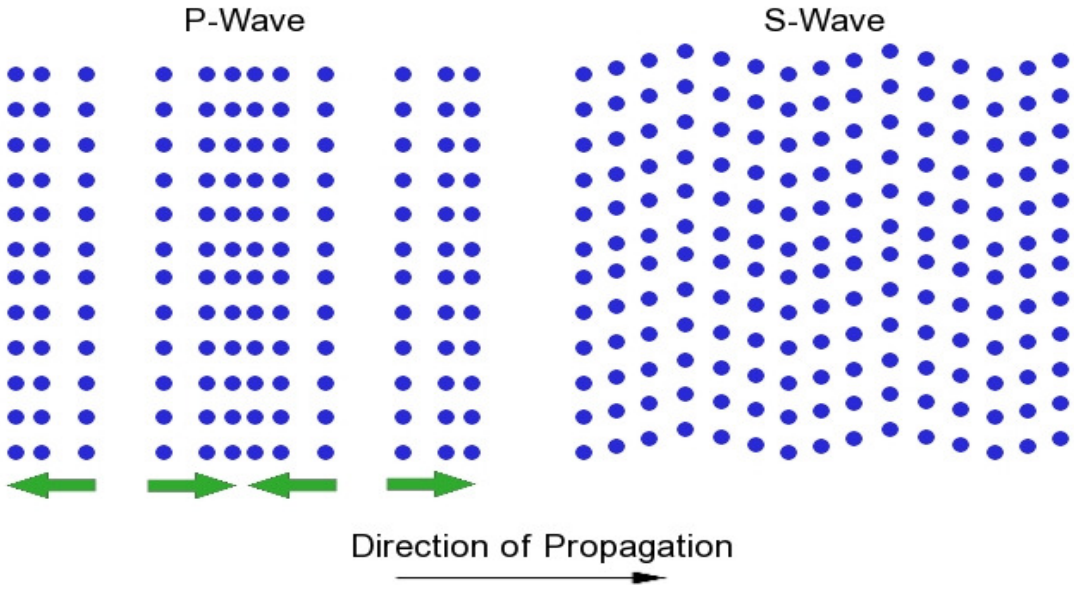

Figure 2.6. P-wave and S-wave particle motion (adapted from Sharma 1986).

Adams and Williamson studied the compressibility of rocks and found that compressibility decreases as pressure is increased (1923). Compressibility is defined as the reciprocal of the bulk modulus, K (Goodman 1989), displayed in equation 2.5. It follows that Young's Modulus increases steadily with low pressures and then flattens out with higher pressures. Recalling equation 2.12 and assuming that density increase is negligible, an increase in Young's Modulus will result in increasing P-wave velocity for lower pressures, with little to no increase at higher pressures.

An increase in P-wave velocity in rocks with application of pressure is attributed to the closure of cracks and pore space (Wyllie et al. 1958; Thill 1973; Toksöz et al. 1976; Seya et al. 1979; Young and Maxwell 1992). Open pores and microfractures will either diffract seismic waves or cause a decrease in velocity as the wave travels through the open space. Most rocks show some decrease in porosity with pressure and an increase in P-wave velocity, with the exception of some rocks, such as dolomite, with a high matrix density (Yale 1985). The P-wave velocity gradient is usually highest at low pressures and then begins to level out at higher pressures (Prasad and Manghnani 1997). Velocity can be used to infer stress distribution but the relationship is not linear. At higher confining stresses little difference will be seen in velocity.

Saturation and pore fluid also affect velocity, because these parameters affect density and elastic moduli (Toksöz et al. 1976). P- and S-wave velocities will increase more rapidly with respect to pressure for a dry rock specimen than for a wet rock specimen. This is because pore pressure acts against confining pressure so that effective pressure is lower for a saturated sample than for a dry sample (King 1966; Jones and Wang 1981) . S-wave velocity is less sensitive to saturation than P-wave velocity (Popp and Kern 1994). Also, seismic velocity can vary with the direction of the bedding plane in rock. Cox gives a range of values from 1.0 to 1.45 for the ratio between P-wave velocity parallel and perpendicular to the bedding plane (Cox 1999).

Several studies have been conducted to explore the effect of various parameters on seismic velocity in rocks. Nur and Simmons subjected cylindrical samples of Barre granite to uniaxial loading, and varied the angle of the load. They measured P- and S-wave velocity in the sample, and found a velocity increase with increased stress. They also found that the magnitude of the velocity increase was dependent on the stress direction and direction of P-wave propagation. The most significant velocity change occurred when the wave was propagated perpendicular to the load (Nur and Simmons 1969). Toksöz and others used observed laboratory data, some from the 1969 study of Nur and Simmons, to model velocity for *in situ* rock given porosity, saturation, overburden, and pore fluid pressure (1976). Eberhart-Phillips and others measured the effects of pressure, clay content, and porosity on the velocity of 64 sandstone samples and they also found an exponential increase in velocity at low pressures that tapered off to a linear increase for higher pressures (1989).

2.3.3. Source Location

The location of sources in relation to the area under tomographic study is extremely important. Ideally, the mass under study should be completely surrounded by sources and

receivers. While this is relatively easy to achieve in a medical setting, it is less easily achieved in the geophysical setting.

Passive or active sources may be used in geophysical velocity tomography. The advantage to using active sources is that their location may be optimized, so that the body of interest is surrounded by the most favorable geometry that is feasible given the limitations of where receivers and sources may be placed. Examples of active sources used in underground mines are hammer strikes against roof and rib bolts, mining equipment, and controlled explosions. The disadvantage to these sources is that a person must be physically present to initiate the hammer blow or explosion, or determine the location of the mining equipment. Therefore, these active sources are not generally feasible for long term studies.

Mining-induced microseismic events may be used as passive sources for seismic velocity tomography of mines. The advantage to using these sources is that a person does not need to be physically present to initiate them, and they are practical for long term, remote studies. However, location of the events is not physically measured, but calculated from arrival times at receivers, so some error may be present in the locations. Also, ray density for passive events is less uniform leaving some regions with less data than others. Figure 2.8 compares active and passive source geometries along with subsequent straight ray coverage.

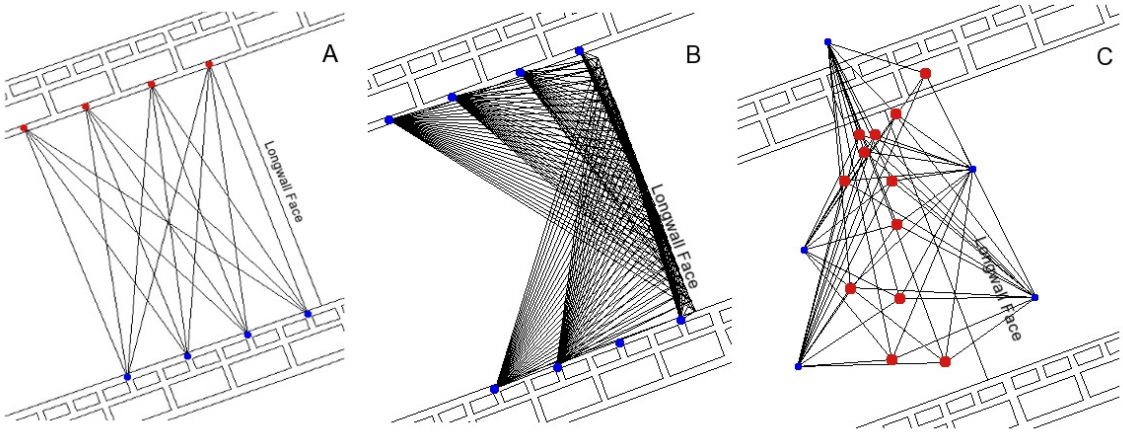

Figure 2.7. Passive and active source-receiver configurations on a longwall panel. Figure 2.8A shows raypaths for headgate-mounted receivers with sources initiated on the tailgate. Figure 2.8B displays straight raypaths for receivers mounted in the head- and tail- gates with the longwall shearer used as a source. Rays for one pass of the shearer are shown. Figure 2.8C displays passive source configuration with 12 mining-induced microseismic events and 5 surface-mounted receivers above the panel. Sources are displayed in red and receivers are displayed in blue.

Seismic event location is a complex subject that is only briefly reviewed here. The impact of event location quality on passive velocity tomography methods cannot be

underestimated, because any error in event location is translated into error in the tomogram. Swanson and others list four steps for locating seismic events (1992):

1. Determine the spatial coordinates of the receivers
2. Measure the arrival times at each station generated by the event
3. Establish a model of the seismic velocity structure in the rock mass of interest
4. Solve for the location of the event

Factors that can cause source location error are:

- Bias of the location technique
- Receiver array geometry
- Uncertainty in receiver positions
- Errors in picking the arrival times
- Uncertainty in the seismic velocity structure

(Swanson et al. 1992; Hardy 2003)

2.3.4. Inverse Theory and Methods

According to Menke, inverse theory is "an organized set of mathematical techniques for reducing data to obtain useful information about the physical world on the basis of inferences drawn from observations" (1989). Most inverse problems are ill-posed, meaning that they often have an infinite number of solutions that will fit the data, and a few of these solutions are reasonable when *a priori* data are considered (Hole 1992). While the idea of an ill-posed problem is somewhat abstract it is simpler to define the well-posed problem (Hadamard 1902; Hadamard 1952; Tarantola 1987; Mosegaard and Tarantola 2002; Yagola et al. 2002):

- A solution exists
- The solution is unique
- The solution depends on continuous data

The ill-posed problem does not meet one or more of the preceding requirements.

Inverse problems may be underdetermined or overdetermined; the underdetermined problem has more unknowns than data, while the opposite is true of the overdetermined problem. For example, in three-dimensional velocity tomography an overdetermined system has more rays than voxels (Tarantola 1987; Menke 1989; Manthei 1997).

Jackson and Tweeton define two categories of iterative methods: Fourier transformation and convolution and series expansion methods. Fourier transformation and convolution methods are used routinely in medical tomography, but they require particular source-receiver

configurations and generally are not appropriate for geophysical problems (Jackson and Tweeton 1994; Kalra et al. 1999).

Series expansion methods include matrix inversion methods and iterative methods. Matrix inversion methods consist of: back-projection, least-squares, damped least-squares, and singular value decomposition (Jackson and Tweeton 1994). The following equation is an expression of the time required for a seismic ray to travel from a source to a receiver and is the basis of velocity tomography, simply stating that the time a seismic ray takes to travel from one point to another is equal to the slowness of the area traversed times the distance the ray travels:

$$t_i = \sum_{j=1}^{M} p_j d_{ij} \qquad (i = 1 \ldots N) \qquad \text{[Eq. 2.14]}$$

t_i = travel time of the i^{th} ray (s)

p_j = slowness in the j^{th} voxel (s/m)

d_{ij} = distance of the i^{th} ray in the j^{th} voxel (m)

N = number of observations

M = number of pixels or voxels

(Jackson and Tweeton 1994).

This equation can also be expressed in matrix form as:

$$\boldsymbol{T} = \boldsymbol{DP} \qquad \text{[Eq. 2.15]}$$

$\boldsymbol{T}$= column vector of travel times (N x 1)

$\boldsymbol{P}$= column vector of slowness values (M x 1)

$\boldsymbol{D}$= matrix of ray distances (N x M)

By inverting the matrix $\boldsymbol{D}$, the slowness matrix, $\boldsymbol{P}$, can be solved for:

$$\boldsymbol{P} = \boldsymbol{D^{-1}T} \qquad \text{[Eq. 2.16]}$$

If $\boldsymbol{D}$ is a singular matrix, which is often the case, then this calculation is not accomplished so directly. The back-projection technique allows for use of the transpose of the distance matrix, $\boldsymbol{D}$:

$$\boldsymbol{P} = \boldsymbol{D^{*T}T} \qquad \text{[Eq. 2.17]}$$

The least-squares solution provides for the following:

$$\boldsymbol{P} = \left(\boldsymbol{D^T D}\right)^{-1}\boldsymbol{D^T T} \qquad \text{[Eq. 2.18]}$$

However, $\boldsymbol{D^T D}$ may also be singular, so a damped least-squares method may be utilized:

$$\boldsymbol{P} = \left(\boldsymbol{D^T D} + \lambda \boldsymbol{I}\right)^{-1}\boldsymbol{D^T T} \qquad \text{[Eq. 2.19]}$$

λ = damping parameter

$\boldsymbol{I}$ = Identity Matrix (M x M)

The damping parameter in equation 2.19 controls the process of minimization of the data misfit and the model norm (Aki and Lee 1976; Spakman 1993). The data misfit is the difference between the measured and predicted data, while the norm is a way of sizing and ranking data. There are several ways to calculate norms, thoroughly reviewed by Menke (1989).

Equations 2.15 through 2.19 are presented in the notation used by Jackson and Tweeton, who give a detailed review of these methods (1994).

Singular Value Decomposition (SVD) (Golub and Reinsch 1971) is an algorithm that decomposes the data into eigenvectors. SVD is an appropriate method for small problems, but may be computationally inefficient for large data sets because it produces large, dense matrices (Bording et al. 1987; Deidda and Ranieri 2005).

The matrix inversion methods are effective, but require considerable computational power for large datasets. As affordable computers become more powerful this issue becomes less substantial, but iterative methods may be implemented at much lower computational cost. The most referenced methods are Algebraic Reconstructive Technique (ART), and Simultaneous Iterative Reconstructive Technique (SIRT) (Gilbert 1972). They are both subsets of Kaczmarz' method for solving series expansion problems (Kaczmarz 1937; Stewart 1991; Lo and Inderwiesen 1994). Additionally, multiplicative algebraic reconstructive technique (MART) is occasionally cited in the literature (Stewart 1991). ART and SIRT both involve perturbing a velocity matrix until a solution converges. ART perturbs one ray path at a time and then updates the model. Conversely, SIRT perturbs all of the raypaths and calculates a model correction for each, then averages all of the corrections before updating the model. SIRT algorithms converge to a solution more slowly than ART algorithms, but they also tend to be more stable once they have converged (Gilbert 1972; Dines and Lytle 1979; Guney et al. 1992). Dines and Lytle published experimental data contrasting convergence time and stability for ART and SIRT, displayed in Figure 2.8.

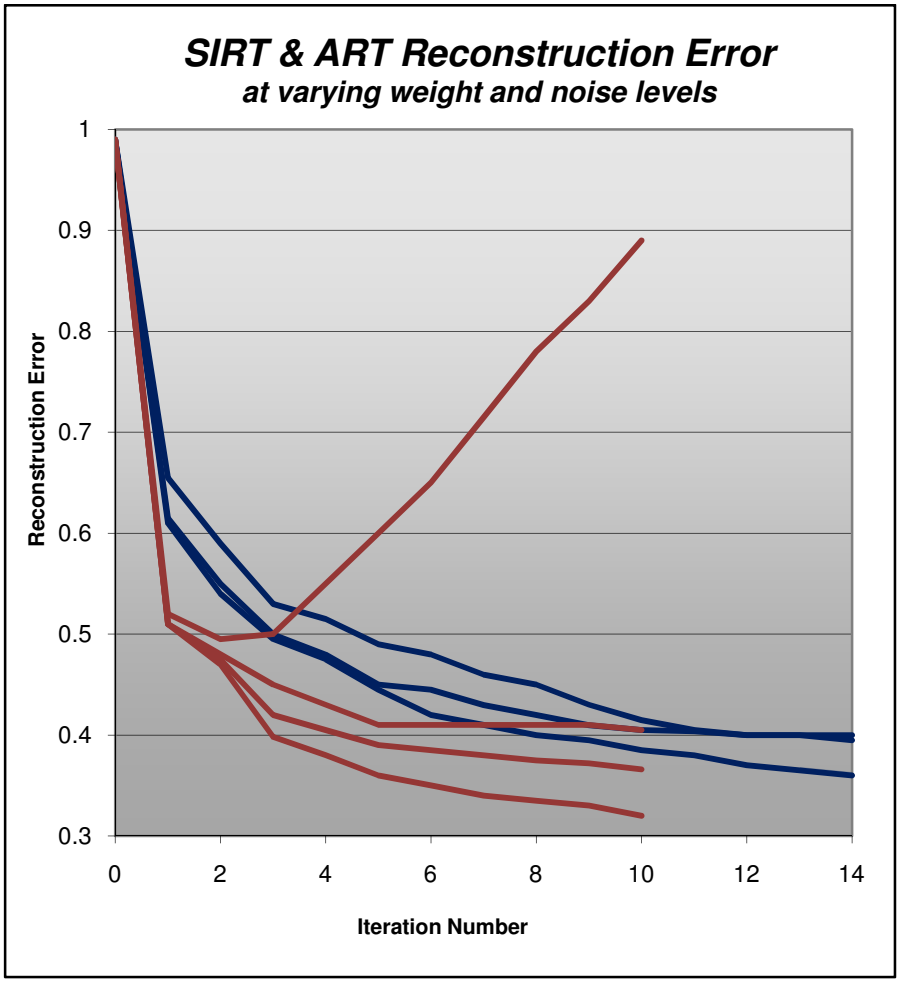

Figure 2.8. Experimental Convergence for SIRT and ART (Dines and Lytle 1979). The SIRT experiment is shown in blue, while the ART experiment is shown in red.

Double difference tomography refers to a hybrid form of tomography where the microseismic event location method is linked to the velocity model determined through inversion, so as the velocity model is updated, the event locations are recalculated. Waldhauser and Ellsworth point to several studies indicating that joint inversion for hypocenters and velocity structure can help account for biases in the initial three-dimensional velocity structure used for determining event locations (Crosson 1976; Michael 1988; Kissling et al. 1994; Waldhauser and Ellsworth 2000).

2.3.5. Resolution and Error

Resolution is one of the most important parameters to consider when evaluating tomograms. Resolution can be defined in several different ways and determined qualitatively and quantitatively. In imaging, resolution generally refers to the "sharpness" of the image.

Soldati and Boschi define resolution as "the highest spatial frequency at which a tomographic image is expected to be meaningful, limited by quality of the data and adequacy of the parameterization," (2005), while Menke states that the rows of the data resolution matrix "describe how well neighboring data can be independently predicted or resolved" (1989). Resolution is typically dependent on three factors: the distribution of the velocity, the source-receiver geometry, and the wavelength (Dyer and Worthington 1988). Higher velocity contrasts will cause more ray bending and more uneven ray coverage, which can adversely affect resolution. Also, source-receiver geometry will affect ray coverage. Some authors indicate that resolution is related to wavelength with theoretical resolution being about one wavelength (Friedel et al. 1997; Watanabe et al. 1999). Others indicate that objects smaller than the first Fresnel zone cannot be distinguished (Böhm et al. 2000), while Tselentis and others found that structures smaller than their 1 km wavelength could be resolved (2007). Soldati and Boschi state that data noise is more of a factor in resolution than data coverage (2005).

When a resolution matrix is calculated, the farther the matrix deviates from the identity matrix, **I,** the poorer the resolution (Aki and Lee 1976; Tarantola 1987; Menke 1989). The reliability of a model can be characterized by this resolution matrix, but synthetic tests including checkerboard tests can also be used to determine resolution (Tong 2000; Rawlinson and Sambridge 2003; Zhang and Thurber 2003). Ray density plots may also be appropriate for a qualitative description of resolution (Deidda and Ranieri 2005). Soldati and Boschi indicate that the use of synthetic tomograms and checkerboard tests is implemented because they are computationally cheap compared to calculation of a resolution matrix, and that modern computing power allows for this computation. They also assert that the resolution matrix is more rigorous than synthetic tests or ray density plots (Soldati and Boshi 2005), while others disagree (Deidda and Ranieri 2005). The resolution matrix can only be calculated for direct inverse techniques (Deidda and Ranieri 2005; Soldati and Boshi 2005), so while the best way to determine resolution is debatable, synthetic methods must be employed for iterative inverse techniques such as SIRT and ART.

Menke gives a simple description of resolution matrix calculation. First, the inverse problem is defined as:

$$\mathbf{Gm=d} \qquad \text{[Eq. 2.20]}$$

Where,

G is the data kernel (ray distance per cell),

m is a matrix of model parameters (slowness), and

d is a matrix of data (travel times)

The solution to this problem is $\mathbf{m}^{est}=\mathbf{G}^{-g}\mathbf{d}$ [Eq. 2.21]

Where,

$\mathbf{m}^{est}$ is the estimate of model parameters,

$\mathbf{G}^{-g}$ is the inverse of $\mathbf{G}$.

It follows that:

$\mathbf{m}^{est} = \mathbf{G}^{-g}\mathbf{d}^{obs} = \mathbf{G}^{-g}[\mathbf{G}\mathbf{m}^{true}] = [\mathbf{G}^{-g}\mathbf{G}]\mathbf{m}^{true} = \mathbf{R}\mathbf{m}^{true}$ [Eq. 2.22]

Where,

$\mathbf{d}^{obs}$ are the observed data,

$\mathbf{m}^{true}$ is the true, but unknown set of model parameters, and

$\mathbf{R}$ is the resolution matrix

(Menke 1989).

Equation 2.22 illustrates that resolution relates the estimated model parameters with the true model parameters. Menke also gives a visual demonstration of what the resolution matrix means. He shows a matrix with one peak plotted in each row that corresponds with the diagonal of the matrix. As the peaks narrow near the main diagonal the model, $\mathbf{m}^{est}$, is better resolved (Menke 1989).

In synthetic tomography the starting model is comparable to $\mathbf{m}^{true}$, and the calculated model is comparable to $\mathbf{m}^{est}$, so a comparison of the two models gives an idea of resolution.

There are several examples in the literature of the use of ray density plots and synthetic tomography to determine resolution. Deidda and others used SIRT to map a retaining wall and indicated that ray density is an appropriate alternative to resolution (2005). Tselentis and others imaged checkerboards with a ±10% velocity perturbation and added Gaussian noise (2007). Monteiller and others estimated resolution with checkerboard tests and show multiple reconstructions (2005). Běhounková and others produced checkerboard tests of the Earth's mantle (2005). Clement and others conducted a tomography experiment with synthetic data, comparing their results to the original model (2000.)

There is a tradeoff between resolution and variance, another important consideration. Improved resolution equates to poorer variance. A perfectly resolved tomogram would theoretically have one ray traversing each voxel. This would equate to poor data variance, where good data variance would involve many rays traversing each voxel. Variance is a measure of uncertainty in the pixel value, and pixel size should be chosen so that variance and resolution are optimized.

2.4. Applications of Tomography to Mining

Applications of tomography are extensive; tomography is utilized in medicine, geology, mining, structural investigations, and fluid flow processes. In the mining industry applications of tomography are in exploration and ore delineation, mapping of geologic structures and discontinuities, and imaging of the state of stress.

There are several examples of the use of tomography as an exploration tool, often in conjunction with borehole exploration. Crosshole tomography was used to delineate a massive sulphide deposit at a base metal mine in Canada (McGaughey and Vallee 1997); Crosshole seismic tomography in the Kambalda nickel district in Australia using active sources imaged a low velocity zone that was thought to be massive nickel sulphide. However, further exploration showed the velocity anomaly was actually due to chemical alteration in the host rock (Greenhalgh et al. 2003).

Seismic tomography has also been used extensively to map faults and other structures that can impede production or endanger miners. A longwall coal mine in England was experiencing production delays due to faults in the coal seam. Velocity tomography with active sources was successfully used to map a fault in the seam ahead of mining (Mason 1981). Watanabe and Sassa conducted two experiments in mines in Japan with the aim of imaging faults. Both active seismic velocity tomography and seismic attenuation tomography were used for areas between three galleries. They were able to image faults in both cases, but more clearly with attenuation tomography (Watanabe and Sassa 1996). A longwall mine in South Africa was experiencing similar problems and mapped a sandstone channel ahead of mine with active velocity tomography. Mining verified the channel, although the location was slightly different. This was attributed to incomplete ray coverage (Hanna and Haramy 1998; Hanson et al. 2002). In a room and pillar coal mine there was suspicion that old workings may be present near the current workings due to drifts discovered at the outcrop of the seam. Velocity tomography with active sources was implemented, and showed that the workings did not extend far from the outcrop. Subsequent mining did not encounter any old works (Hanson et al. 2002).

There is also precedent for the use of velocity tomography in monitoring coal bed methane wells. Crosswell tomograms were generated over three years between three wells in the Powder River Basin in Wyoming. The area was surveyed prior to dewatering and a decrease in velocity was detected after dewatering as gas saturation in the seam increased (Harris and Akintunde 2005).

There are numerous examples in the literature of the use of velocity tomography for inference of stress distribution in mines. One of the first such studies was conducted in a

Hungarian longwall mine by Körmendi and others. Active velocity tomography displayed low velocity zones in areas of broken rock and high velocity zones immediately in front of the face. The high velocity zone did not always redistribute with face advance, probably due to the fault structure. Also, velocity increases during a production stoppage were imaged (Körmendi et al. 1986). At Lockerby Mine in Canada, which mines in a nickel-rich deposit, a sill pillar was imaged with active sources. The low velocity zone corresponded with drill samples that were extensively fractured while the high velocity zone corresponded with samples showing severe core disking (Young and Maxwell 1992).

Maxwell and Young describe two case studies implementing velocity tomography. The first was conducted at the Underground Research Lab in Canada using active sources. Known stress changes and fractured areas were successfully mapped. The second study imaged a sill pillar in a South African Gold Mine using active sources. High velocity zones were imaged ahead of mining (Maxwell and Young 1993). In another paper, they describe a study at Strathcona Mine in Canada, mining a steeply dipping copper nickel sulfide deposit. Active sources were used to image active areas, then they back calculated the sources using source location methods and generate a passive tomogram; the two tomograms were comparable (Maxwell and Young 1995).

Friedel and others imaged a pillar at Foidel Creek Mine in Colorado using active velocity tomography. They were able to image a velocity footprint that was consistent with expected pillar stress (Friedel et al. 1996). Friedel and others also used active velocity tomography to image areas of Homestake Mine and Lucky Friday Mine. They found velocity changes occurred with failure and stope advance (Friedel et al. 1997)

An Australian longwall coal mine was experiencing periodic shield loading due to discontinuous caving. Attenuation tomography was used image to low attenuation at midface, corresponding with high stress. The low attenuation zone occurred periodically in concert with caving (Hanna and Haramy 1998; Hanson et al. 2002). The same papers describe the use of attenuation tomography at a bump prone longwall coal mine in Germany. Over five days they imaged a low attenuation zone corresponding with the expected front abutment zone. They also conducted drilling stress monitoring that indicated agreement with the tomograms (Hanna and Haramy 1998; Hanson et al. 2002).

Scott and others imaged a pillar at Homestake Mine using active sources. Laboratory testing of core samples showed that P-wave velocity was lower in the field than the laboratory, which was attributed to large cracks in the rock mass (1999).

Wright and others conducted active velocity tomography in a South African iron ore mine and showed large velocity variations as a tunnel was excavated agreeing with expected stress redistribution (2000).

Westman and others conducted seismic attenuation tomography using active sources at a longwall mine, and were able to demonstrate correlation between increased shield leg pressure and low attenuation zones. Additionally, the low attenuation zones were the most seismically active (Westman et al. 2001).

Scott and others conducted a velocity tomography study at Edgar experimental Mine in Colorado. They were able to image know geological features. Also, velocity changes in the tomogram correlated well with stress zones in a finite difference model, and field velocities correlated well with ultrasonic measurement of core in the laboratory (Scott et al. 2004).

At Palabora Mining Company's copper mine in South Africa passive velocity tomography was implemented to determine if the stress state in the mine could be imaged. Tomograms confimed what was known about the state of stress in the mine (Glazer and Lurka 2007).

References

Adams, L. and E. Williamson (1923). "On the compressibility of minerals and rocks at high pressures." Journal of the Franklin Institute **195**: 475-531.

Aki, K. and W. Lee (1976). "Determination of three-dimensional velocity anomalies under a seismic array using first p arrival times from local earthquakes." Journal of Geophysical Research **81**(23): 4381-4397.

Albright, J., P. Halleck, C. Pearson and M. Fehler (1981). Subsurface subsidence damage monitoring; seismic tomography and microgravimetry. Workshop on surface subsidence due to underground mining, Morgantown, WV, West Virginia University.

Alcott, J., P. Kaiser and B. Simser (1998). "Use of microseismic source parameters for rockburst hazard assessment." Pure and Applied Geophysics **153**: 41-66.

Arjang, B. and G. Herget (1997). "In situ ground stresses in the Canadian hardrock mines: an update." International Journal of Rock Mechanics & Mining Sciences and Geomechanics Abstracts **34**(3): 652.

Badr, S., R. Mendoza, S. Kieffer, M. Salamon and U. Ozbay (2003). Numerical modeling of longwalls in deep coal mines. 22nd International Conference on Ground Control in Mining, Morgantown, WV, West Virginia University.

Barla, G., M. Barla, A. Chiappone, U. Rabagliati and L. Repetto (2003). Continuum and discontinuum modelling of a high rock cut. ISRM - Technology Roadmap for Rock Mechanics, South African Institute of Mining and Metallurgy.

Bauer, E., G. Chekan and L. Steiner (1997). "Stability Evaluation of Extended Cut Mining in Underground Coal Mines." International Journal of Rock Mechanics, Mining Sciences, and Geomechanics Abstracts **34**(3): 664.

Běhounková, M., H. Čižkova and C. Matyska (2005). "Resolution tests of global geodynamic models by travel-time tomography." Geophysical Research Abstracts **7**: 343-364.

Blahut, R. (2004). Theory of Remote Image Formation. Cambridge, Cambridge University Press.

Blake, W., F. Leighton and W. Duvall (1974). Microseismic techniques for monitoring the behavior of rock structures: Bulletin 665, US Bureau of Mines.

Blès, J. and B. Feuga (1986). The Fracture of Rocks. New York, North Oxford Academic Publisher Ltd.

Böhm, G., P. Galuppo and A. Vesnaver (2000). "3D adaptive tomography using Delaunay triangles and Voronoi polygons." Geophysical Prospecting **48**: 723-744.

Bording, R., A. Gersztenkorn, L. Lines, J. Scales and S. Treitel (1987). "Applications of seismic travel-time tomography." The Geophysical Journal of the Royal Astronomical Society **90**: 285-303.

Bracewell, R. (1956). "Strip integration in radio astronomy." Australian Journal of Physics **9**: 198-217.

Brady, B. (1977). "Anomalous seismicity prior to rockbursts: Implications for earthquake prediction." Pure and Applied Geophysics **115**(102): 357-374.

Brady, B. and E. Brown (1985). Rock Mechanics for Underground Mining. London, George Allen & Unwin.

Braüner, G. (1994). Rockbursts in Coal Mines and Their Prevention. Rotterdam, AA Balkema.

Cain, S., R. Horn, I. Williams, G. Karabin and S. Phillipson (2001). Report of Investigation: Double Fatal Fall of Ground, Underground Metal Mine (Silver), Galena Mine. M. S. a. H. Administration. Wallace, ID, MSHA.

Clement, W. and M. Knoll (2000). Tomographic inversion of crosshole radar data: confidence in results. Symposium on the Application of Geophysics to Environmental and Engineering Problems, Arlington, VA, Environmental and Engineering Geophysical Society.

Cook, N. (1963). The seismic location of rockbursts. The 5th Rock Mechanics Symposium, Pergamon Press.

Cormack, A. (1992). Nobel Lecture: Early two-dimensional reconstruction and recent topics stemming from it. Nobel Lectures, Physiology or Medicine 1979-1980. Singapore, World Scientific Publishing Co.

Coulomb, C. (1773). "Sur une application des règles de maximis et minimis à quelque problèmes de statique relatifs à l'architecture." Mémoires de l'Académie Royale de Science **7**: 343-382.

Cox, M. (1999). Static Corrections for Seismic Reflection Surveys. Tulsa, OK, Society of Exploration Geophysicists.

Crosson, R. (1976). "Crustal structure modeling of earthquake data 1. Simultaneous least squares estimation of hypocenter and velocity parameters." Journal of Geophysical Research **81**(17): 3036-3045.

Crouch, S. and C. Fairhurst (1974). "Mechanics of Coal Mine Bumps." Transactions **256**: 317-322.

Deans, S. (1983). The Radon Transform and Some of its Applications. New York, Wiley.

Deidda, G. and G. Ranieri (2005). "Seismic tomography imaging of an unstable embankment." Engineering Geology **82**: 32-42.

Dines, K. and R. Lytle (1979). "Computerized geophysical tomography." Proceedings of the IEEE **67**(7): 1065-1076.

Dowling, N. (1998). Mechanical Behavior of Materials: Engineering Methods for Deformation, Fracture, and Fatigue: 2nd ed. Upper Saddle River, NJ, Prentice Hall.

Dyer, B. and M. Worthington (1988). "Some Sources of Distortion in Tomographic Velocity Images." Geophysical Prospecting **36**: 209-222.

Eberhart-Phillips, D., D.-H. Han and M. Zoback (1989). "Empirical relationships among seismic velocity, effective pressure, porosity, and clay content in sandstone." Geophysics **54**(1): 82-90.

Ellenberger, J., F. Chase, C. Mark, K. Heasley and J. Marshall (2003). Using Site Case Histories of Multiple Seam Coal Mining to Advance Mine Design. 22nd International Conference on Ground Control in Mining, Morgantown, WV, West Virginia University.

Ellenberger, J. and K. Heasley (2000). Coal mine seismicity and bumps: Historical case studies and current field activity. 19th International Conference on Ground Control in Mining, Morgantown, WV, West Virginia University.

Filimonov, Y., A. Lavrov and V. Shkuratnik (2005). "Technical Note: Effect of Confining Stress on Acoustic Emission in Ductile Rock." Strain **41**: 33-35.

Friedel, M., M. Jackson, E. Williams, M. Olson and E. Westman (1996). "Tomographic imaging of coal pillar conditions: observations and implications." International Journal of Rock Mechanics, Mining Sciences, and Geomechanics Abstracts **33**(3): 279-290.

Friedel, M., D. Scott and T. Williams (1997). "Temporal imaging of mine-induced stress change using seismic tomography." Engineering Geology **46**: 131-141.

Gale, W., C. Mark, D. Oyler and J. Chen (2004). Computer simulation of ground behavior and rock bolt interaction at Emerald Mine. 23rd International Conference on Ground Control in Mining, Morgantown, WV, West Virginia University.

Ge, M. (2005). "Efficient mine microseismic monitoring." International Journal of Coal Geology **64**: 44-56.

Gilbert, P. (1972). "Iterative methods for the three-dimensional reconstruction of an object from projections." Journal of Theoretical Biology **36**: 105-117.

Glazer, S. and A. Lurka (2007). Application of passive seismic tomography to cave mining operations based on experience at Palabora Mining Company, South Africa. The Southern African Institute of Mining and Metallurgy 1st International Symposium on Block and Sub-Level Caving, Cape Town, South Africa.

Golub, G. and C. Reinsch (1971). Contribution I-10: Singular Value Decomposition and Least Squares Solution. Linear Algebra: Handbook for Automatic Computation. F. Bauer. New York, Springer-Verlag. **2**.

Goodman, R. (1989). Introduction to Rock Mechanics: 2nd ed. New York, John Wiley and Sons.

Greenhalgh, S., B. Zhou and S. Cao (2003). "A crosswell seismic experiment for nickel sulphide exploration." Journal of Applied Geophysics **53**.

Griffith, A. (1921). "The Phenomena of Rupture and Flow in Solids." Philosophical Transactions of the Royal Society of London. **221**: 162-198.

Guney, R., E. Benson and A. Sarwar (1992). Imaging of the Earth by Iterative Reconstruction Methods. Theory and Practice of Geophysical Data Inversion: Proceedings of the 8th International Mathematical Geophysics Seminar on Model Optimization in Exploration Geophysics 1990. A. Vogel. Braunschweig, Wiesbaden, Veiweg. **5**.

Gustavsson, M., H. Israelson, S. Ivansson, P. Moren and J. Pihl (1982). "The seismic crosshole method in crystalline rock." SEG Abstracts **1982**(1): 471-472.

Hadamard, J. (1902). "Sur Les Problèmes Aux Dérivées Partielles Et Leur Significaiton Physique." Princeton University Bulletin(49-52).

Hadamard, J. (1952). Lectures on Cauchy's Problem in Linear Partial Differential Equations. New York, Dover Publications.

Hanna, K. and K. Haramy (1998). Ground control and geologic assessment in mining through the use of geophysical tomographic imaging. Geomechanics/Ground Control in Mining Underground Construction Conference, Wollongong, NSW, Australia.

Hanson, D., T. Vandergrift, M. DeMarco and K. Hanna (2002). "Advanced techniques in site characterization and mining hazard detection for the underground coal industry." International Journal of Coal Geology **50**: 275-301.

Haramy, K., J. Magers and J. McDonnell (1988). Mining under strong roof. 7th International Conference on Ground Control in Mining, Morgantown, WV.

Hardy, H. (2003). Acoustic Emission / Microseismic Activity. Lisse, Balkema.

Harris, J. and M. Akintunde (2005). Time-lapse seismic monitoring of coalbed natural gas production; a case study from the Powder River Basin: Report 55, Geological Survey of Wyoming**:** 109-126.

Heasley, K. (1998). Numerical modeling of coal mines with a laminated displacement-discontinuity code, PhD. Golden, CO: Colorado School of Mines, Department of Mining and Earth Systems Engineering.

Heasley, K., J. Ellenberger and P. Jeran (2001). An analysis of rock failure around a deep longwall using microseismics. 20th International Conference on Ground Control in Mining, Morgantown, WV, West Virginia University.

Hebblewhite, B. and J. Simpson (2001). "Wider longwall faces may not be better." Mining Technology: IMM Transactions Section A **110**(1): 11-17.

Herget, G. (1988). Stresses in Rock. Rotterdam, AA Balkema.

Hoek, E. and E. Brown (1980). "Empirical strength criterion for rock masses." Journal of Geotechnical Engineering Division: ASCE **106**(GT9): 1013-1035.

Hole, J. (1992). "Nonlinear high-resolution three-dimensional seismic travel time tomography." Journal of Geophysical Research **97**(B5): 6553-6562.

Iannacchione, A., T. Bajpayee and J. Edwards (2007). Forecasting roof falls with monitoring technologies - a look at the Moonee Colliery experience. 24th International Conference on Ground Control in Mining, Morgantown, WV, West Virginia University.

Iannacchione, A., T. Batchler and T. Marshall (2004). Mapping hazards with microseismic technology to anticipate roof falls - a case study. 23rd International Conference on Ground Control in Mining, Morgantown, WV, West Virginia University.

Iannacchione, A., G. Esterhuizen, T. Bajpayee, P. Swanson and M. Chapman (2005). Characteristics of mining-induced seismicity associated with roof falls and roof caving

events. 40th U.S. Rock Mechanics Symposium, Anchorage, AK, American Rock Mechanics Association.
Jackson, M. and D. Tweeton (1994). Report of Investigations 9497: MIGRATOM - Geophysical Tomography Using Wavefront Migration and Fuzzy Constraints. B. o. Mines.
Jaeger, J., N. Cook and R. Zimmerman (2007). Fundamentals of Rock Mechanics: Fourth Edition. Malden, MA, Blackwell Publishing.
Jensen, S. and H. Thybo (2002). "Moho topography and lower crustal wide-angle reflectivity around the TEXZ in southern Scandinavia and northeastern Europe." Tectonophysics **360**(1-4): 187-213.
Jeremic, M. (1985). Strata Mechanics in Coal Mining. Boston, AA Balkema.
Jones, L. and H. Wang (1981). "Ultrasonic velocities in Creataceous shales from the Williston basin." Geophysics **46**(3): 288-296.
Kaczmarz, S. (1937). "Angenaherte auflosung von systemen linearer gleichungen." Bull. Acad. Pol. Sci. Lett. **35**: 355-357.
Kalra, A., J. Showalter and J. Fulford (1999). "Subbottom profile of ARSRP sediment pond as determined from vertical towed array data." Geo-Marine Letters **18**: 247-250.
Karabin, G. and M. Evanto (1999). Experience with the boundar-element method of numerical modeling to resolve complex ground control problems. 2nd International Workshop on Coal Pillar Mechanics and Design.
Kelly, M. (2000). "3D Aspects of longwall geomechanics." Australian Coal Review **9**: 20-25.
King, M. (1966). "Wave velocities in rocks as a funciton fo changes in overburden pressure and pore fluid saturants." Geophysics **31**(1): 50-73.
Kissling, E., W. Ellsworth, D. Eberhart-Phillips and U. Kradolfer (1994). "Initial reference models in local earthquake tomography." Journal of Geophysical Research **99**(B10): 19635-19646.
Kneisley, R. and K. Haramy (1992). Large-scale strata response to longwall mining: a case study: Report of Investigations 9427. NIOSH**:** 1-24.
Körmendi, A., T. Bodoky, L. Hermann, L. Dianiska and T. Kàlmàn (1986). "Seismic measurements for safety in Mines." Geophysical Prospecting **34**: 1022-1037.
Li, T., M. Cai and M. Cai (2007). "A review of mining-induced seismicity in China." International Journal of Rock Mechanics & Mining Sciences **44**: 1149-1171.
Lo, T.-w. and P. Inderwiesen (1994). Fundamentals of Seismic Tomography. Tulsa, OK, Society of Exploration Geophysicists.
Maleki, H., E. Zahl and J. Dunford (1997). Development of a Statistical-Analytical Approach for Assessing Coal Bump Potential. 16th International Conference on Ground Control in Mining, Morgantown, WV, WVU.
Maleki, H., E. Zahl and J. Dunford (1999). A hybrid statistical-analytical method for assessing violent failure in U.S. coal mines. Workshop on Coal Pillar Mechanics and Design. Pittsburg, PA, NIOSH**:** 139-144.
Manthei, G. (1997). Seismic Tomography on a Pillar in a Postash Mine. 4th International Symposium on Rockbursts and Seismicity in Mines, Krakow, Poland.
Mark, C. and M. Gadde (2008). Global trends in coal mine horizontal stress measurements. 27th International Conference on Ground Control in Mining, Morgantown, WV, West Virginia University.
Martino, J. and N. Chandler (2004). "Excavation-induced damage studies at the Underground Research Laboratory." International Journal of Rock Mechanics & Mining Sciences **41**: 1413-1426.
Mason, I. (1981). "Algebraic reconstruction of a two-dimensional velocity inhomogeneity in the High Hazles seam of Thoresby colliery." Geophysics **46**(3): 298-308.

Maxwell, S. and R. Young (1993). "A comparison between controlled source and passive source seismic velocity images." Bulletin of the Seismological Society of America **83**(6): 1813-1834.

Maxwell, S. and R. Young (1995). "A controlled in-situ investigation of the relationship between stress, velocity and induced seismicity." Geophysical Research Letters **22**(9): 1049-1052.

Maxwell, S. and R. Young (1996). "Seismic imaging of rock mass responses to excavation." International Journal of Rock Mechanics, Mining Sciences, and Geomechanics Abstracts **33**(7): 713-724.

McGaughey, W. and M. Vallee (1997). Ore delineation in three dimensions. Exploration 97: Fourth Decennial International Conference on Mineral Exploration.

Menke, W. (1989). Geophysical Data Analysis: Discrete Inverse Theory. San Diego, Academic Press, Inc.

Michael, A. (1988). "Effects of three-dimensional velocity structure on the seismicity of the 1984 Morgan Hill, California, aftershock sequence." Bulletin of the Seismological Society of America **78**(3): 1199-1221.

Mohorovicic, A. (1909). "Das Beben." Jb. Met. Obs. Zagreb **9**: 1-63.

Mohr, O. (1900). "Welche Umstände bedingen die Elastizitätsgrenze und den Bruck eines Materials." Zeitschrift des Vereines deutsher Ingenieure **44**: 1-12.

Mohr, O. (1914). Abhandlungen aus dem Gebiete der Technische Mechanik: 2nd ed. Berlin, Ernst und Sohn.

Monteiller, V., J.-L. Got, J. Virieux and P. Okubo (2005). "An efficient algorithm for double difference tomography and location in heterogeneous media, with an application to the Kilauea Volcano." Journal of Geophysical Research **110**: 22.

Mosegaard, K. and A. Tarantola (2002). Probabilistic Approach to Inverse Problems, Academic Press for the International Association of Seismology and Physics of the Earth Interior.

Munk, W. and C. Wunsch (1979). "Ocean acoustic tomography; a scheme for large scale monitoring." Deep-Sea Research. Part A: Oceanographic Research Papers **26**(2): 123-161.

Nur, A. and G. Simmons (1969). "Stress-Induced Velocity Anisotropy in Rock: An Experimental Study." Journal of Geophysical Research **74**(27): 6667-6674.

Obert, L. (1941). Use of subaudible noises for the prediction of rock bursts, US Bureau of Mines. **RI 3555**.

Obert, L. and W. Duvall (1967). Rock Mechanics and the Design of Structures in Rock. New York, John Wiley and Sons.

Pande, G., G. Beer and J. Williams (1990). Numerical Methods in Rock Mechanics. New York, John Wiley and Sons.

Pariseau, W. (2007). "Fitting failure criteria to laboratory strength tests." International Journal of Rock Mechanics & Mining Sciences **44**(4): 637-646.

Peng, S. (1986). Coal Mine Ground Control. New York, Wiley.

Peng, S. and H. Chiang (1983). Longwall Mining. New York, Wiley.

Popp, T. and H. Kern (1994). "The influence fo dry and water saturated cracks on seismic velocities of crustal rocks - a comparison of experimental data with theoretical model." Surveys in Geophysics **15**: 443-465.

Prasad, M. and M. Manghnani (1997). "Effects of pore and differential pressure on compressional wave velicty and quality factor in Berea and Michigan sandstones." Geophysics **62**(4): 1163-1176.

Procházka, P. (2004). "Application of discrete element metods to fracture mechaics of rock bursts." Engineering Fracture Mechanics **71**: 601-618.

Prugger, A. and D. Gendzwill (1993). Fracture mechanism of microseisms in Saskatchewan potash mines. Rockbursts and Seismicity in Mines. R. Young, AA Balkema**:** 239-244.

Radon, J. (1917). "Uber die Bestimmung von Funktionen durch ihre Integral-werte langs gewisser Manningfaltigkeiten." Berichte Sachsische Akademie der Wissenchaften. Leipzip, Math. - Phys. Kl. **69**: 262-267.

Rawlinson, N. and M. Sambridge (2003). Seismic traveltime tomography of the crust and lithosphere. Advances in Geophysics. R. Dmowska, Academic Press. **46:** 81-197.

Salamon, M. (1970). "Stability, instability and design of pillar workings." International Journal of Rock Mechanics & Mining Sciences **7**: 613-631.

Scott, D., J. Girard, T. Williams and D. Denton (1999). Comparison of seismic velocity tomography, strain relief, and ultrasonic velocity measurements to evaluate stress in an underground pillar. Society for Mining, Metallurgy, and Exploration, Inc. (SME) Annual Meeting Denver, CO.

Scott, D., T. Williams and M. Friedel (1997). Investigation of a rock-burst site, Sunshine Mine, Kellogg, Idaho. Symposium on Rockbursts and Seismicity in Mines, Krakow, Poland.

Scott, D., T. Williams, D. Tesarik, D. Denton, S. Knoll and J. Jordan (2004). Geophysical methods to detect stress in underground mines: Report of Investigations 9661. NIOSH**:** 23.

Seya, K., I. Suzuki and H. Fujiwara (1979). "The change in ultrasonic wave velocities in triaxially stressed brittle rock." Journal of Physics of the Earth **27**(5): 409-421.

Shah, K. and J. Labuz (1995). "Damage mechanisms in stressed rock from acoustic emission." Journal of Geophysical Research **100**(B8): 15527-15539.

Sharma, P. (1986). Geophysical Methods in Geology. New York, Elsevier.

Soldati, G. and L. Boshi (2005). "The resolution of whole Earth seismic tomographic models." Geophysical Journal International **161**: 143-153.

Spakman, W. (1993). Iterative strategies for non-linear travel time tomography using global earthquake data. Seismic Tomography: Theory and Practice. H. Iyer and K. Hirahara. London, Chapman and Hall.

Stewart, R. (1991). Exploration Seismic Tomography: Fundamentals. Tulsa, OK, Society of Exploration Geophysicists.

Swanson, P. and F. Boler (1995). The magnitude 5.3 seismic event and collapse of the Solvay Trona Mine: Analysis of Pillar/Floor Failure Stability, Bureau of Mines**:** 86-95.

Swanson, P., L. Estey, F. Boler and S. Billington (1992). Accuracy and Precision of Microseismic Event Locations in Rock Burst Research Studies. Denver, CO, Bureau of Mines. **RI 9395**.

Swanson, P., L. Estey, F. Boler and S. Billington (1992). Accuracy and precision of microseismic event locations in rock burst research studies: Report of Investigations 9395. NIOSH**:** 39.

Tarantola, A. (1987). Inverse Problem Theory: Methods for Data Fitting and Model Parameter Estimation. Amsterdam, Elsevier.

Thill, R. (1973). Acoustic Methods for Monitoring Failure in Rock. 14th Symposium on Rock Mechanics, University Park, PA.

Toksöz, M., C. Cheng and A. Timur (1976). "Velocities of seismic waves in porous rocks." Geophysics **41**(4): 621-635.

Tong, C. (2000). "Model parameterisation and assessment in travel time seismic tomography: a user's perspective." Lithos Science Report **2**: 101-107.

Tselentis, G.-A., A. Serpetsidaki, N. Martakis, E. Sokos, P. Paraskevopoulos and S. Kapotas (2007). "Local high-resolution passive seismic tomography and Kohonen neural networks - Application at the Rio-Antirio Strait, central Greece." Geophysics **72**(4): B93-B106.

Vandergrift, T. and J. Garcia (2005). Highwall mining in a multiple-seam, western United States setting design and performance. 24 International Conference on Ground Control in Mining, Morgantown, WV, West Virginia University.

Waldhauser, F. and W. Ellsworth (2000). "A double-difference earthquake location algorithm: method and application to the Northern Hayward Fault, California." Bulletin of the Seismological Society of America **90**(6): 1353-1368.

Watanabe, T., T. Matsuoka and Y. Ashida (1999). Seismic traveltime tomography using Fresnel volume approach. 69th SEG Annual Meeting.

Watanabe, T. and K. Sassa (1996). "Seismic attenuation tomography and its application to rock mass evaluation." International Journal of Rock Mechanics, Mining Sciences, and Geomechanics Abstracts **33**(5): 467-477.

Westman, E., K. Heasley, P. Swanson and S. Peterson (2001). A correlation between seismic tomography, seismic events, and support pressure. 38th U.S. Rock Mechanics Symposium, Washington, D.C., AA Balkema.

Wright, C., E. Walls and D. d. J. Carneiro (2000). "The seismic velocity distribution in the vicinity of a mine tunnel at Thabazimbi, South Africa." Journal of Applied Geophysics **44**: 369-382.

Wyllie, R., A. Gregory and G. Gardner (1958). "An experimental investigation of factors affecting elastic wave veloicties in porous media." Geophysics **23**(3): 459-493.

Yagola, A., A. Leonov and V. Titarenko (2002). "Data errors and an error estimation for ill-posed problems." Inverse Problems in Engineering **10**(2): 117-129.

Yale, D. (1985). "Recent advances in rock physics." Geophysics **50**(12): 2480-2491.

Young, R. and S. Maxwell (1992). "Seismic characterization of a highly stressed rock mass using tomographic imaging and induced seismicity." Journal of Geophysical Research **97**(B9): 12361-12373.

Zhang, H. and C. Thurber (2003). "Double-difference tomography: the method and its application to the Hayward Fault, California." Bulletin of the Seismological Society of America **93**(5): 1875-1889.

Zingano, A., J. Koppe and J. Costa (2005). Modeling the arc-effect of a coal mine roof. 24th International Conference on Ground Control in Mining, Morgantown, WV, West Virginia University.

Zipf, R. (2001). Pillar design to prevent collapse of room-and-pillar mines. Underground Mining Methods: Engineering Fundamentals and International Case Studies. W. Hustrulid and R. Bullock, SME**:** 493-511.

Chapter 3
Time-lapse Passive Seismic Velocity Tomography of Longwall Coal Mines: A Comparison of Methods

Abstract

Bumps in underground coal mines are violent events that result from a buildup of stress, usually in mines underlain and overlain by massive strata. Seismic velocity tomography can be implemented to infer stress distribution at mines and determine when a dangerous situation is developing. Three different methods were employed to compare time-lapse passive seismic tomograms at three different mines. One of the datasets is well sampled with a dense receiver array while the other two data sets are more sparsely sampled. Parameterization and results were compared using GeoTom, TomoDD, and SIMULPS. TomoDD and SIMULPS both allow for variable gridding and relocation of microseismic events while GeoTOM does not. All three methods produced consistent results for the well sampled data set with clear high velocity zones in areas where abutment stress is expected and low velocity zones corresponding with gob. SIMULPS could not be applied to the other two data sets due to the sparse receiver arrays. TomoDD proved to be the most suitable method for generating tomograms from mining-induced microseismic events, but the sparse datasets did not yield images that consistently display stress features, and the stress features that were evident, namely low velocity regions correlating with gob, were significantly smeared.

3.1. Introduction

Seismic velocity tomography has been utilized repeatedly in underground mines to produce velocity images that are used to infer stress. However, long-term passive seismic tomography, which uses mining-induced microseismic events as sources is still relatively immature, but it is a promising technology for the remote and continuous monitoring of a mine on a global scale. Five of eighteen fatalities occurring in coal mines this year-to-date were the result of fall of roof, rib, or highwall. The tragic accident at Crandall Canyon last year increased awareness of the need for improved stress monitoring. This technology may be able to detect areas of relatively high stress in a mine so that precautionary measures can be taken, improving safety for miners working underground and positively impacting productivity. In order to

implement passive seismic velocity tomography various event-receiver configurations and methods of tomographic inversion are explored to determine which methods and configurations are most appropriate for underground mines.

3.2. Background

3.2.1. Tomography

Tomography gained recognition as a medical diagnostic tool (Cormack 1992) but also has many other applications. A tomogram is produced by propagating energy through some mass - a human body, a metal structure, or a rock mass, for example, and then measuring some response of the energy through the mass. These measurements can then be used to produce an image of the interior of the body. Passive seismic velocity tomography utilizes mining induced microseismic events as the energy sources and measures the p-wave arrival time of the seismic wave after it passes through the rock mass. The p-wave is the first part of the seismic wave to arrive and generally the easiest to measure. Next, the rock mass is discretized into three-dimensional cubes, or voxels, and a velocity is assigned to each voxel based on the time a segment of the seismic ray took to pass through the voxel, producing a three-dimensional model that can be sliced in areas of interest.

The premise of velocity tomography is that the seismic wave velocity through the rock mass is closely related to the elastic constants of the material (Adams and Williamson 1923). With the application of pressure to rocks an increase in p-wave velocity occurs as a result of the closure of microcracks and pore space. Velocity can then be used to infer stress; however, the relationship is not linear. Velocity typically levels out at high stress and may even drop prior to failure as microcracks begin to coalesce.

3.2.2. Inversion Methods

Inverse methods are used to generate tomograms due to the fact that tomography problems are ill-posed; there are usually an infinite number of solutions for a tomography problem because the problem will have more unknowns than data or because there may be more data than unknowns, but the data is inconsistent. However, when other information about the problem is considered only a few of these solutions are likely (Hole 1992). Velocity tomography relies on the measurement of the travel time of seismic rays from a source to a receiver. The travel times are organized into a matrix **T** (1 x N), the distances traveled in each voxel into another matrix, **D** (N x M), and a slowness matrix, **P**, (1 x M) is unknown, so that **P** can be

calculated by multiplying the inverse of **D** by **T** as shown in equation 1, below (Jackson and Tweeton 1994).

$$\mathbf{P} = \mathbf{D}^{-1}\mathbf{T} \qquad \text{[Eq. 1]}$$

Since **D** is often a singular matrix the calculation cannot be accomplished directly leading to the development of various inversion methods. Three inversion programs were implemented to produce the tomograms presented in this paper: GeoTom, TomoDD, and SIMULPS.

GeoTom is a commercially available program that implements an iterative inversion process, SIRT, Simultaneous Iterative Reconstructive Technique (Gilbert 1972). An initial velocity model is provided by the user and then modified. First, a set of travel times is calculated through the model, and these travel times are then subtracted from the measured times to determine a residual time (Jackson and Tweeton 1994). These residual times are used to correct the model and the process is repeated. The user specifies the number of iterations, and determines whether straight or curved raypaths are assumed. A smoothing constant, which weights the velocity at a node by the velocities at surrounding nodes can also be applied.

TomoDD, written by Zhang and Thurber, is available for download and was developed for use in earthquake tomography. TomoDD is a double-difference method that jointly relocates events and determines a velocity model (Zhang and Thurber 2003). Double-difference tomography relies on the idea that if the distance between two seismic events is small compared to the distance from the events to the receivers they will have similar travel times. Thus, the difference between calculated and measured travel times between two events at one receiver can be used to adjust the position of the events (Waldhauser and Ellsworth 2000). TomoDD allows for variable gridding, the interval between the x-, y-, and z- nodes in the inversion grid can be varied so that a finer grid may be applied in areas that are well sampled and a more course grid in areas that are not as well sampled. This is especially useful for passive sources because raypath density is rarely consistent.

SIMULPS, written by Evans, Eberhart-Phillips, and Thurber, and updated by others, is also available for download and was also developed for use in earthquake tomography. Like TomoDD, this program relocates seismic events and generates a velocity model, and allows for variable gridding. Both SIMULPS and TomoDD use a damped-least-squares inversion. Damped-least-squares combines the squared data misfit with the norm of the model perturbations and minimizes them at each iteration (Evans et al. 1994). A damping factor is input by the user for both TomoDD and SIMULPS. In SIMULPS the damping factor is determined by examining a plot of the data misfit against the model variance (Evans et al. 1994). The ideal damping value is in the "elbow" of this trade-off curve. In TomoDD examination of a condition number output

by the program is used to determine the damping value. The condition number, the ratio of the smallest to largest eigenvalue, should be between 40 and 80 with damping values between 1 and 100 (Waldhauser and Ellsworth 2000).

3.2.3 Applications of Tomography

There are numerous examples of utilization of tomography to infer the state of stress at a mine in the literature (Young and Maxwell 1992; Maxwell and Young 1993; Wright et al. 2000; Scott et al. 2004). There are several examples specific to longwall mines utilizing velocity tomography (Körmendi et al. 1986) and attenuation tomography (Hanna and Haramy 1998; Westman et al. 2001; Hanson et al. 2002). However, very few examples of long-term time-lapse passive seismic tomography can be found (Glazer and Lurka 2007; Luxbacher et al. 2008). Most of the studies employ active sources such as blasts or hammer strikes and are conducted over the short term. Active sources make long term studies impractical. By utilizing mining induced microseismic events as passive sources, long-term, remote studies are feasible.

3.3. Case Studies

Tomograms were generated from three different coal mines operating longwall systems. Two of the mines are located in the Western United States, and these mines will be referred to as US Western I and US Western II. Both of these mines are fairly deep and overlain by massive strata, making them susceptible to bumps. The third mine, Moonee Colliery, located in New South Wales, Australia is overlain by massive conglomerate and experiences large caving events that often result in windblasts.

3.3.1. US Western I

The data for US Western I Mine were collected over an 18-day period in 1997. Average overburden at the mine is 350 meters, with coal seam height ranging from 2.6 to 3.0 meters. The seam is overlain by 2-7 meters of sandstone and underlain by 35 meters of sandstone. The mine has experienced bumps in the past mainly in the tailgate entry.

The panel under investigation is 250 meters wide with a previously mined panel to the tailgate side and an unmined panel to the headgate side. Over the course of the study the face retreated 431 meters, averaging about 24 meters per day. Sixteen geophones were assembled on the surface above the panel to monitor and locate microseismic events. Figure A.1 in Appendix A displays the panel geometry and relative receiver locations, along with face locations. The face retreated through a series of backfilled entries about halfway through the study. These entries

were mined for escapeway purposes and are evident in Figure A.1. The raw data include 172, 632 P-wave arrival times from 11,696 microseismic events.

3.3.2. US Western II

NIOSH began monitoring this mine in 2005, and the data used in this study range from November 2007 to January 2008 with 12 days during this period investigated. Seismometers are located above this mine and a neighboring mine covering an area of approximately 250 square kilometers. Ten triaxial strong motion seismometers and one short period seismometer at each strong motion site were installed. Only five stations are utilized in this research. Overburden is approximately 440 meters in the area of interest.

Multiple seam mining has occurred in the vicinity of the longwall panel under investigation. Additionally, during retreat of the longwall, retreat room-and-pillar mining was occurring to the south. The longwall panel to the immediate south is previously mined while the panel to the north has not been mined. Figure A.2, in Appendix A, displays the locations of the receivers in relation to the longwall panel and the area of room and pillar mining. Figure A.3 displays the longwall geometry in detail, along with the 12 face locations.

3.3.3. Moonee Colliery

These data are part of a multi-year study at Moonee Colliery in Australia. Longwall panels at the mine are 100 meters wide and overlain by 90 to 170 meters of Teralba Conglomerate. The geometry of the panel and the nature of the conglomerate cause discontinuous caving. The roof may hang behind the shields for large spans before failure in one or several large falls. These falls often cause serious windblasts, especially dangerous to miners at the working face. 14 Hz, three component geophones were installed in 10 meter deep roof boreholes along the headgate and tailgate entries. A total of four geophones were advanced with the longwall face (Iannacchione et al. 2005). The portion of the dataset used in this study consists of 9,383 microseismic events and 24,972 P-wave arrival times collected from February to October 1998. 24-hour periods prior to 15 major falls were examined.

The Moonee Colliery panel geometry, face locations, and fall locations are displayed in Figures A.4 through A.7 in Appendix A.

3.4. Experimental Procedure

3.4.1. Data Reduction

The US Western I data set consists of event locations, station locations, arrival times at stations, event magnitudes, and error descriptors. Only events that that reported arrival times by at least 10 of 16 stations were included in the set. A layered initial velocity model, determined from measurements at the site was included. To convert arrival times to travel times, the ray that arrived to the station array first was propagated through the layered initial velocity model and assigned a travel time. This travel time was then added to the remaining arrival times for that event. The data sets for US Western II and Moonee Colliery included similar data, but travel times were already calculated. Also, these data sets did not include initial velocity models, so homogeneous initial velocity models based on average velocity were used. Also straight raypath velocities were examined and any velocities above 10,000 m/s were removed from the data sets. These velocities are likely the result of poor arrival time picks, and could produce high velocity artifacts in the tomograms. Pink phyllite has one of the highest p-wave velocities at 7,100 m/s (Carmichael 1989). A value of 10,000 m/s was chosen to account for additional curvature in the ray.

3.4.2. Inversion Parameters

Choosing the inversion parameters is one of the more complex aspects of seismic velocity tomography and is generally accomplished through trial and error, adjusting the input parameters and then evaluating output parameters. Also, it is difficult to compare the parameters for different inversion methods. The most important input parameters in GeoTom are the smoothing constraints, the velocity range, and the number of curved and straight ray iterations. Travel time residuals are examined to determine if further changes should be made. For all three data sets a smoothing constant of 0.02 and 20 straight ray and 20 curved ray iterations were used. These values allowed the residuals to stabilize in all three cases. Dines and Lytle indicate that while SIRT may take more time to converge to a solution than other iterative methods, the solution is stable (Dines and Lytle 1979). For the US Western I data set an anisotropy factor of 1.1 was used. A value of 1.1 indicates that the waves travel 1.1 times faster parallel to the anisotropy vector than normal to the vector; this vector is near vertical. Values of 0.8 to 1.4 were tested and 1.1 minimized the travel time residuals. This data set included an anisotropy vector normal to the layers. An anisotropy value of 1.0 was determined to be sufficient for the other two data sets. Anisotropy refers to the variation of a characteristic of a material with the direction of

measurement. In this case, p-wave velocity can vary as measured parallel or perpendicular to the bedding plane.

Important parameters in TomoDD include damping, weighting, and number of iterations. The damping factor damps the hypocentral adjustments if the adjustment vector becomes large or unstable. For the US Western I data damping factors between 120 and 150 were used resulting in condition numbers from 45 to 66. It was more difficult to achieve the recommended ranges for the US Western II data and the Moonee Colliery data. For Moonee Colliery damping factors of 30 to 50 were used resulting in condition numbers of 15 to 68. For the US Western II data damping factors of 20 to 30 were used resulting in condition numbers of 10 to 29. TomoDD is limited by the distribution and number of receiver stations which explains why a more favorable set of condition numbers could not be obtained for the US Western II data set. The weighting factors refer to smoothing in the x, y, and z directions – factors of 3 to 5 were used for all three data sets. Fourteen to 32 iterations were used. Both TomoDD and SIMULPS also relocate the microseismic events to better fit the model.

In SIMULPS a damping parameter of 500 was used for the US Western I data set. This parameter was determined experimentally. SIMULPS could not be used for the Moonee Colliery and US Western II data sets due to the low number of stations, 4 and 5, respectively. SIMULPS did not accept the events with so few travel times.

The US Western II data set was significantly reduced. The data were measured by ten receivers spaced over a large area that covers 2 mines. Event density was high at each of the mines and very sparse in between the two mines. This caused several problems. First, in GeoTom which does not allow for variable gridding the required grid size was far too large for meaningful imaging. A grid size that is significantly larger than the mine geometry dimensions does not provide any information at the mine level. Also, even though TomoDD and SIMULPS allow for variable gridding fine gridding in one area will produce a grid that is fine in one dimension in another area that may not have a sufficient number of raypaths. Figure 3.1 illustrates this concept. A fine grid is applied to area A, shown in blue, where there are many events which results in a fine grid in the x direction in area B, shown in orange where there are few events.

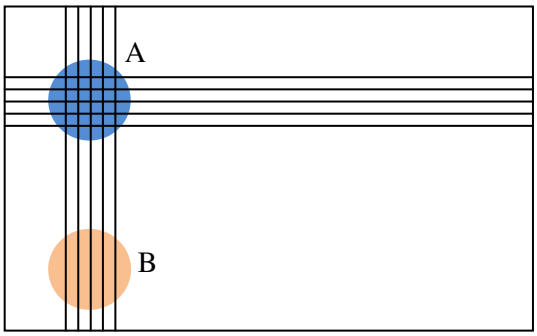

Figure 3.1. Variable Gridding.

Subsequently, the US Western II dataset was reduced to include only events and receivers in the vicinity of the mine of interest. Approximately 20% of the microseismic events were removed from the limited time periods analyzed.

3.4.3. Imaging

All of the output velocity data were plotted in a commercial program that creates three dimensional images. Plan view velocity tomograms at seam level were generated using various velocity scales and pixels not traversed by rays are shown in white. The white zones vary significantly between inversion methods due to the variable gridding that is used in TomoDD and SIMULPS. Additionally, because a different display program was used for the SIMULPS tomograms, a different sampling grid caused there to be more white space in the SIMULPS results. The experimental procedure is summarized in the flowchart in Figure 3.2.

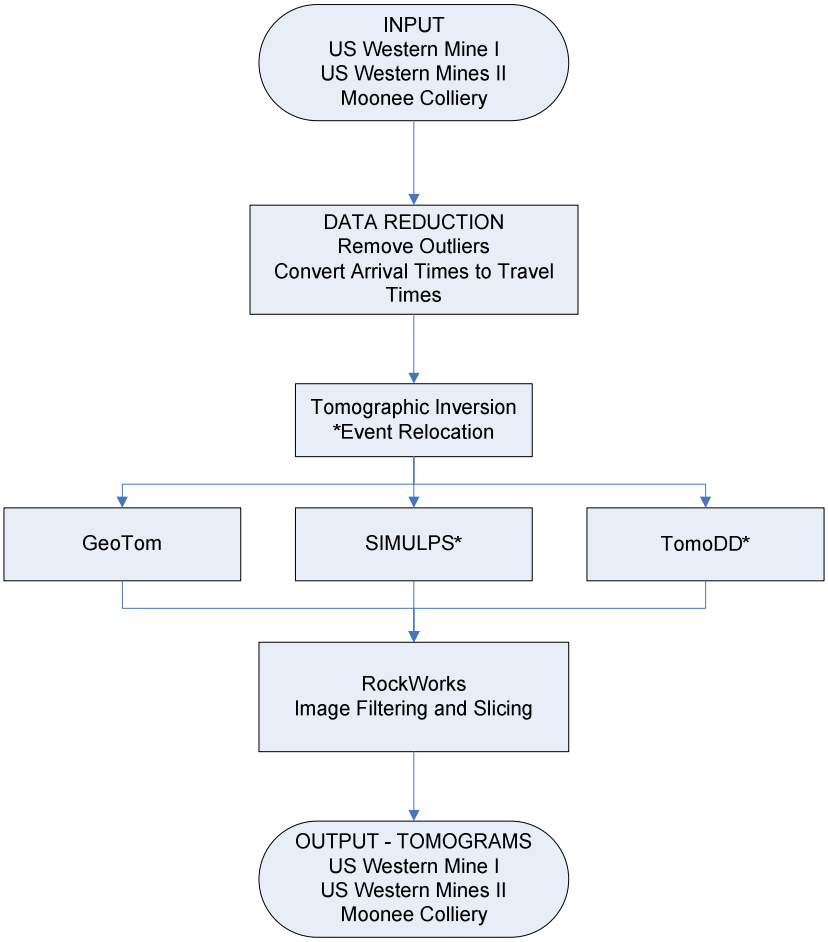

Figure 3.2. Experimental Procedure.

3.5. Results

A complete set of results is displayed in Appendices B, C, and D. Appendix B displays GeoTom, TomoDD, and SIMULPS tomograms for each of the 14 days for the US Western I data. Appendix C displays GeoTom and TomoDD tomograms for each of the 12 days for the US Western II data, and Appendix D displays GeoTom and TomoDD tomograms for the 14 24-hour periods prior to large roof caving events at Moonee Colliery. The three methods are displayed in Figures 3.3 to 3.5 for select days.

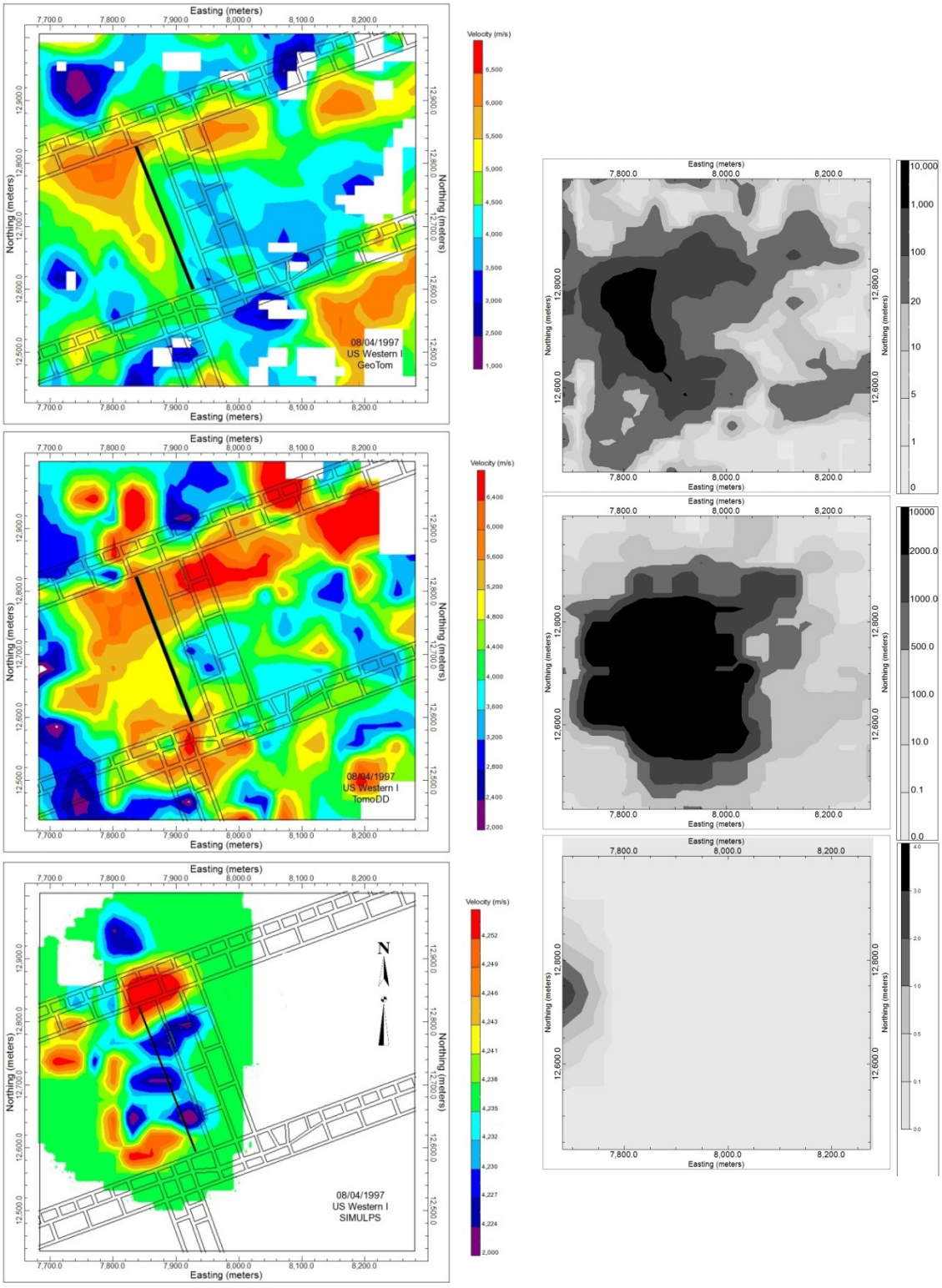

Figure 3.3. US Western I velocity tomograms for GeoTom, TomoDD, and SIMULPS on 08/04/97 are shown on the left. The direction of mining is northeast to southwest and face locations are drawn in black. To the right, a raypath density plot for GeoTom and derivative weight sum plots for TomoDD and SIMULPS are displayed in grayscale. Scales show number of raypaths and derivative weight sums, respectively.

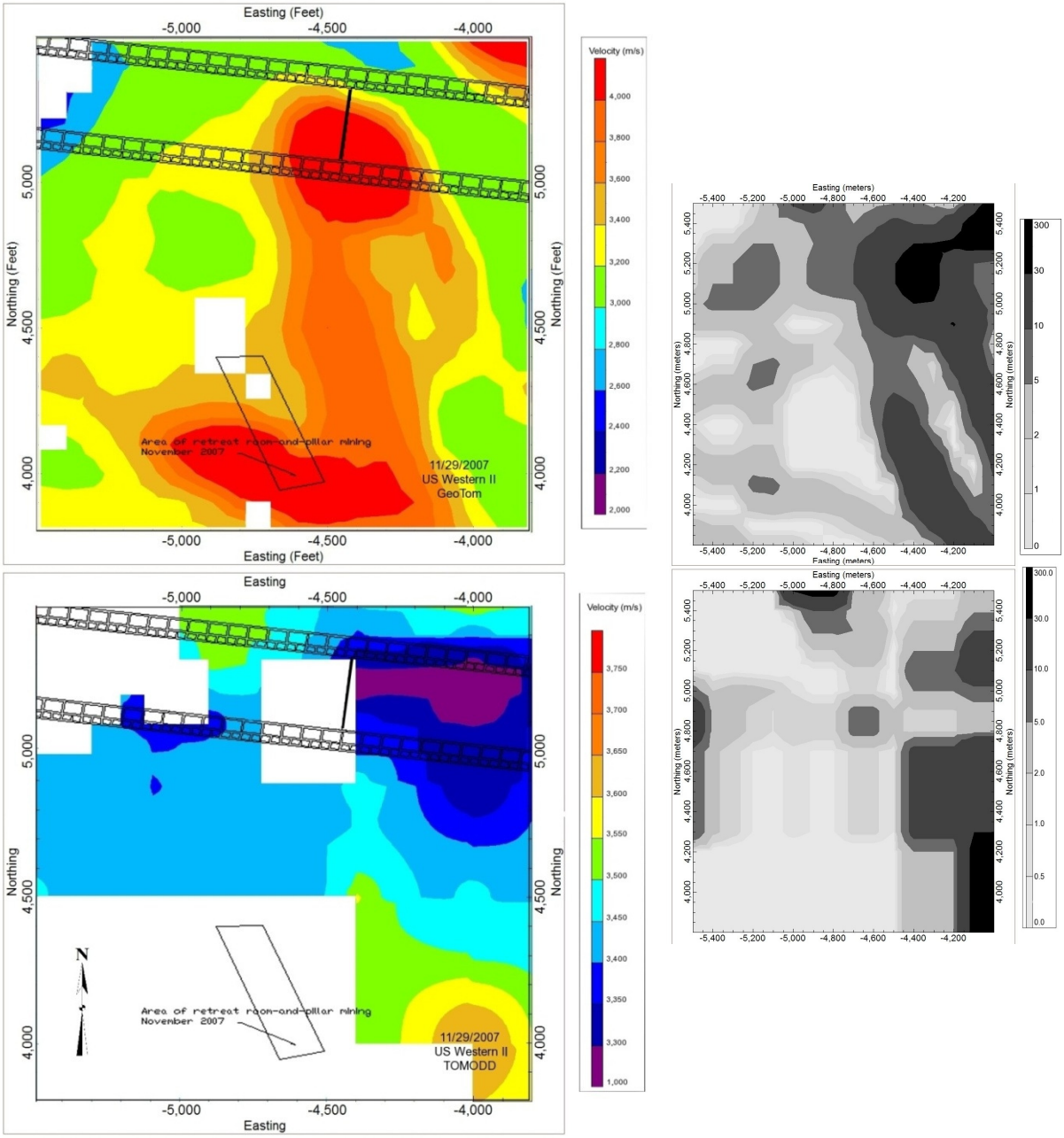

Figure 3.4. US Western II velocity tomograms for GeoTom and TomoDD on 11/29/07 are shown on the left. The direction of mining is east to west and face locations are drawn in black. To the right, a raypath density plot for GeoTom and a derivative weight sum plot for TomoDD are displayed in grayscale. Scales show number of raypaths and derivative weight sum, respectively.

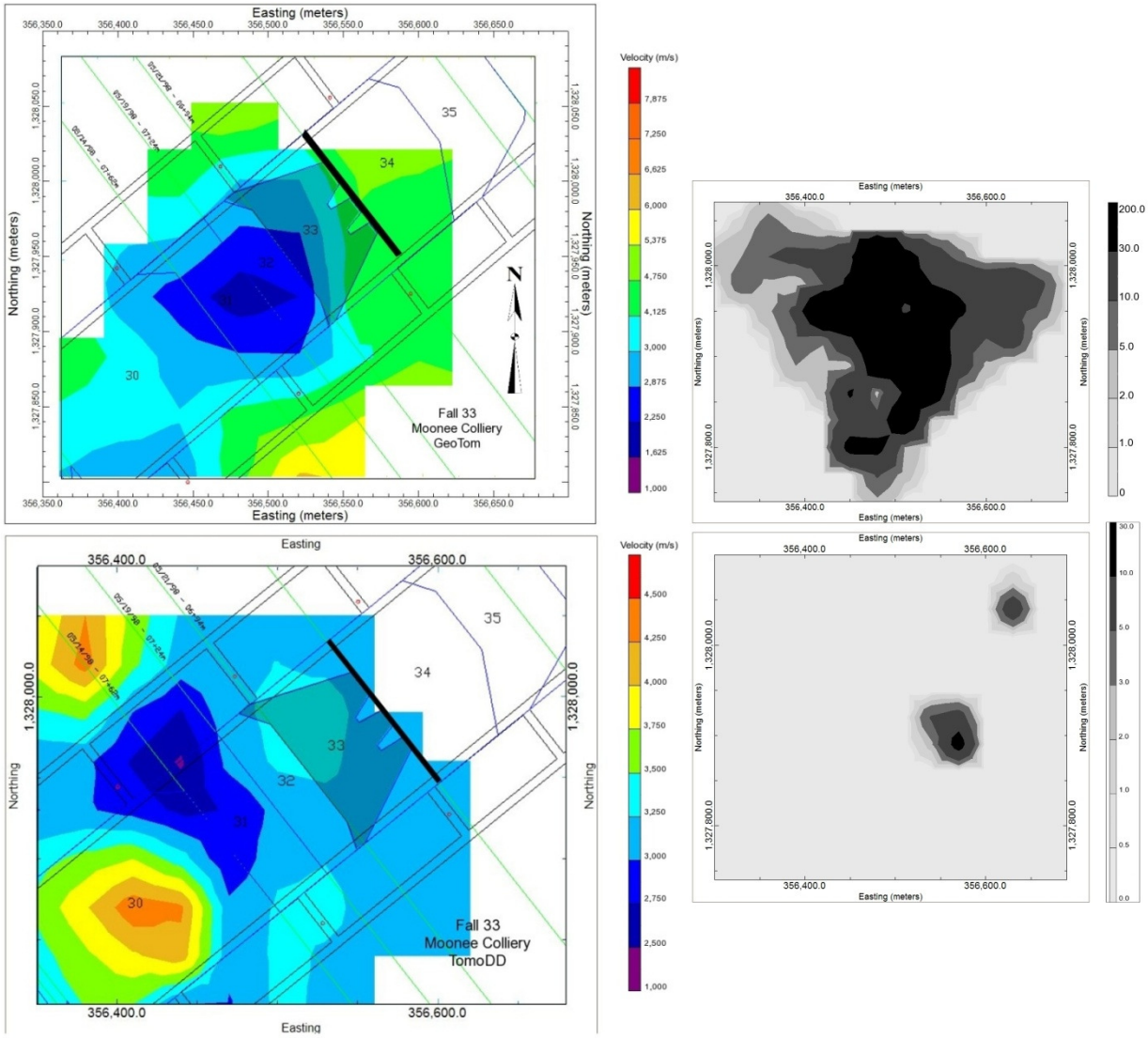

Figure 3.5. Moonee Colliery velocity tomograms for GeoTom and TomoDD for the 24-hour period prior to fall 33 are shown on the right. The direction of mining is southwest to northeast and face locations are drawn in black. To the right, a raypath density plot for GeoTom and a derivative weight sum plot for TomoDD are displayed in grayscale. Scales show number of raypaths and derivative weight sum, respectively.

Before examining the velocity patterns an examination of velocity scale is instrumental. The range for each scale varies significantly depending upon the inversion method utilized. For example, in Figure 3.3, the range is about 5,500 m/s for GeoTom, 4,400 m/s for TomoDD, and only 28 m/s for SIMULPS. Similar differences are evident in the other two data sets. The extremely low range for the SIMULPS data is most likely due to the high damping value that was used. This damping value was determined by plotting data misfit versus model variance, for

several different iterations and choosing the value that falls in the "elbow" of the curve as suggested by the user's manual (Evans et al. 1994).

Examination of Figure 3.3 reveals evidence of high velocity zones just ahead of the face and along the northern gateroad, corresponding with areas where front and tailside abutment stresses would be expected. Additionally, a low velocity zone can be seen just behind the face corresponding with the location of the gob. It is interesting to note that beginning on 08/04/97, the day shown in Figure 3.3, the seismic events begin to shift towards the tailgate, possibly for two reasons. First, there was little retreat the previous day and the tailgate is subject to time-dependent deformation. Also, this is the area where the axis of an anticline intersects the tailgate (Swanson 2008). In each of the three tomograms a higher velocity zone is evident toward the tailgate side. Both the GeoTom and TomoDD tomograms contain significantly more noise than the SIMULPS tomogram. This is most likely due to the very high damping value of 500 that was applied during the SIMULPS inversion. Appendix B reveals that forward and side abutment high velocity zones are clearly visible every day except for 07/21/97 and 07/24/97 in all three tomograms. Detailed discussion of the backfilled entries is included in Chapter 5.

Figure 3.4 displays US Western II tomograms for GeoTom and TomoDD, and these tomograms do not appear to be in agreement with each other. The GeoTom tomogram displays a large area of high velocity near the face while the TomoDD tomogram displays a low velocity zone just behind the face. That low velocity zone is fairly consistent in the TomoDD tomograms, occurring on 11 of 12 days, but the GeoTom tomograms do not appear to show redistribution of stress features on a daily basis. The fact that the low velocity zone is consistent may be indicative of gob development, but could also indicate that system errors are consistent. In addition to the longwall, an area to the south was being mined by retreat room-and-pillaring in November, but there is not sufficient ray coverage in TomoDD to image any velocity anomalies. The four November tomograms displayed in Appendix C show a large high velocity zone around this area in GeoTom. It is certainly likely that a high velocity zone would correspond with that area, but in terms of area this is too large to be probable. There has been multiple seam mining in this area which could impact the image, but the geometry is unknown, which warrants further investigation. One problem with these tomograms is that no rays are shown in the area of the longwall face, where a cluster of events would be expected, for the TomoDD inversion. This is most likely due to unconstrained event relocation in the vertical direction.

Figure 3.5 displays GeoTom and TomoDD tomograms for Fall 33 of the Moonee Colliery data. Both tomograms image a low velocity zone just behind the fall. Since these images are generated from events occurring 24 hours prior to the fall the area of the fall would be

expected to either display high velocity or low velocity. High velocity may be expected due to buildup of stress prior to failure while the low velocity might be expected as the roof cracks prior to collapse. Because of the complicated mechanics at this site it is difficult to determine if any stress features are being imaged. Examination of Appendix D shows that in several instances a higher velocity zone is imaged at the fall for both GeoTom and TomoDD methods. This is true for falls 30, 31, and 36. However, in many cases the tomograms are completely inconsistent, including falls 20, 21, and 22, or ray coverage is inadequate to image the area, as for Fall 29.

3.6. Discussion and Conclusions

GeoTom, TomoDD, and SIMULPS all image high velocity zones in areas of side and forward abutment for the US Western I data. These features consistently redistribute with face advance and a low velocity zone in the gob area is also consistently present. This dataset has considerably more raypaths on a daily basis than the other two. Of the three days presented in Figures 3.3 to 3.5 US Western I tomograms are generated from over 8,000 raypaths, while US Western II tomograms are generated from only 319 raypaths and Moonee Colliery tomograms are generated from 225 raypaths. The TomoDD tomograms seem to be more consistent from day to day for these data sets.

TomoDD and SIMULPS, both programs that allow variable gridding and event relocation appear to produce the most consistent models, especially in the case of TomoDD for the more sparsely sampled US Western II and Moonee Colliery datasets. Synthetic tomography results in Chapter 4 also indicate that these methods are favorable. Event relocations are shown below in Figure 3.6 for each of the three data sets. These techniques may be further improved by improved constraint of the microseismic event locations. The change in locations in the x- and y-directions seems reasonable as displayed below in Figure 3.6. However, many of the events migrated above the seam in the z- direction for the US Western data sets. This is likely due to a two-dimensional source-receiver geometry that does not constrain the events well vertically. Manually constraining the microseismic event elevations could further improve the tomograms.

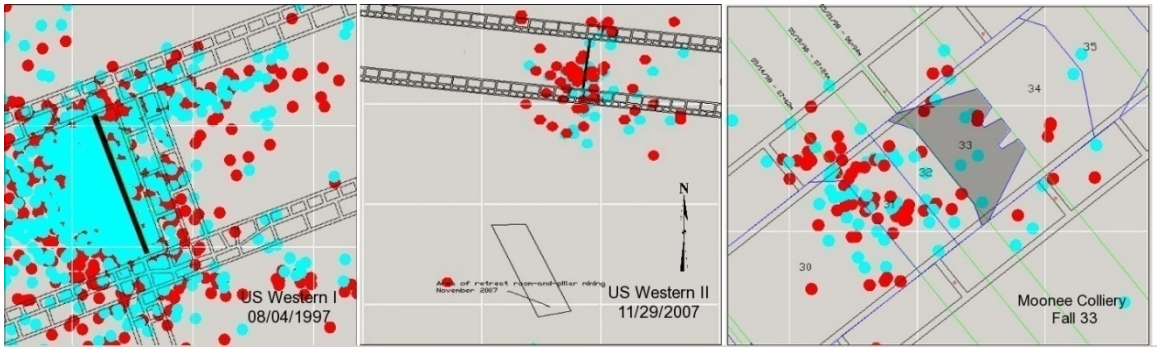

Figure 3.6. Plan view of event relocations for US Western I 08/04/97, US Western II 11/29/07, and Moonee Colliery Fall 33. Original locations are shown in red and TomoDD relocations are shown in blue.

In comparing the three methods for the three datasets it is evident that the methods that allow for variable gridding are more appropriate, especially for sparse data. However, even variable gridding does not allow very inconsistent data to be imaged well because a fine grid in one area will still result in some medium gridded areas that may not be sampled, as shown in Figure 3.1. Future research should include investigation of adaptive gridding with irregular shapes (Sambridge and Gudmundsson 1998). This gridding could prove especially useful for seismic tomography of mines where very dense event distributions quickly give way to sparser distributions, but significantly more computational power is required. Additionally, this research indicates that passive seismic velocity would not be appropriate for mines with relatively few mining induced microseismic events unless a dense receiver array is implemented. The US Western I data set proves that high velocity zones can be imaged in abutment stress areas and shown to redistribute using several different techniques.

Chapter 3 References

Adams, L. and E. Williamson (1923). "On the compressibility of minerals and rocks at high pressures." Journal of the Franklin Institute **195**: 475-531.

Carmichael, R. (1989). Practical Handbook of Physical Properties of Rocks and Minerals. Boca Raton, CRC Press.

Cormack, A. (1992). Nobel Lecture: Early two-dimensional reconstruction and recent topics stemming from it. Nobel Lectures, Physiology or Medicine 1979-1980. Singapore, World Scientific Publishing Co.

Dines, K. and R. Lytle (1979). "Computerized geophysical tomography." Proceedings of the IEEE **67**(7): 1065-1076.

Evans, J., D. Eberhart-Phillips and C. Thurber (1994). User's manual for SIMULPS12 for imaging vp and vp/vs: A derivative of the "Thurber" tomographic inversion SIMUL3 for local earthquakes and explosions. USGS.

Gilbert, P. (1972). "Iterative methods for the three-dimensional reconstruction of an object from projections." Journal of Theoretical Biology **36**: 105-117.

Glazer, S. and A. Lurka (2007). Application of passive seismic tomography to cave mining operations based on experience at Palabora Mining Company, South Africa. The Southern African Institute of Mining and Metallurgy 1st International Symposium on Block and Sub-Level Caving, Cape Town, South Africa.

Hanna, K. and K. Haramy (1998). Ground control and geologic assessment in mining through the use of geophysical tomographic imaging. Geomechanics/Ground Control in Mining Underground Construction Conference, Wollongong, NSW, Australia.

Hanson, D., T. Vandergrift, M. DeMarco and K. Hanna (2002). "Advanced techniques in site characterization and mining hazard detection for the underground coal industry." International Journal of Coal Geology **50**: 275-301.

Hole, J. (1992). "Nonlinear high-resolution three-dimensional seismic travel time tomography." Journal of Geophysical Research **97**(B5): 6553-6562.

Iannacchione, A., G. Esterhuizen, T. Bajpayee, P. Swanson and M. Chapman (2005). Characteristics of mining-induced seismicity associated with roof falls and roof caving events. 40th U.S. Rock Mechanics Symposium, Anchorage, AK, American Rock Mechanics Association.

Jackson, M. and D. Tweeton (1994). Report of Investigations 9497: MIGRATOM - Geophysical Tomography Using Wavefront Migration and Fuzzy Constraints. B. o. Mines.

Körmendi, A., T. Bodoky, L. Hermann, L. Dianiska and T. Kàlmàn (1986). "Seismic measurements for safety in Mines." Geophysical Prospecting **34**: 1022-1037.

Luxbacher, K., E. Westman, P. Swanson and M. Karfakis (2008). "Three-dimensional time-lapse velocity tomography of an underground longwall panel." International Journal of Rock Mechanics & Mining Sciences **45**(4): 478-485.

Maxwell, S. and R. Young (1993). "A comparison between controlled source and passive source seismic velocity images." Bulletin of the Seismological Society of America **83**(6): 1813-1834.

Sambridge, M. and O. Gudmundsson (1998). "Tomographic systems of equations with irregular cells." Journal of Geophysical Research **103**(B1): 773-781.

Scott, D., T. Williams, D. Tesarik, D. Denton, S. Knoll and J. Jordan (2004). Geophysical methods to detect stress in underground mines: Report of Investigations 9661. NIOSH**:** 23.

Swanson, P. (2008). Email: Simulps preliminary results. E. Westman. Blacksburg, VA.

Waldhauser, F. and W. Ellsworth (2000). "A double-difference earthquake location algorithm: method and application to the Northern Hayward Fault, California." Bulletin of the Seismological Society of America **90**(6): 1353-1368.

Westman, E., K. Heasley, P. Swanson and S. Peterson (2001). A correlation between seismic tomography, seismic events, and support pressure. 38th U.S. Rock Mechanics Symposium, Washington, D.C., AA Balkema.

Wright, C., E. Walls and D. d. J. Carneiro (2000). "The seismic velocity distribution in the vicinity of a mine tunnel at Thabazimbi, South Africa." Journal of Applied Geophysics **44**: 369-382.

Young, R. and S. Maxwell (1992). "Seismic characterization of a highly stressed rock mass using tomographic imaging and induced seismicity." Journal of Geophysical Research **97**(B9): 12361-12373.

Zhang, H. and C. Thurber (2003). "Double-difference tomography: the method and its application to the Hayward Fault, California." Bulletin of the Seismological Society of America **93**(5): 1875-1889.

Chapter 4
Synthetic Method for the Assessment of Passive Seismic Velocity Tomography

Abstract

Synthetic tomography was used to evaluate the application of various inversion programs for passive seismic velocity tomography of underground coal mines for inference of stress redistribution. Three inversion methods: GeoTom, TomoDD, and SIMULPS, were evaluated for three different data sets. Synthetic tomography requires building an initial velocity model that approximates the true velocity state at each mine, and then inverting for the calculated velocity model using measured source-receiver locations and travel times. One day for each of the three data sets was chosen, and two to three synthetic tomograms for that day were generated and compared to the initial velocity model. The synthetic tomography revealed that one data set was too poorly sampled to prove useful for seismic velocity tomography, and also showed that the inversion schemes that allow for variable gridding and event relocation are best. Synthetic tomography is also shown to be useful for the assessment of source-receiver configuration.

4.1. Introduction

Passive seismic velocity tomography applied in underground mines holds promise as a tool for inferring information about the state of stress in the mine on a global scale. However, the nature of tomography makes it difficult to determine how much confidence can be placed in any given image. Many parameters involved in the calculation of a model, including the number of microseismic events, number of receivers, source-receiver geometry, corresponding raypath density, size and geologic characteristics of the study area will impact the quality of the tomogram. Synthetic tomography can be used to analyze experimental tomograms and to design systems to collect seismic data for tomography.

Characterization of stress in underground mines has generally involved localized measurement of stress, which is then interpolated to determine stress mine wide or over a larger area. Seismic velocity tomography allows for sampling of a large area, such as an entire mine, or active panel in a mine. Passive seismic velocity tomography in underground mines requires using mining induced microseismic events as sources with receivers mounted in or above the mine to receive the signal. The travel times along the source to receiver path are then used to create a

velocity image which can be used to infer relative stress distribution in the mine. Passive tomography is an excellent tool for long-term monitoring because it does not require any active initiation of a source, such as an explosion or hammer blow. However, because the microseismic event location is not planned the geometry of the raypaths is not always ideal, and it can be difficult to determine how this geometry impacts the tomogram.

A velocity tomogram is generated by dividing the area under consideration into cubes, or voxels, and assigning a velocity value to each voxel based on the time a segment of the seismic ray took to pass through the voxel. The group of voxels that make up the mass form a three-dimensional image that can be sliced. Due to the nature of the inversion processes used to produce the image it can be difficult to ascertain where the data are informing the model and where there is a lack of data. Most inverse problems are ill-posed (Hadamard 1952; Mosegaard and Tarantola 2002); they have an infinite number of solutions with a few that are appropriate when other information about the site is considered (Hole 1992). One way to determine where an image is well constrained is to examine the ray paths.

Another method for evaluating a tomogram is synthetic tomography. In synthetic tomography a "true" velocity model is assumed. This model should have a velocity pattern and range that approximates the expected experimental model. The experimental source and receiver locations are located on the initial velocity model and synthetic travel times are calculated through the model. Once the synthetic travel times are calculated the same procedure is followed for the synthetic data as for the experimental data. The synthetic tomogram is then compared to the user generated initial velocity model to determine how successful the method was at imaging the true velocity conditions.

Synthetic tomography may be used prior to designing a seismic system to determine optimum source and receiver location or implemented after seismic data is collected to assess the reliability of the resulting tomogram.

Synthetic tomograms were generated for three longwall panels at different mines. An initial velocity model is generated that is expected to resemble the true velocity at the mines. Actual calculated source and measured receiver locations for one 24-hour period, per mine, are used to determine travel times. These travel times are then utilized to generate tomograms using three different inversion methods. The resulting three tomograms for each mine are compared to the initial velocity model to assess how closely they resemble the starting model, and which method may be best suited to passive seismic tomography in underground mines.

4.2. Background

Passive seismic tomography involves propagating seismic waves through the rock mass surrounding a mine and measuring their travel time. Mining-induced microseismic events are utilized as passive sources and their arrival times are measured by receivers usually placed in the mine or on the surface above the mine. These travel times allow a velocity image to be generated. The velocity image allows for assumptions to be made about the state of stress in the rock as the speed of the seismic wave through the rock is dependent upon various attributes of the rock. A seismic wave may travel more quickly through a rock that is being loaded due to the closure of microcracks and pore space. The velocity may continue to increase with load until microcracks began to coalesce and then velocity may decrease just prior to failure (Wyllie et al. 1958; Thill 1973; Toksöz et al. 1976; Seya et al. 1979; Prasad and Manghnani 1997).

Long-term passive seismic velocity tomography is particularly well suited for the mining industry. Because mining-induced sources are utilized there is opportunity for remote and long-term monitoring over large areas. However, passive sources rarely create optimum source-receiver geometry so a critical examination of tomograms is especially important as they may contain artifacts or severely distorted features. Artifacts are defined as velocity anomalies in a tomogram that do not represent any real feature. They are high or low velocity anomalies that appear in poorly constrained areas as the inversion algorithm attempts to fit the model to the measured data.

There are several methods for inverting for velocity, and they can generally be subdivided into matrix inversion methods and iterative methods (Jackson and Tweeton 1994). A thorough discussion of inversion methods is given in Chapter 3.

Synthetic tomography is one way of determining resolution of a tomogram in a qualitative sense. Resolution refers to the "sharpness" of an image. Various authors disagree on the theoretical resolution can be imaged – it ranges from one wavelength (Friedel et al. 1996; Watanabe et al. 1999) to less than a wavelength (Tselentis et al. 2007). Others have indicated that resolution is more dependent on data noise than wavelength (Soldati and Boshi 2005).

When synthetic tomography is used to determine resolution, resolution is only determined qualitatively. Often, checkerboard tests are employed which involve an initial velocity model with a checkerboard pattern (Tong 2000; Rawlinson and Sambridge 2003; Zhang and Thurber 2003). By varying the size and contrast of the checkers one can determine the smallest feature that can be imaged and the corresponding contrast. An initial velocity model that approximates the true velocity of a mass can also be used to evaluate if a method or source receiver configuration is appropriate for an application.

4.3. Case Studies

Tomograms were generated from three different coal mines operating longwall systems. Two of the mines are located in the Western United States, and these mines will be referred to as US Western I and US Western II. Both of these mines are fairly deep and overlain by massive strata, leaving them susceptible to bumps. The third mine, Moonee Colliery, located in New South Wales, Australia is overlain by massive conglomerate and experiences large caving events.

4.3.1. US Western I

The data for US Western I Mine were collected over an 18-day period in 1997. Average overburden at the mine is 350 meters, with coal seam height ranging from 2.6 to 3.0 meters. The seam is overlain by 2-7 meters of sandstone and underlain by 35 meters of sandstone. The mine has experienced bumps in the past, mainly in the tailgate entry.

The panel under investigation is 250 meters wide with a previously mined panel to the tailgate side and an unmined panel to the headgate side. Over the course of the study the face retreated 431 meters, averaging about 24 meters per day. Sixteen geophones were assembled on the surface above the panel to monitor and locate microseismic events. Figure A.1 in Appendix A displays the panel geometry and relative receiver locations, along with face locations. The face retreated through a series of backfilled entries about halfway through the study. These entries were mined for escapeway purposes and are evident in Figure A.1. The raw data include 172, 632 P-wave arrival times from 11,696 microseismic events.

4.3.2. US Western II

NIOSH began monitoring this mine in 2005, and the data used in this study range from November 2007 to January 2008 with 12 days during this period investigated. Seismometers are located above this mine and a neighboring mine covering an area of approximately 250 square kilometers. Ten triaxial strong motion seismometers and 10 short period seismometers were installed. Overburden is approximately 440 meters in the area of interest.

Multiple seam mining has occurred in the vicinity of the longwall panel under investigation. Additionally, during retreat of the longwall, retreat room-and-pillar mining was occurring to the south. The longwall panel to the immediate south was previously mined while the panel to the north has not been mined. Figure A.2, in Appendix A, displays the locations of the receivers in relation to the longwall panel and the area of retreat room and pillar mining. Figure A.3 displays the longwall geometry in detail, along with the 12 daily face locations.

4.3.3. Moonee Colliery

The third set of data is part of a multi-year study at Moonee Colliery in Australia. Longwall panels at the mine are 100 meters wide and overlain by 90 to 170 meters of Teralba Conglomerate. The geometry of the panel and the nature of the conglomerate cause discontinuous caving. The roof may hang behind the shields for large spans before failure in one or several large falls. These falls often cause serious windblasts, especially dangerous to miners at the working face. 14 Hz, three component geophones were installed in 10 meter deep roof boreholes along the headgate and tailgate entries. A total of four geophones were advanced with the longwall face (Iannacchione et al. 2005). 24-hour periods prior to 15 major falls were examined.

The Moonee Colliery panel geometry, face locations, and fall locations are displayed in Figures A.4 through A.7 in Appendix A.

4.4. Experimental Procedure

4.4.1. Determination of Abutment Stress

An initial velocity model was developed empirically based on stress abutment data found in the literature and an assumed velocity-stress relationship. While this method does not accurately describe the state of stress or velocity in any of the mines it does provide a velocity model that approximates the velocity pattern found in a longwall coal mine. The purpose of synthetic tomography is to determine if the methods utilized with measured data are likely to produce an image that is indicative of the true velocity. Therefore, it is important to use a starting model that is similar to the true velocity, but not imperative that extensive stress modeling be undertaken to develop the model. The velocity models were developed to approximate the velocity changes caused by abutment stress around the panels.

Abutment stress occurs in underground mines as ore is extracted along the boundary where the material is removed (Peng and Chiang 1983). In longwall mining this stress is transferred immediately in front of the face and to the sides of the panel. Formation of gob behind the advancing face allows for stress relief. Abutment stress is generally larger on the tailgate side, if it is adjacent to a mined out panel. At seam level, front abutment pressure is detectable at a lateral distance of about 1 times the overburden, and is more evident about 100 feet outby the face at which point stress starts to increase to its peak at 3 to 20 feet outby the face (Peng and Chiang 1983; Yasitli and Unver 2005; Whittles et al. 2006). In weak roof maximum abutment stress along the faceline occurs at the corners of the face, while in stronger roof it often

occurs midface (Peng and Chiang). In addition to vertical stress redistribution, joints faults and horizontal stress orientation may contribute to larger or smaller abutment stresses and more erratic failure. These factors are not taken into consideration in development of the models presented in this paper.

Hanna and others indicate that abutment pressure is present at 0.25 times the depth ahead of the longwall face, while significant increases can be seen at 0.1 times the depth for the US Western I mine (Hanna et al. 1991). Tailgate abutment pressure patterns were similar with the peak stress measuring approximately 1.5 times the headgate stress. They also indicate that these values are in agreement with data from other mines in the western United States so these observations were also used in determining the stress model for the US Western II data set.

4.4.2. Initial Velocity Model Development

The relationship between stress and p-wave velocity is complicated. Even with extensive stress and velocity testing of the strata the relationship is still highly influenced by geologic anomalies, topography, and water and gas saturation.

Velocity distributions for each data set were used to develop the initial velocity model. The velocity histograms for the data sets were examined and a front abutment velocity was chosen at one standard deviation above the mean. The velocity histograms included all straight ray velocities below 10,000 m/s calculated from the arrival times for the days analyzed. Headgate side abutment velocity was chosen at ½ times standard deviation above the mean velocity, while tailgate side abutment velocity was chosen at 1 times the standard deviation above the mean velocity. Mean velocity was applied in all other areas but the gob. Due to the broken material that comprises the gob a significantly lower velocity would be expected here, although at some point compaction of the gob will cause some velocity increase. A gob velocity was chosen at one standard deviation below the mean. This velocity was applied from the face inby a distance of 0.6 times the overburden (Maleki et al. 1984). Velocities for abutment zones and gob in each of the three initial velocity models are summarized below in Table 3.1.

Table 4.1. Velocities for Initial Models.

Zone	US Western I	US Western II	Moonee Colliery
Front Abutment	7,221 m/s	4,653 m/s	6,392 m/s
Side Abutment	6,313 m/s	4,223 m/s	5,338 m/s
Gob	3,634 m/s	2,935 m/s	2,176 m/s
Background Velocity	5,405 m/s	3,794 m/s	4,284 m/s

Travel times were calculated using a Dijkstra algorithm, which is computationally expensive but very robust. A Dijkstra algorithm is basically a shortest-path algorithm (Golden 1976). The user inputs the number of cells to divide the velocity model by, which determines how much curvature the seismic rays are allowed. The program calculates all of the possible travel times per ray and chooses the smallest travel time. The US Western II and Moonee velocity models were divided by 25 in the x-, y-, and z- directions, while the US Western I velocity model was only divided by 20 due to the high number of rays involved in the calculation.

4.4.3. Inversion Methods

Since tomography programs are usually either overdetermined, more data than equations or underdetermined, more equations than data, inverse methods must be used to solve for a velocity model. Velocity tomography relies on the measurement of the travel time of seismic rays from a source to a receiver through a mass. When the mass is discretized into voxels the rays are also discretized. Since travel times, velocities, and distances along the full ray path can easily be determined the velocity of discrete sections of the ray can be solved for and assigned to the voxel the part of ray traverses. These voxels then form a three-dimensional velocity image.

Three inversion programs were implemented to produce the tomograms presented in this paper: GeoTom, TomoDD, and SIMULPS.

GeoTom is a commercially available program that implements an iterative inversion process, SIRT, Simultaneous Iterative Reconstructive Technique (Gilbert 1972). An initial velocity model is provided by the user and then modified. First, a set of travel times is calculated through the model, and these travel times are then subtracted from the measured times to determine a residual time (Jackson and Tweeton 1994). These residual times are used to correct the model and the process is repeated. The user specifies the number of iterations, and determines whether straight or curved raypaths are assumed. A smoothing constant, which weights the velocity at a node by the velocities at surrounding nodes can also be applied.

TomoDD, written by Haijiang Zhang and Clifford Thurber, is available for download and was developed for use in earthquake tomography. TomoDD is a double-difference method that jointly relocates events and determines a velocity model (Zhang and Thurber 2003). Double-difference tomography relies on the idea that if distance between two seismic events is small compared to the distance from the events to the receivers they will have similar travel times. Thus, the difference between calculated and measured travel times between two events at one receiver can be used to adjust the position of the events (Waldhauser and Ellsworth 2000). TomoDD allows for variable gridding, the interval between the x-, y-, and z- nodes in the inversion grid can be varied so that a finer grid may be applied in areas that are well sampled and a more course grid in areas that are not as well sampled. This is especially useful for passive sources because raypath density is rarely consistent.

SIMULPS is also available for download and was also developed for use in earthquake tomography (Evans et al. 1994). This program relocates seismic events and generates a velocity model. Like TomoDD, it allows for variable gridding. Both SIMULPS and TomoDD use a damped-least-squares inversion. Damped-least-squares combines the squared data misfit with the norm of the model perturbations and minimizes them at each iteration (Evans et al. 1994). A damping factor is input by the user for both TomoDD and SIMULPS. In SIMULPS the damping factor is determined by examining a plot of the data misfit against the model variance (Evans et al. 1994). The ideal damping value is in the "elbow" of this trade-off curve. In TomoDD examination of a condition number output by the program is used to determine the damping value. The condition number, the ratio of the smallest to largest eigenvalue, should be between 40 and 80 with damping values between 1 and 100 (Waldhauser and Ellsworth 2000).

4.5. Results

After the three dimensional tomograms were generated they were sliced at approximately seam level for each mine and examined in plan view. Areas not traversed by seismic rays are shown in white. Figure 4.1 displays the initial velocity model, and the synthetic model for the three inversion methods for the US Western I data set on 08/01/97. Figure 4.2 displays the raypath density and derivative weight sums for GeoTom, TomoDD, and SIMULPS, respectively. Derivative weight sums are provided in TomoDD and SIMULPS output, rather than number of rays. Previous studies have used the derivative weight sum as an indicator of resolution with higher derivative weight sums indicating a better resolved image (Sallares et al. 2000).

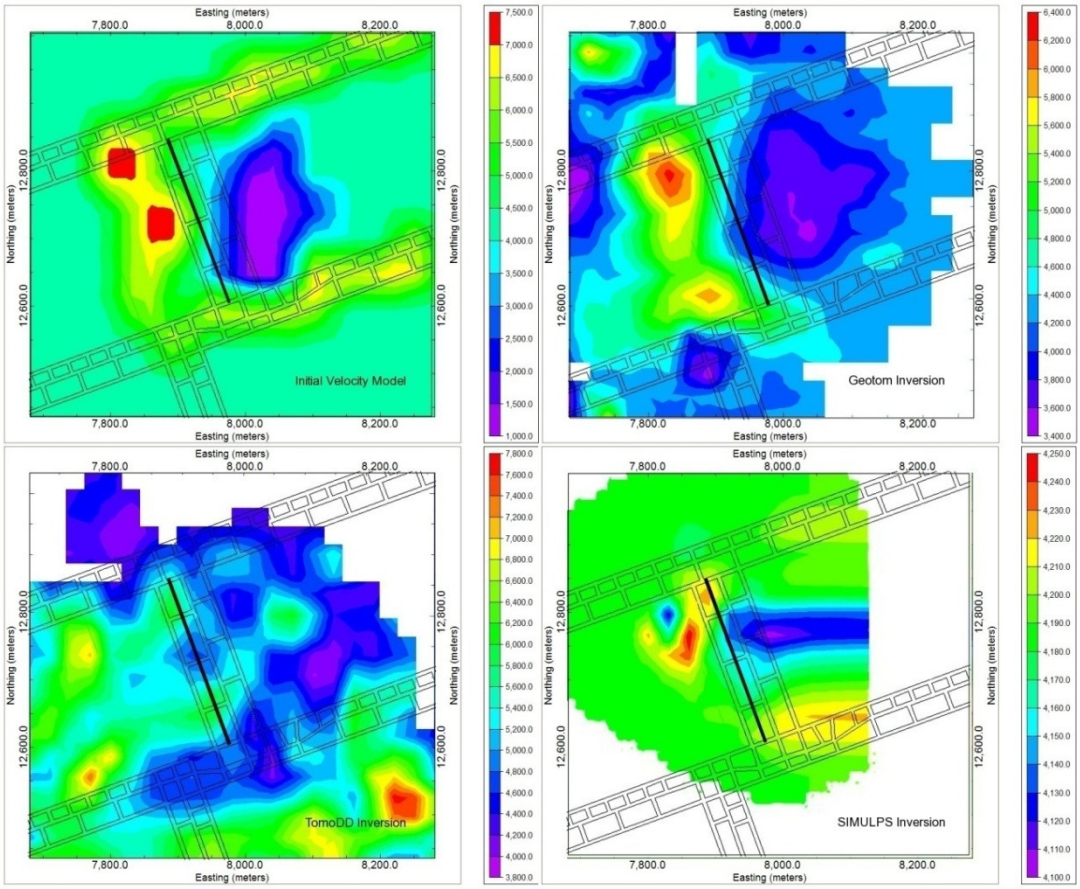

Figure 4.1. Synthetic tomograms, plan view at seam level, for US Western I on 08/01/97. Clockwise from the top left are the initial velocity model, GeoTom model, TomoDD model, and SIMULPS model. Velocity scales are in m/s.

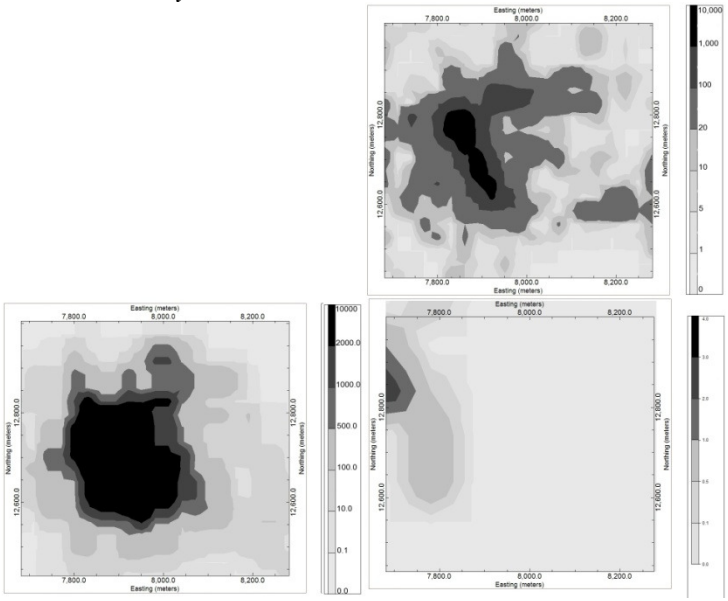

Figure 4.2. Raypath density and derivative weight sum distribution for GeoTom (top right), TomoDD (bottom left), and SIMULPS (bottom right) on 08/01/97 for US Western I.

It is evident in examining Figure 4.1 that each of the three methods was successful in imaging both forward abutment stress and gob. The GeoTom and TomoDD methods cause the gob region to be smeared while the gob is underrepresented by the SIMULPS inversion. Figure 4.2 reveals the highest raypath density and derivative weight sum distribution around the face, as expected, since this is where microseismic event activity is concentrated.

Figure 4.3 displays the initial velocity model, and the synthetic models for the GeoTom and TomoDD inversion methods for the US Western II data set on 11/29/07, with raypath density and derivative weight sum distribution for the two methods displayed to the right of the velocity tomograms.

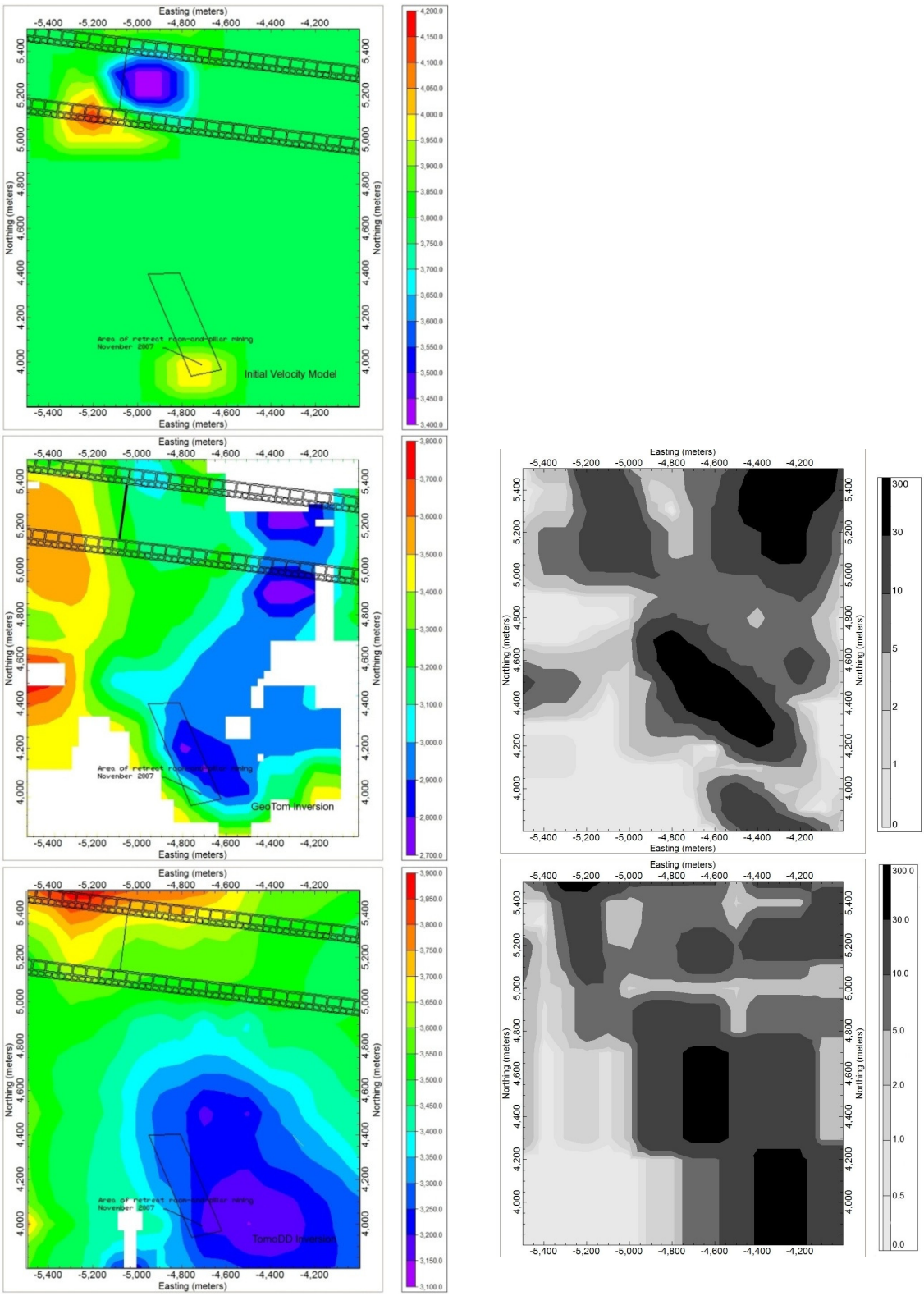

Figure 4.3. Synthetic tomograms, plan view at seam level, for US Western II on 01/11/97. From top to bottom are the initial velocity model, GeoTom model, and TomoDD model. Velocity scales are in m/s. Raypath density and derivative weight sum distribution for GeoTom and TomoDD are shown to the right in grayscale.

Figure 4.4 displays the initial velocity model, and the synthetic models for the GeoTom and TomoDD inversion methods for the Moonee Colliery data for the 24-hour period prior to fall 35, with raypath density and derivative weight sum distribution for the two methods displayed to the right of the velocity tomograms. SIMULPS was not applied to the US Western II and Moonee Colliery mines due to a low receiver count. This is discussed in detail in Chapter 3.

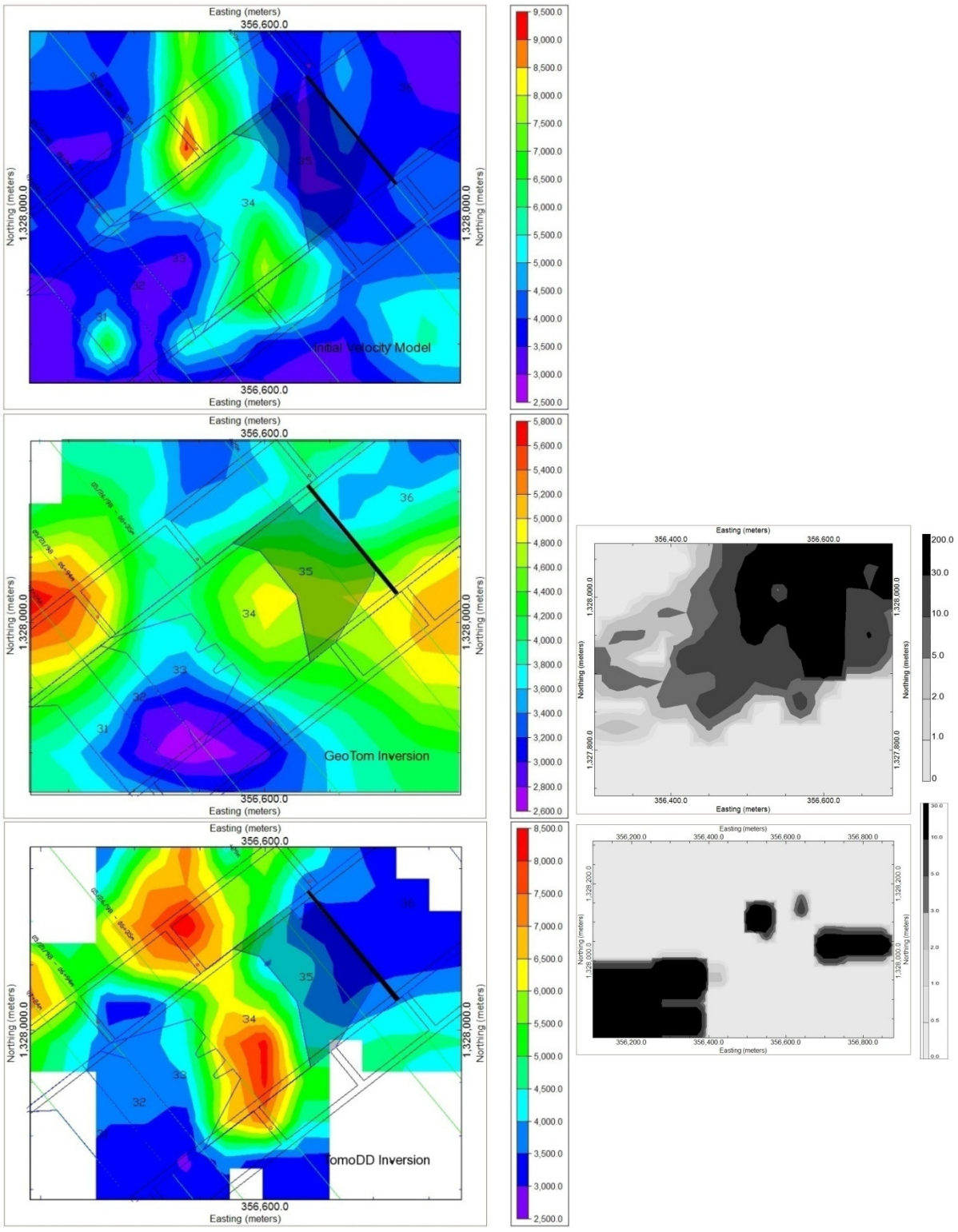

Figure 4.4. Synthetic tomograms, plan view at seam level, for Moonee Colliery Fall 35. From top to bottom are the initial velocity model, GeoTom model, and TomoDD model. Velocity scales are in m/s. Raypath density and derivative weight sum distribution for GeoTom and TomoDD are shown to the right in grayscale.

In Figure 4.4, a high velocity zone that should correspond with Fall 35 appears slightly behind the fall, probably because of the course sampling grid. Both the GeoTom and TomoDD tomograms show relative agreement with the initial velocity model, although the high velocity zone is more smeared in the GeoTom tomogram. In order to quantitatively compare the experimental synthetic tomograms to the initial velocity models, velocity values from the grid files were plotted against each other. Figures 4.5 through 4.7 show these plots for US Western I, US Western II, and Moonee Colliery, respectively.

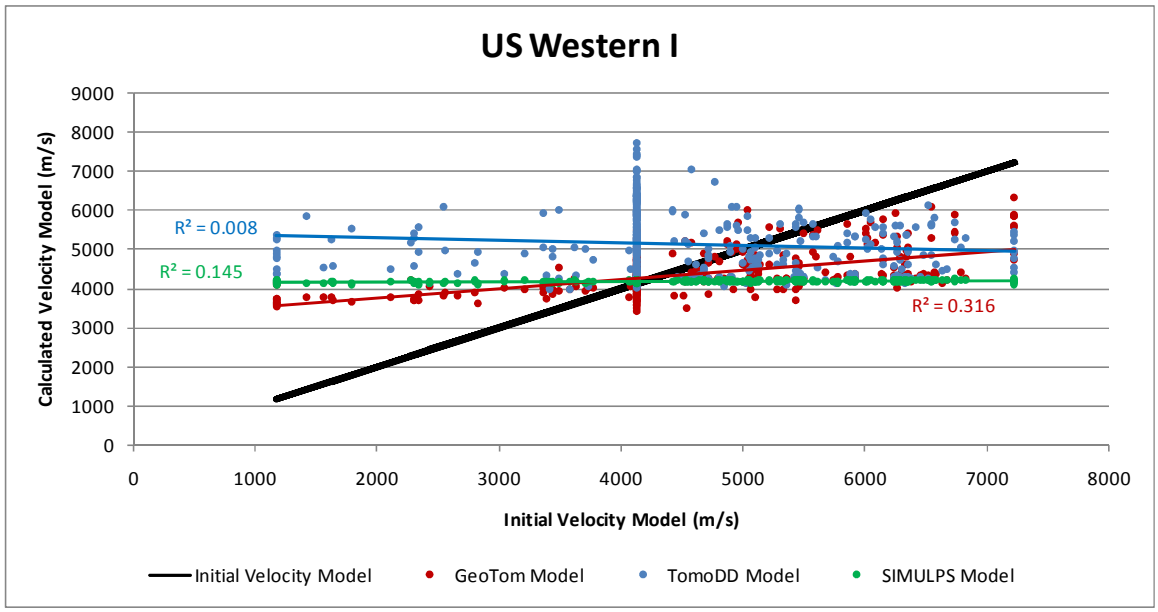

Figure 4.5. US Western I Velocity Comparison Plot.

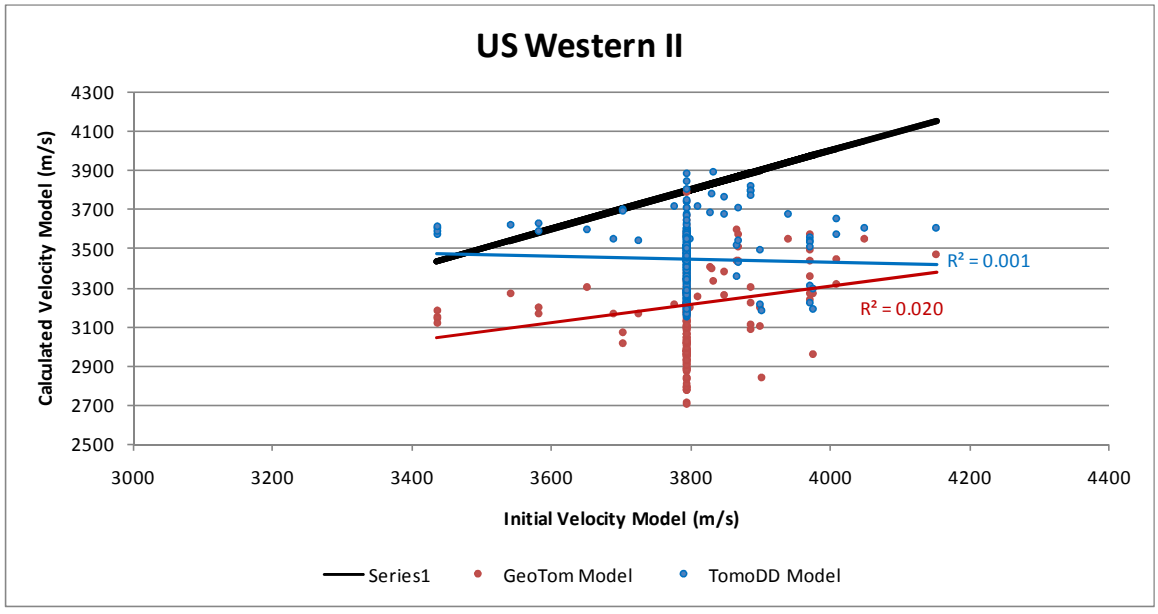

Figure 4.6. US Western II Velocity Comparison Plot.

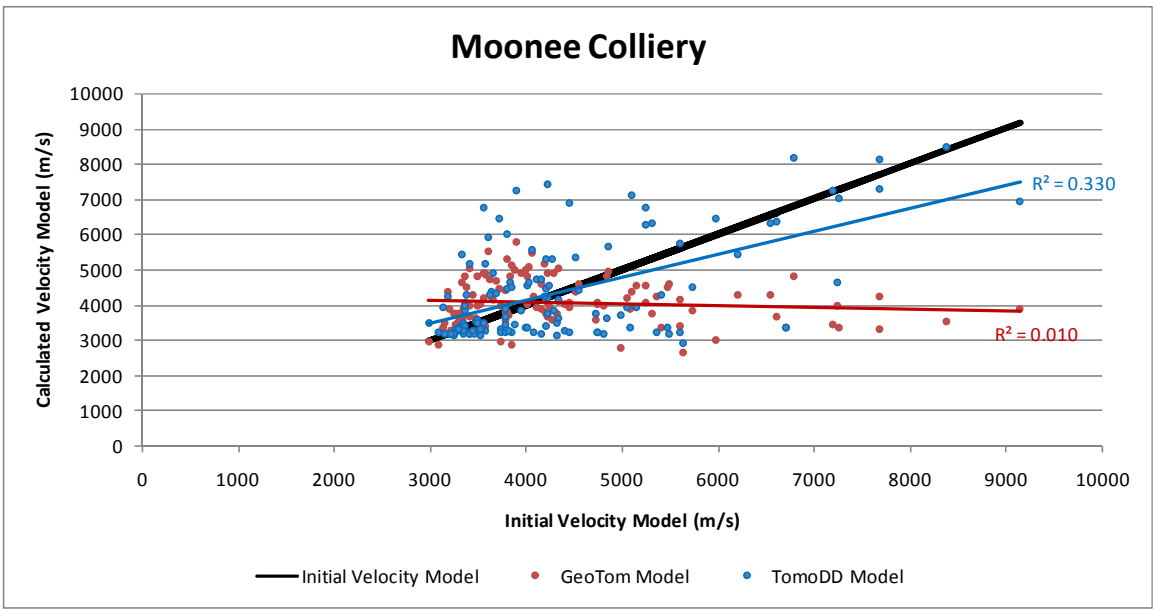

Figure 4.7. US Western Moonee Colliery Velocity Comparison Plot.

The velocity values from the initial velocity model are plotted on the x-axis, while the values from corresponding grid points on the synthetic models are plotted on the y-axis. The heavy black line indicates where the points would fall if a synthetic tomogram exactly matched the initial velocity model, the ideal case. The slopes of the lines for the synthetic tomograms indicate how well the velocity pattern agrees with the initial velocity model. As the slope approaches 1 the agreement improves. The intercept of the trend lines indicates how closely the velocity ranges agree with the initial velocity model. GeoTom appears to give the closest fit for US Western I and US Western II, while TomoDD appears to give the closest fit for Moonee Colliery.

4.6. Discussion and Conclusions

In examining the images in Figure 4.1, GeoTom appears to image the starting model the best. SIMULPS also shows agreement with the starting model. The narrowing of the abutment and gob zones is likely the result of heavy damping applied in the inversion scheme which helps remove noise from the data.

Although the velocity comparison plots indicate that GeoTom fits the US Western II data best, neither method fits the initial model well. Both methods imaged the forward abutment zone, but they also both imaged a smeared low velocity zone. This is likely due to inadequate ray

density. The source receiver geometry for this data set is not ideal. In looking at Figure A.2 it is evident that none of the receivers fall directly over the area of interest. Also, the event count is fairly low with only 176 events measured for January 11, a relatively high count for this data set, so ray density is not sufficient for either method. In comparing the ray density plots in Figures 4.2, 4.3, and 4.4 it is evident that generally rays are most dense in active mining areas, correlating with microseismic activity as expected, and also that the US Western II and Moonee datasets are much sparser than the US Western I dataset. Maximum number of rays on the US Western I scale is 10,000, while on the US Western II scale it is 300 rays and 200 rays for the Moonee scale.

Figure 4.4, displaying Moonee Colliery tomograms, shows that both the GeoTom and TomoDD methods agree well with the initial velocity model, but that TomoDD most closely resembles the initial velocity model. The slope of the TomoDD line in Figure 4.7 also indicates better agreement.

Synthetic tomography allows for several conclusions to be drawn about the adequacy of the data and the applicability of the inversion schemes. First, the importance of appropriate source-receiver configuration and an adequate number of events cannot be understated. The US Western II dataset is simply not dense enough to provide adequate information for any of these methods. Next, the inversion programs that allow for variable gridding and event relocation seem to be superior. They allow the user to fit an inversion grid that takes advantage of areas of high raypath density without underconstraining the areas with low density.

TomoDD probably did not provide the best agreement for the US Western I dataset because of the microseismic event relocations. Since the receivers are all mounted well above the area of interest, the events are not well constrained in the vertical direction, and were relocated a significant distance above the seam, which probably caused the tomogram not to fit the initial velocity model as well. GeoTom does not relocate events. Constraining the event locations in the z direction would probably improve the TomoDD tomogram.

Synthetic tomography proved to be useful in evaluating source receiver geometry and inversion method. TomoDD and SIMULPS appear to be the superior techniques, although neither is robust when used in conjunction with a sparse dataset. The observations made from the synthetic tomograms can help to determine the best inversion method and troubleshoot source-receiver configurations.

Chapter 4 References

Evans, J., D. Eberhart-Phillips and C. Thurber (1994). User's manual for SIMULPS12 for imaging vp and vp/vs: A derivative of the "Thurber" tomographic inversion SIMUL3 for local earthquakes and explosions. USGS.

Friedel, M., D. Scott, M. Jackson, T. Williams and S. Killen (1996). "3-D tomographic imaging of anomalous stress conditions in a deep US gold mine." Journal of Applied Geophysics **36**: 1-17.

Gilbert, P. (1972). "Iterative methods for the three-dimensional reconstruction of an object from projections." Journal of Theoretical Biology **36**: 105-117.

Golden, B. (1976). "Shortest-Path Algorithms: A Comparison." Operations Research **24**(6): 1164-1168.

Hadamard, J. (1952). Lectures on Cauchy's Problem in Linear Partial Differential Equations. New York, Dover Publications.

Hanna, K., K. Haramy and T. Ritzel (1991). Automated Longwall Mining for Improved Health and Safety at the Foidel Creek Mine. SME Annual Meeting, Denver, CO.

Hole, J. (1992). "Nonlinear high-resolution three-dimensional seismic travel time tomography." Journal of Geophysical Research **97**(B5): 6553-6562.

Iannacchione, A., G. Esterhuizen, T. Bajpayee, P. Swanson and M. Chapman (2005). Characteristics of mining-induced seismicity associated with roof falls and roof caving events. 40th U.S. Rock Mechanics Symposium, Anchorage, AK, American Rock Mechanics Association.

Jackson, M. and D. Tweeton (1994). Report of Investigations 9497: MIGRATOM - Geophysical Tomography Using Wavefront Migration and Fuzzy Constraints. B. o. Mines.

Maleki, H., W. Hustrulid and D. Johnson (1984). Pressure Measurements in the Gob. Rock Mechanics in Productivity and Production - 25th Symposium on Rock Mechanics

Mosegaard, K. and A. Tarantola (2002). Probabilistic Approach to Inverse Problems, Academic Press for the International Association of Seismology and Physics of the Earth Interior.

Peng, S. and H. Chiang (1983). Longwall Mining. New York, Wiley.

Prasad, M. and M. Manghnani (1997). "Effects of pore and differential pressure on compressional wave velicty and quality factor in Berea and Michigan sandstones." Geophysics **62**(4): 1163-1176.

Rawlinson, N. and M. Sambridge (2003). Seismic traveltime tomography of the crust and lithosphere. Advances in Geophysics. R. Dmowska, Academic Press. **46:** 81-197.

Sallares, V., J. Danobeitia and E. Flueh (2000). "Seismic tomography with local earthquakes in Costa Rica." Tectonophysics **329**(1-4): 61-78.

Seya, K., I. Suzuki and H. Fujiwara (1979). "The change in ultrasonic wave velocities in triaxially stressed brittle rock." Journal of Physics of the Earth **27**(5): 409-421.

Soldati, G. and L. Boshi (2005). "The resolution of whole Earth seismic tomographic models." Geophysical Journal International **161**: 143-153.

Thill, R. (1973). Acoustic Methods for Monitoring Failure in Rock. 14th Symposium on Rock Mechanics, University Park, PA.

Toksöz, M., C. Cheng and A. Timur (1976). "Velocities of seismic waves in porous rocks." Geophysics **41**(4): 621-635.

Tong, C. (2000). "Model parameterisation and assessment in travel time seismic tomography: a user's perspective." Lithos Science Report **2**: 101-107.

Tselentis, G.-A., A. Serpetsidaki, N. Martakis, E. Sokos, P. Paraskevopoulos and S. Kapotas (2007). "Local high-resolution passive seismic tomography and Kohonen neural

networks - Application at the Rio-Antirio Strait, central Greece." Geophysics **72**(4): B93-B106.

Waldhauser, F. and W. Ellsworth (2000). "A double-difference earthquake location algorithm: method and application to the Northern Hayward Fault, California." Bulletin of the Seismological Society of America **90**(6): 1353-1368.

Watanabe, T., T. Matsuoka and Y. Ashida (1999). Seismic traveltime tomography using Fresnel volume approach. 69th SEG Annual Meeting.

Whittles, D., I. Lowndes, S. Kingman, C. Yates and S. Jobling (2006). "Influence of geotechnical factors on gas flow experienced in a UK longwall coal mine panel." International Journal of Rock Mechanics & Mining Sciences **43**: 369-387.

Wyllie, R., A. Gregory and G. Gardner (1958). "An experimental investigation of factors affecting elastic wave veloicties in porous media." Geophysics **23**(3): 459-493.

Yasitli, N. and B. Unver (2005). "3-D numerical modelling of stresses around a longwall panel with top coal caving." International Journal of Rock Mechanics & Mining Sciences **42**(2): 219-235.

Zhang, H. and C. Thurber (2003). "Double-difference tomography: the method and its application to the Hayward Fault, California." Bulletin of the Seismological Society of America **93**(5): 1875-1889.

Chapter 5
Applications of Passive Seismic Velocity Tomography at Longwall Coal Mines in the Western US

Abstract

A double difference earthquake tomography and relocation algorithm was used to generate time lapse velocity tomograms of two longwall mines in the western United States to determine if the method could image high velocity zones correlating with high stress in abutment zones. If the method is able to image these high stress zones then it holds promise as a tool for delineating stress transition processes. Mining induced microseismic events were utilized as passive sources at both mines and surface arrays acted as receivers. The first mine, US Western I, had a relatively compact source-receiver configuration and high microseismic activity, resulting in a dense raypath distribution. The second mine, US Western II, had a receiver array that covered a much larger area with fewer events cataloged, resulting in a fairly sparse raypath distribution. High velocity zones were imaged in areas of side and forward abutment stress for the US Western I data. Low velocity zones were imaged in areas of the gob, and these velocity zones redistributed with face retreat. For the US Western II data set a low velocity zone was consistently imaged in the gob area that redistributed with face advance, but high velocities correlating with abutment stress were not evident.

5.1. Introduction

Passive seismic velocity tomography is a technology that has the potential to provide real time inference of stress redistribution at a mine on a global scale. Current monitoring of stress in underground coal mines involves localized measurement of stress, and interpolation of the measurements. Seismic velocity tomography is unique because it allows for noninvasive measurement of a large rock mass. When mining-induced seismic events, or passive sources, are utilized this measurement may be remote and continuous, and practical over a long term.

There are many examples of seismic velocity tomography experiments in underground mines (Körmendi et al. 1986; Maxwell and Young 1995; Friedel et al. 1996; Maxwell and Young 1996; Young and Collins 2001), but very few of them utilize long term, passive sources (Glazer and Lurka 2007; Luxbacher et al. 2008). If passive sources can be used to image typical longwall

abutment stress patterns then this technology has applications for inferring the existence of other high stress anomalies, and forecasting major failure events, such as bumps.

Long term passive seismic velocity tomography has been shown to image high velocity zones in these abutment stress regions, and to show their redistribution with face advance (Luxbacher et al. 2008). Two longwall microseismic data sets are inverted to determine if this original case study can be improved, and if the results are repeatable with a sparser data set.

5.2. Background

5.2.1. Velocity tomography

Velocity tomography relies on the premise that if the travel time and length of a seismic ray are known then the velocity along the ray may be calculated and the velocities of segments of the ray can also be calculated. This allows a rock mass surrounding a mine to be propagated with seismic rays – the source is typically controlled and may include hammer strikes, and blasts – the travel times are measured by strategically placed receivers, and then the mass is divided into 3 dimensional cubes, called voxels. The velocity in each of these voxels is determined and a velocity picture is generated from the voxels. If passive sources, such as mining-induced microseismic events, are used, these rays can be measured remotely and the velocity images created at regular time intervals. Over the long term, the velocity images can be examined to determine if any unusual high velocity anomalies are occurring. The caveat is that now the areas of the mine that are traversed by rays can only be controlled by the receivers, so their configuration must be carefully considered.

When a rock mass is under pressure pore space and microcracks begin to close, allowing seismic rays to propagate through the mass more quickly because they do not have to traverse as many air interfaces. Due to this relationship, high velocity zones may be used to infer high stress in a mine. There are exceptions – rocks with a very dense matrix will not show the velocity contrast that more porous rock will demonstrate (Yale 1985). Also, this relationship is not a strictly linear one. Typically, the p-wave velocity gradient of rocks under load is high at low pressures and levels out at higher pressures (Prasad and Manghnani 1997). Also, before failure, the velocity may drop as microcracks coalesce.

5.2.2. Longwall Abutment Stress

Abutment stress occurs in underground mines as ore is extracted along the boundary where the material is removed (Peng and Chiang 1983). In longwall mining this stress is transferred immediately in front of the face and to the sides of the panel. Formation of gob

behind the advancing face allows for stress relief. Abutment stress is generally larger on the tailgate side, if it is adjacent to a mined out panel. Front abutment pressure is usually detectable at a lateral distance of about 1 times the overburden (Peng and Chiang 1983). These stresses would be expected to appear as high velocity zones in a seismic velocity tomogram.

5.3. Site Descriptions

Tomograms were generated from two different coal mines operating longwall systems. Both of the mines are located in the Western United States, and these mines will be referred to as US Western I and US Western II. The mines are fairly deep with about 350 and 440 meters of overburden, respectively. Also, massive strata are present above and below the seams. Bumps in underground coal mines usually occur where the roof and floor are massive and competent, and generally at depths greater than 300 meters. Both mines are at risk for bumps, making them appropriate sites for case studies for the application of passive seismic velocity tomography.

5.3.1. US Western I

These data were collected over an 18-day period in 1997. Average overburden at the mine is 350 meters, with coal seam height ranging from 2.6 to 3.0 meters. The seam is overlain by 2-7 meters of sandstone and underlain by 35 meters of sandstone. The mine has experienced bumps in the past, mainly in the tailgate entry of the longwall.

The longwall panel under investigation is 250 meters wide with a previously mined panel to the tailgate side and an unmined panel to the headgate side. Over the course of the study the face retreated 431 meters, averaging about 24 meters per day. Sixteen geophones were assembled on the surface to monitor and locate microseismic events. Figure A.1 in Appendix A displays the panel geometry and relative receiver locations, along with face locations. The face retreats through a series of backfilled entries about halfway through the study. These entries were mined for escapeway purposes and are evident in Figure A.1. The entries were backfilled with a light-weight cement and carried some of the load, although not all because the cement stiffness was less than the pillars. No unusual events were observed as the shearer mined through the entries (Seymour et al. 1998).

5.3.2. US Western II

NIOSH began monitoring this mine in 2005, and the data used in this study range from November 2007 to January 2008 with 12 days during this period investigated. Seismometers are located above this mine and another mine covering an area of approximately 250 square

kilometers. Ten triaxial strong motion seismometers and one short period seismometer were installed. Overburden is approximately 440 meters in the area of interest.

The longwall panel under investigation is 250 meters wide and averaged about 9.5 meters of retreat per day over the course of four months, November 2007 to January 2008. Multiple seam mining has occurred in the vicinity of the longwall panel under investigation, but the geometry of the overlying workings is not known to the author. Additionally, during retreat of the longwall, retreat room-and-pillar mining was taking place to the south during November. The longwall panel to the immediate south is previously mined while the panel to the north has not been mined. Figure A.2, in Appendix A, displays the locations of the receivers in relation to the longwall panel and the area of room and pillar mining. Figure A.3 displays the longwall geometry in more detail, along with the 12 face locations.

5.4. Tomogram Generation

Several different methods were used to generate tomograms at these sites, as detailed in Chapter 3, and TomoDD was determined to be the most appropriate inversion algorithm. All of the results presented in this paper were calculated using TomoDD.

5.4.1. Data Description

The raw data for the US Western I site include 172,632 p-wave arrival times from 11,696 microseismic events. There was an average of 650 events per day with a maximum of 1,450 events. The event distribution is displayed in Figure 5.1. The area of interest for US Western I is shown in Figure A.1 and is 0.34 square kilometers.

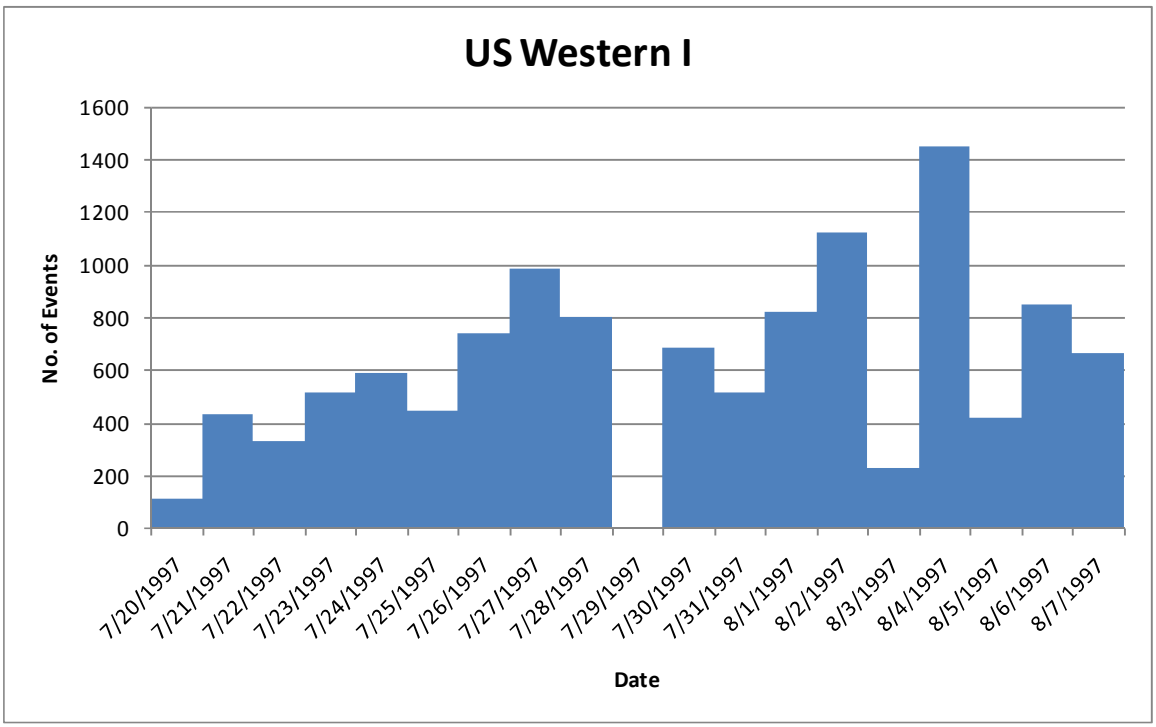

Figure 5.1. US Western I Microseismic Event Distribution.

Additionally, a layered initial velocity model was developed, based on measurements at the site and includes a vector normal to the bedding planes. This layered model is displayed as a one dimensional velocity model in Figure 5.2.

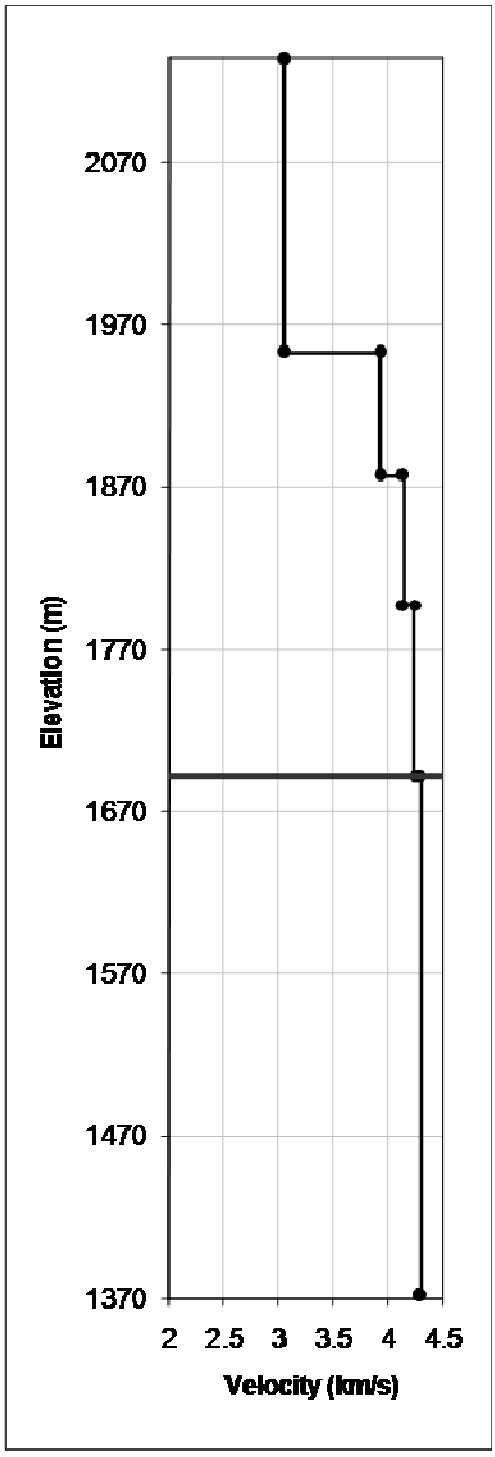

Figure 5.2. US Western II Initial Velocity Model. The black line indicates the approximate location of the coal seam.

The raw data for the US Western II site include 35,297 p-wave arrival times from 7,009 events There was an average of 60 events per day with a maximum of 187 events. The event distribution is displayed in Figure 5.3.

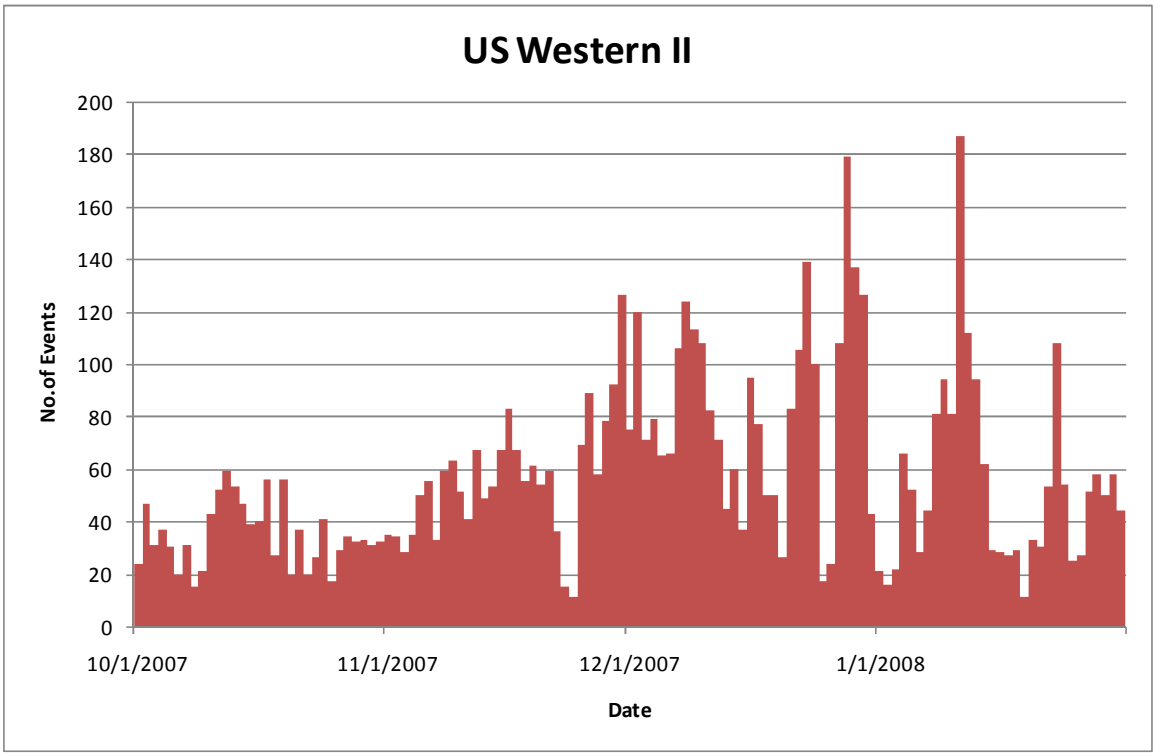

Figure 5.3. US Western II Microseismic Event Distribution.

The area of interest for US Western II is shown in Figures A.2 and A.1 in Appendix A and is approximately 2.53 square kilometers.

Also, straight raypath velocities were examined and any velocities above 10,000 m/s were removed from both of the data sets. These velocities are likely the result of poor arrival time picks, and could produce high velocity artifacts in the tomograms. Pink phyllite has one of the highest p-wave velocities at 7,100 m/s (Carmichael 1989), so it would be reasonable to remove values greater than this. A value of 10,000 m/s was chosen to account for additional curvature in the ray. A homogenous initial velocity model with a velocity of 3,440 m/s, average velocity of the data set, was assumed for US Western II.

Examination of these data indicate that the US Western II dataset is more sparse than the US Western I dataset. There are less events per day and less receivers to measure travel times, so the US Western II model will be traversed by far fewer raypaths than the US Western I model.

Approximately 20% of the raypaths were removed from the US Western II dataset because of inconsistent spatial distribution that did not allow for gridding that would produce meaningful results at the mine level. A detailed explanation may be found in Chapter 3.

5.4.2. Inversion Algorithm and Parameterization

The two Western US case studies present tomograms that are generated by a double difference, damped least squares relocation algorithm. This algorithm, along with a Simultaneous Reconstructive Technique algorithm, and another damped least squares relocation algorithm were utilized to generate tomograms for experimental and synthetic data, and was determined to be the most appropriate method. These method comparisons and selection criteria are detailed in Chapters 3 and 4.

The double difference algorithm, TomoDD, written by Haijiang Zhang and Clifford Thurber, is available for download and was developed for use in earthquake tomography. It is based on the double difference relocation algorithm, HypoDD (Waldhauser 2001). TomoDD is a double-difference method that jointly relocates events and determines a velocity model (Zhang and Thurber 2003). There are several examples in the literature of its use in earthquake relocation and tomography (Waldhauser and Ellsworth 2000; Zhang and Thurber 2003; Dunn and Chapman 2006), but no applications to mining. The assumption behind double-difference tomography is that if distance between two seismic events is small compared to the distance from the events to the receivers they will have similar travel times. The difference between calculated and measured travel times between two events at one receiver can then be used to adjust the position of the events (Waldhauser and Ellsworth 2000). TomoDD allows for variable gridding; the interval between the x-, y-, and z- nodes in the inversion grid can be varied so that a finer grid may be applied in areas that are well sampled and a courser grid in areas that are not as well sampled. This is especially useful for passive sources because raypath density is rarely consistent, and areas of high microseismic activity can be imaged with a fine grid.

Important parameters in TomoDD include damping, weighting, and number of iterations. The damping factor damps the hypocentral adjustments if the adjustment vector becomes large or unstable. In TomoDD, examination of a condition number output by the program is used to determine the damping value. The condition number, the ratio of the smallest to largest eigenvalue, should be between 40 and 80 with damping values between 1 and 100 (Waldhauser and Ellsworth 2000). For the US Western I data damping factors between 120 and 150 were used resulting in condition numbers from 45 to 66. It was more difficult to achieve the recommended ranges for the US Western II. For the US Western II data damping factors of 20 to 30 were used

resulting in condition numbers of 10 to 29. TomoDD is limited by the distribution and number of receiver stations which explains why a more favorable set of condition numbers could not be obtained for the US Western II data set. The weighting factors refer to smoothing in the x, y, and z directions – factors of 3 to 5 were used for both data sets. Fourteen to 32 iterations were run.

5.4.3. Procedure

After data reduction the data were divided by day. For the US Western I data, tomograms were generated for each day. For the US Western II data, 12 days with the most events were chosen to be processed. After the parameters were determined and the data output from TomoDD, the velocity models were plotted in a three dimensional imaging program and sliced laterally at seam level.

5.5. Results

Select results for the US Western I case study are displayed in Figure 5.4. They include plan view tomograms at seam level for: 07/25/97, 07/27/97, 07/28/97, 07/31/97, 08/01/97, and 08/04/97. Derivative weight sum plots are displayed for the same days in Figure 5.5. Previous tomography studies have utilized derivative weight sums as a measure of resolution, with higher values indicating better resolved areas (Sallares et al. 2000). Fourteen days of the study are displayed in Appendix B.

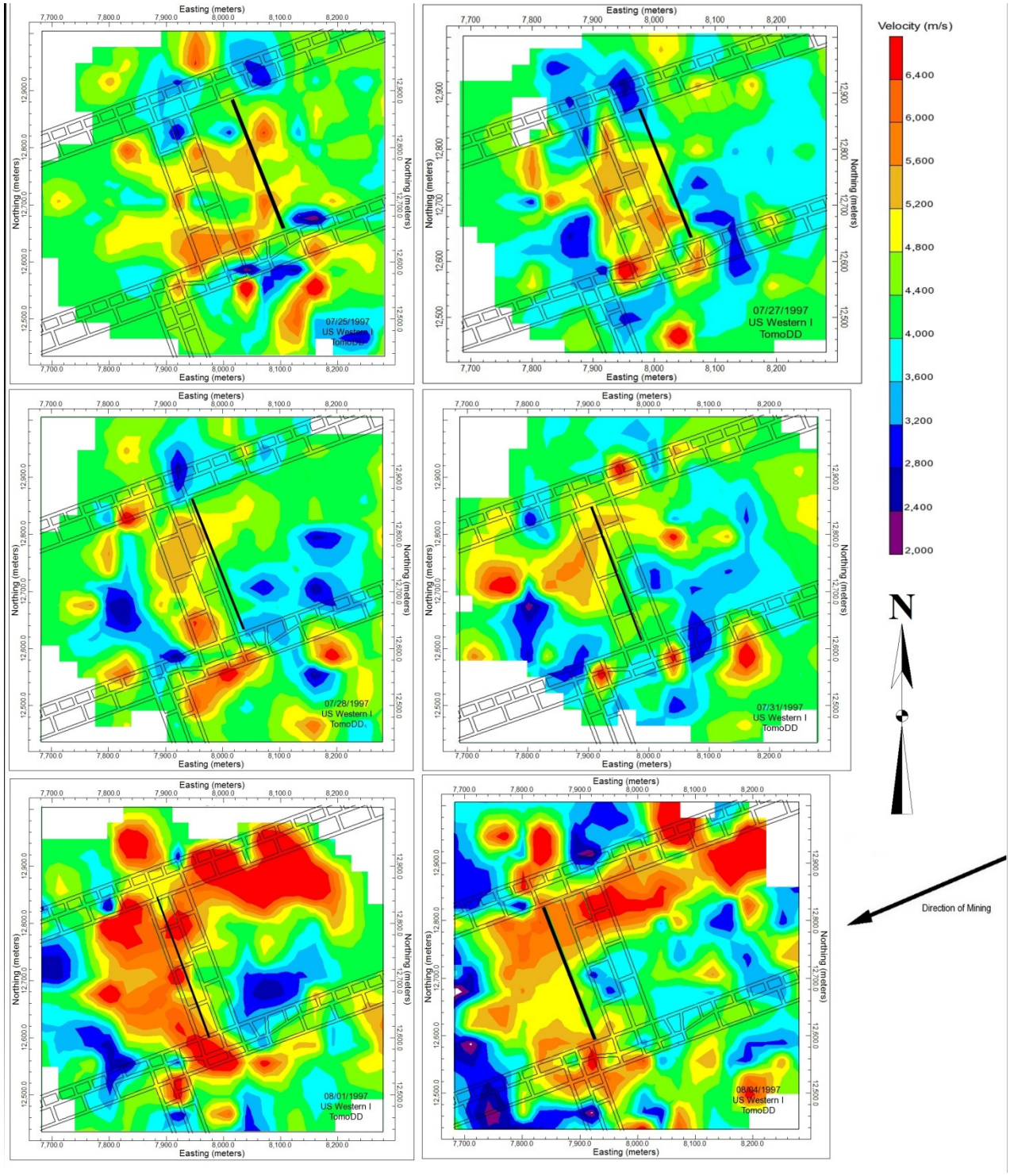

Figure 5.4. Plan view velocity tomograms at seam level for US Western I. Direction of mining is northeast to southwest. Face locations are shown in black and pixels not traversed by rays are shown in white.

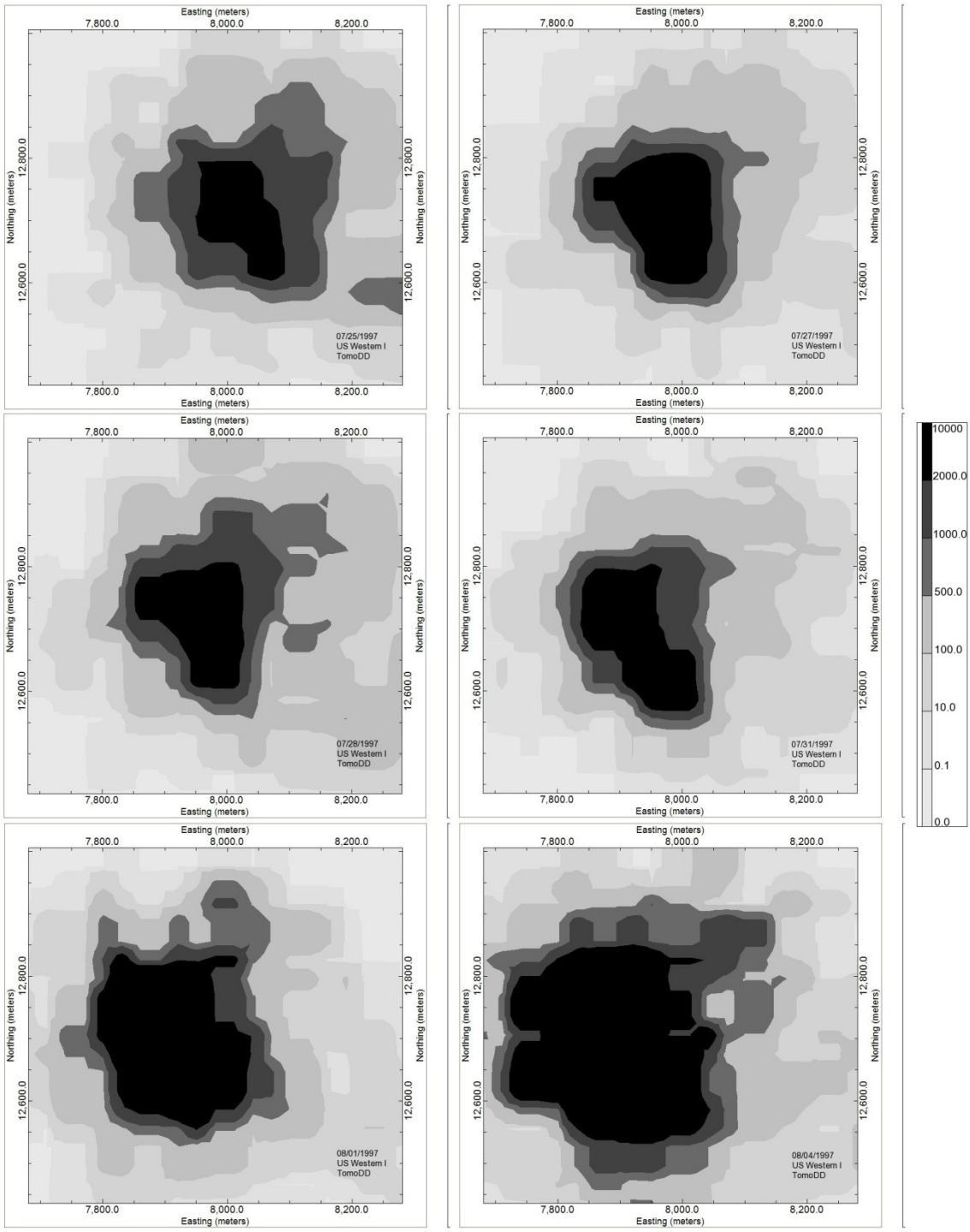

Figure 5.5. Derivative weight sum distribution corresponding with velocity tomograms in Figure 5.4.

The six tomograms displayed in Figure 5.4 consistently image a high velocity zone in front of the face, a relatively lower velocity zone in the gob area and a high velocity zone along the tailgate (the northern gateroad). These features can be seen to redistribute with face retreat. It

is also interesting to notice that during the first 3 days, as the face approaches the cross-entries, the high velocity zone extends from the face through the entries. After the face begins mining through the entries the high velocity zone redistributes in front of the face. Similar behavior might be expected of the front abutment stress if the pillars around the backfill were supporting some of the abutment load. Also, the high velocity zone becomes relatively higher and distributes inby, along the tailgate on 08/03/97. A power move on 08/02/97 caused the face to remain stationary for most of the day which could have contributed to a shift in stress. Also the tailgate is close to the axis of an anticline on this day (Swanson 2008). Also, high derivative weight sum values are observed in the vicinity of the face, corresponding with areas of high microseismic activity.

Select results for the US Western II case study are displayed in Figure 5.6. They include plan view tomograms at seam level for: 11/28/07, 11/29/07, 11/30/07, 12/28/07, 01/11/08, 01/12/08. Derivative weight sum plots are displayed for the same days in Figure 5.7. Twelve days of the study are displayed in Appendix C.

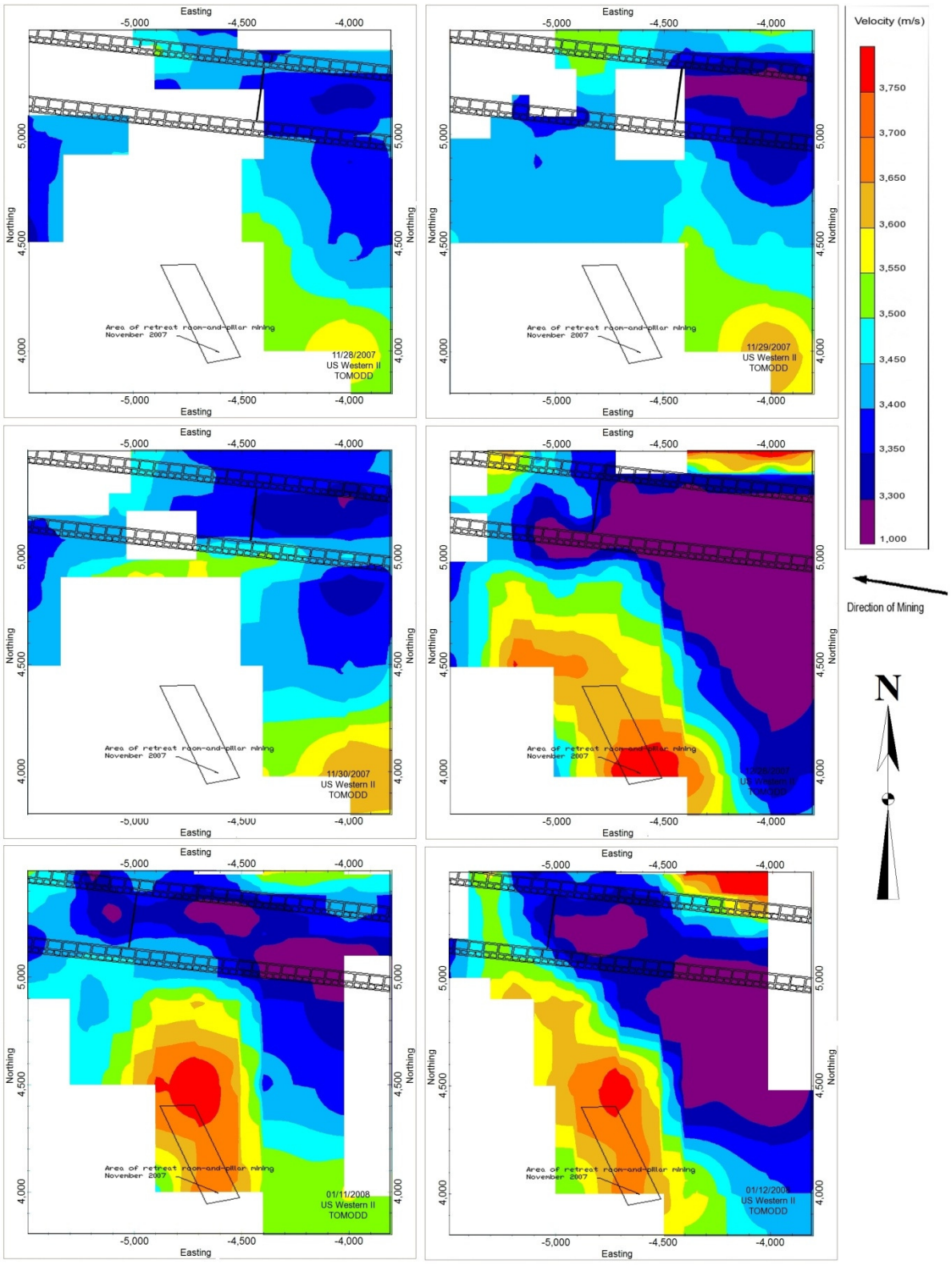

Figure 5.6. Plan view tomograms at seam level for US Western II. Direction of mining is east to west. Face locations are shown in black and pixels not traversed by rays are shown in white.

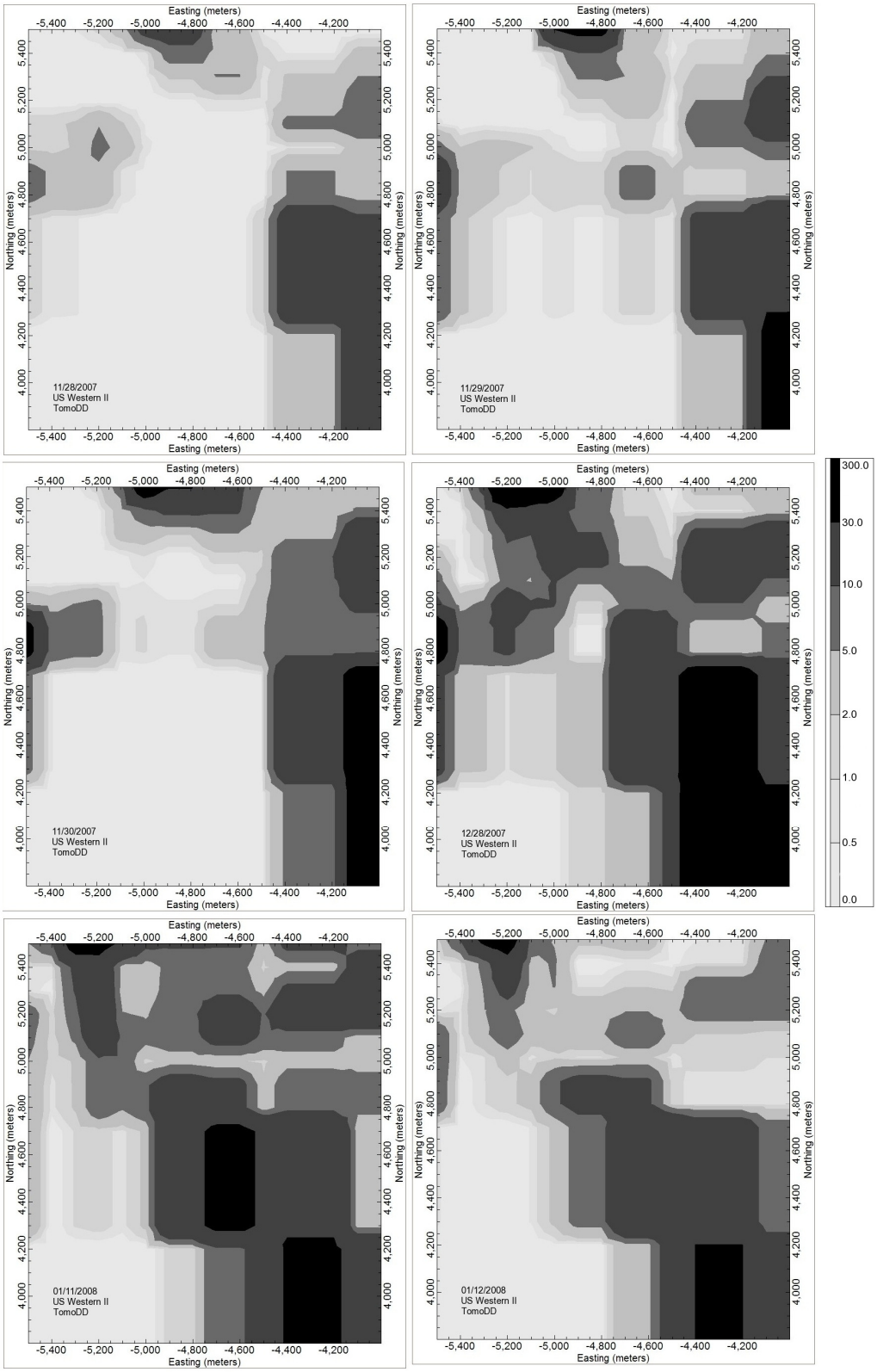

Figure 5.7. Derivative weight sum distribution corresponding with velocity tomograms in Figure 5.6.

Two features are clearly evident in examining the six tomograms in Figure 5.6. First, a low velocity zone extends from the face inby to the edge of the tomogram on each of the six tomograms. This zone also extends to the southeast. Second, a high velocity zone is present south of the tailgate corner (the southern gateroad is the tailgate) on the last three tomograms. In November, the lower 5% of the panel outlined in the southern zone of the tomogram was mined by retreat room and pillaring. This zone appears to correlate with that panel, but ray coverage was not adequate to image that area in November. The low velocity zone redistributes with face retreat, but the high velocity zone does not appear to redistribute.

5.6. Conclusions and Recommendations

The results for US Western I show that high velocity zones in the forward and side abutment stress areas were consistently imaged and seen to redistribute. Additionally, the zones redistributed as would be expected in light of the backfilled cross entries and known geology. As the face approached the cross entries the high velocity zone extended from the face through the cross entries and began to narrow and shift forward as the face came through the cross entries. The front abutment stress would be expected to behave in this manner since the backfill was less stiff than the coal and the pillars in this area carried additional load. Also, the high velocity zone that extended back along the tailgate for the last two days is explained by the presence of the axis of an anticline and change in retreat rate. Since the TomoDD algorithm images high velocity zones that correlate well with predicted stress abutment zones this technology should be appropriate for imaging high stress anomalies that would be indicative of an impending roof fall or bump assuming the raypath distribution is adequate.

An adaptive gridding algorithm would be more appropriate for passive seismic tomography in underground mines. The variable gridding algorithm used did allow for the area of interest to be gridded more finely, but was still not adequate for the US Western II data set due to the receiver array configuration and spatial variation in event locations. Adaptive gridding is more flexible than variable gridding as it allows for irregular shapes in the grid while the variable gridding only allows for rectangles. The derivative weight sum plots provide some insight into the resolution of the images. If the scales for US Western I and US Western II are compared the black zone for US Western I refers to a range of 2,000 to 10,000 while the black zone for the US Western II data refers to a range of only 30 to 300. As a result, more confidence may be placed in the US Western I tomograms. Even with the suboptimum source receive array configuration the low velocity zone correlating with gob was consistently imaged. However, since the

abutment stresses were not evident as high velocity zones it is unlikely that a similarly sparse data set would prove useful for forecasting bumps.

Chapter 5 References

Carmichael, R. (1989). Practical Handbook of Physical Properties of Rocks and Minerals. Boca Raton, CRC Press.

Dunn, M. and M. Chapman (2006). "Fault orientation in the eastern Tennessee seismic zone: A study using the double-difference earthquake location algorithm." Eastern Section Seismological Research Letters **77**(4): 494-504.

Friedel, M., M. Jackson, E. Williams, M. Olson and E. Westman (1996). "Tomographic imaging of coal pillar conditions: observations and implications." International Journal of Rock Mechanics, Mining Sciences, and Geomechanics Abstracts **33**(3): 279-290.

Glazer, S. and A. Lurka (2007). Application of passive seismic tomography to cave mining operations based on experience at Palabora Mining Company, South Africa. The Southern African Institute of Mining and Metallurgy 1st International Symposium on Block and Sub-Level Caving, Cape Town, South Africa.

Körmendi, A., T. Bodoky, L. Hermann, L. Dianiska and T. Kàlmàn (1986). "Seismic measurements for safety in Mines." Geophysical Prospecting **34**: 1022-1037.

Luxbacher, K., E. Westman, P. Swanson and M. Karfakis (2008). "Three-dimensional time-lapse velocity tomography of an underground longwall panel." International Journal of Rock Mechanics & Mining Sciences **45**(4): 478-485.

Maxwell, S. and R. Young (1995). "A controlled in-situ investigation of the relationship between stress, velocity and induced seismicity." Geophysical Research Letters **22**(9): 1049-1052.

Maxwell, S. and R. Young (1996). "Seismic imaging of rock mass responses to excavation." International Journal of Rock Mechanics, Mining Sciences, and Geomechanics Abstracts **33**(7): 713-724.

Peng, S. and H. Chiang (1983). Longwall Mining. New York, Wiley.

Prasad, M. and M. Manghnani (1997). "Effects of pore and differential pressure on compressional wave velicty and quality factor in Berea and Michigan sandstones." Geophysics **62**(4): 1163-1176.

Sallares, V., J. Danobeitia and E. Flueh (2000). "Seismic tomography with local earthquakes in Costa Rica." Tectonophysics **329**(1-4): 61-78.

Seymour, B., D. Tesarik, M. Larson and J. Shoemaker (1998). Stability of Backfilled Cross-Panel Entries During Longwall Mining. 17th International Conference on Ground Control in Mining, Morgantown, WV, West Virginia University.

Swanson, P. (2008). Email: Simulps preliminary results. E. Westman. Blacksburg, VA.

Waldhauser, F. (2001). hypoDD - A Program to Compute Double-Difference Hypocenter Locations, USGS.

Waldhauser, F. and W. Ellsworth (2000). "A double-difference earthquake location algorithm: method and application to the Northern Hayward Fault, California." Bulletin of the Seismological Society of America **90**(6): 1353-1368.

Yale, D. (1985). "Recent advances in rock physics." Geophysics **50**(12): 2480-2491.

Young, R. and D. Collins (2001). "Seismic studies of rock fracture at the Underground Research Laboratory, Canada." International Journal of Rock Mechanics & Mining Sciences **28**: 787-799.

Zhang, H. and C. Thurber (2003). "Double-difference tomography: the method and its application to the Hayward Fault, California." Bulletin of the Seismological Society of America **93**(5): 1875-1889.

Chapter 6
Passive Seismic Velocity Tomography of a Longwall Panel with Episodic Caving

Abstract

Passive seismic velocity tomograms are generated from a microseismic data set collected at Moonee Colliery in Australia. Previous analyses of these data almost always showed an increase in microseismic event occurrence frequency prior to a large roof fall in the gob, but they did not always give an adequate amount of time to warn personnel of the impending fall. Unique conditions at this mine have contributed to episodic caving as the face retreats, and larger falls were well documented. A double difference damped least squares algorithm is used to generate velocity tomograms for 24 hour periods prior to 14 of these falls. Velocity anomalies were imaged in the area of the fall, but they were not consistently high or low.

6.1. Introduction

Seismic velocity tomography has proven useful for inferring relative stress in underground coal mines, but has rarely been applied over the long term. This is because most experiments have relied upon active sources, including hammer strikes, longwall shearers, and blasts (Körmendi et al. 1986; Friedel et al. 1996; Watanabe and Sassa 1996; Manthei 1997; Westman et al. 2001; Westman 2004). These methods require active participation and planning, and are only practical in the short term. Passive seismic velocity tomography, which utilizes mining induced microseismic events, on the other hand, allows for remote and continuous monitoring and could be implemented for near real time imaging of a rock mass. Tomography requires a fairly dense distribution of events to generate an image, generally, at least 24 hours of monitoring, so the image cannot be defined as real time.

Passive seismic velocity tomograms were generated from the Moonee Colliery data set using three inversion algorithms. Evaluation of these algorithms is discussed in detail in Chapters 3 and 4. TomoDD, a double difference damped least squares event relocation method, was determined to be the most suitable method and is presented in detail here. Fourteen tomograms were generated, each for a 24-hour period before a major fall to determine if a velocity anomaly can be identified in the vicinity of the fall and something about the change in stress inferred from the image.

6.2. Background

Moonee Colliery is located just north of Sydney, Australia. The mine was employing a longwall system with a narrow face, about 100 meters, in low overburden containing strong and massive strata. The combination of these conditions led to inconsistent caving. When the roof behind the longwall did cave, a high volume of material was involved in the fall and often caused serious windblasts. On January 22, 1998, 6 miners were injured by one of the windblasts and a microseismic system was later installed (Iannacchione et al. 2007). The operators found that microseismic event frequency typically increased substantially just before a fall, allowing them to warn the longwall crew some of the time; however, the increase was often so close to the fall that there was not adequate time to issue a warning (Fowler et al. 2003; Sharma and Fowler 2004).

Since microseismic monitoring proved successful in forecasting caving events at this mine the next logical step is to investigate whether the same data could be used to image velocity anomalies in the strata that would indicate an impending caving event.

Ideally, as a longwall face retreats the roof behind the face will cave continuously with mining, relieving stress ahead of mining. Iannacchione and others describe the roof falls at Moonee Colliery as periodic or episodic in nature because they are not closely related to the short term mining rate. Rather, the longwall face retreats while the roof stays up behind the shields. As mining progresses the hanging roof eventually becomes unstable and falls in one or several large masses (Iannacchione et al. 2007).

6.2.1. Velocity tomography

Velocity tomography is a noninvasive method for imaging a mass. A velocity tomogram is generated by dividing the area under consideration, a rock mass, in this instance, into cubes, or voxels, and assigning a velocity value to each voxel based on the time a segment of the seismic ray took to pass through the voxel. The group of voxels that make up the mass form a three-dimensional image that can be sliced in areas of interest, such as active faces.

Due to the nature of the inversion processes used to produce the image it can be difficult to ascertain where the data are informing the model and where there is a lack of data. Most inverse problems are ill-posed (Hadamard 1952; Mosegaard and Tarantola 2002), meaning they have an infinite number of solutions with a few that are appropriate when other information about the site is considered (Hole 1992). One way to determine where an image is well constrained is to examine the ray paths. Also, the derivative weight sum at each voxel can be examined to determine relative resolution of the image, with higher derivative weight sums equating to a better resolved regionsall(Sallares et al. 2000).

6.3. Site Description

6.3.1. General

This mine employs longwall mining with panels that are 100 meters wide and overlain by 30 to 35 meters of Teralba Conglomerate (Hayes 2001). The narrow panels were designed to control subsidence, but the geometry of the panel and the nature of the conglomerate caused discontinuous caving. The conglomerate was actually arching over the extracted area a substantial distance prior to failure. Overburden ranges from 90 to 170 meters. The panel geometry is shown in Figures A.4 to A.7 in Appendix A.

6.4. Tomogram Generation

6.4.1. Data Description

These data are part of a multi-year study at Moonee Colliery in Australia. 14 Hz, three component geophones were installed in 10 meter deep roof boreholes along the headgate and tailgate entries. A total of four geophones were advanced with the longwall face (Iannacchione et al. 2005). These geophones were advanced almost daily to provide optimum coverage of the uncaved area, and over 200 holes were drilled over the course of the study. The portion of the dataset used in this study consists of 5,403 microseismic events and 14,124 P-wave arrival times collected from February to October 1998. Microseismic events average 32 per day with a maximum of 165 events. The event distribution is displayed in Figure 6.1. The area of interest is about 0.30 square kilometers.

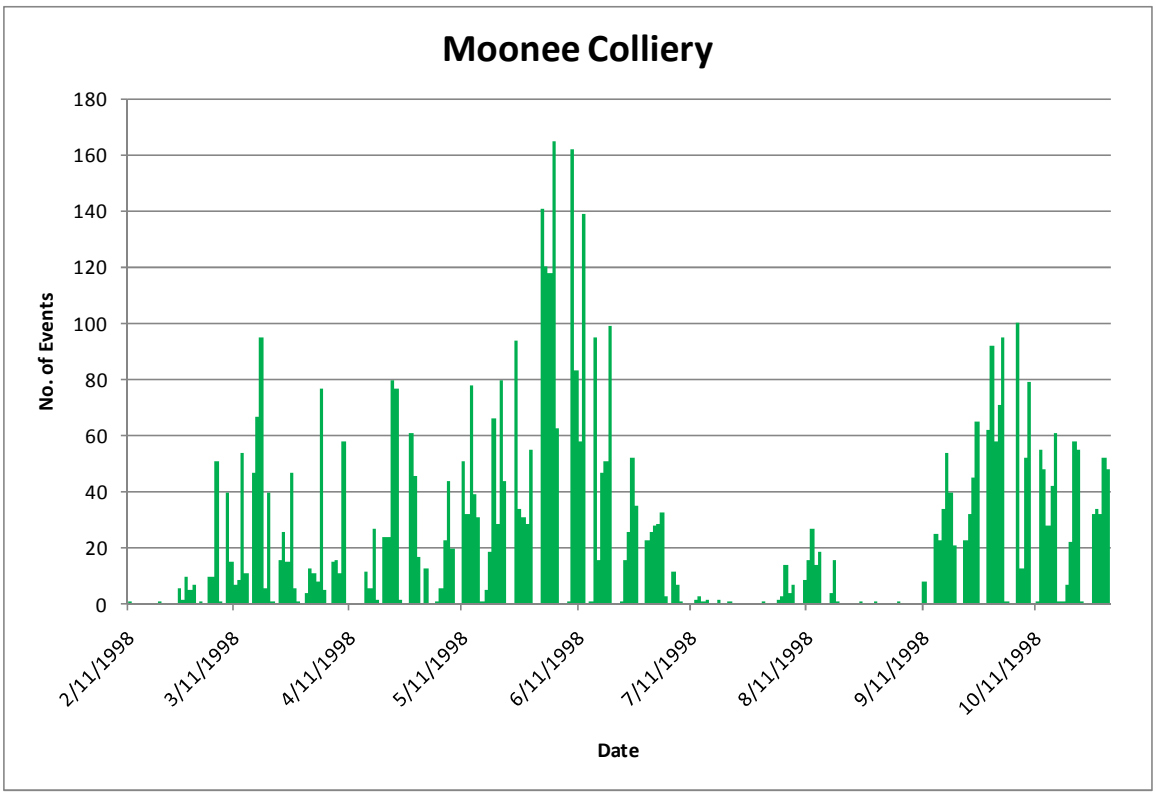

Figure 6.1. Moonee Colliery Microseismic Event Distribution.

.

6.4.2. Inversion Algorithm and Parameterization

A double difference algorithm, TomoDD, written by Haijiang Zhang and Clifford Thurber, is available for download and was developed for use in earthquake tomography. It is based on the double difference relocation algorithm, HypoDD (Waldhauser 2001). TomoDD is a double-difference method that jointly relocates events and determines a velocity model (Zhang and Thurber 2003). There are several examples in the literature of its use in earthquake relocation and tomography (Waldhauser and Ellsworth 2000; Zhang and Thurber 2003; Dunn and Chapman 2006), but no applications to mining. The assumption behind double-difference tomography is that if distance between two seismic events is small compared to the distance from the events to the receivers they will have similar travel times. The difference between calculated and measured travel times between two events at one receiver can then be used to adjust the position of the events (Waldhauser and Ellsworth 2000). TomoDD allows for variable gridding; the interval between the x-, y-, and z- nodes in the inversion grid can be varied so that a finer grid may be applied in areas that are well sampled and a courser grid in areas that are not as well

sampled. This is especially useful for passive sources in mines where events are usually very dense at the active face and scarce in outer regions.

Important parameters in TomoDD include damping, weighting, and number of iterations. The damping factor damps the hypocentral adjustments if the adjustment vector becomes large or unstable. In TomoDD, examination of a condition number output by the program is used to determine the damping value. The condition number, the ratio of the smallest to largest eigenvalue, should be between 40 and 80 with damping values between 1 and 100 (Waldhauser and Ellsworth 2000). For the Moonee Colliery data damping values of 30 to 50 produced condition numbers between 15 and 68. TomoDD is limited by the distribution and number of receiver stations which explains why a more favorable set of condition numbers could not be obtained for this data set since only four receivers are installed. The weighting factors refer to smoothing in the x, y, and z directions – factors of 3 to 5 were used for both data sets. Fourteen iterations were run.

6.4.3. Procedure

Major roof falls were mapped over the course of this data collection. Information on a total of 34 falls was provided with the seismic data, and included geometry and volume of material, along with the time of the fall. The data were then divided into 24 hour increments based on the time of the fall – events occurring 24 hours prior to the fall are used to generate the tomograms for each fall. Straight ray velocities for all source receiver pairs were examined and any pairs with velocities over 10,000 meters/second were removed, because they probably reflect poor arrival time picks. Pink phyllite has one of the highest p-wave velocities at 7,100 m/s (Carmichael 1989). A velocity of 10,000 m/s was chosen to account for ray curvature.

6.5. Results

Results for the Moonee Colliery case study are displayed in Figure 6.2. They include plan view tomograms at seam level for falls: 21&22, 30, 31, 33, 34 and 36. Falls are shaded, and the tomogram is generated from microseismic events that occurred in a 24 hour period before the fall. Also, Figure 6.3 displays the derivative weight sum distributions corresponding to the velocity tomograms in Figure 6.2. Fourteen days of the study are displayed in Appendix D.

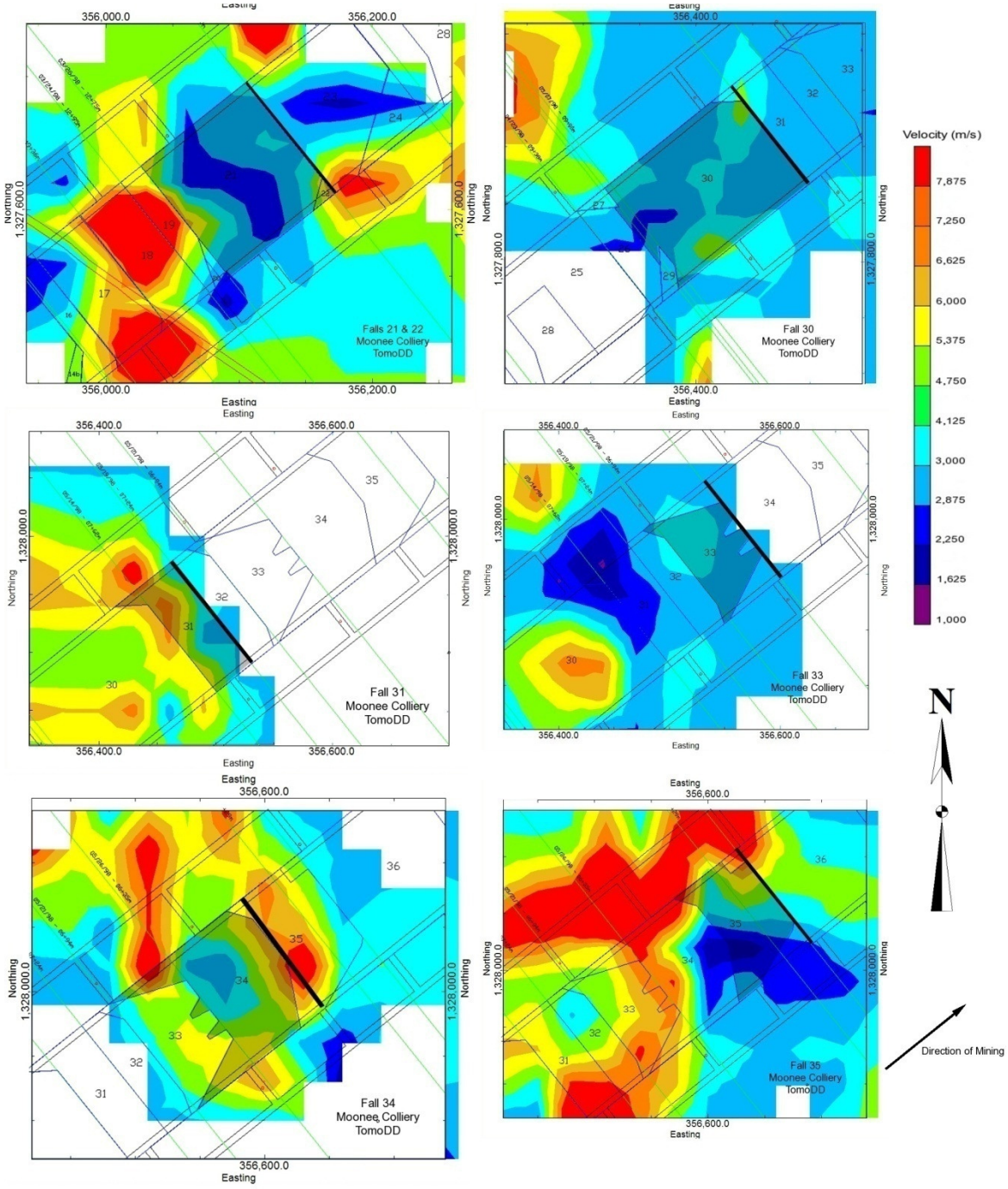

Figure 6.2. Plan view velocity tomograms at seam level for Moonee Colliery. Falls are shaded and face locations are shown in black. The face is retreating from southwest to northeast.

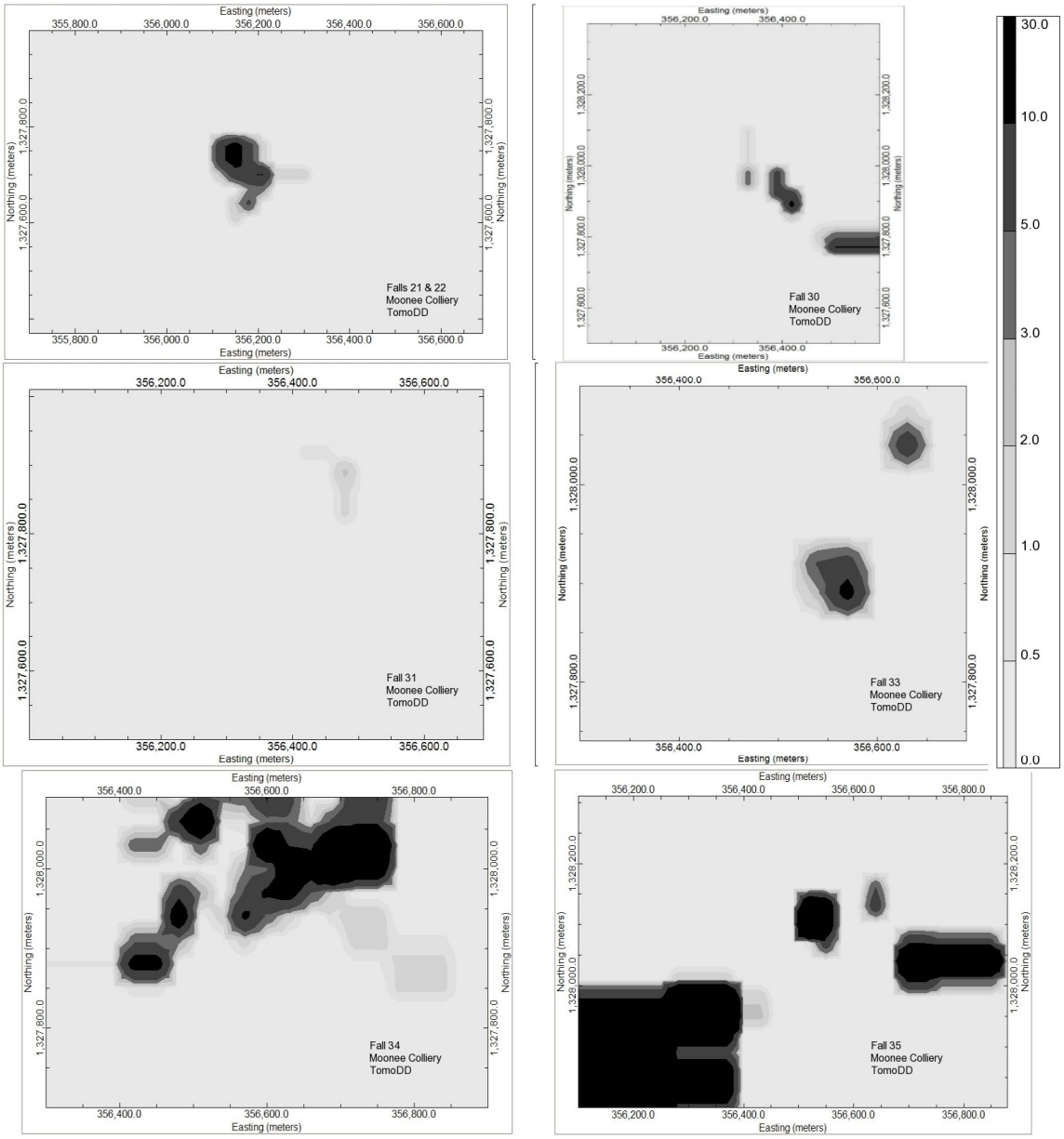

Figure 6.3. Derivative weight sum distribution corresponding with velocity tomograms in Figure 6.2.

Velocity anomalies can be found in the vicinity of the falls. Low velocity anomalies are evident at falls 21 and 22, 34, and 35 while high velocity anomalies are evident at falls 30, 31, and 33. A high velocity anomaly could be explained by the closure of cracks and pore space prior to failure, while the low velocity anomalies could be explained by the coalescence of these cracks just prior to failure. Iannacchione indicates that, "this flurry of [microseismic] activity [prior to the fall] probably signals the coalescence of many smaller fracture surfaces into larger destabilizing structures within the rock…" (Iannacchione et al. 2004). A high velocity anomaly

would be inconsistent with this statement. The anomalies shown in the tomograms cannot be conclusively tied to the falls and are difficult to separate from background noise.

6.6. Conclusions and Recommendations

Although this data set was used to successfully forecast caving events by examination of event frequency over time, the velocity tomography results are inconclusive. This may be due to inadequate ray density. Ray density could be improved for this data set by looking at events over a series of days, rather than 24 hours prior to a caving event. However, using a longer time-increment defeats the purpose of using seismic velocity tomographic to forecast major falls and bumps because it will be more difficult to pinpoint areas that are experiencing a rapid stress buildup if an image is sampled over a series of days rather than hours. In the absence of a high microseismic event count the best method for increasing raypath density is to add more receivers to the array in such a way to optimize raypath density.

It is more likely difficult to draw conclusions from this data using seismic velocity tomography due to the complicated mechanics of failure for this system. A typical fall at Moonee Colliery resembles a half cone with stepped surfaces, with the fall arching back from the face and gateroads (Iannacchione et al. 2005). Iannacchione indicates that many of the microseismic events detected occur during initiation and development of these stepped surfaces. As the microseismic event frequency increases cracking should be taking place, which would result in the imaging of a low velocity zone in the cave area. However, just as frequency begins to increase prior to large scale cracking a high velocity zone, correlating with high stress would be expected. Finally, even as cracking occurs in the roof immediately over the extracted seam the beams above the fall may begin to arch and experience high stress. Depending on the height of the fall this region could also be imaged.

These failure mechanisms lead to ambiguous expectations of the p-wave velocity distribution in the roof prior to a fall. An extensive synthetic tomography study is required to determine if the tomograms are simply imaging different failure mechanisms or if they are inconsistent due to the method used and distribution of the data.

Chapter 6 References

Carmichael, R. (1989). Practical Handbook of Physical Properties of Rocks and Minerals. Boca Raton, CRC Press.

Dunn, M. and M. Chapman (2006). "Fault orientation in the eastern Tennessee seismic zone: A study using the double-difference earthquake location algorithm." Eastern Section Seismological Research Letters **77**(4): 494-504.

Fowler, J., B. Hebblewhite and P. Sharma (2003). Managing the hazard of wind blast / air blast in caving operations in underground mines. International Society for Rock Mechanics 10th Congress: Technology Roadmap for Rock Mechanics, Johannesburg, South Africa, The South African Institute of Mining and Metallurgy.

Friedel, M., M. Jackson, E. Williams, M. Olson and E. Westman (1996). "Tomographic imaging of coal pillar conditions: observations and implications." International Journal of Rock Mechanics, Mining Sciences, and Geomechanics Abstracts **33**(3): 279-290.

Hadamard, J. (1952). Lectures on Cauchy's Problem in Linear Partial Differential Equations. New York, Dover Publications.

Hayes, P. (2001). Moonee Colliery: renewing the economic viability of a mine using microseismic and hydraulic fracturing techniques in massive roof conditions. the 19th International Conference of Ground Control in Mining, Morgantown, WV, WVU.

Hole, J. (1992). "Nonlinear high-resolution three-dimensional seismic travel time tomography." Journal of Geophysical Research **97**(B5): 6553-6562.

Iannacchione, A., T. Bajpayee and J. Edwards (2007). Forecasting roof falls with monitoring technologies - a look at the Moonee Colliery experience. 24th International Conference on Ground Control in Mining, Morgantown, WV, West Virginia University.

Iannacchione, A., T. Batchler and T. Marshall (2004). Mapping hazards with microseismic technology to anticipate roof falls - a case study. 23rd International Conference on Ground Control in Mining, Morgantown, WV, West Virginia University.

Iannacchione, A., G. Esterhuizen, T. Bajpayee, P. Swanson and M. Chapman (2005). Characteristics of mining-induced seismicity associated with roof falls and roof caving events. 40th U.S. Rock Mechanics Symposium, Anchorage, AK, American Rock Mechanics Association.

Körmendi, A., T. Bodoky, L. Hermann, L. Dianiska and T. Kàlmàn (1986). "Seismic measurements for safety in Mines." Geophysical Prospecting **34**: 1022-1037.

Manthei, G. (1997). Seismic Tomography on a Pillar in a Postash Mine. 4th International Symposium on Rockbursts and Seismicity in Mines, Krakow, Poland.

Mosegaard, K. and A. Tarantola (2002). Probabilistic Approach to Inverse Problems, Academic Press for the International Association of Seismology and Physics of the Earth Interior.

Sallares, V., J. Danobeitia and E. Flueh (2000). "Seismic tomography with local earthquakes in Costa Rica." Tectonophysics **329**(1-4): 61-78.

Sharma, P. and J. Fowler (2004). "Wind blasts in longwall panels in underground coalmines." The Journal of The South African Institute of Mining and Metallurgy: 617-626.

Waldhauser, F. (2001). hypoDD - A Program to Compute Double-Difference Hypocenter Locations, USGS.

Waldhauser, F. and W. Ellsworth (2000). "A double-difference earthquake location algorithm: method and application to the Northern Hayward Fault, California." Bulletin of the Seismological Society of America **90**(6): 1353-1368.

Watanabe, T. and K. Sassa (1996). "Seismic attenuation tomography and its application to rock mass evaluation." International Journal of Rock Mechanics, Mining Sciences, and Geomechanics Abstracts **33**(5): 467-477.

Westman, E. (2004). "Use of tomography for inference of stress redistribution in rock " IEEE Transactions on Industry Applications **20**(5): 1413-1417.

Westman, E., K. Heasley, P. Swanson and S. Peterson (2001). A correlation between seismic tomography, seismic events, and support pressure. 38th U.S. Rock Mechanics Symposium, Washington, D.C., AA Balkema.

Zhang, H. and C. Thurber (2003). "Double-difference tomography: the method and its application to the Hayward Fault, California." Bulletin of the Seismological Society of America **93**(5): 1875-1889.

Chapter 7
Discussion and Conclusions

7.1. Summary of Work

Three microseismic data sets from three longwall coal mines were evaluated to determine if time-lapse passive seismic velocity tomography could be utilized for inference of stress in longwall abutment zones and prior to periodic caving events. The first data set, US Western I, was collected over 18 days at a mine in the western United States. The second data set, US Western II, was collected at a different mine in the western United States over four months with much sparser data coverage. The final data set was collected at Moonee Colliery in Australia over 8 months. This mine differed from the others in that episodic caving was an issue. The roof would regularly hang behind the longwall for long spans causing windblasts when it did fail. This data set was also sparse. A total of 42 daily tomograms were produced for US Western I, 14 for each of three inversion methods. A total of 24 daily tomograms were produced for US Western II, 12 for each of two inversion methods. Twenty eight 24-hour periods prior to major falls tomograms were generated for Moonee Colliery, 14 each for two inversion methods. Additionally, synthetic tomograms were produced for each data set.

7.2. Discussion of Results

Three inversion algorithms were evaluated for each mine: GeoTom, a Simultaneous Iterative Reconstructive Technique algorithm; TomoDD, a double difference damped least squares event relocation algorithm; and SIMULPS, a damped least squares event relocation algorithm. All methods showed fairly good agreement and consistently imaged high velocity zones in the forward and tailside abutment regions for US Western I. Additionally, a low velocity zone in the gob area was consistently imaged, and all of these features redistributed with face retreat. For the US Western II data, GeoTom and TomoDD tomograms did not show agreement most days. The TomoDD tomograms did show a low velocity anomaly in the gob region that redistributed with face advance. They also showed a high velocity anomaly that did not redistribute. Moonee Colliery tomograms also did not show agreement between TomoDD and GeoTom. Velocity anomalies were present in the areas of the fall, but these anomalies were not consistently high or low, so they were inconclusive. For US Western II and Moonee Colliery data sets the SIMULPS algorithm did not produce meaningful results due to the low station counts.

Next, one representative day was chosen from each of the three data sets to determine how well a known velocity model could be imaged by each of the methods through synthetic tomography. Three tomograms were produced for US Western I and two each for US Western II and Moonee Colliery. The grid files from these tomograms were compared with grid files from the initial velocity model to evaluate them quantitatively. For the US Western I data the GeoTom model produced an image closer to the starting model than TomoDD did. SIMULPS produced an image that agreed with the model in a qualitative sense, but heavy damping kept it from agreeing quantitatively. For both US Western II and Moonee Colliery the TomoDD images were most similar to the initial velocity models.

Finally, in-depth case studies were conducted on each data set using TomoDD, the double difference damped least squares event relocation algorithm. For the US Western I data set the tomograms consistently imaged high and low velocity zones that correlated with the forward and side abutment stresses, respectively, and could be observed to redistribute with face retreat. Also, this area of the panel had a set of entries cut through it and backfilled with light weight cement. As the face approached the cross-entries a high velocity region could be observed from the face to the cross entries and after the face cut through them this high velocity region narrowed and continued to redistribute just in front of the face. This may be indicative of the cross pillars carrying some forward abutment load because the backfill was less stiff than the coal.

TomoDD images for the US Western II data consistently imaged a low velocity zone in the gob region that redistributed with face retreat. Additionally, a high velocity region was imaged that did not appear to redistribute with face advance or correspond with the geometry. A panel that was retreat room and pillar mined was also present in the vicinity, but ray coverage was not sufficient to produce meaningful data here during the time it was being mined. TomoDD tomograms for the Moonee Colliery data may indicate velocity anomalies around the falls, but the anomalies were not consistently low or high, so these tomograms were fairly inconclusive.

7.3. Conclusions

The importance of source-receiver geometry and raypath density cannot be understated. The US Western I data set had the best source-receiver geometry and most events. Tomograms from this set were consistent for all three inversion methods as a result. However, TomoDD still produced images with low velocity anomalies that redistributed with face retreat for the more sparse US Western II data set. High velocity anomalies as a result of stress abutment zones were not evident. The imaging of these high velocity anomalies is most important if passive seismic velocity tomography is to be used as a tool to identify areas of a mine that are unusually

hazardous due to high stress. The redistribution of any anomaly for this data set is still promising since the data are so sparse. Also, the fact that synthetic tomography indicated that calculated velocity models could be produced that were similar to starting models even for suboptimum source-receiver configuration is promising.

The consistent images from US Western I data, along with the fact that high velocity zones corresponding with abutment stress were imaged repeatedly indicates that a data set similar to the US Western I data set could be used to examine a rock mass on a daily basis for evidence of a high velocity anomaly indicating a dangerous ground condition. This shows that a passive source system that can be monitored remotely is adequate for monitoring velocity to infer stress.

The TomoDD algorithm consistently relocated seismic events far above the coal seam. The fact that the US Western II models still showed low velocity zones correlating with gob indicates that if the event locations can be constrained in the z-direction this algorithm may prove adequate for sparse data sets.

Both TomoDD and SIMULPS allow for variable gridding. The spacing in all three directions for the inversion grid can be varied. This allows the user to compensate for areas that have very few events by increasing the spacing and decreasing the spacing in areas with many events. This type of gridding is well-suited to mining applications with passive sources, because the sources are typically concentrated at the area of active mining with only a few sources in outer regions. Variable gridding is not foolproof because there may still be areas with few events that are finely gridded in one direction. This situation forced the culling of about 20% of the US Western II data so that a grid could be created that was closer to mine geometry dimensions. An adaptive grid that allows irregular shapes might have allowed all of the data to be used.

In conclusion, the US Western I data results indicate that passive seismic velocity tomography can be used to image high velocity zones that correspond with zones of relative stress in a mine and should be pursued as an avenue for long term monitoring of bump-prone mines. Also, the synthetic tomography work indicates that synthetic tomography should be implemented routinely as a means for assessing how well a tomogram fits the unknown "true" velocity, for determining what geometries and contrasts can be imaged, and for designing receiver arrays for passive seismic velocity tomography. Additionally, the relocation algorithms seem to be superior to the SIRT algorithm, especially for the sparser data sets.

7.4. Recommendations for Future Research

This research has shown that passive seismic velocity tomography can produce images that allow for inference of relative stress from seismic velocity. The use of passive sources will

allow operators and researcher to monitor rock masses remotely and continuously which may lead to further understanding of the mechanisms that contribute to ground failure. This research indicates that passive seismic velocity tomography should always be evaluated and designed in conjunction with synthetic tomography, and that variable or adaptive gridding algorithms are most appropriate for the unique geometries encountered in mining applications.

More passive source data sets should be analyzed first for mines such as coal mines that are mining in tabular deposits with uniform geometry. When methods are perfected for these applications, they can be adapted for metal/nonmetal mines that have very complicated geometry. Also, as receivers become more advanced and economically feasible, new and denser configurations can be experimented with and assessed via synthetic tomography. Adaptive gridding schemes should be explored so that all available data can be utilized.

Finally, any opportunity to conduct passive seismic velocity tomography with more traditional methods of stress measurement should be seized, as this could lead the ability to quantify stress from velocity tomogram rather than just infer a relative stress change. As these recommendations are explored new questions will arise, hopefully leading to a technology that can be easily translated for use as a global mine monitoring system in many types of mines, contributing to a safer and more productive environment.

Appendix A

Longwall Panel Geometry and Receiver Locations for US Western I Data, US Western II Data, and Moonee Colliery

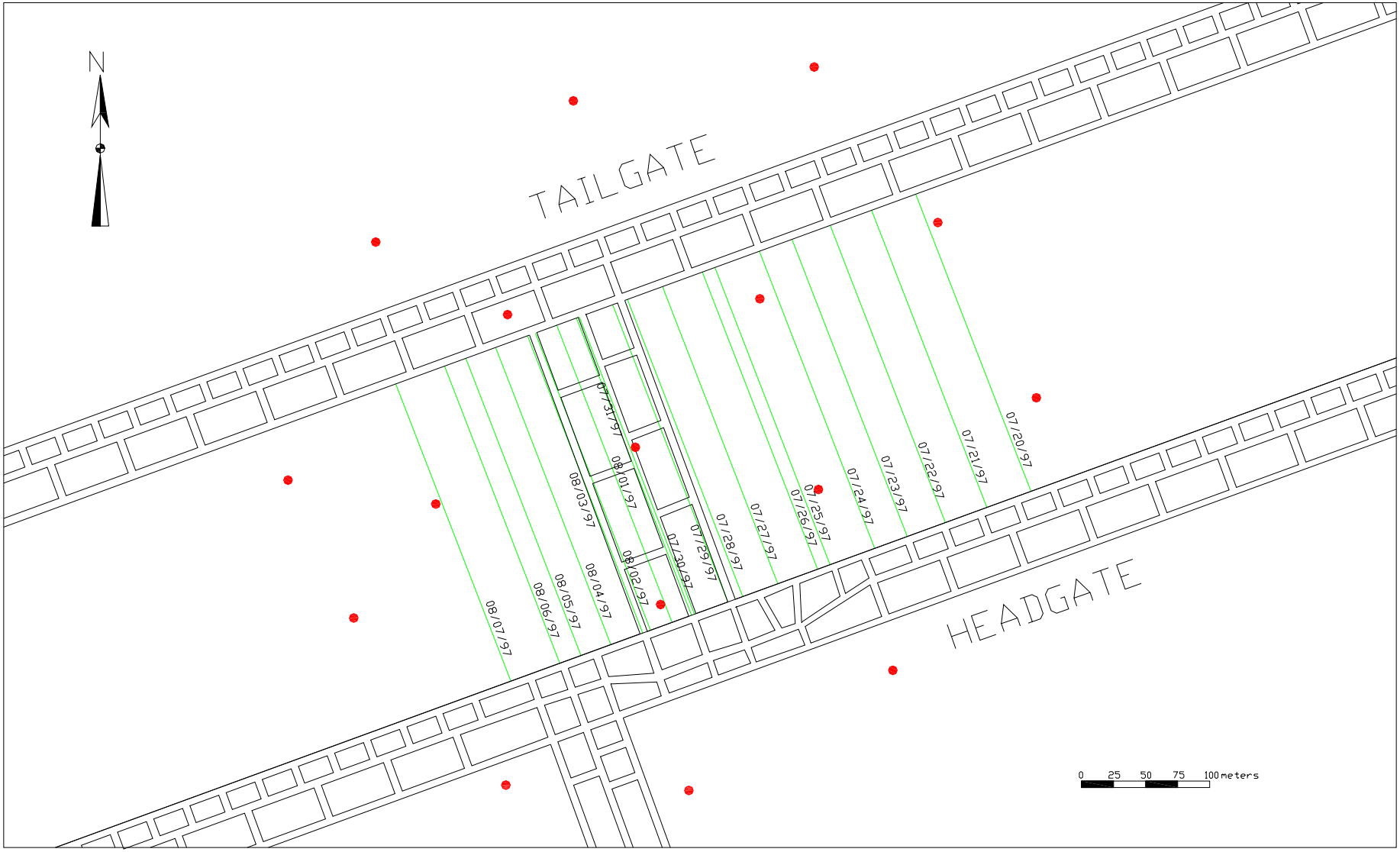

Figure A.1. Plan View of US Western I Longwall. Surface-mounted receivers are shown in red. Daily face locations are shown in green.

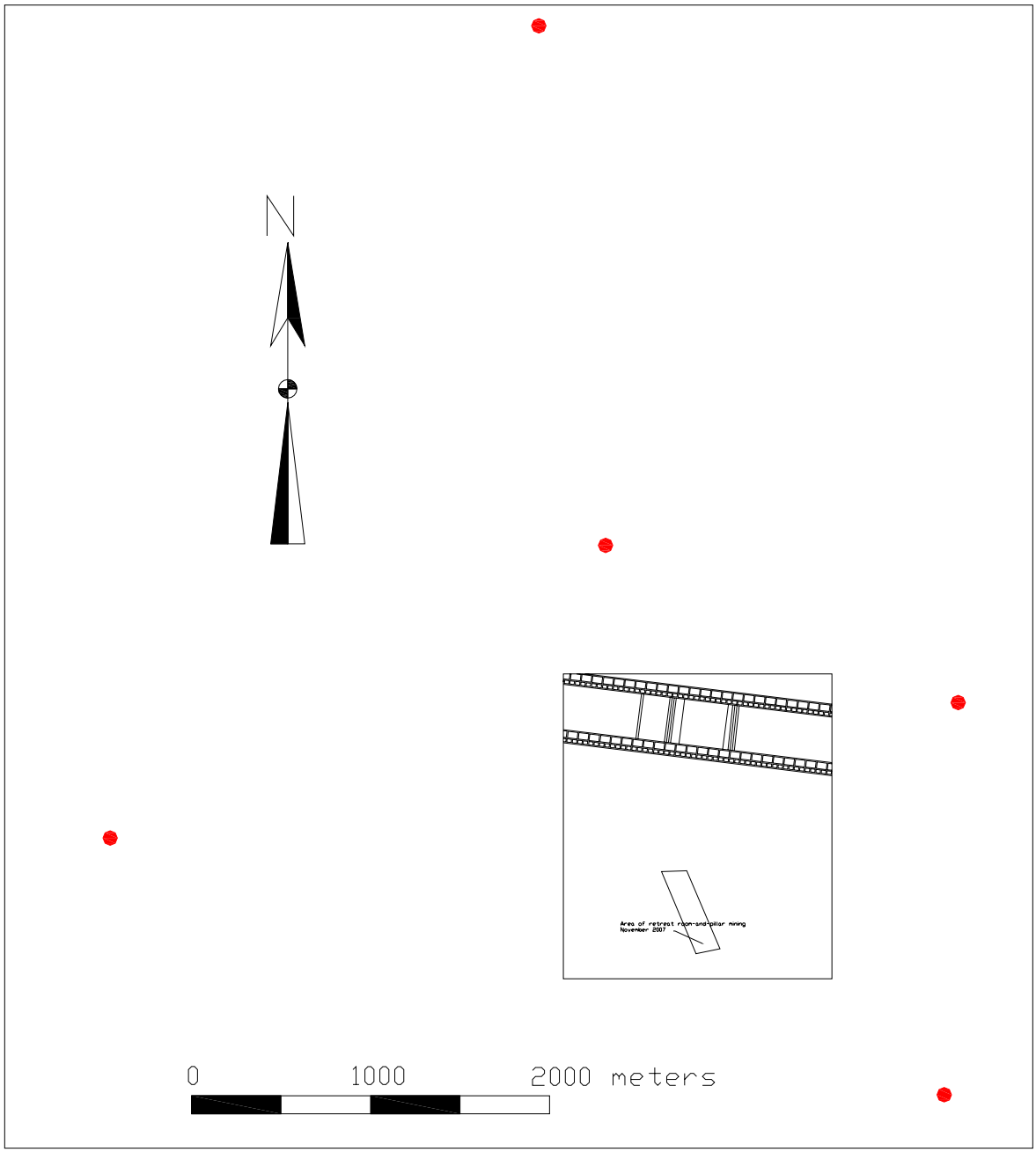

Figure A.2. Plan view of US Western II area of interest and relative receiver locations (shown in red).

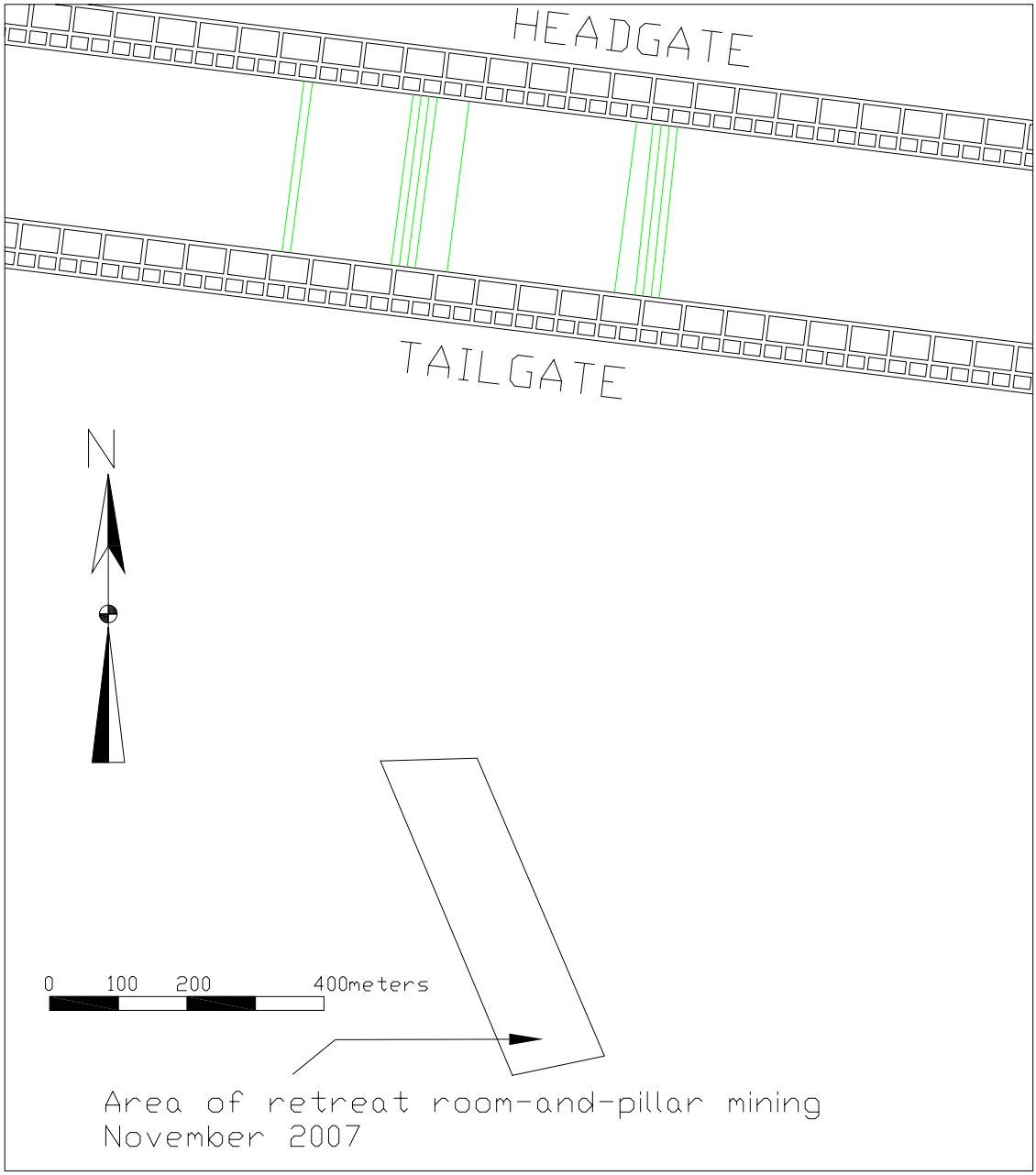

Figure A.3. Plan View of US Western II Longwall Geometry. Face locations are shown in green. The longwall retreats from east to west and face locations are 11/26/07, 11/28/07, 11/29/07, 11/30/08, 12/02/07, 12/23/07, 12/27/07, 12/28/07, 12/29/07, 12/30/07, 01/11/08, and 01/12/08, respectively.

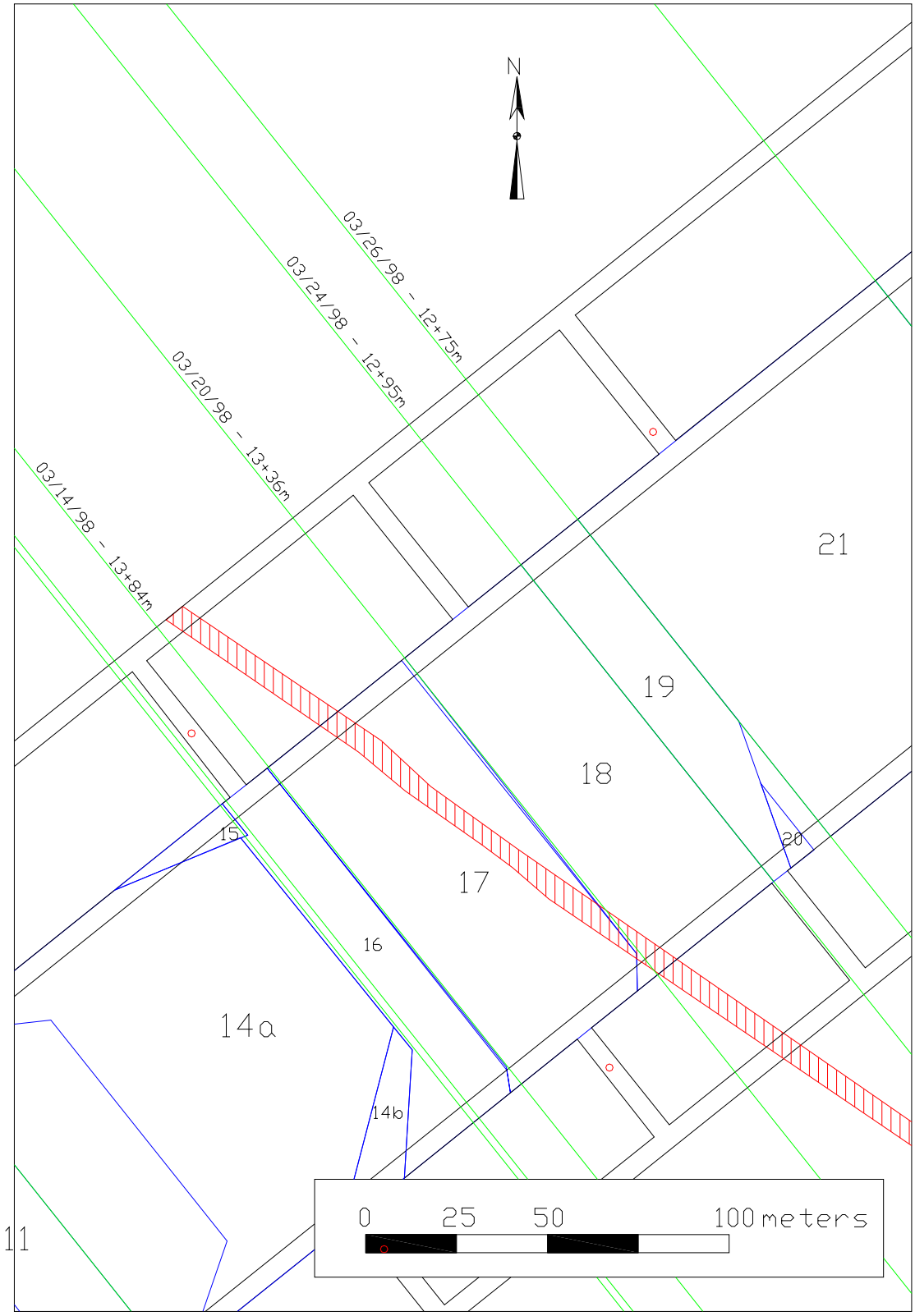

Figure A.4. Plan View of Moonee Colliery Longwall with face locations in green, receivers in red, and falls outlined in blue and numbered. Also, a dyke is shown in red.

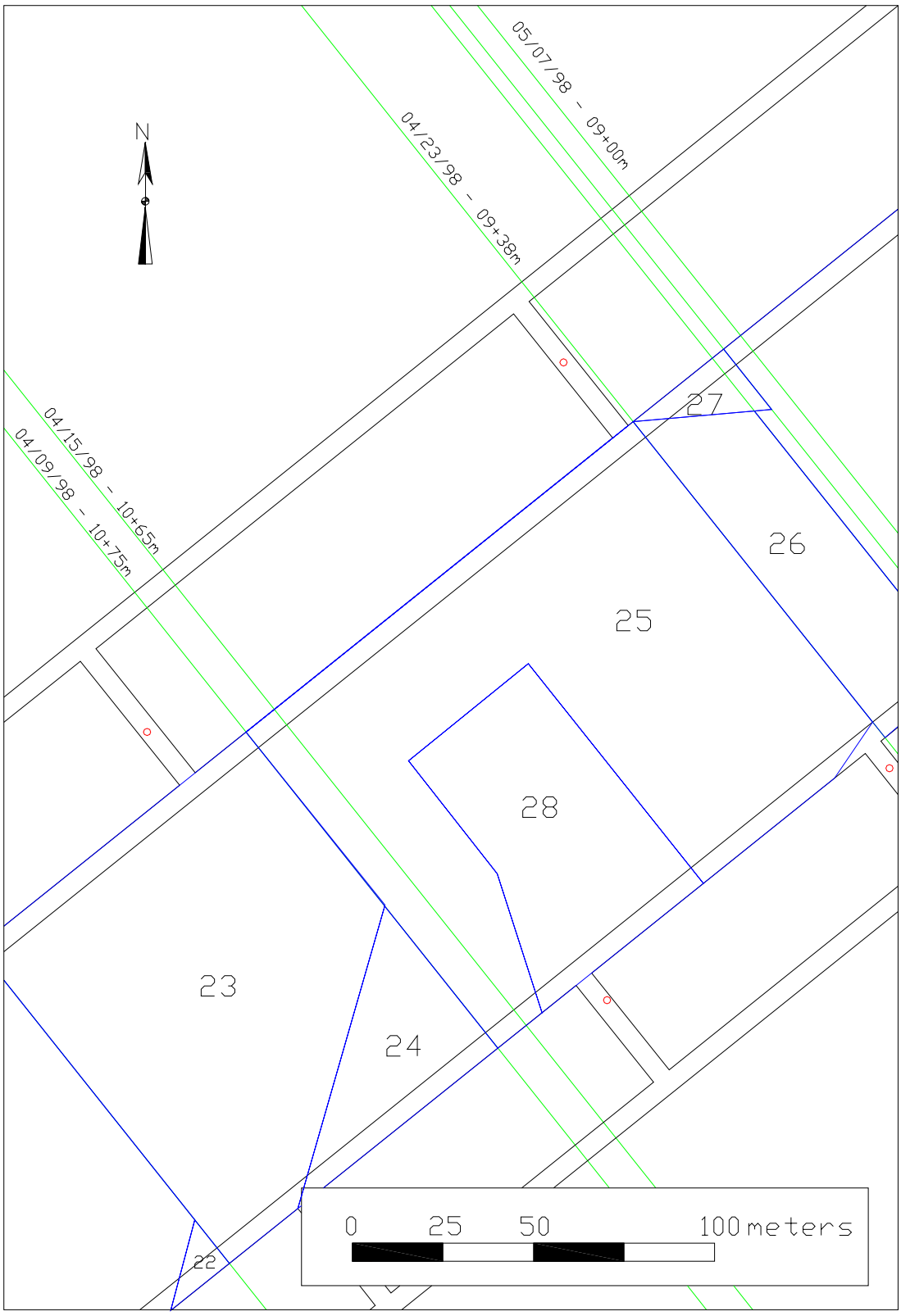

Figure A.5. Plan View of Moonee Colliery Longwall with face locations in green, receivers in red, and falls outlined in blue and numbered.

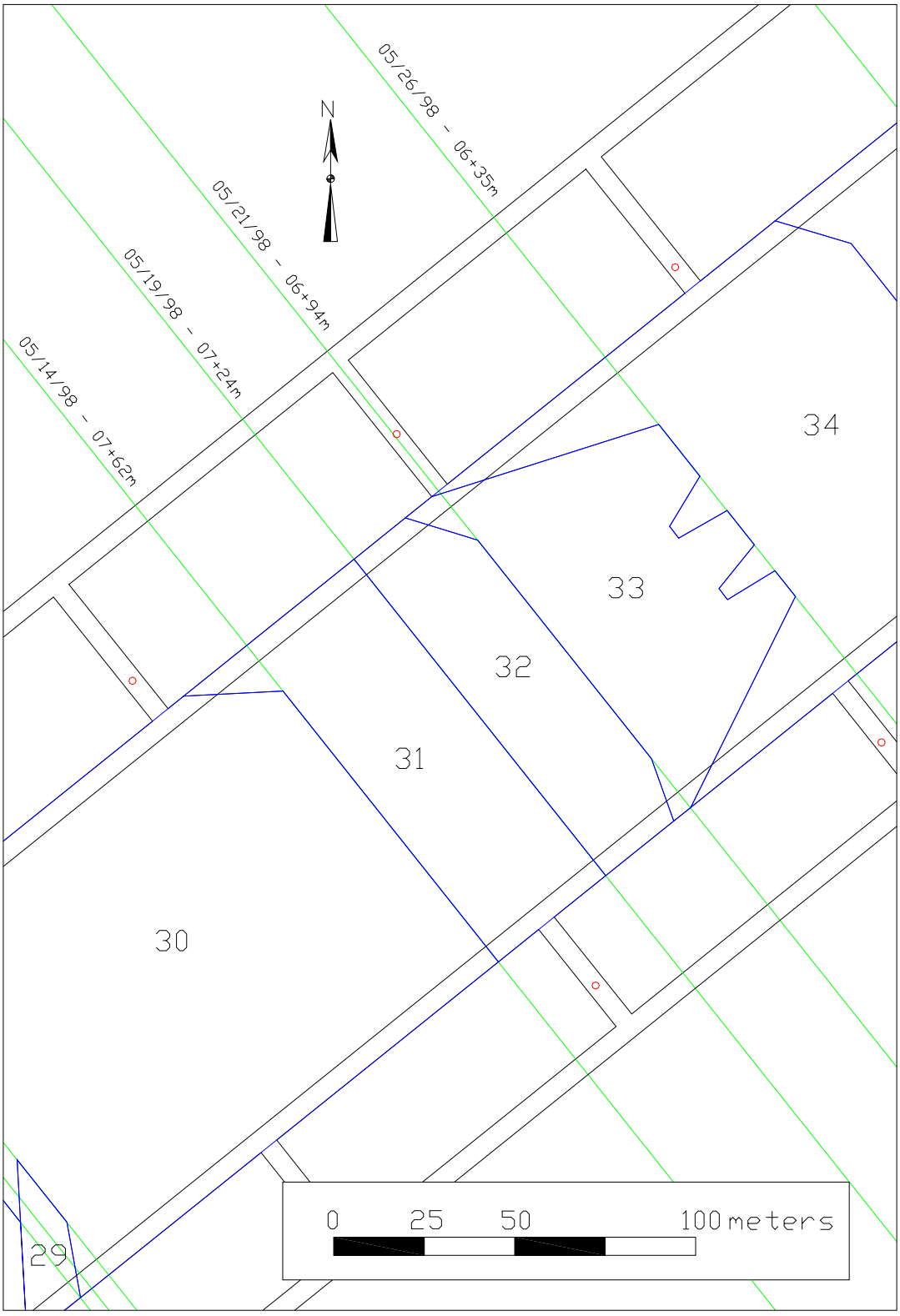

Figure A.6. Plan View of Moonee Colliery Longwall with face locations in green, receivers in red, and falls outlined in blue and numbered.

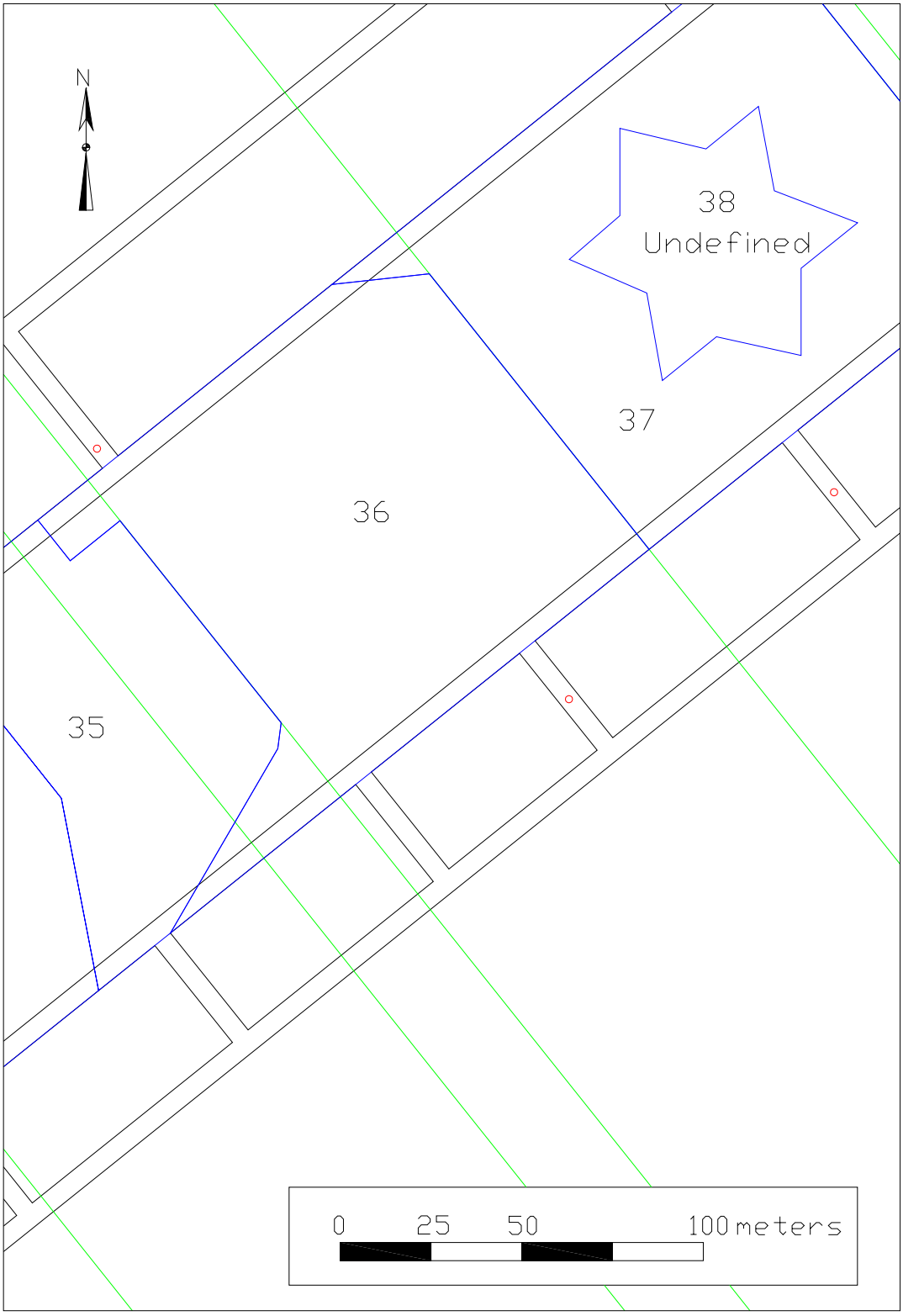

Figure A.7. Plan View of Moonee Colliery Longwall with face locations in green, receivers in red, and falls outlined in blue and numbered.

Appendix B

US Western I Plan View Velocity Tomograms generated by GeoTom, TomoDD, and SIMULPS.

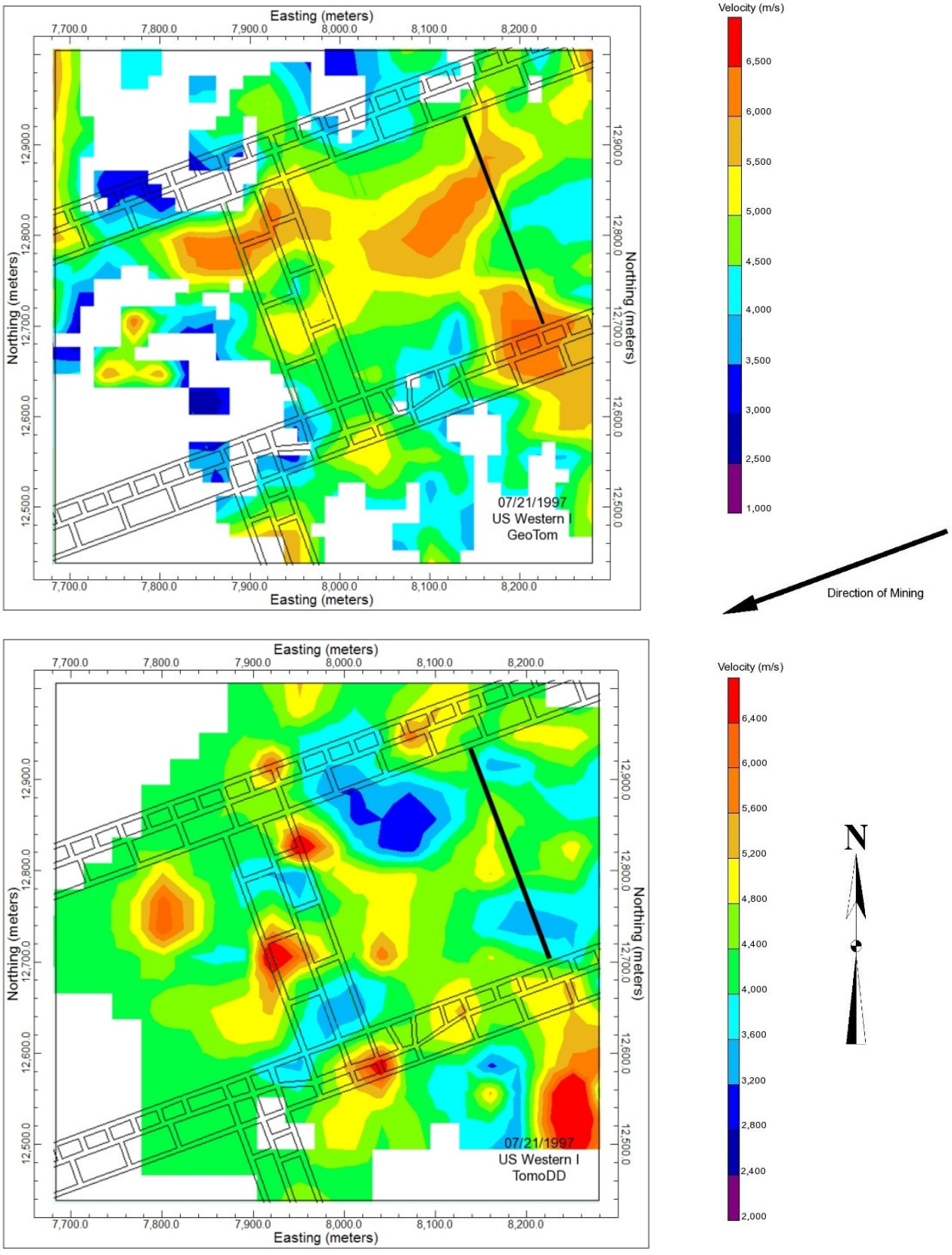

Figure B.1. Plan View Velocity Tomograms at seam level, Z = 1695 meters, for 07/21/97. Areas not traversed by rays are shown in white.

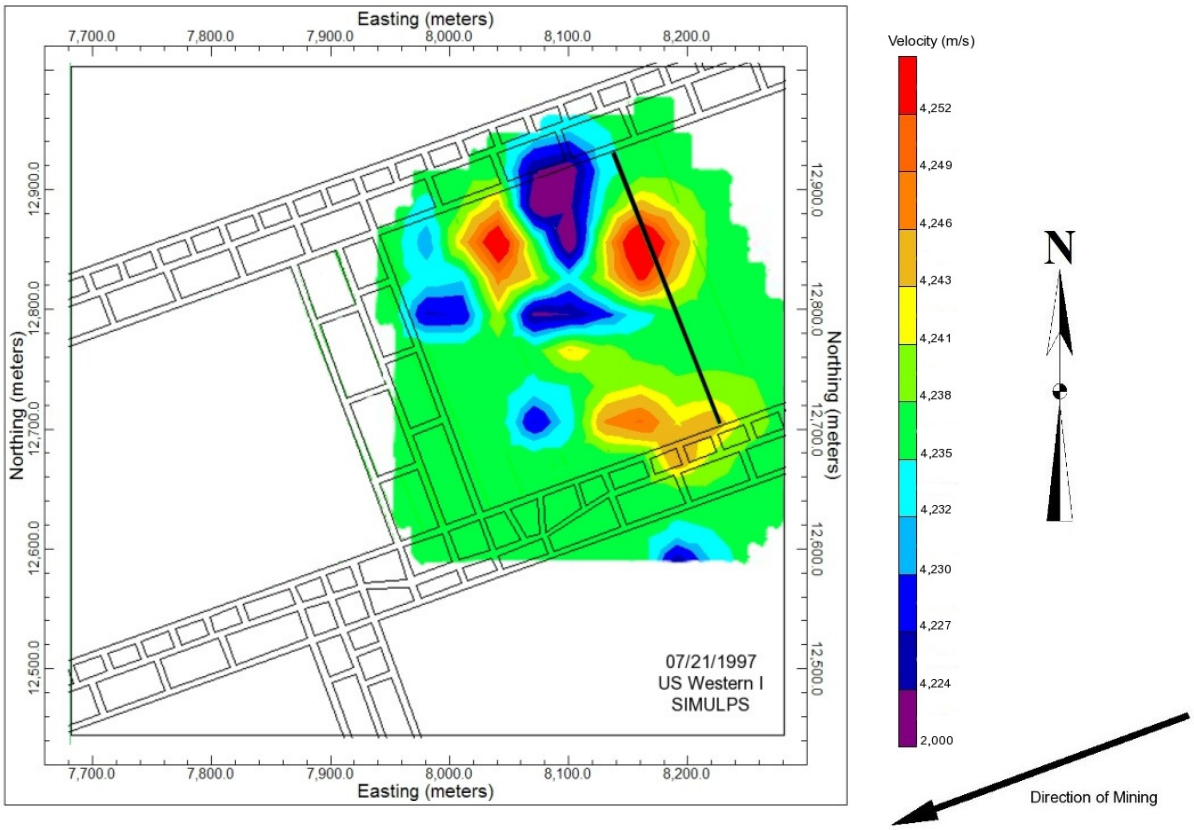

Figure B.2. Plan View Velocity Tomogram at seam level, Z = 1695 meters, for 07/21/97. Areas not traversed by rays are shown in white.

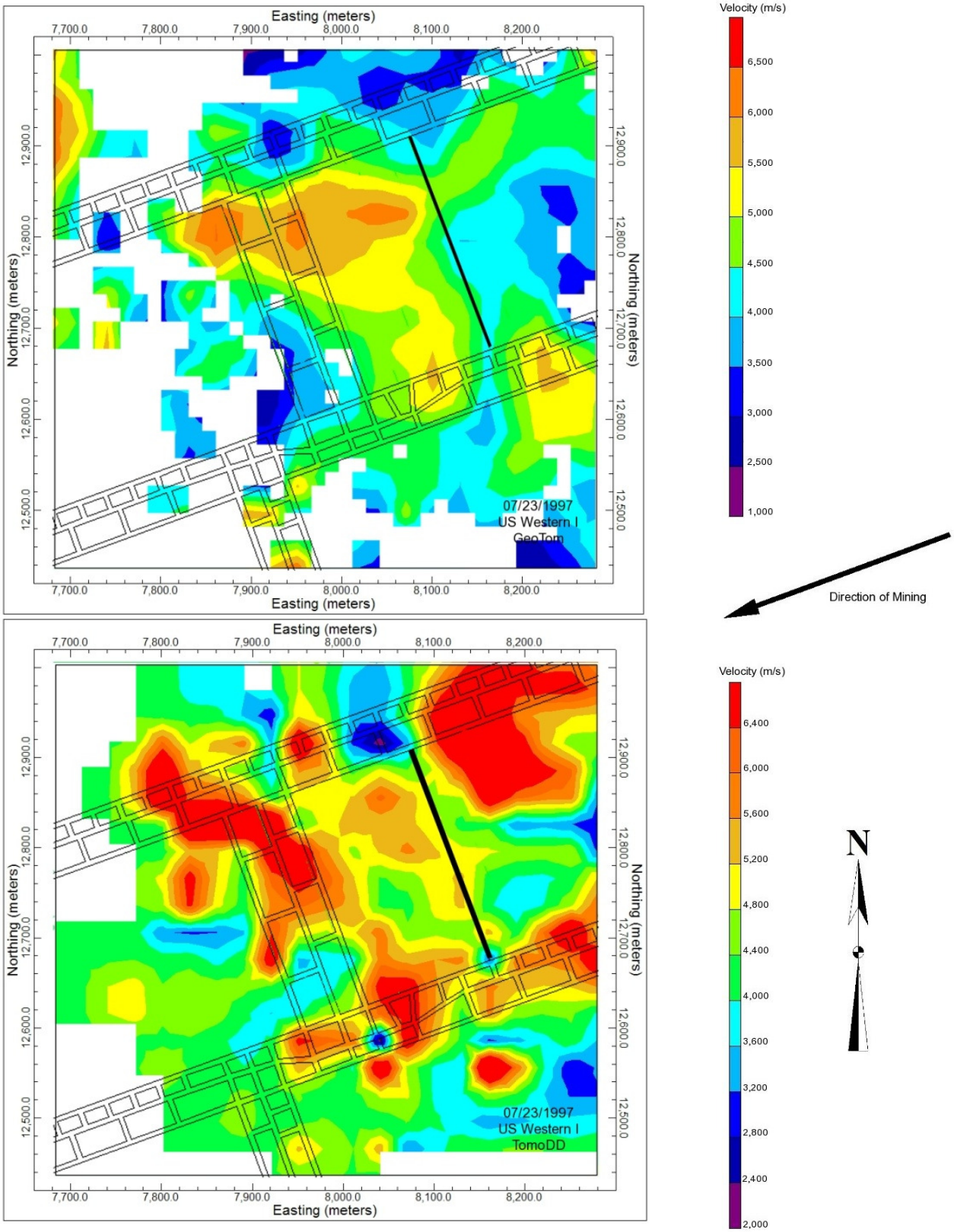

Figure B.3. Plan View Velocity Tomograms at seam level, Z = 1695 meters, for 07/23/97. Areas not traversed by rays are shown in white.

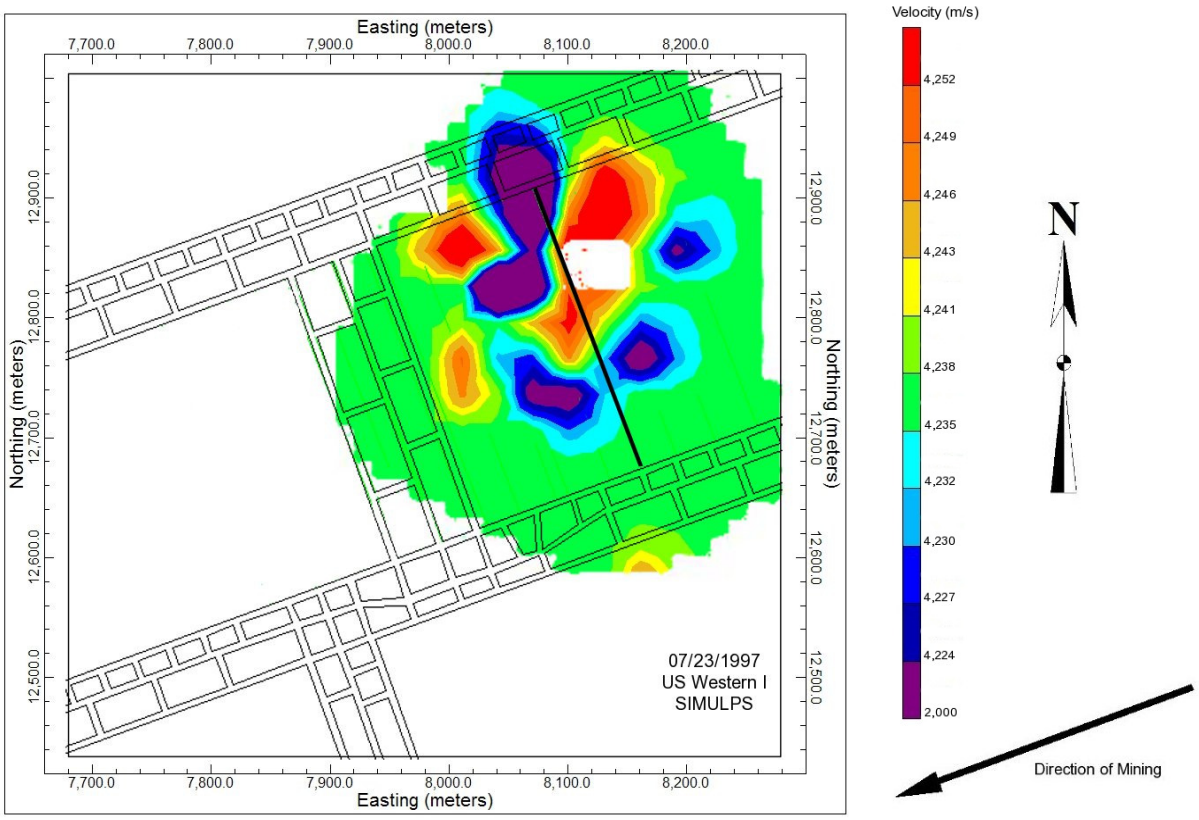

Figure B.4. Plan View Velocity Tomogram at seam level, Z = 1695 meters, for 07/23/97. Areas not traversed by rays are shown in white.

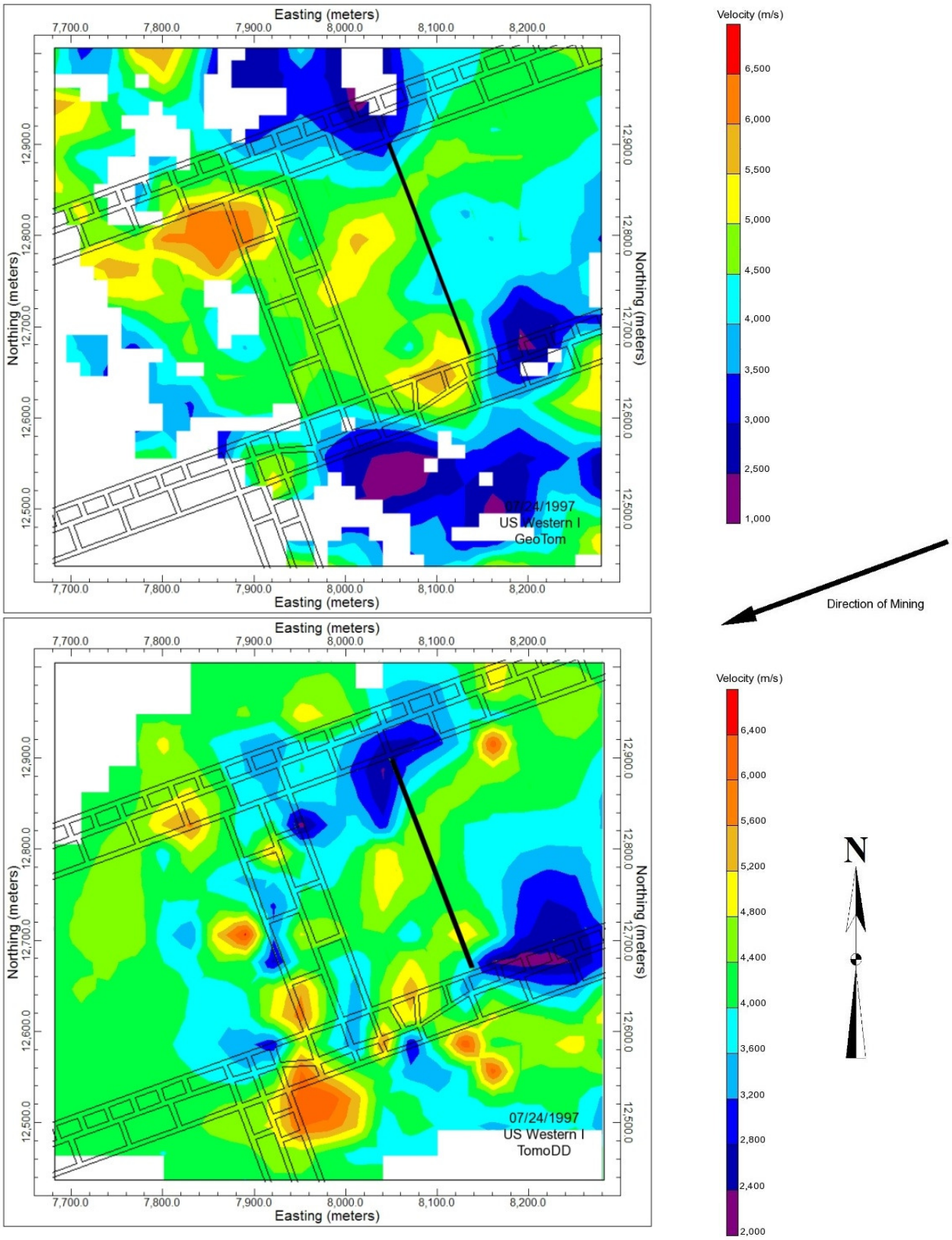

Figure B.5. Plan View Velocity Tomograms at seam level, Z = 1695 meters, for 07/24/97. Areas not traversed by rays are shown in white.

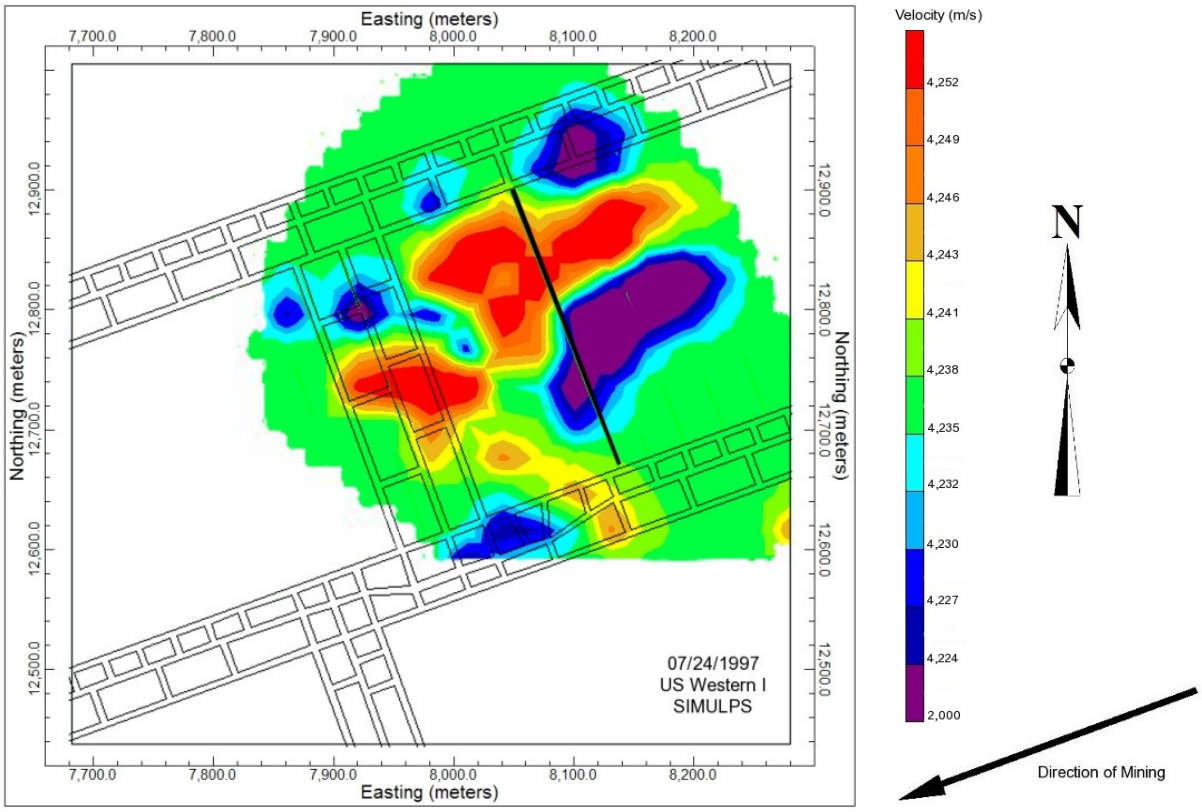

Figure B.6. Plan View Velocity Tomogram at seam level, Z = 1695 meters, for 07/24/97. Areas not traversed by rays are shown in white.

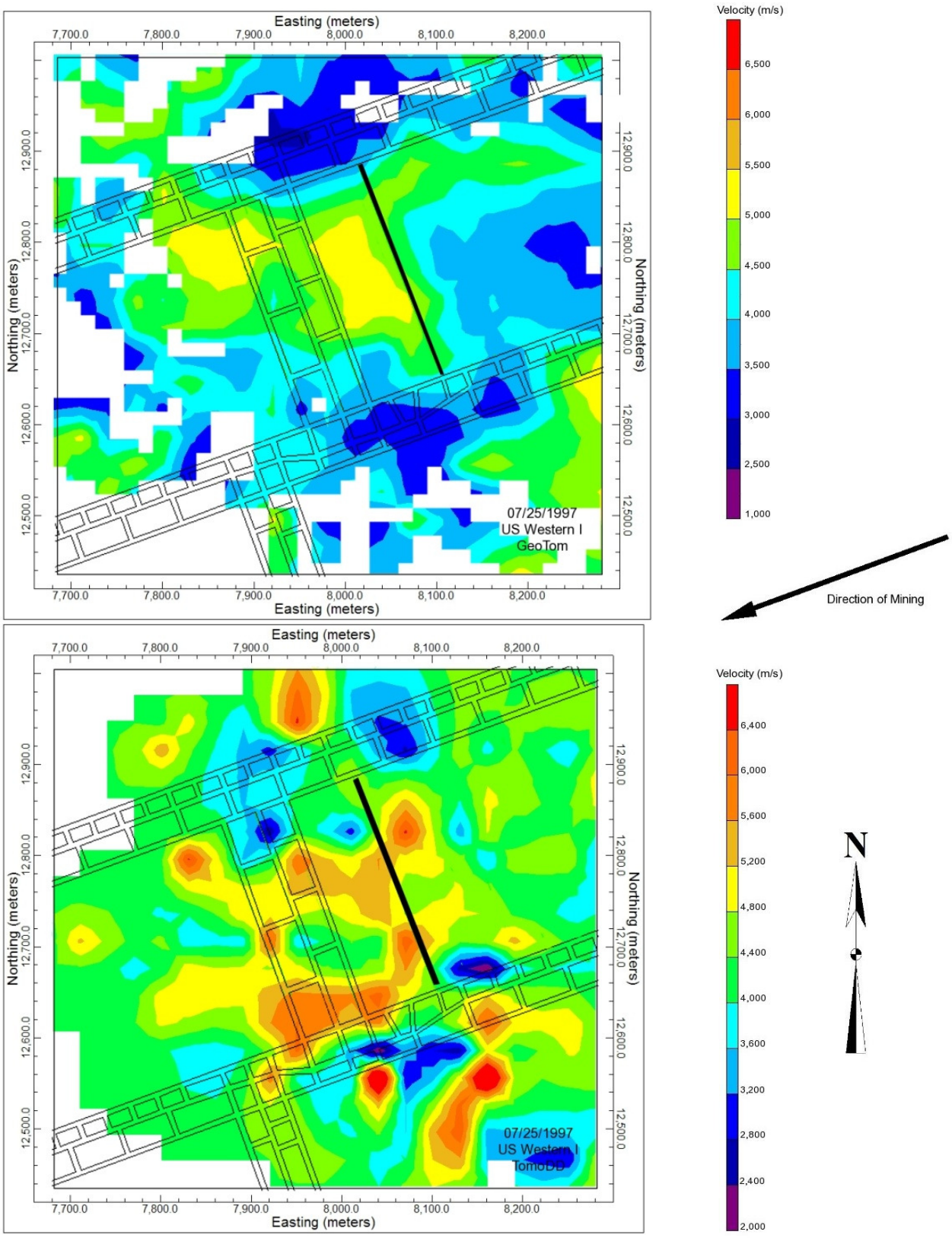

Figure B.7. Plan View Velocity Tomograms at seam level, Z = 1695 meters, for 07/25/97. Areas not traversed by rays are shown in white.

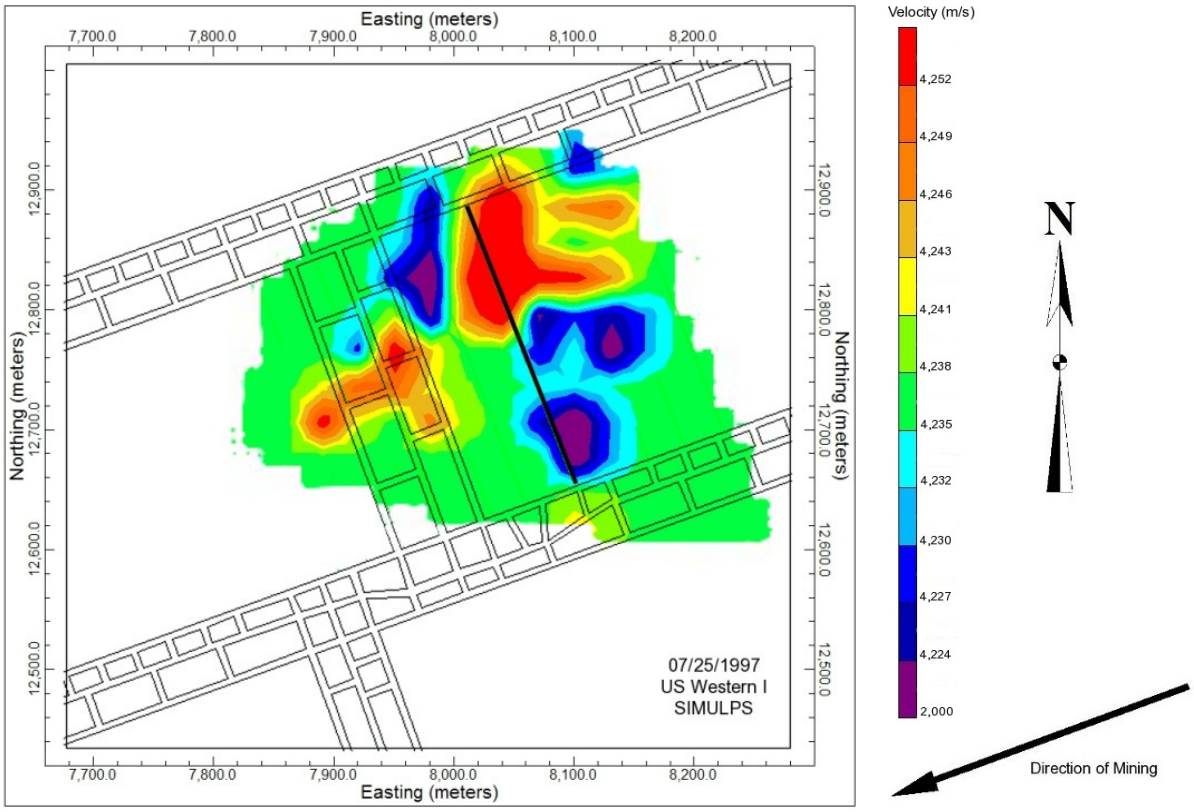

Figure B.8. Plan View Velocity Tomogram at seam level, Z = 1695 meters, for 07/25/97. Areas not traversed by rays are shown in white.

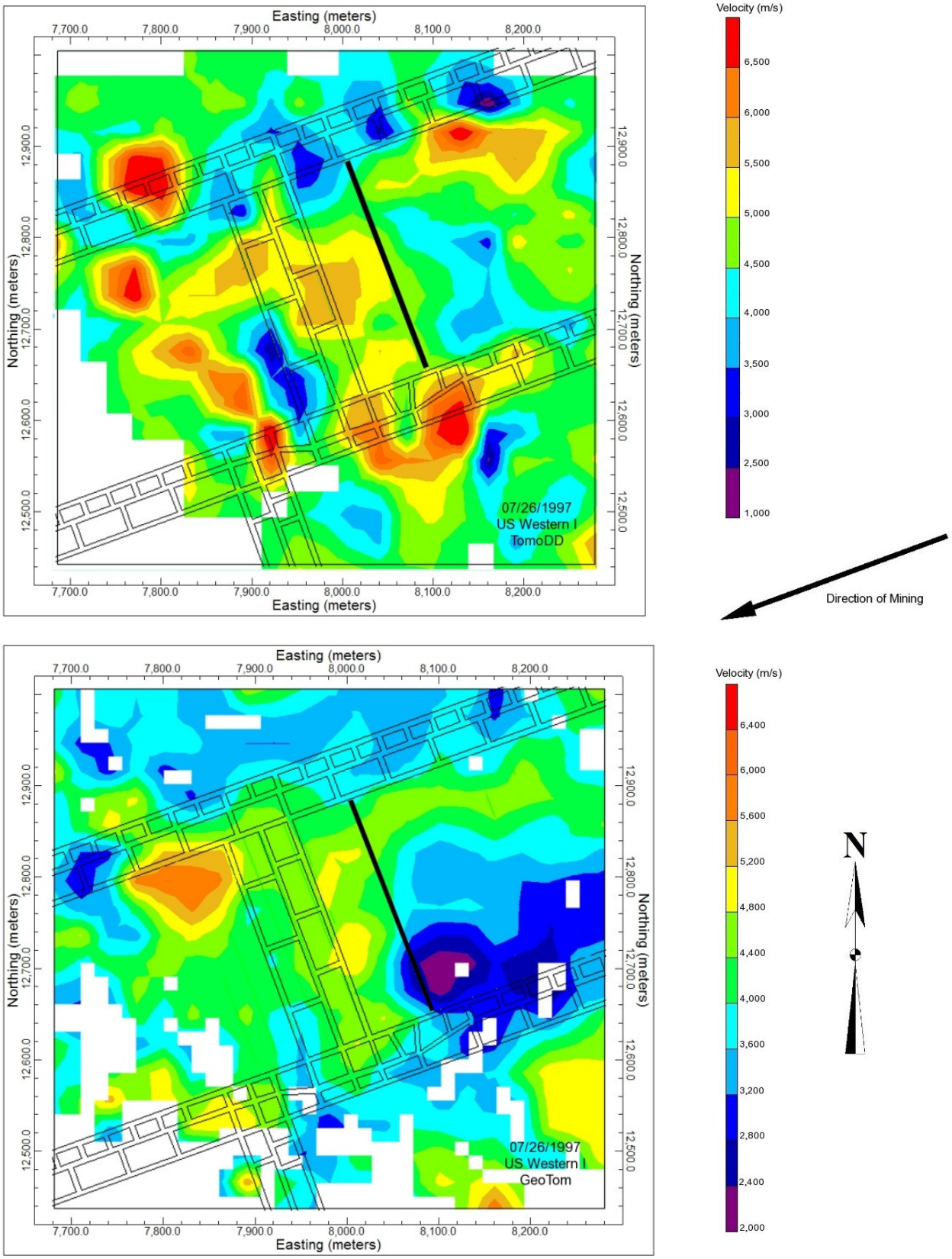

Figure B.9. Plan View Velocity Tomograms at seam level, Z = 1695 meters for 07/26/97. Areas not traversed by rays are shown in white.

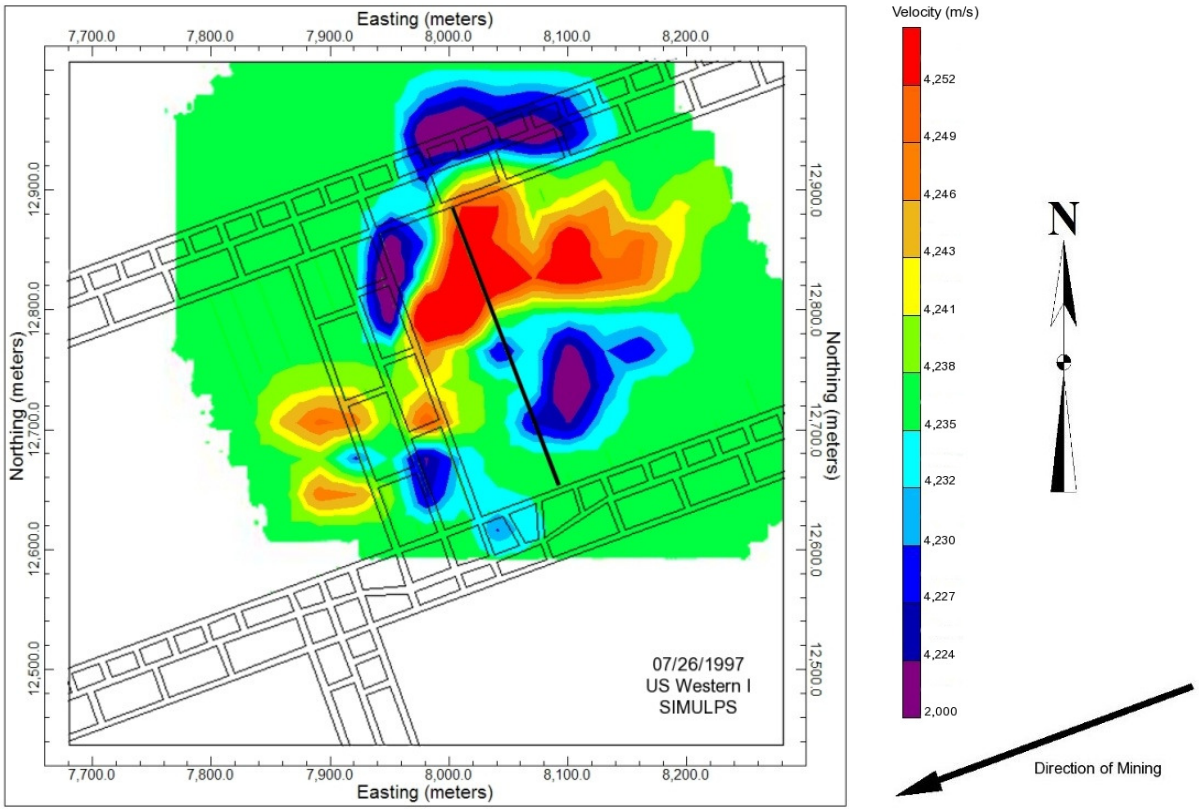

Figure B.10. Plan View Velocity Tomogram at seam level, Z = 1695 meters, for 07/26/97. Areas not traversed by rays are shown in white.

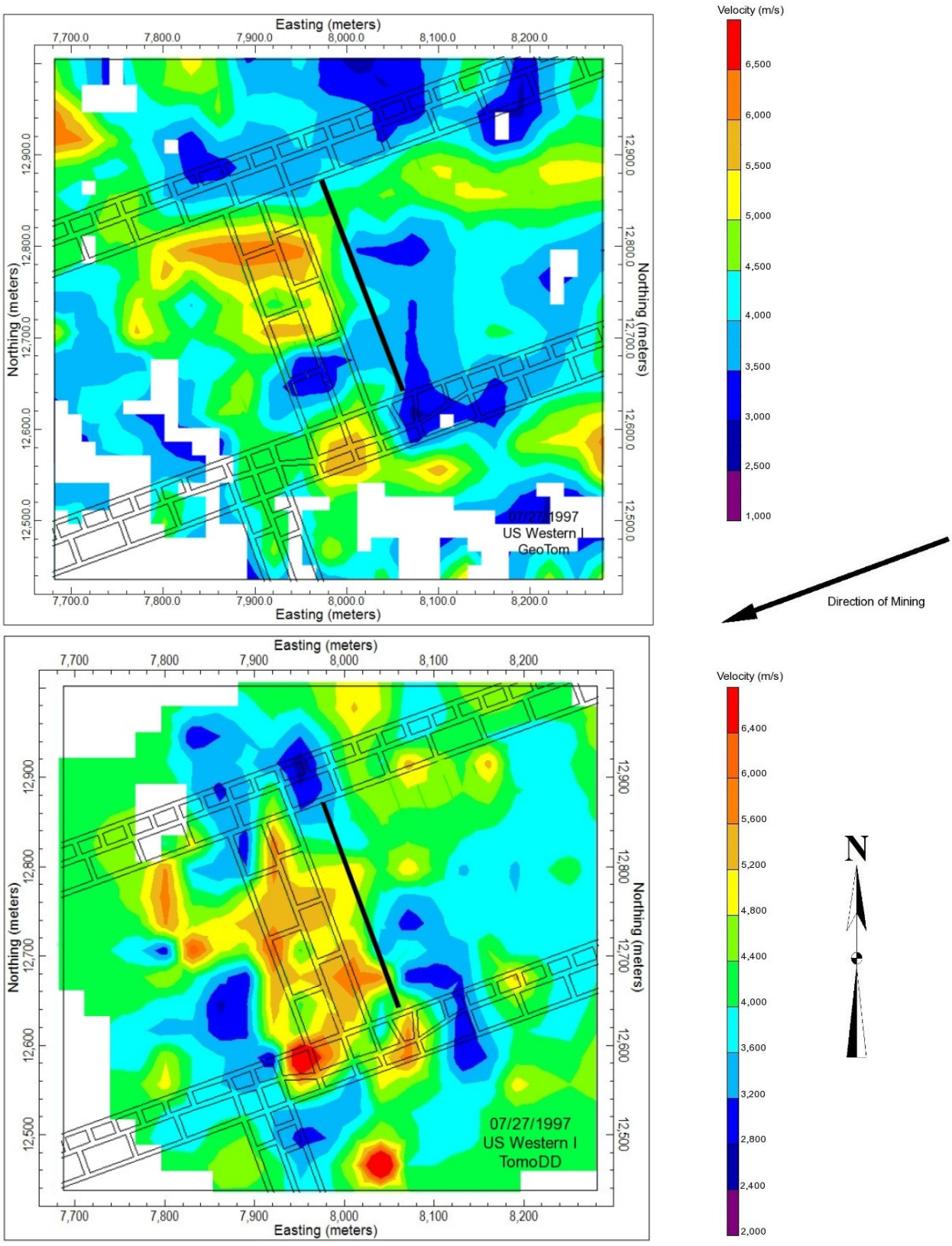

Figure B.11. Plan View Velocity Tomograms at seam level, Z = 1695 meters, for 07/27/97. Areas not traversed by rays are shown in white.

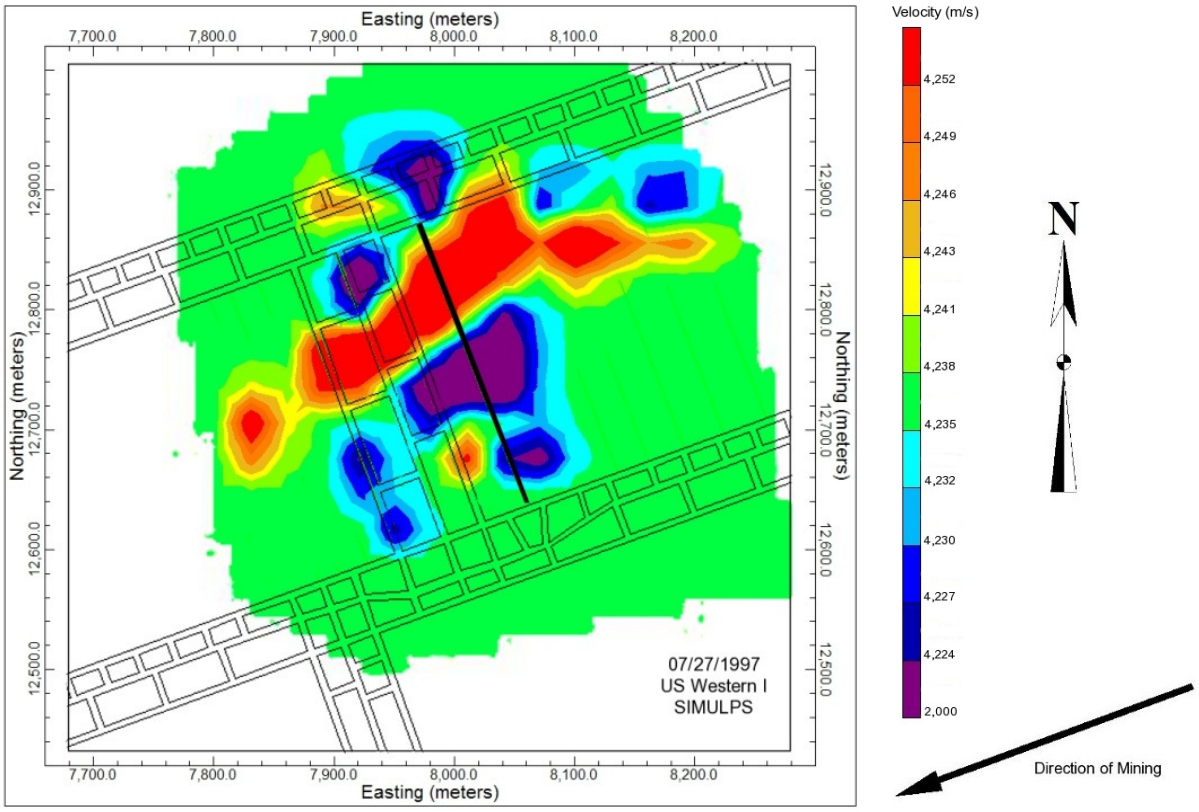

Figure B.12. Plan View Velocity Tomogram at seam level, Z = 1695 meters, for 07/27/97. Areas not traversed by rays are shown in white.

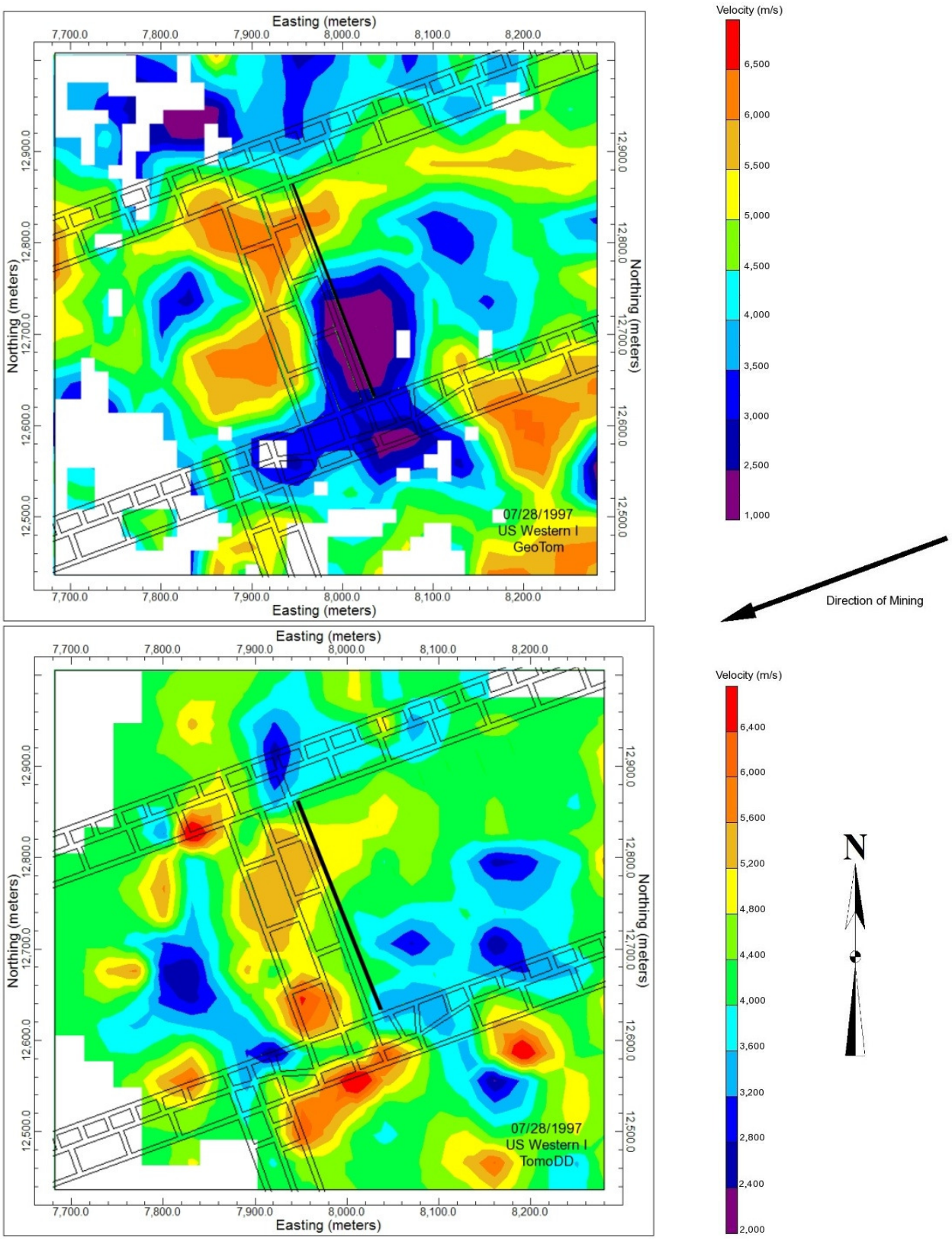

Figure B.13. Plan View Velocity Tomograms at seam level, Z = 1695 meters for 07/28/97. Areas not traversed by rays are shown in white.

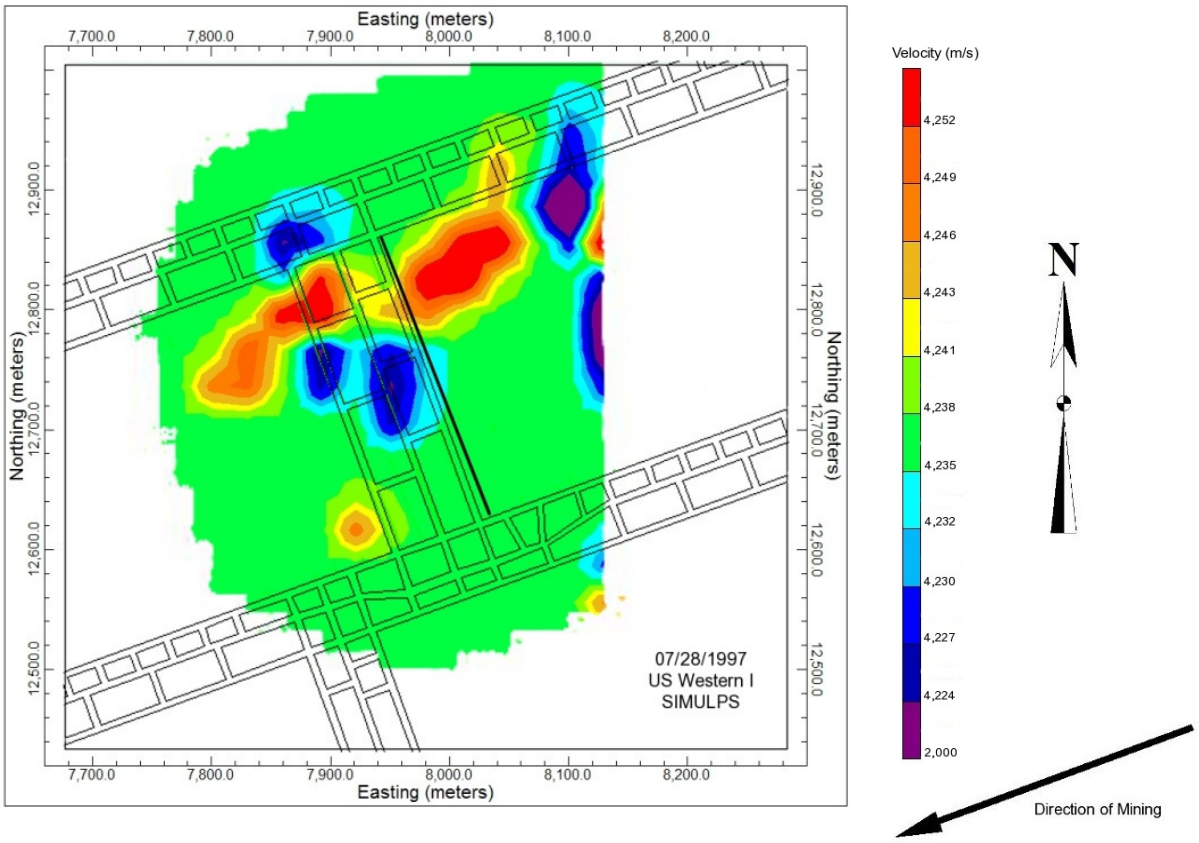

Figure B.14. Plan View Velocity Tomogram at seam level, Z = 1695 meters, for 07/28/97. Areas not traversed by rays are shown in white.

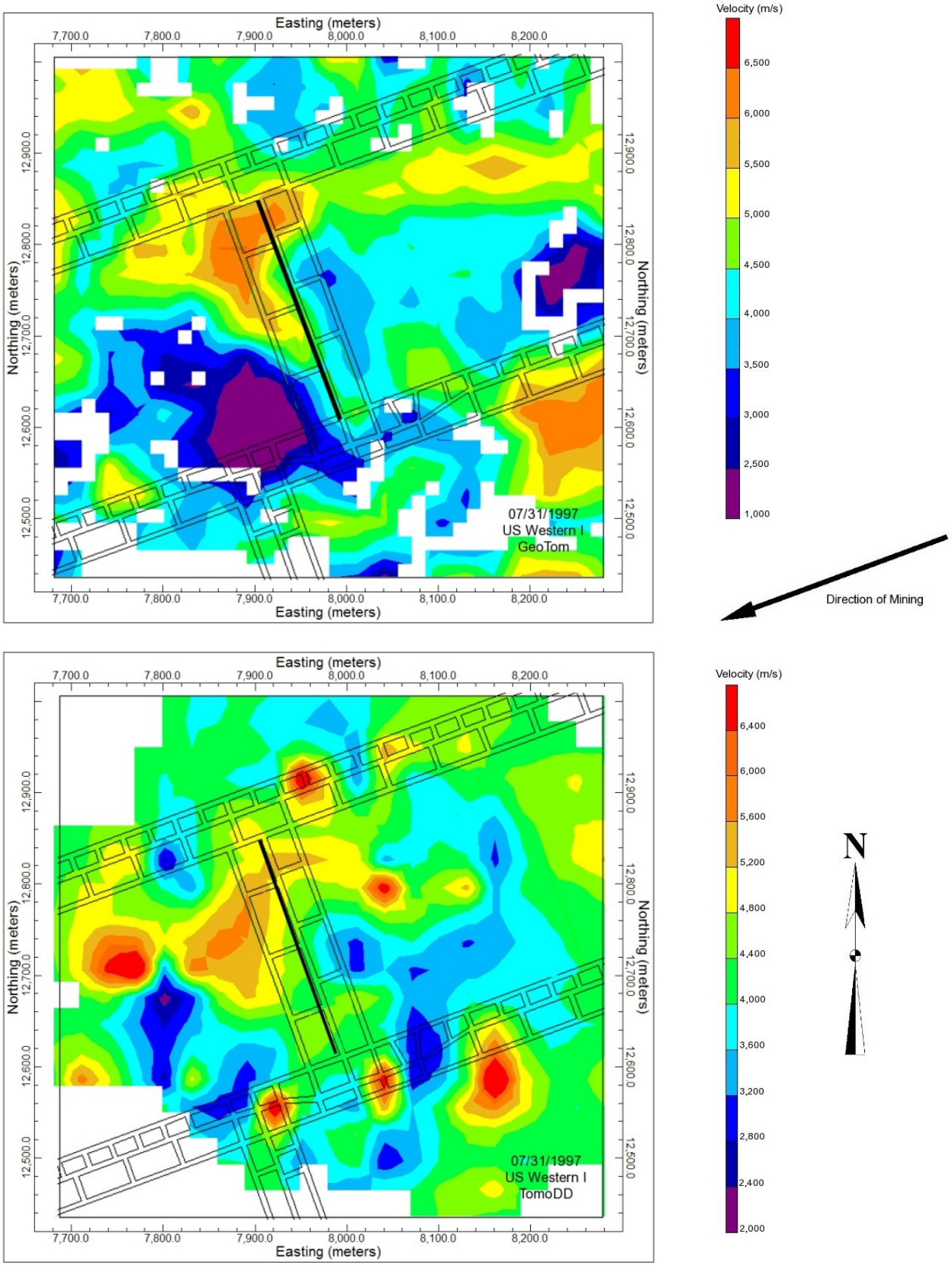

Figure B.15. Plan View Velocity Tomograms at seam level, Z = 1695 meters, for 07/31/97. Areas not traversed by rays are shown in white.

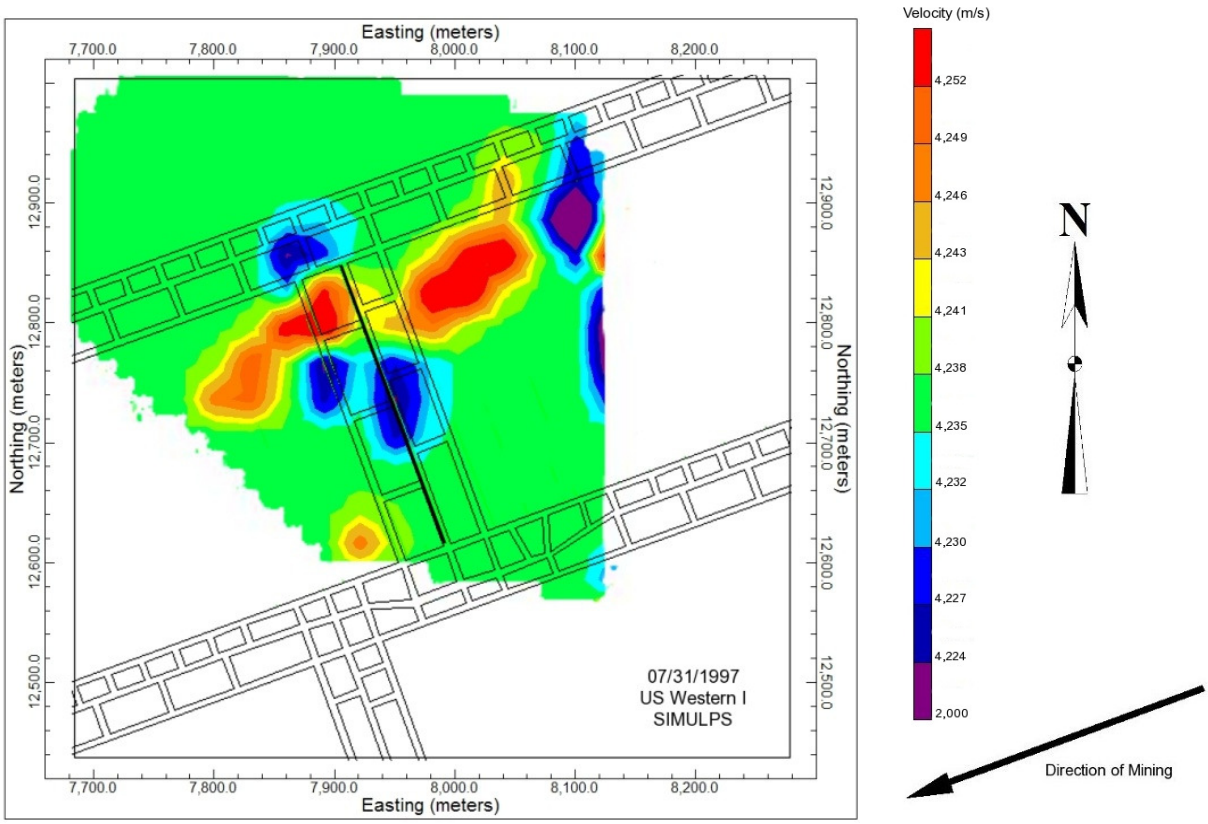

Figure B.16. Plan View Velocity Tomogram at seam level, Z = 1695 meters, for 07/31/97. Areas not traversed by rays are shown in white.

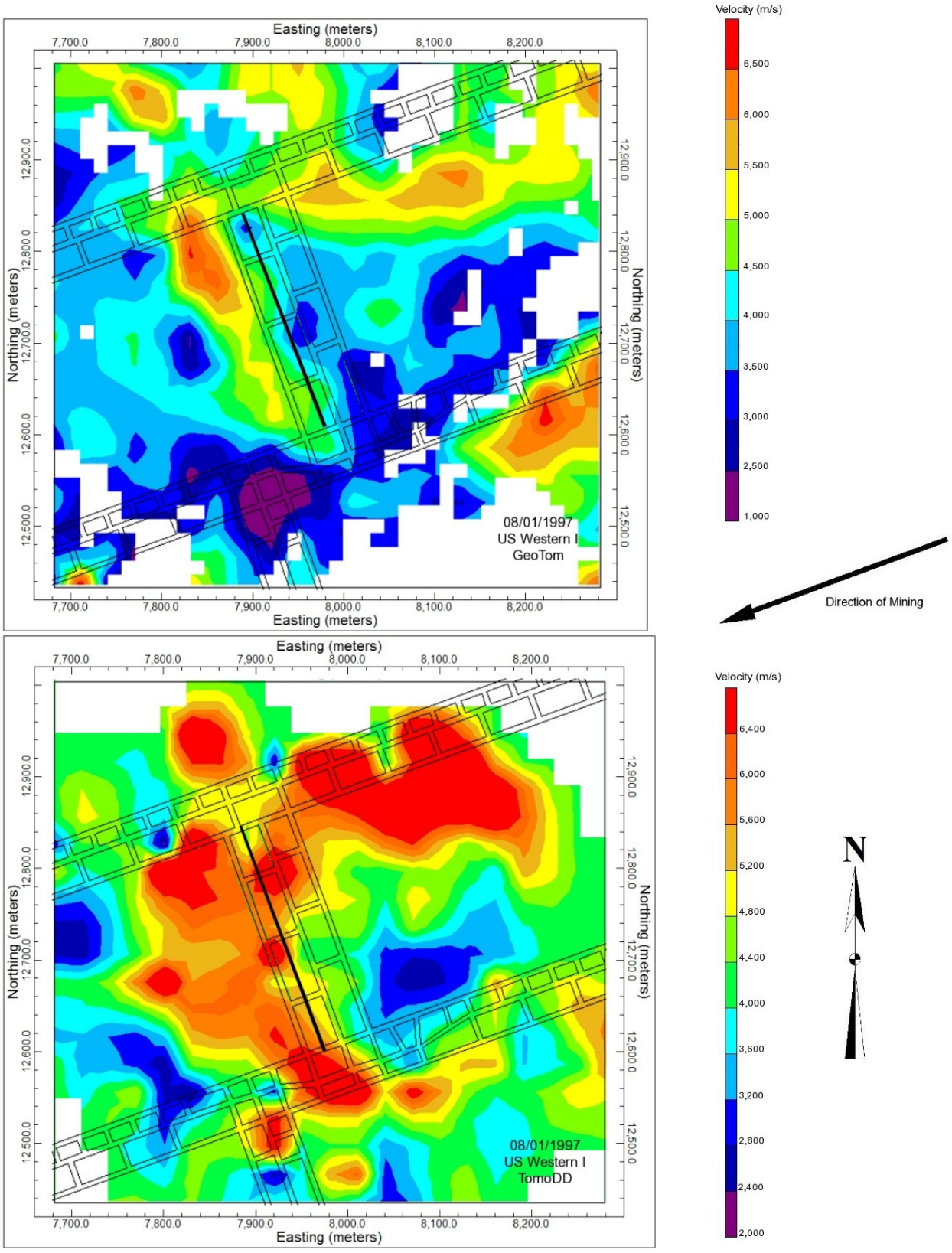

Figure B.17. Plan View Velocity Tomograms at seam level, Z = 1695 meters, for 08/01/97. Areas not traversed by rays are shown in white.

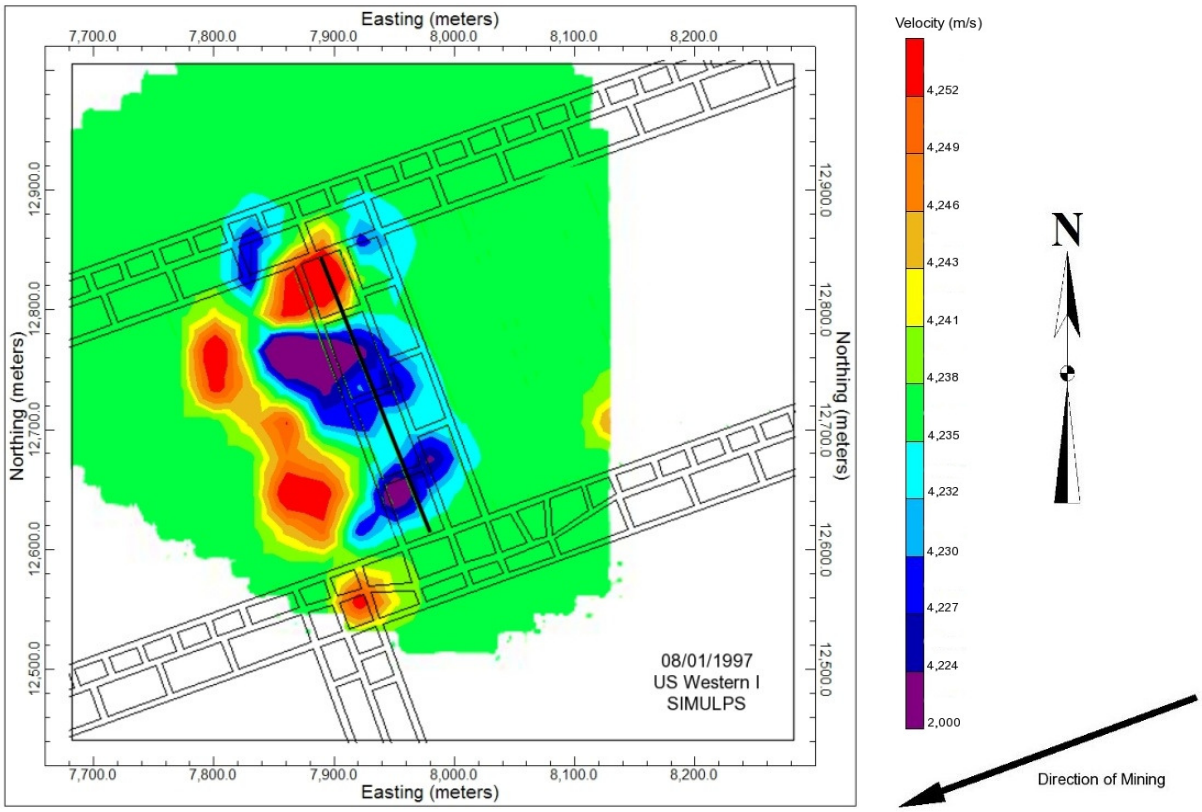

Figure B.18. Plan View Velocity Tomogram at seam level, Z = 1695 meters, for 08/01/97. Areas not traversed by rays are shown in white.

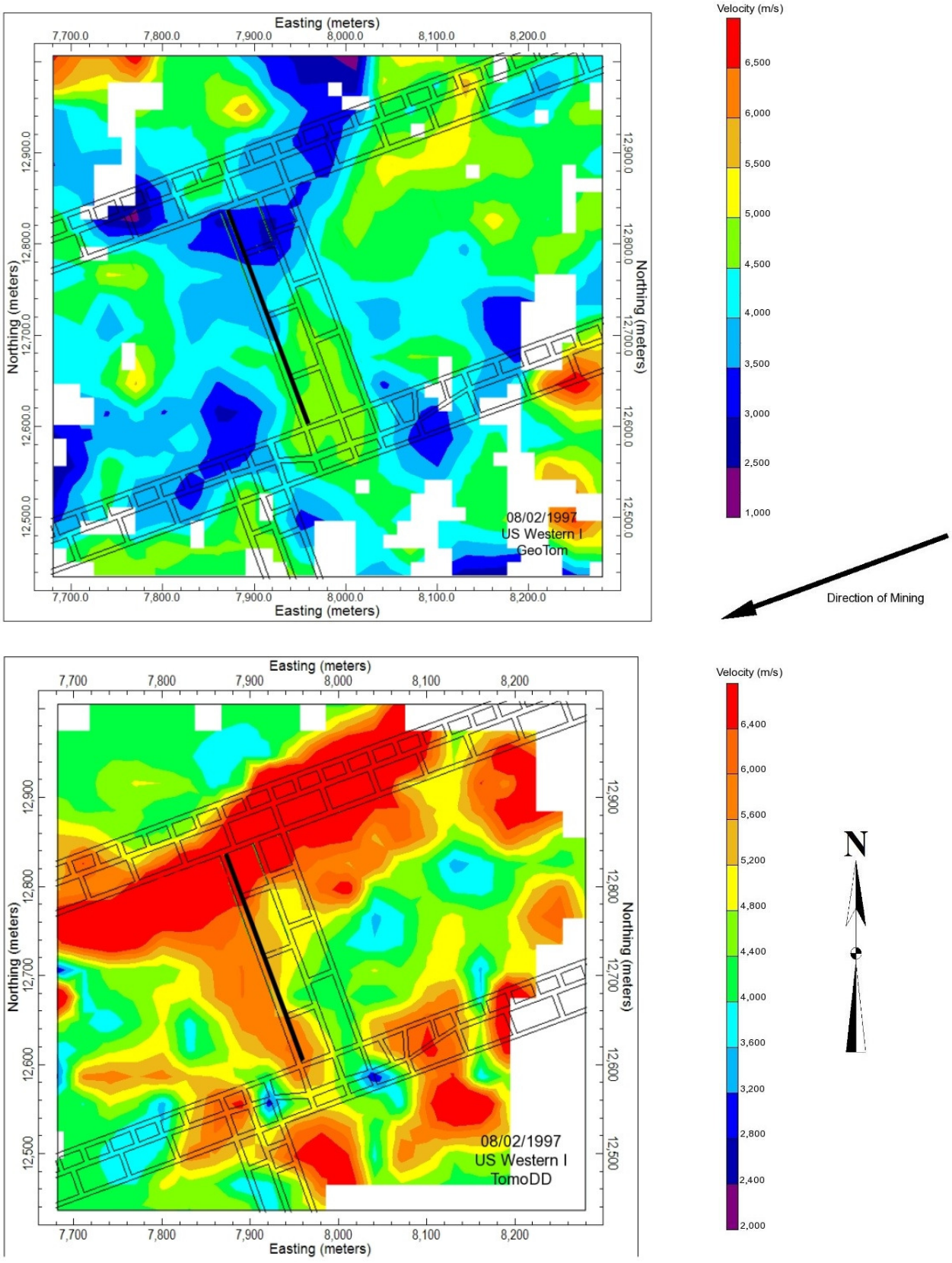

Figure B.19. Plan View Velocity Tomograms at seam level, Z = 1695 meters, for 08/02/97. Areas not traversed by rays are shown in white.

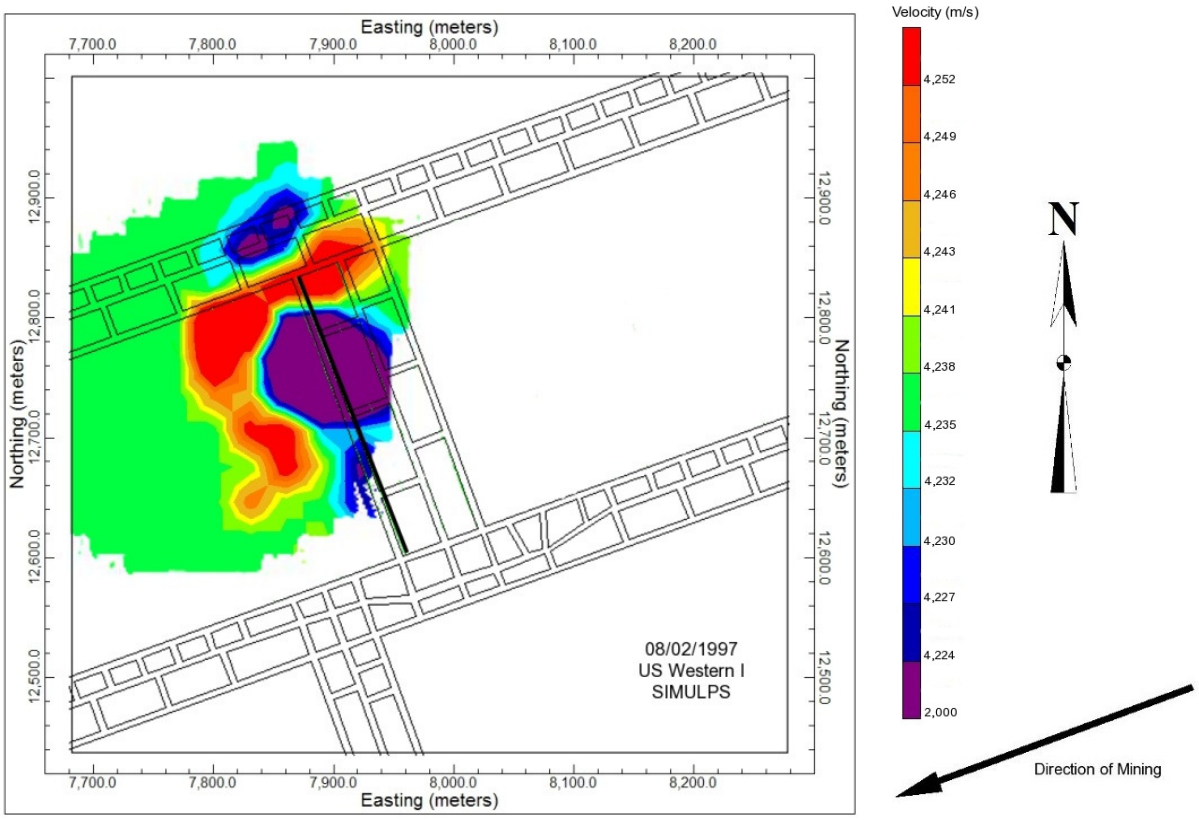

Figure B.20. Plan View Velocity Tomogram at seam level, Z = 1695 meters, for 08/02/97. Areas not traversed by rays are shown in white.

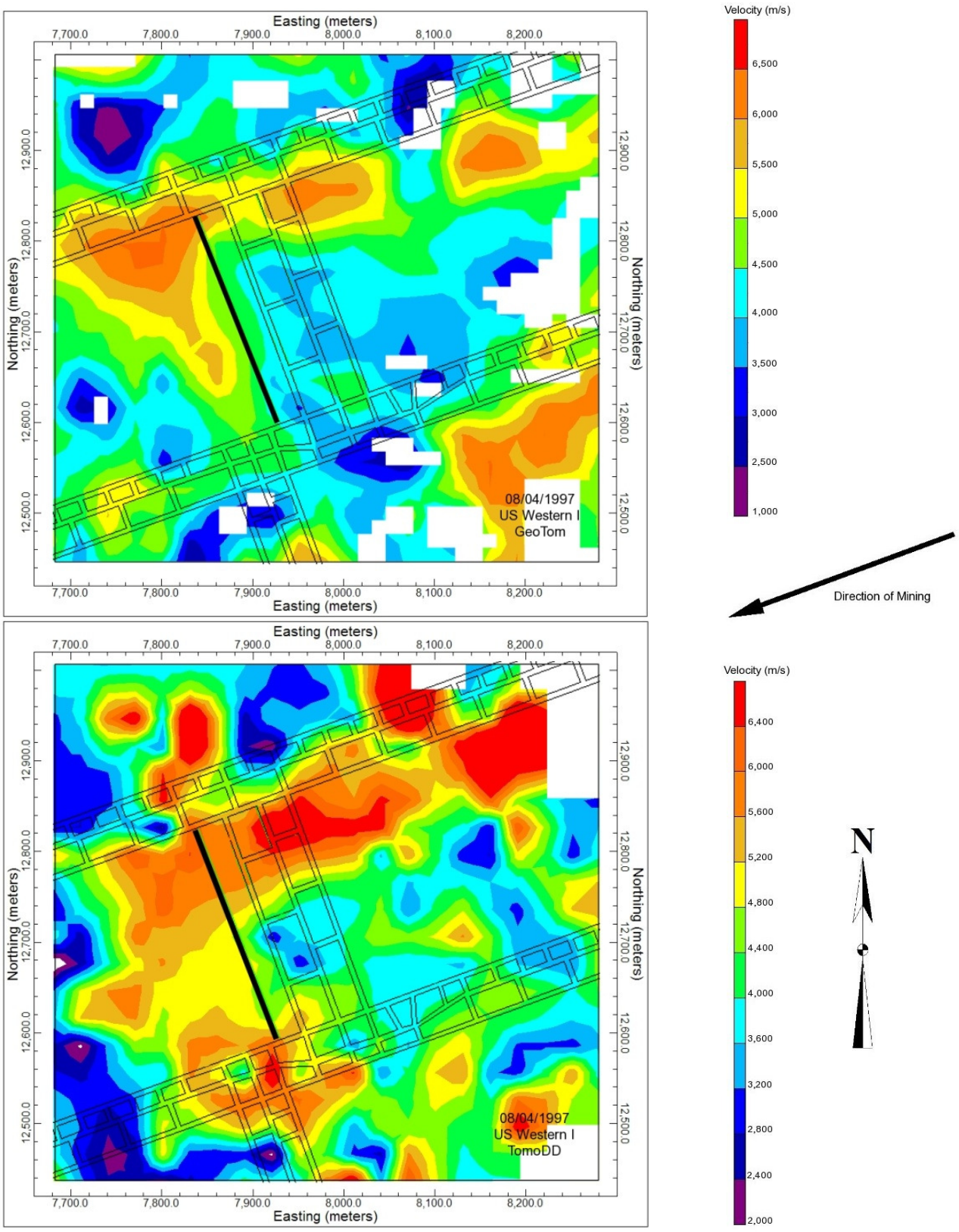

Figure B.21. Plan View Velocity Tomograms at seam level, Z = 1695 meters, for 08/04/97. Areas not traversed by rays are shown in white.

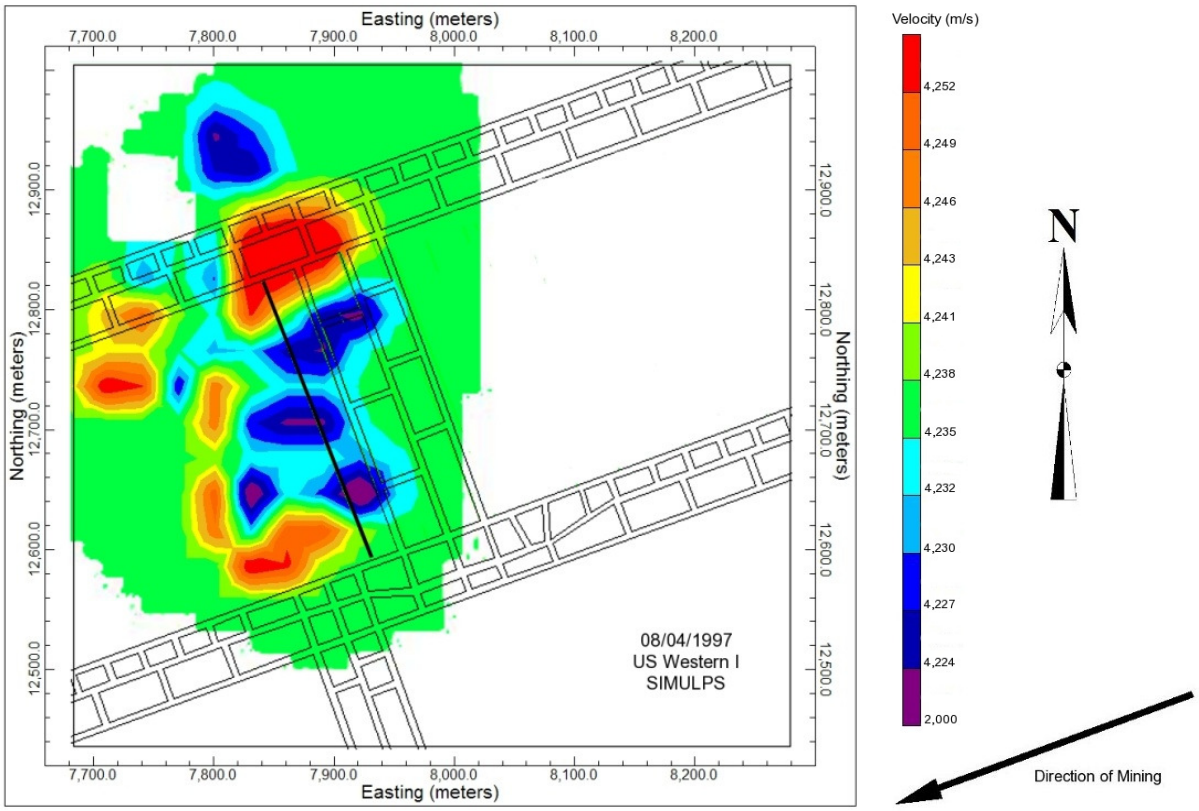

Figure B.22. Plan View Velocity Tomogram at seam level, Z = 1695 meters, for 08/04/97. Areas not traversed by rays are shown in white.

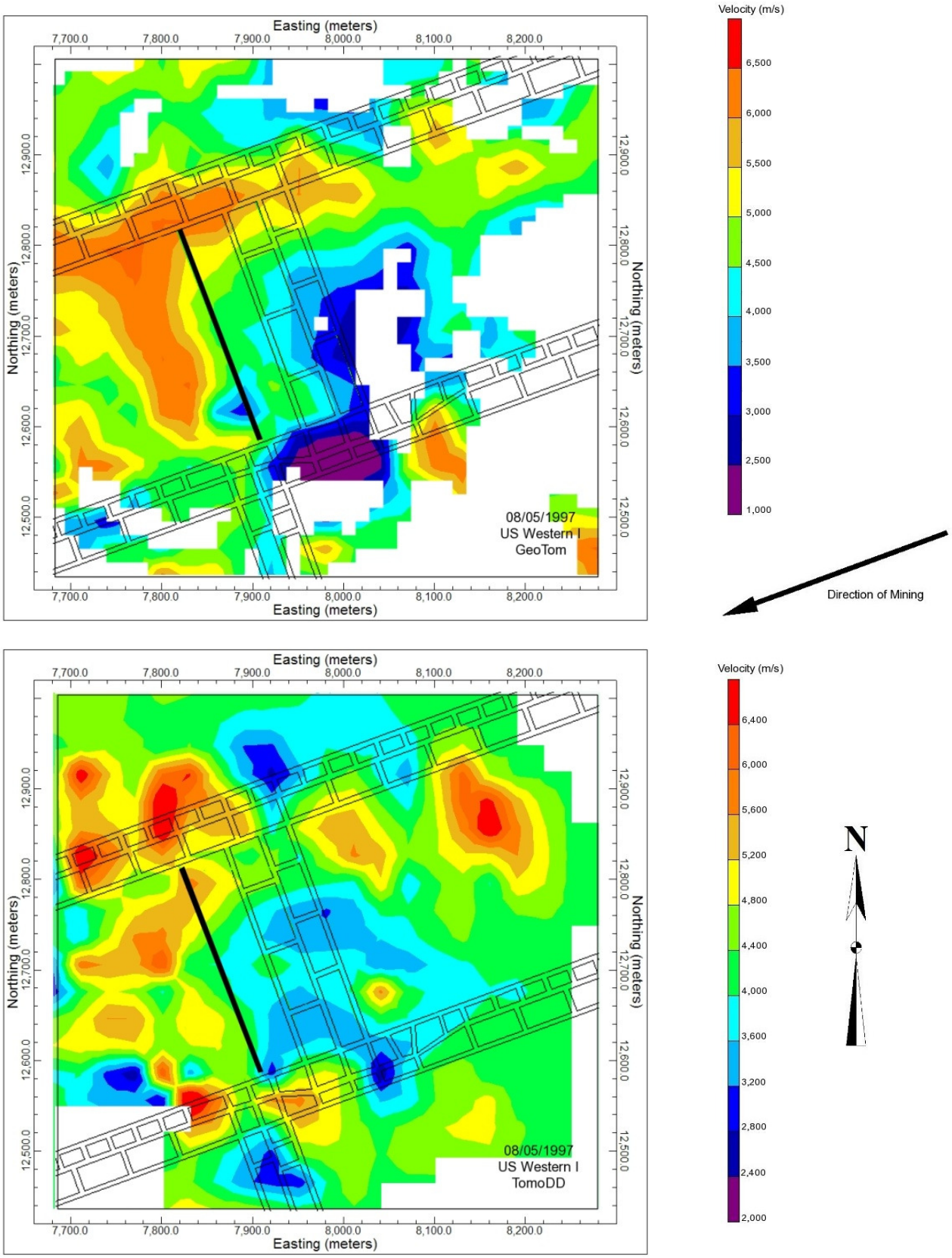

Figure B.23. Plan View Velocity Tomograms at seam level, Z = 1695 meters, for 08/05/97. Areas not traversed by rays are shown in white.

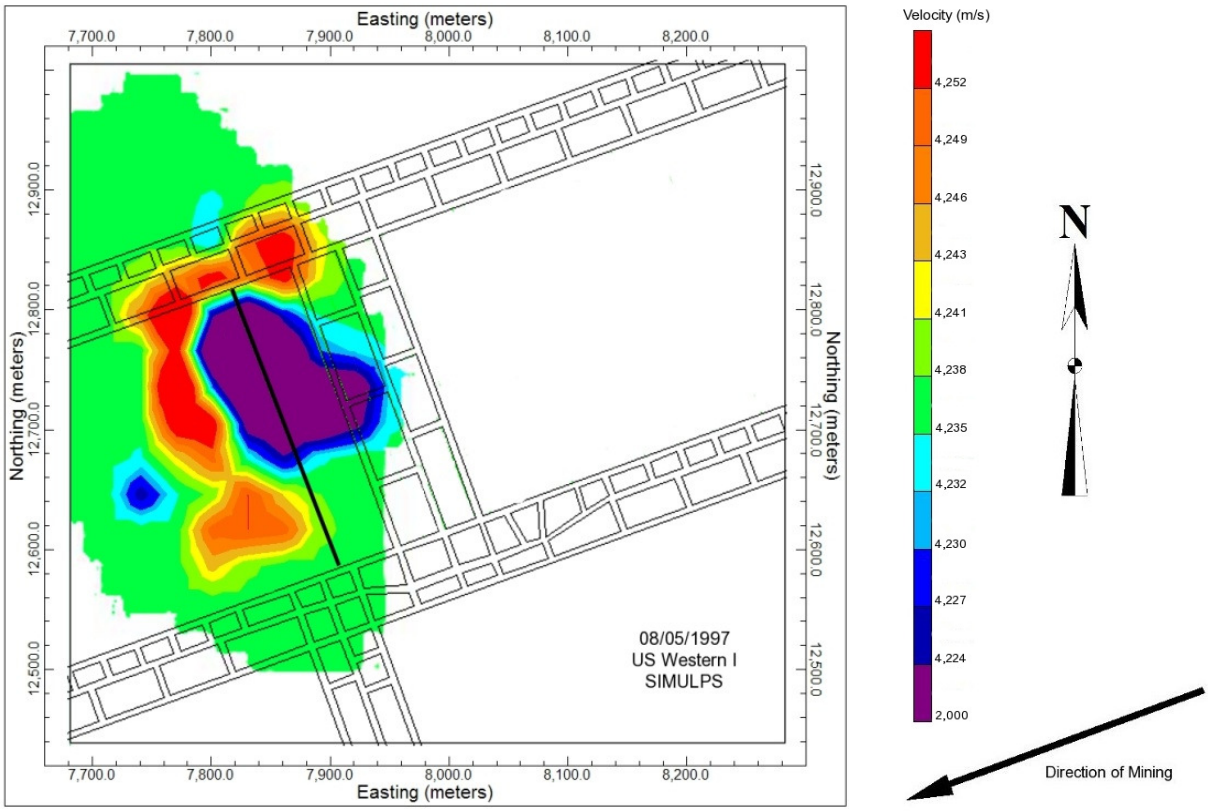

Figure B.24. Plan View Velocity Tomogram at seam level, Z = 1695 meters, for 08/05/97. Areas not traversed by rays are shown in white.

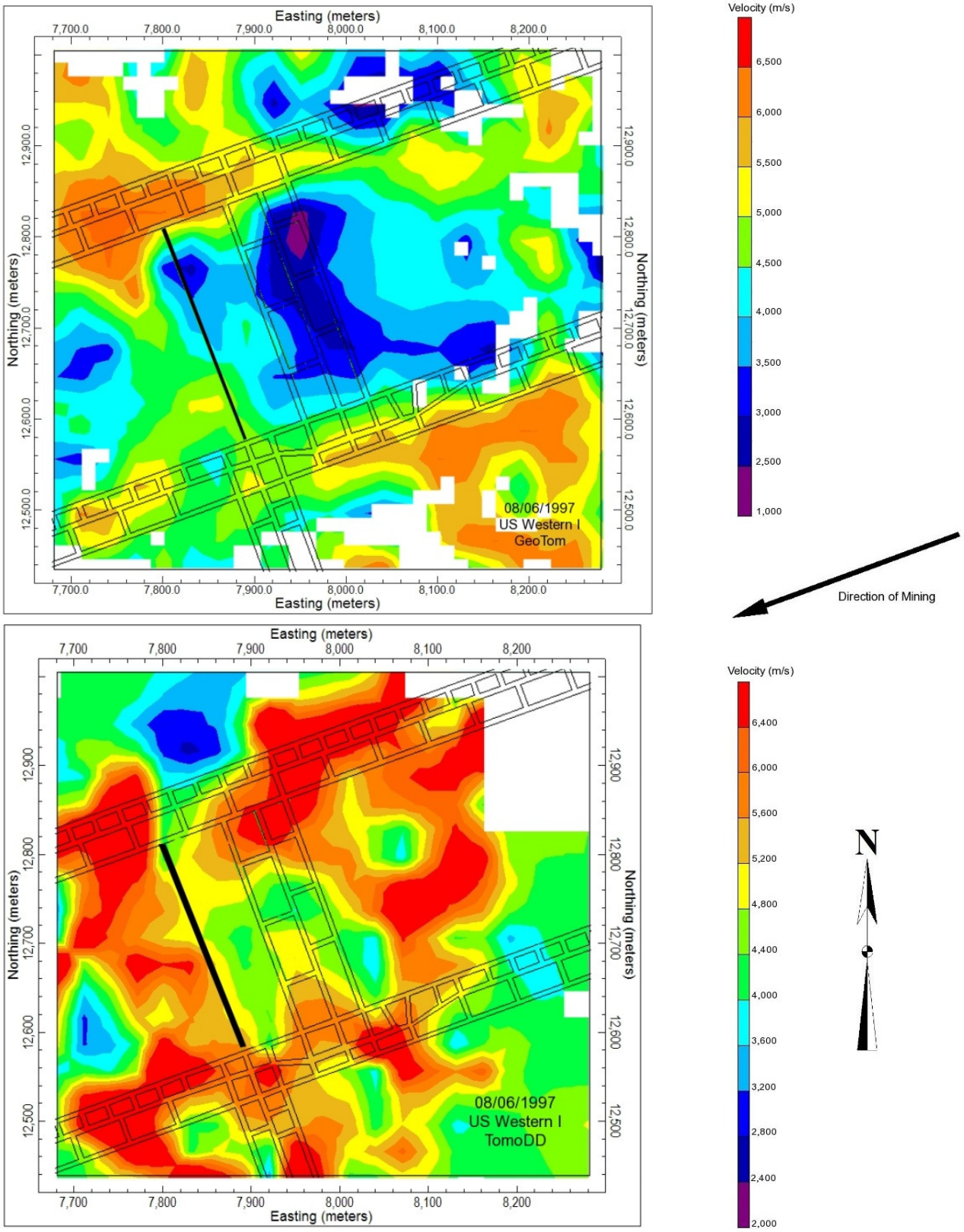

Figure B.25. Plan View Velocity Tomograms at seam level, Z = 1695 meters, for 08/06/97. Areas not traversed by rays are shown in white.

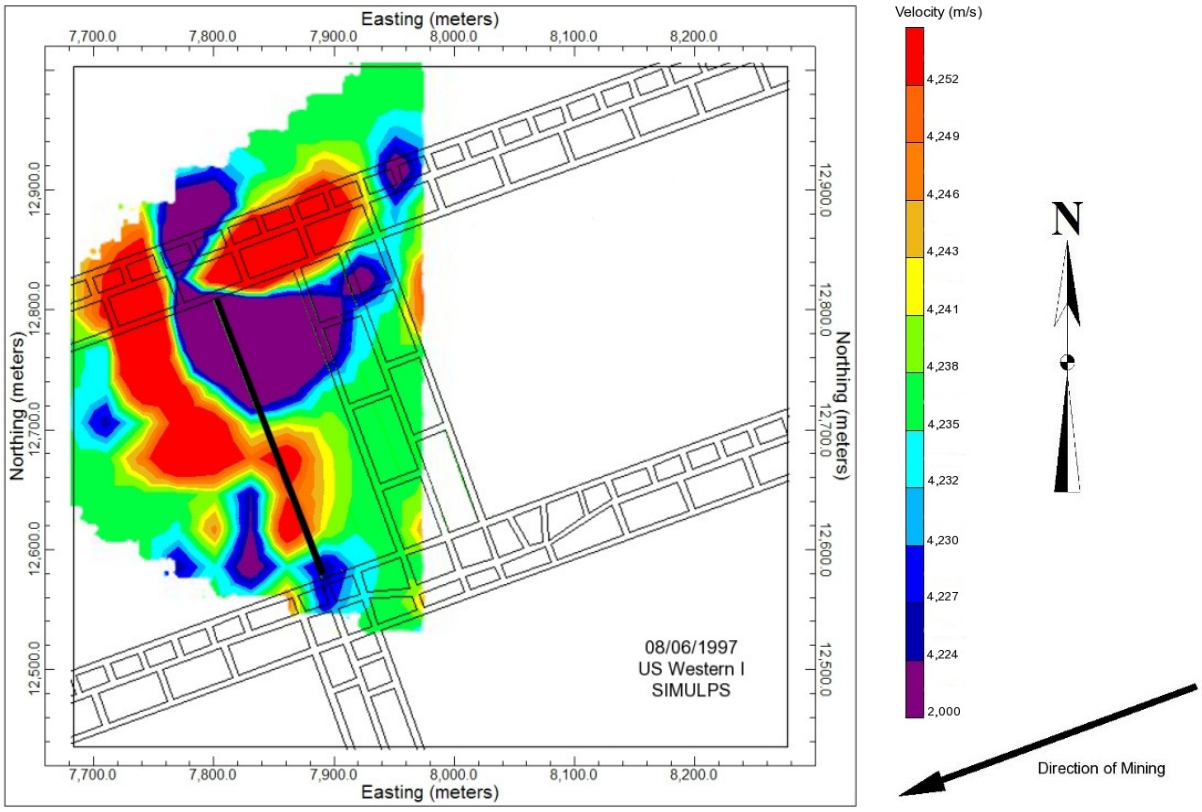

Figure B.26. Plan View Velocity Tomogram at seam level, Z = 1695 meters, for 08/06/97. Areas not traversed by rays are shown in white.

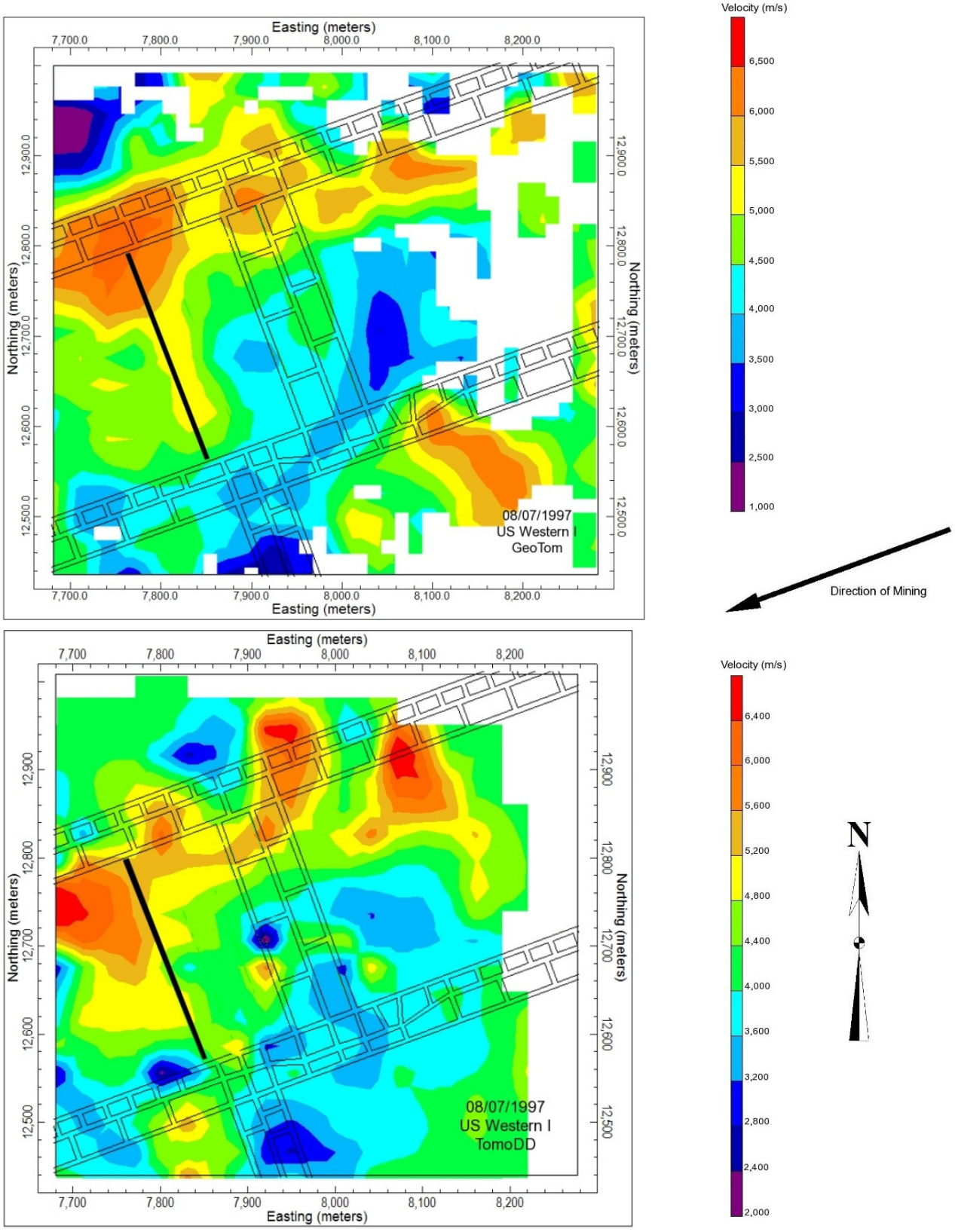

Figure B.27. Plan View Velocity Tomograms at seam level, Z = 1695 meters, for 08/07/97. Areas not traversed by rays are shown in white.

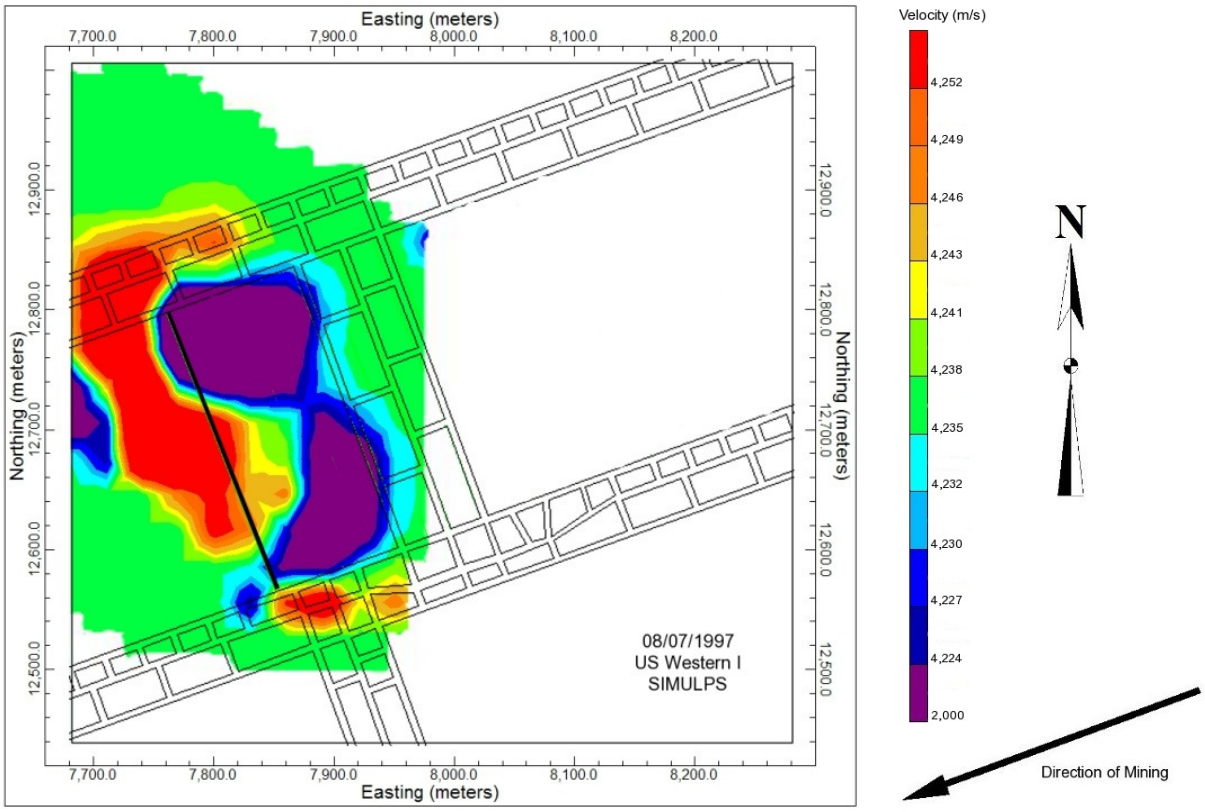

Figure B.28. Plan View Velocity Tomogram at seam level, Z = 1695 meters, for 08/07/97. Areas not traversed by rays are shown in white.

Appendix C

US Western II Plan View Velocity Tomograms generated by GeoTom and TomoDD.

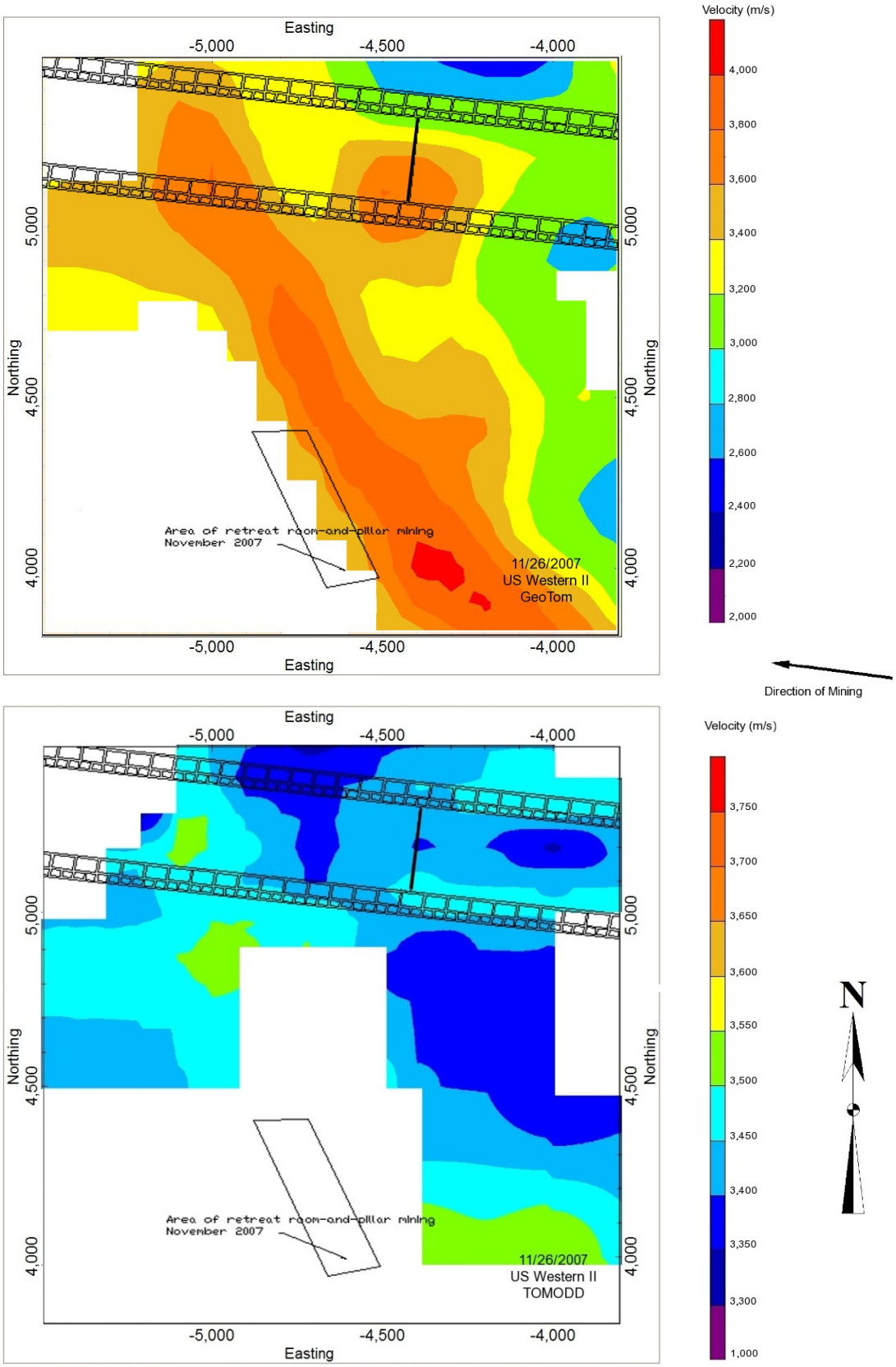

Figure C.1. Plan View Velocity Tomograms at seam level, Z = 7498 meters, for 11/26/07. Areas not traversed by rays are shown in white.

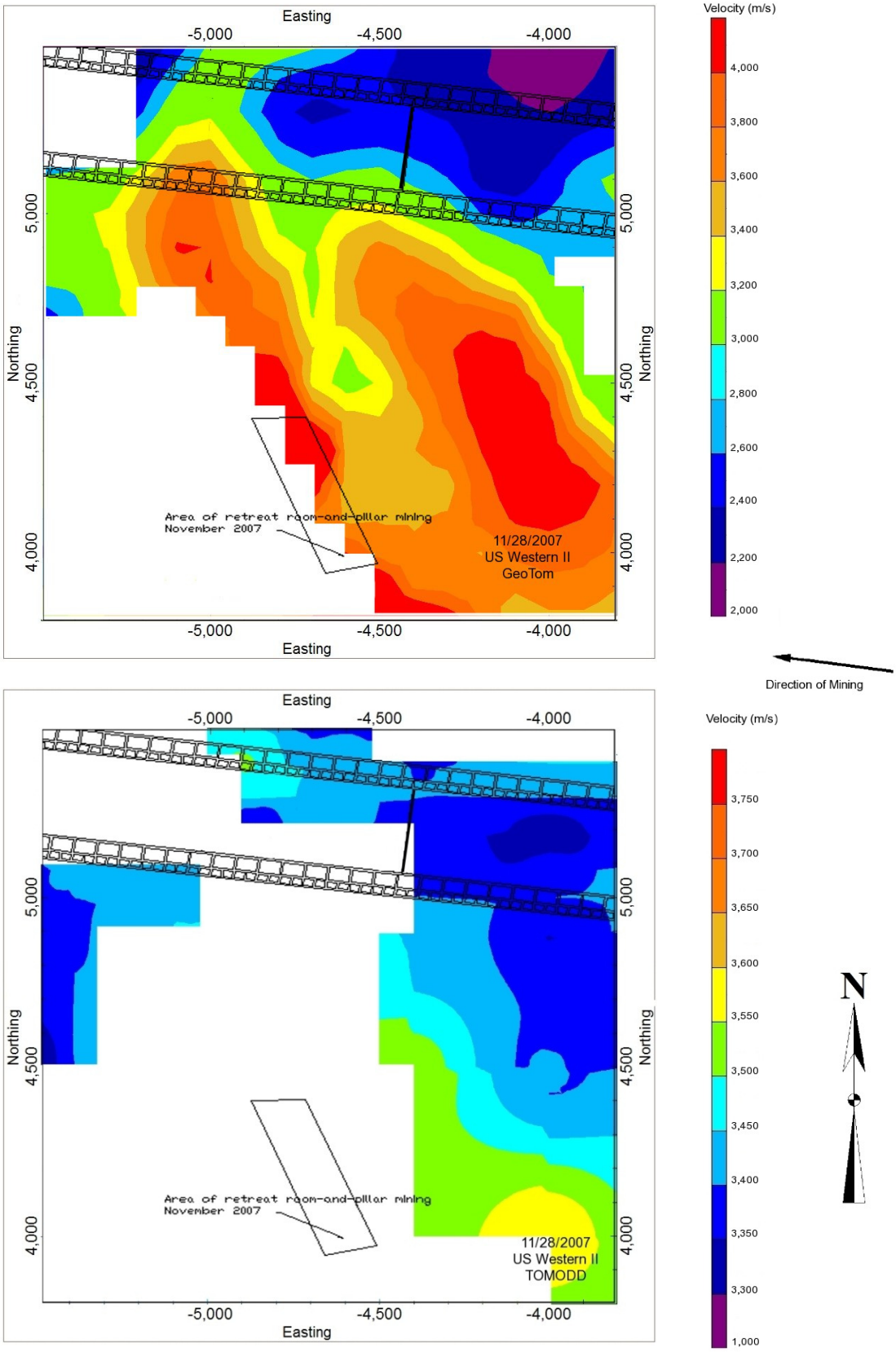

Figure C.2. Plan View Velocity Tomograms at seam level, Z = 7498 meters, for 11/28/07. Areas not traversed by rays are shown in white.

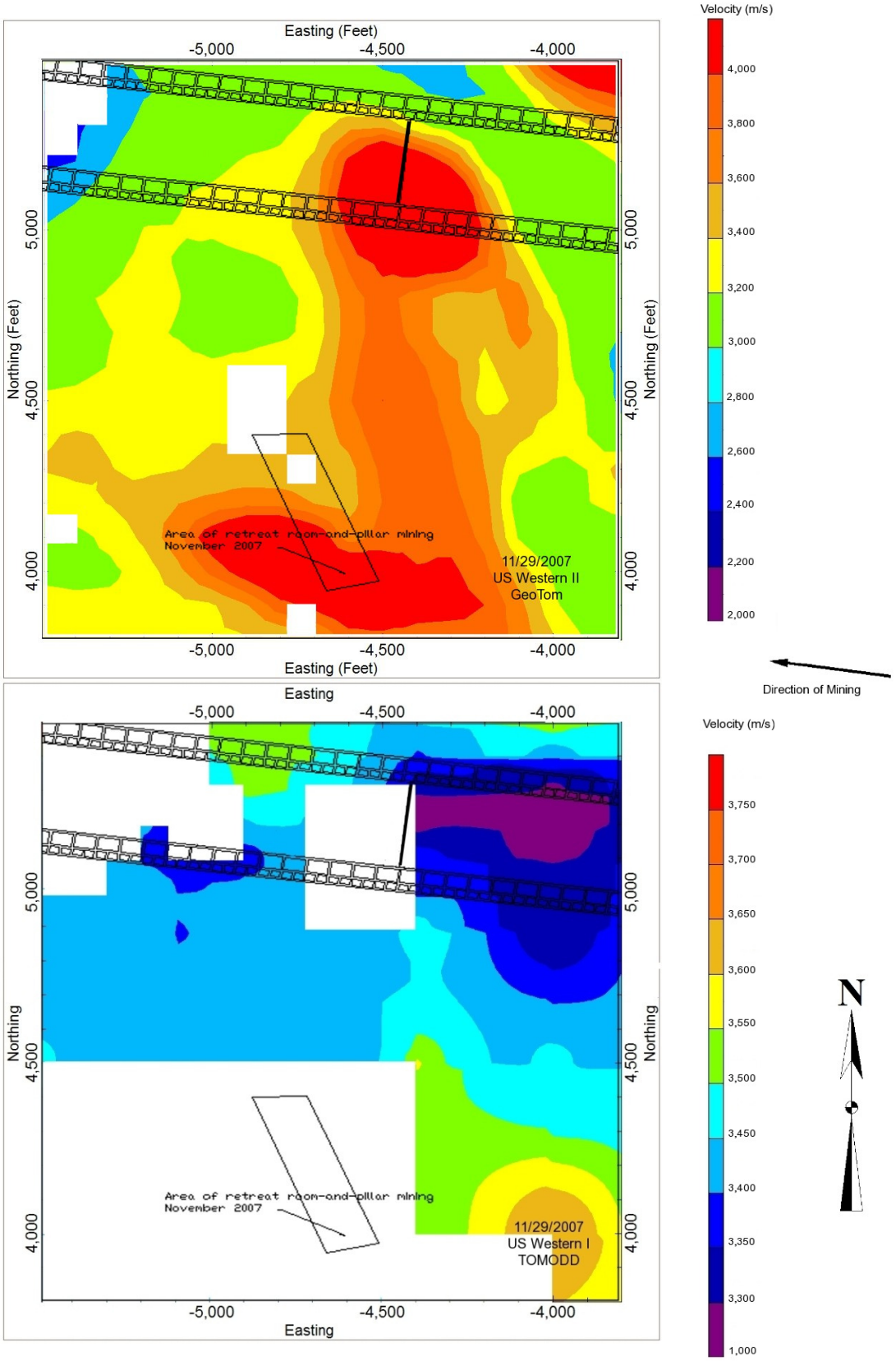

Figure C.3. Plan View Velocity Tomograms at seam level, Z = 7498 meters, for 11/29/07. Areas not traversed by rays are shown in white.

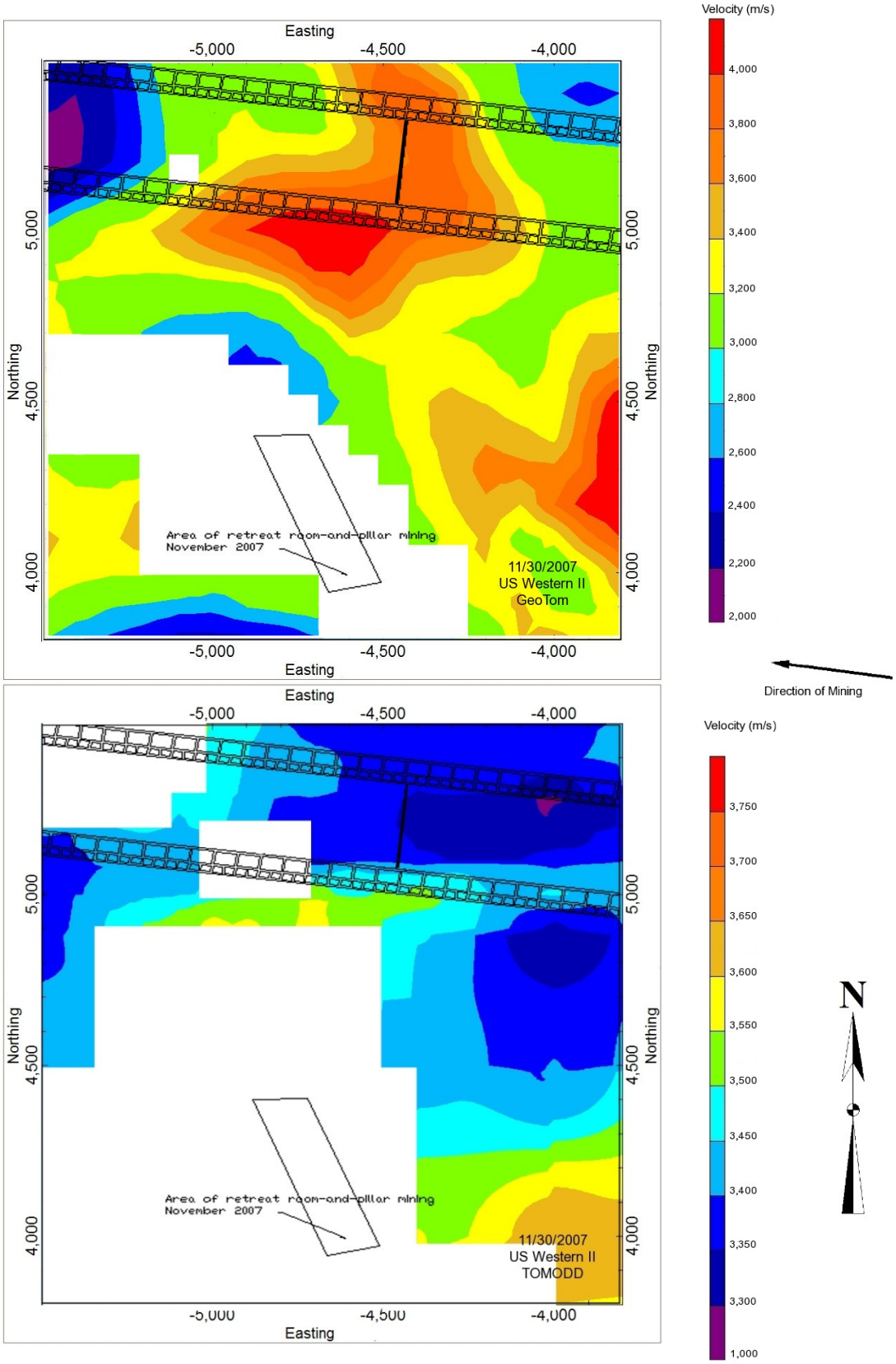

Figure C.4. Plan View Velocity Tomograms at seam level, Z = 7498 meters, for 11/30/07. Areas not traversed by rays are shown in white.

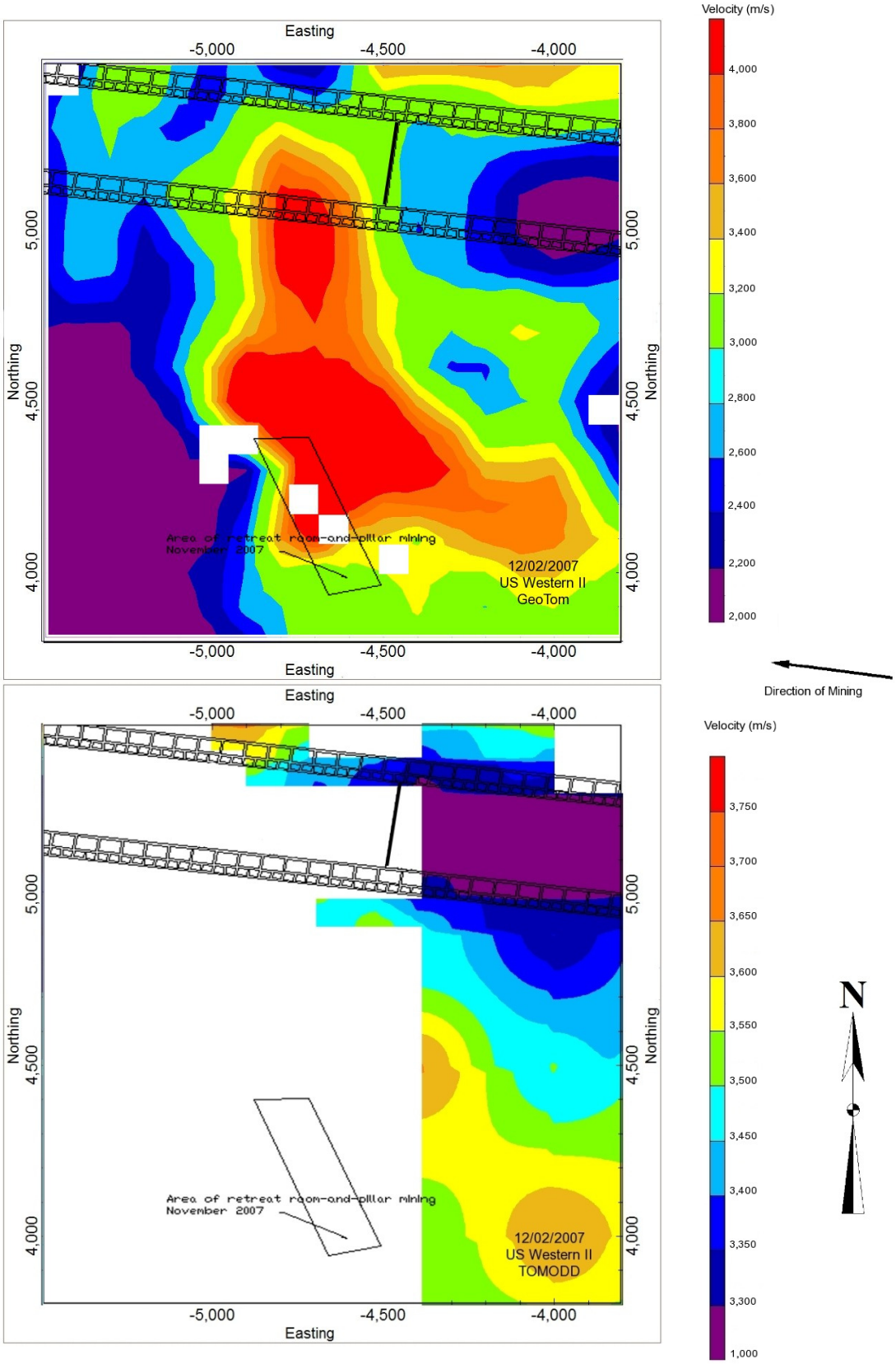

Figure C.5. Plan View Velocity Tomograms at seam level, Z = 7498 meters, for 12/02/07. Areas not traversed by rays are shown in white.

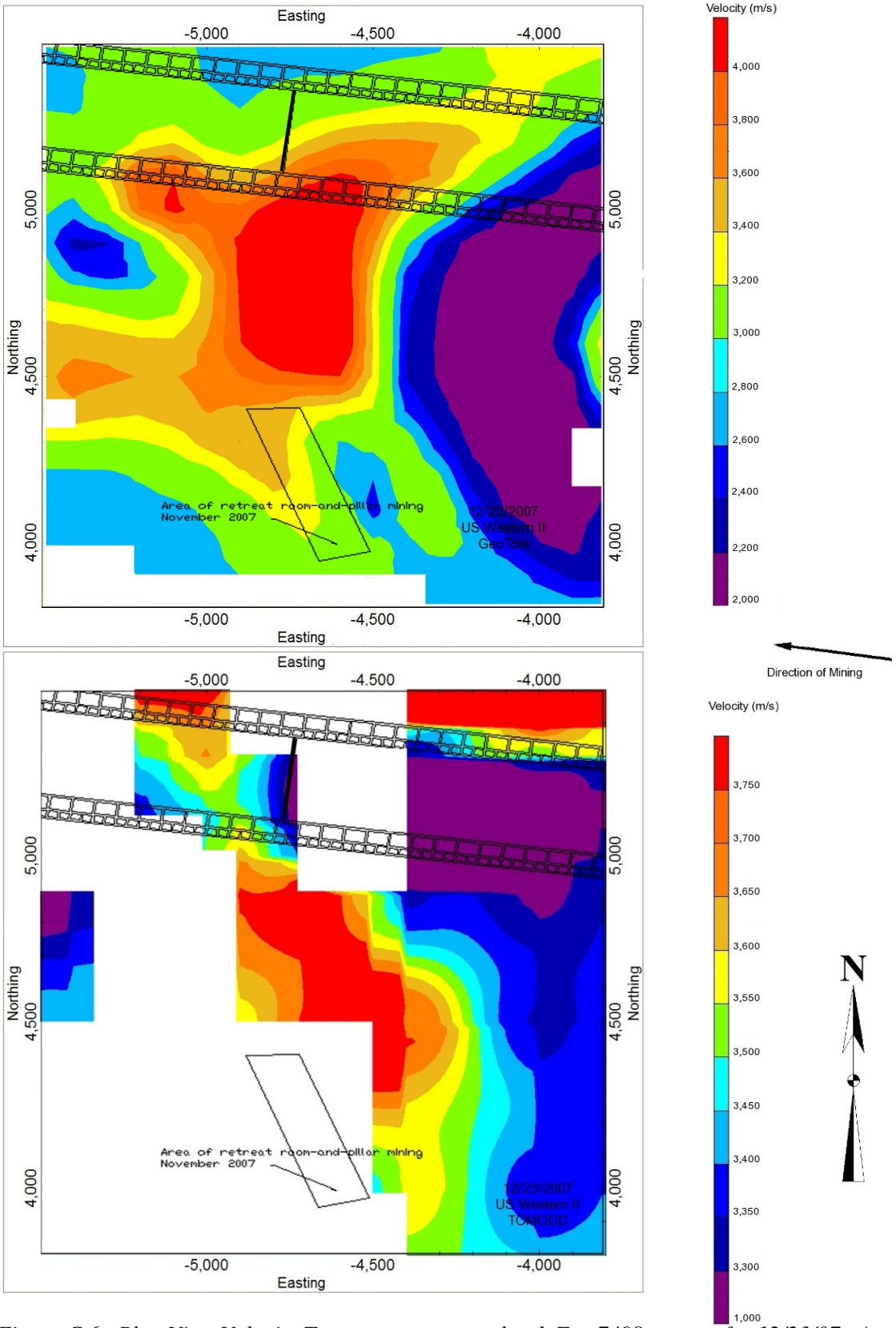

Figure C.6. Plan View Velocity Tomograms at seam level, Z = 7498 meters, for 12/23/07. Areas not traversed by rays are shown in white.

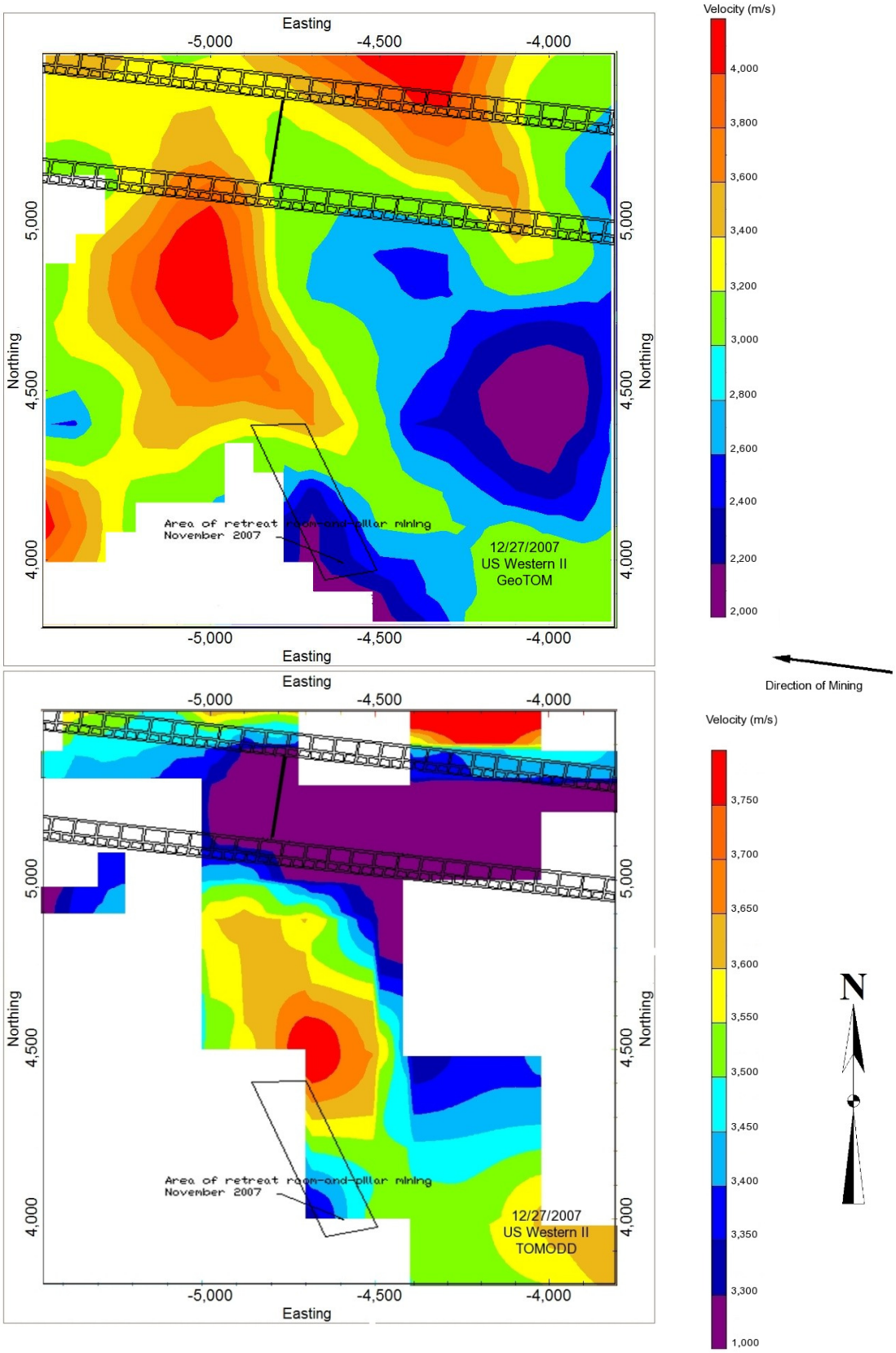

Figure C.7. Plan View Velocity Tomograms at seam level, Z = 7498 meters, for 12/27/07. Areas not traversed by rays are shown in white.

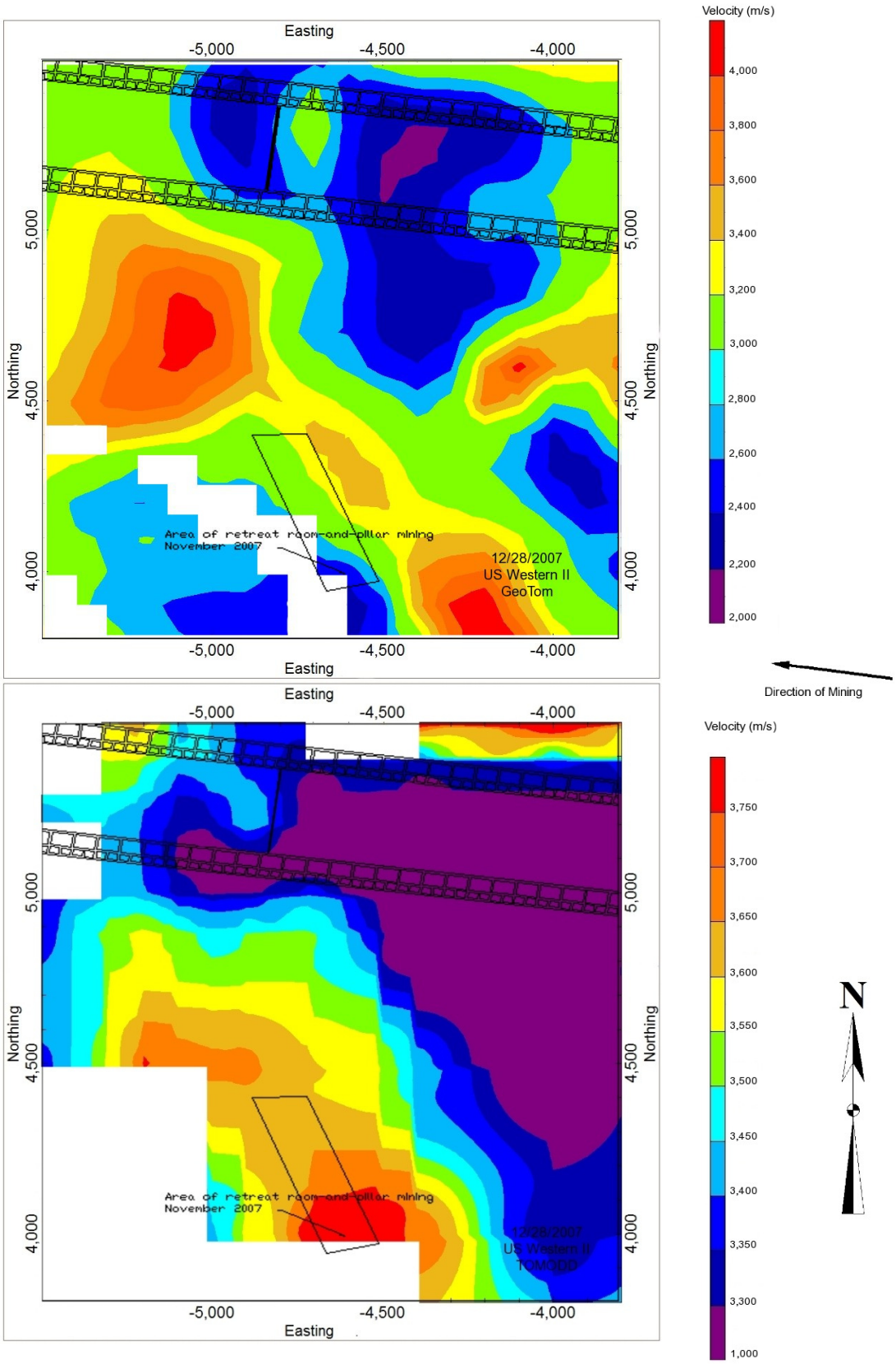

Figure C.8. Plan View Velocity Tomograms at seam level, Z = 7498 meters, for 12/28/07. Areas not traversed by rays are shown in white.

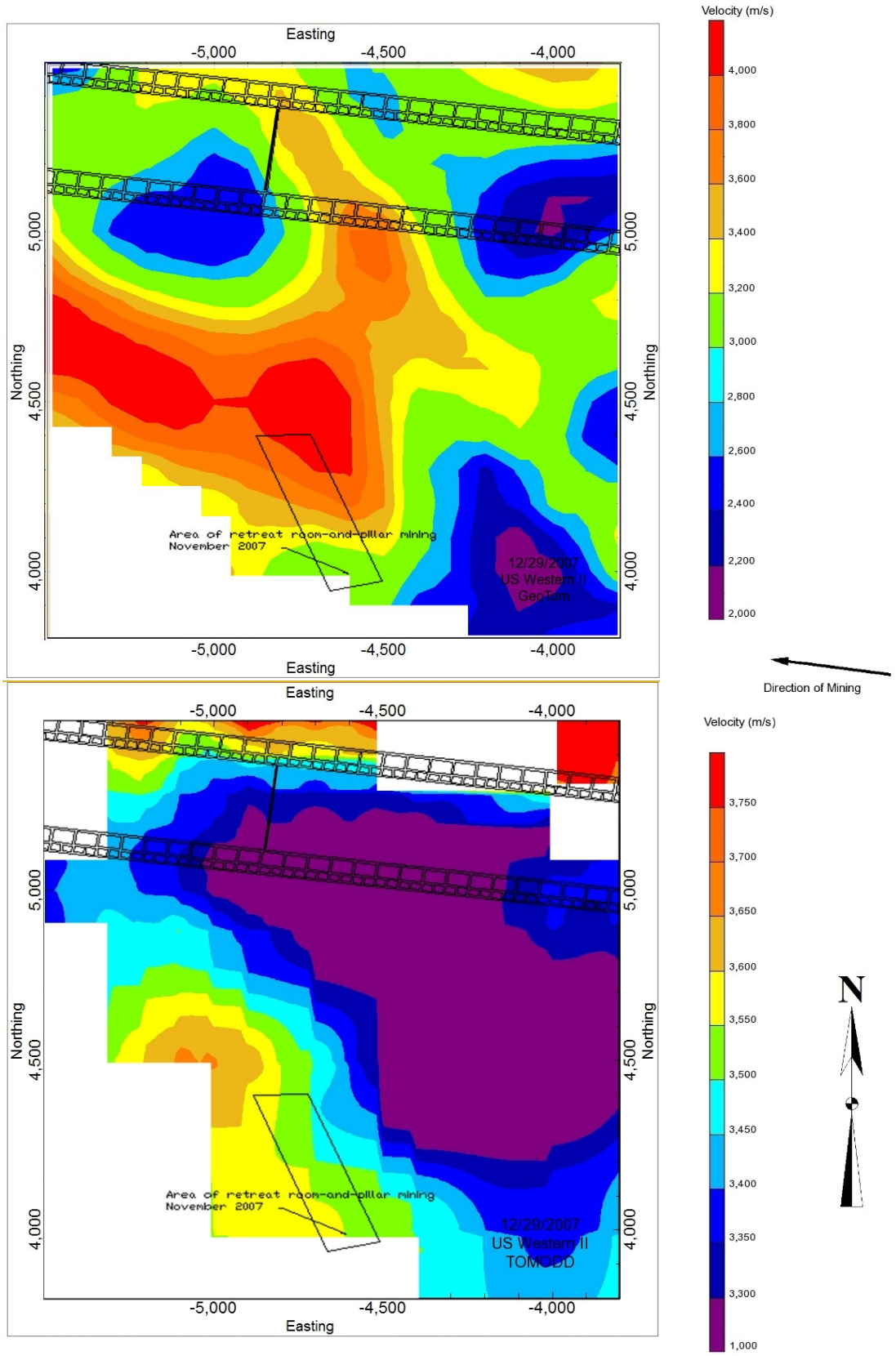

Figure C.9. Plan View Velocity Tomograms at seam level, Z = 7498 meters, for 12/29/07. Areas not traversed by rays are shown in white.

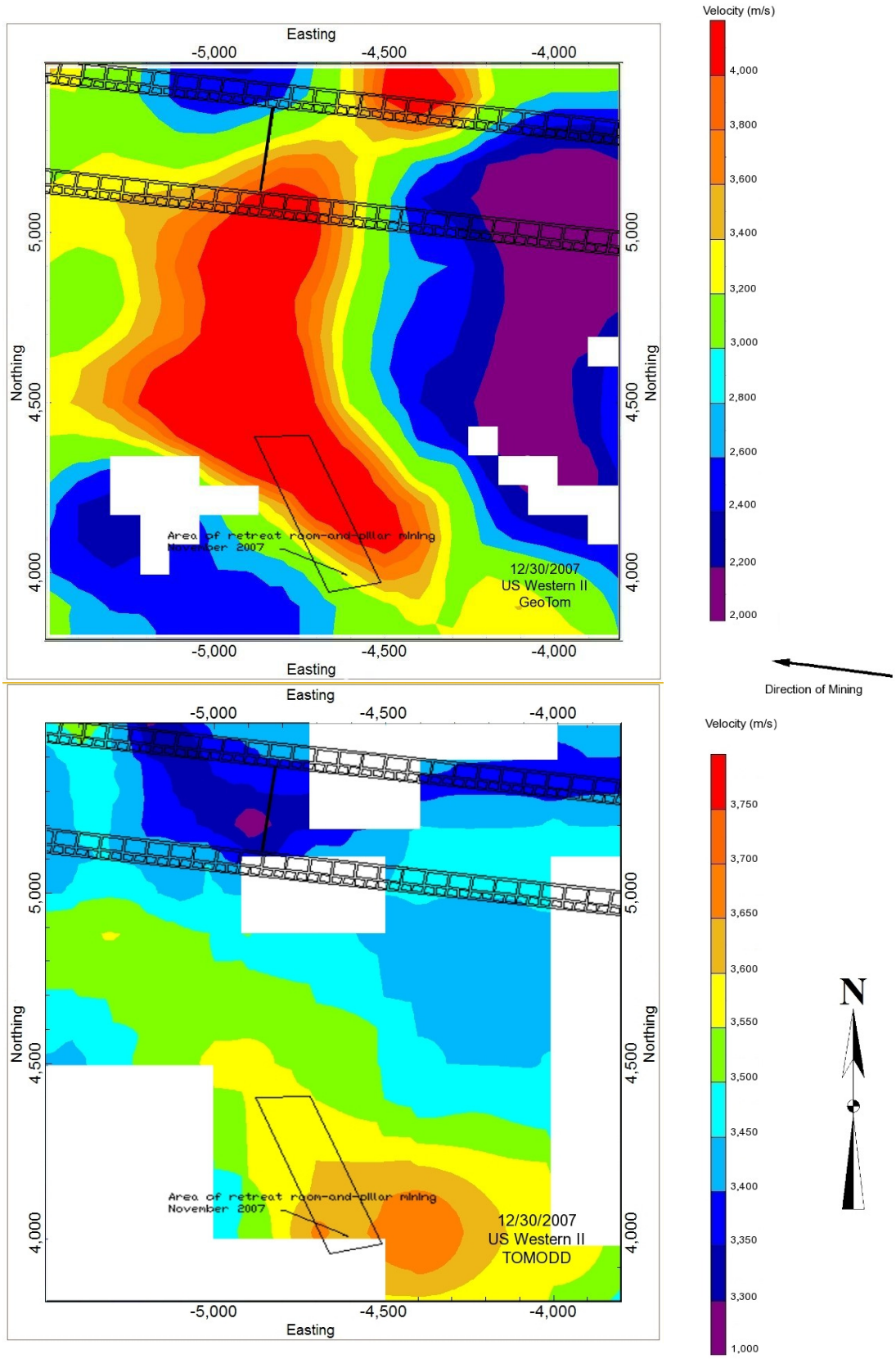

Figure C.10. Plan View Velocity Tomograms at seam level, Z = 7498 meters, for 12/30/07. Areas not traversed by rays are shown in white.

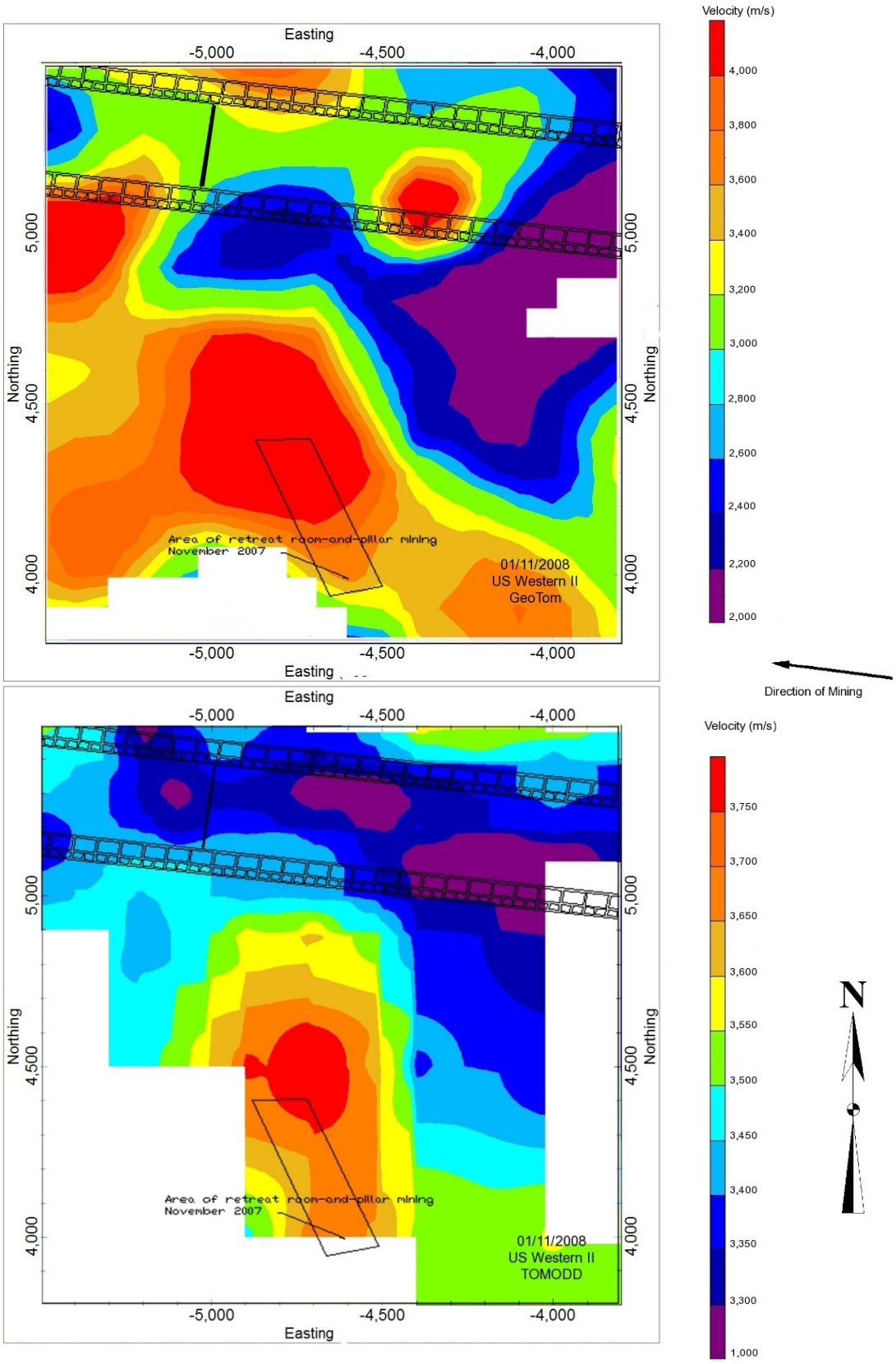

Figure C.11. Plan View Velocity Tomograms at seam level, Z = 7498 meters, for 01/11/08. Areas not traversed by rays are shown in white.

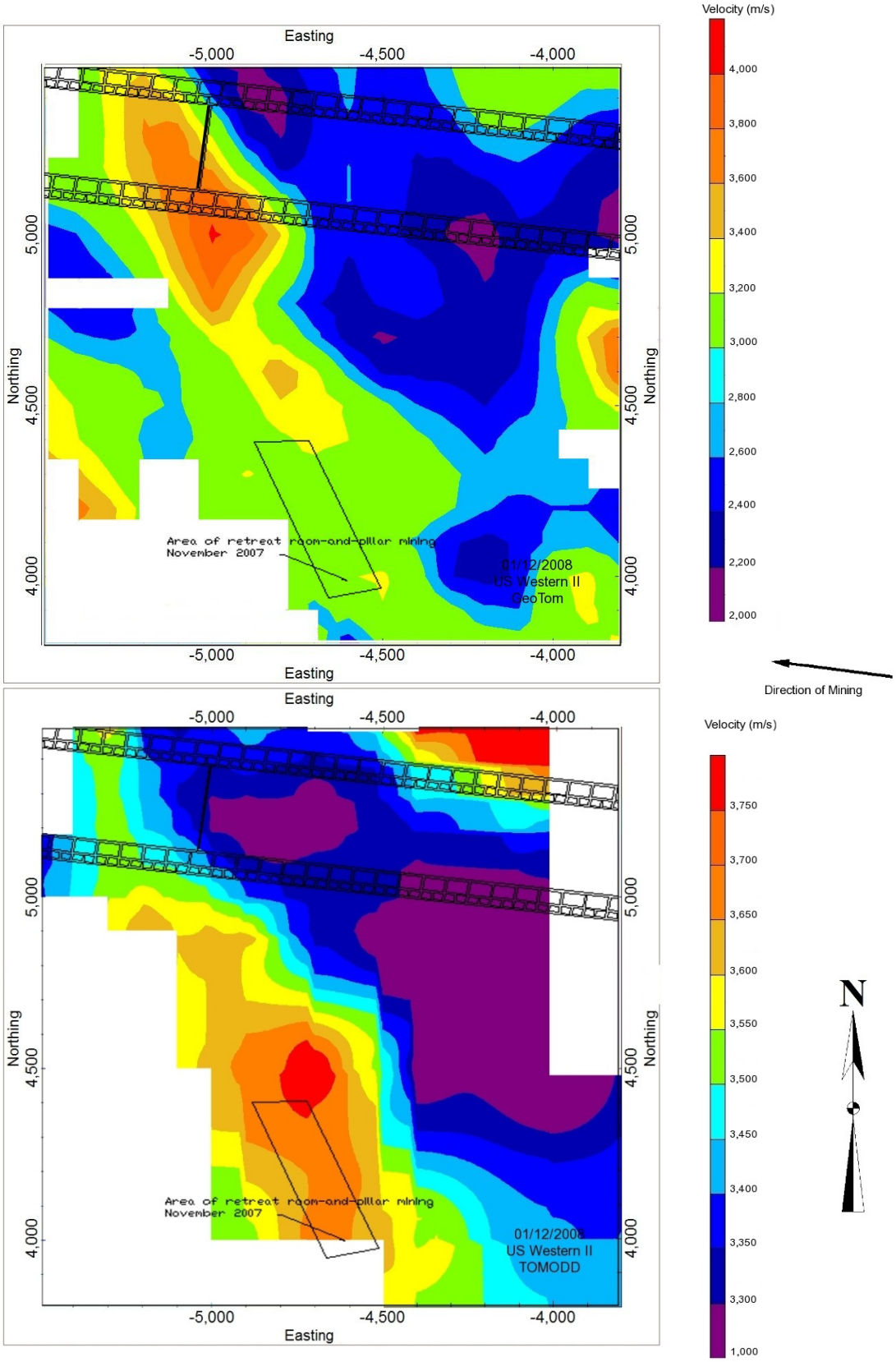

Figure C.12. Plan View Velocity Tomograms at seam level, Z = 7498 meters, for 01/12/08. Areas not traversed by rays are shown in white.

Appendix D

Moonee Colliery Plan View Velocity Tomograms generated by GeoTom and TomoDD.

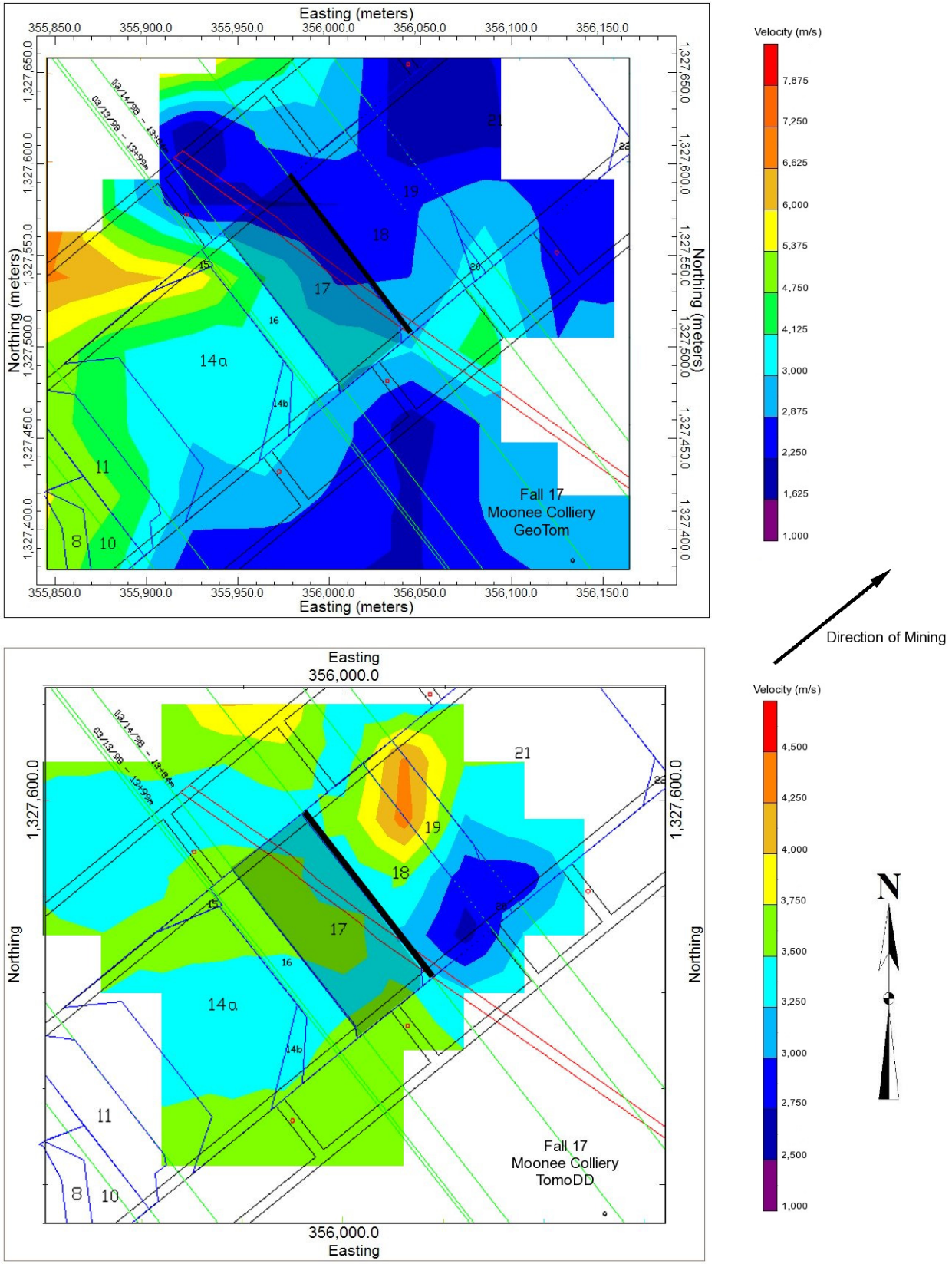

Figure D.1. Plan View Velocity Tomograms at seam level for Fall 17. Areas not traversed by rays are shown in white.

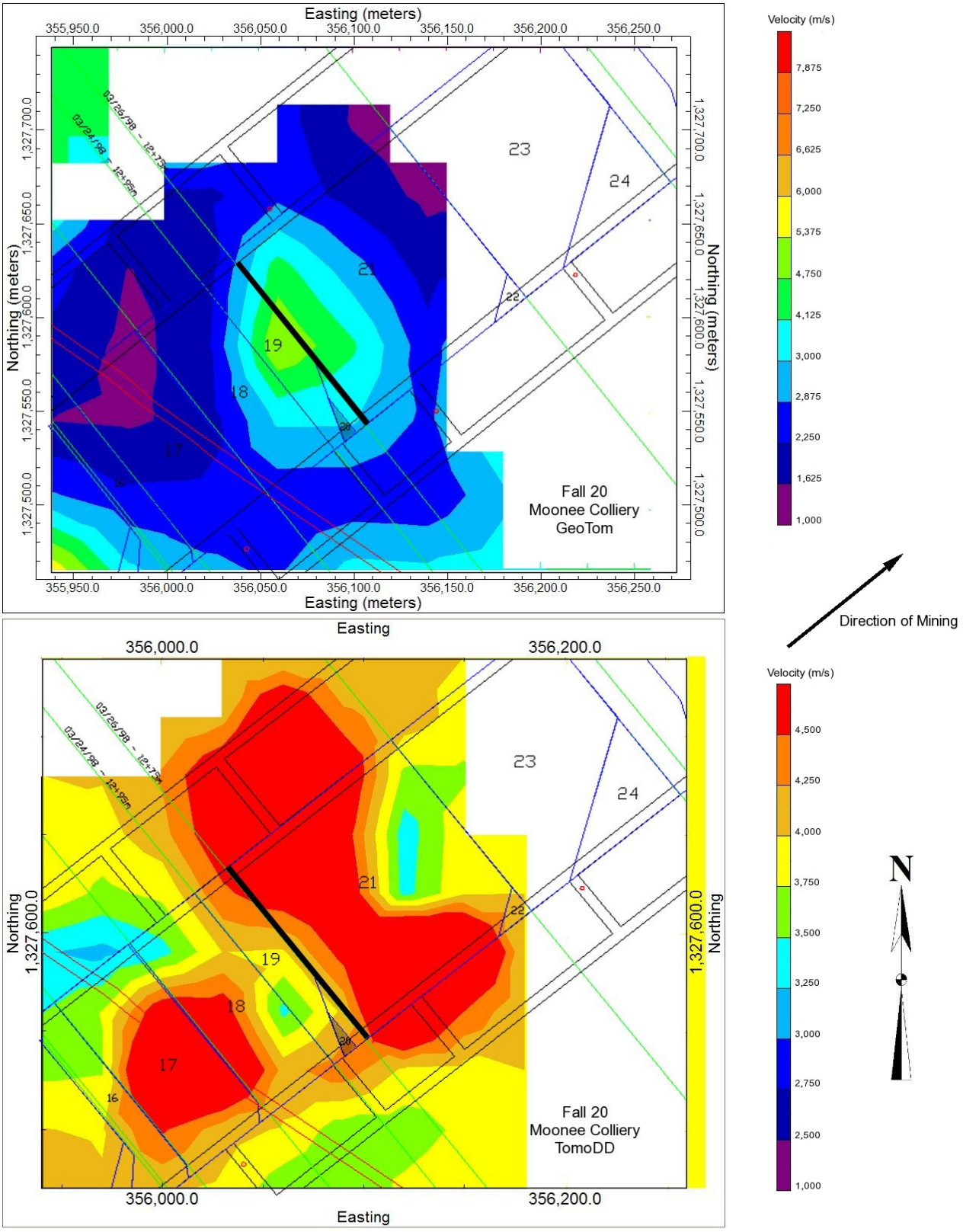

Figure D.2. Plan View Velocity Tomograms at seam level for Fall 20. Areas not traversed by rays are shown in white.

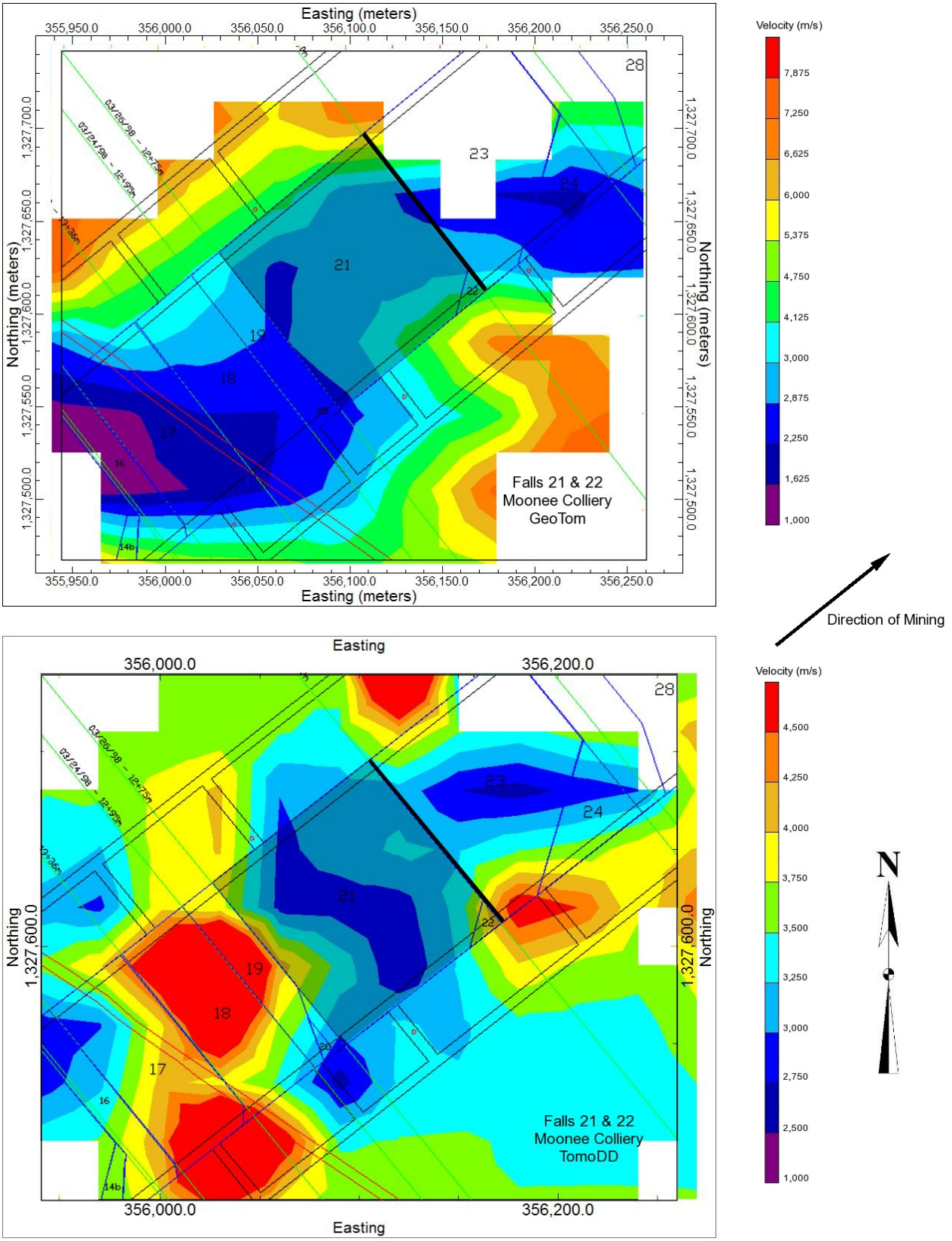

Figure D.3. Plan View Velocity Tomograms at seam level for Falls 21 and 22. Areas not traversed by rays are shown in white.

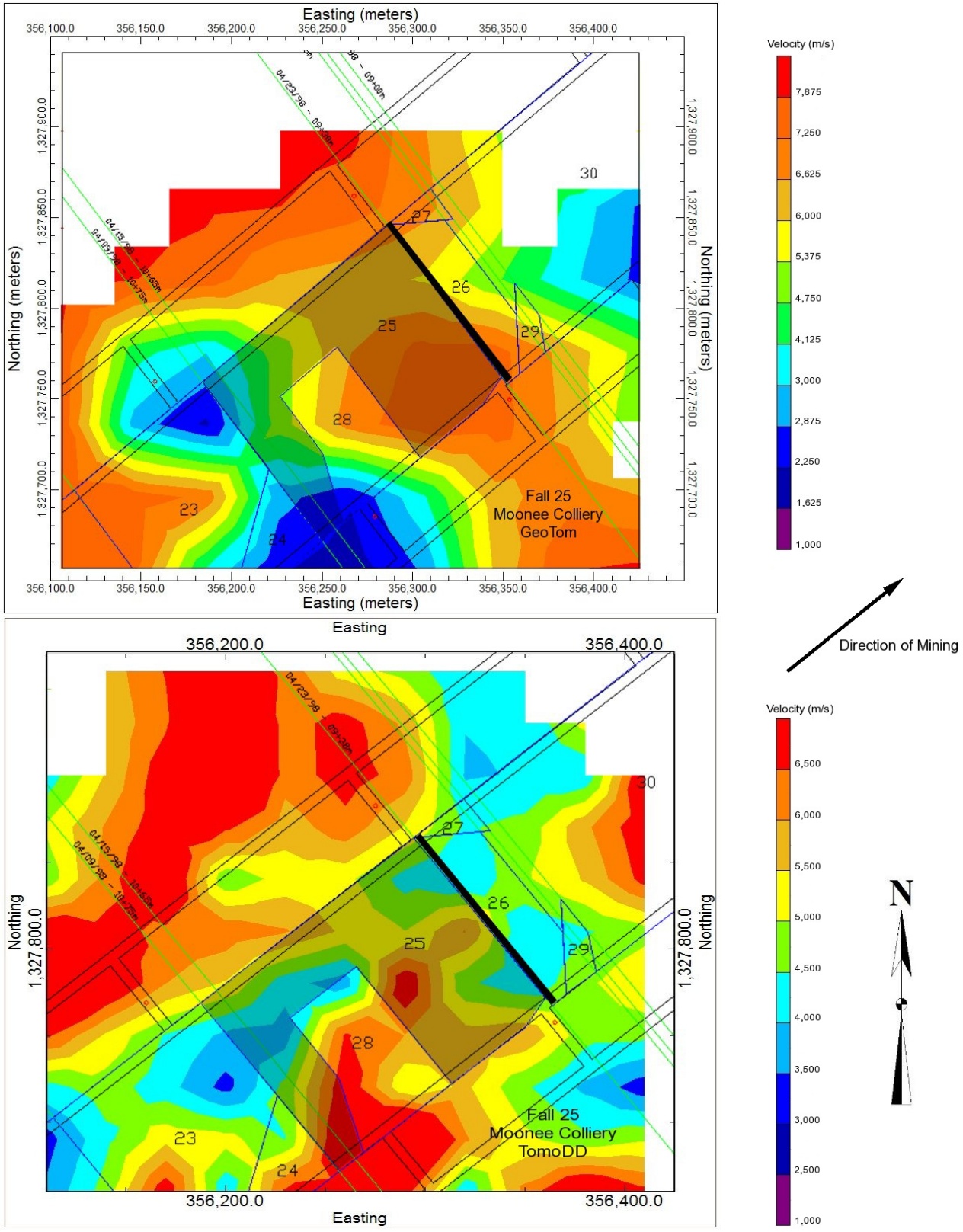

Figure D.4. Plan View Velocity Tomograms at seam level for Fall 25. Areas not traversed by rays are shown in white.

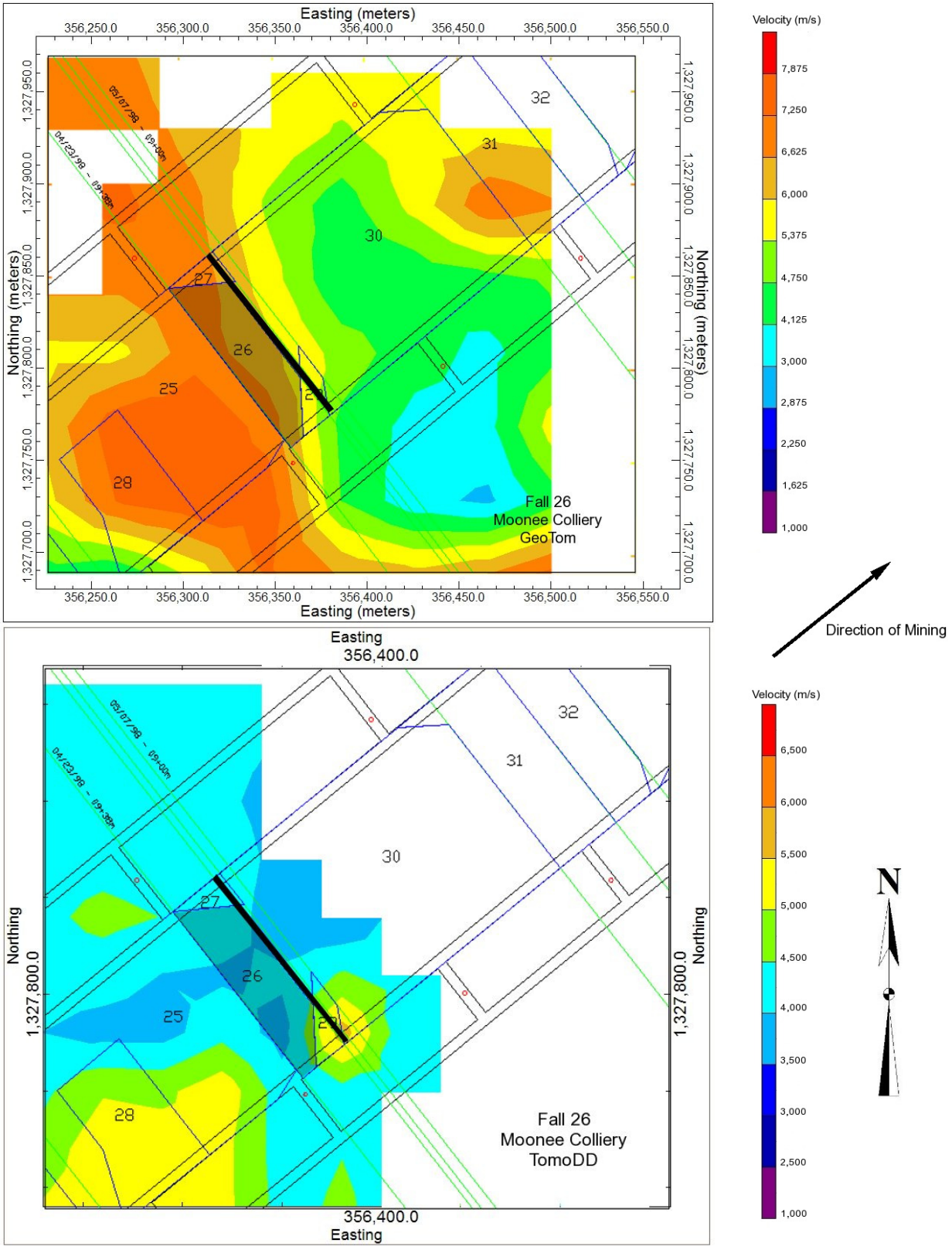

Figure D.5. Plan View Velocity Tomograms at seam level for Fall 26. Areas not traversed by rays are shown in white.

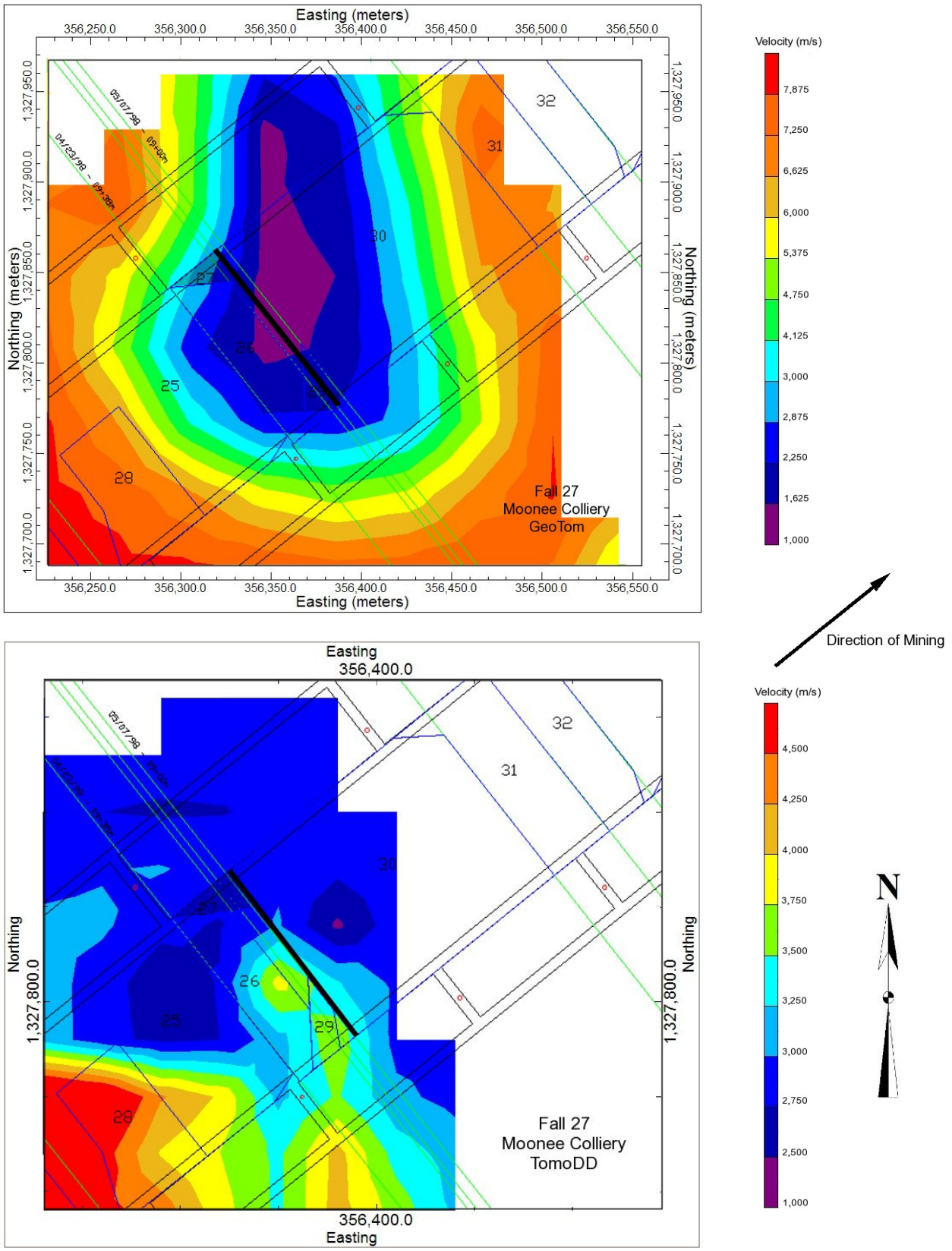

Figure D.6. Plan View Velocity Tomograms at seam level for Fall 27. Areas not traversed by rays are shown in white.

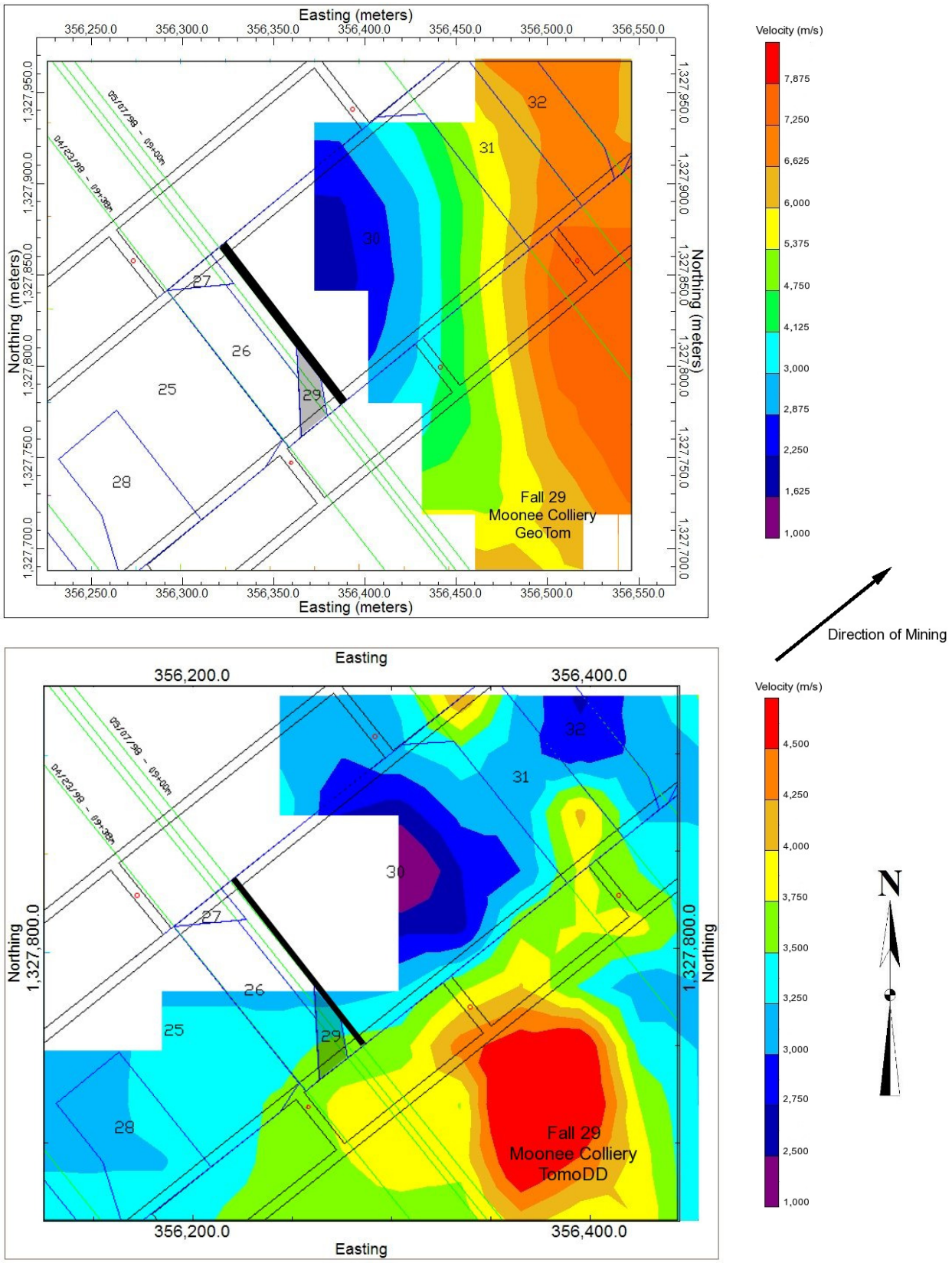

Figure D.7. Plan View Velocity Tomograms at seam level for Fall 29. Areas not traversed by rays are shown in white.

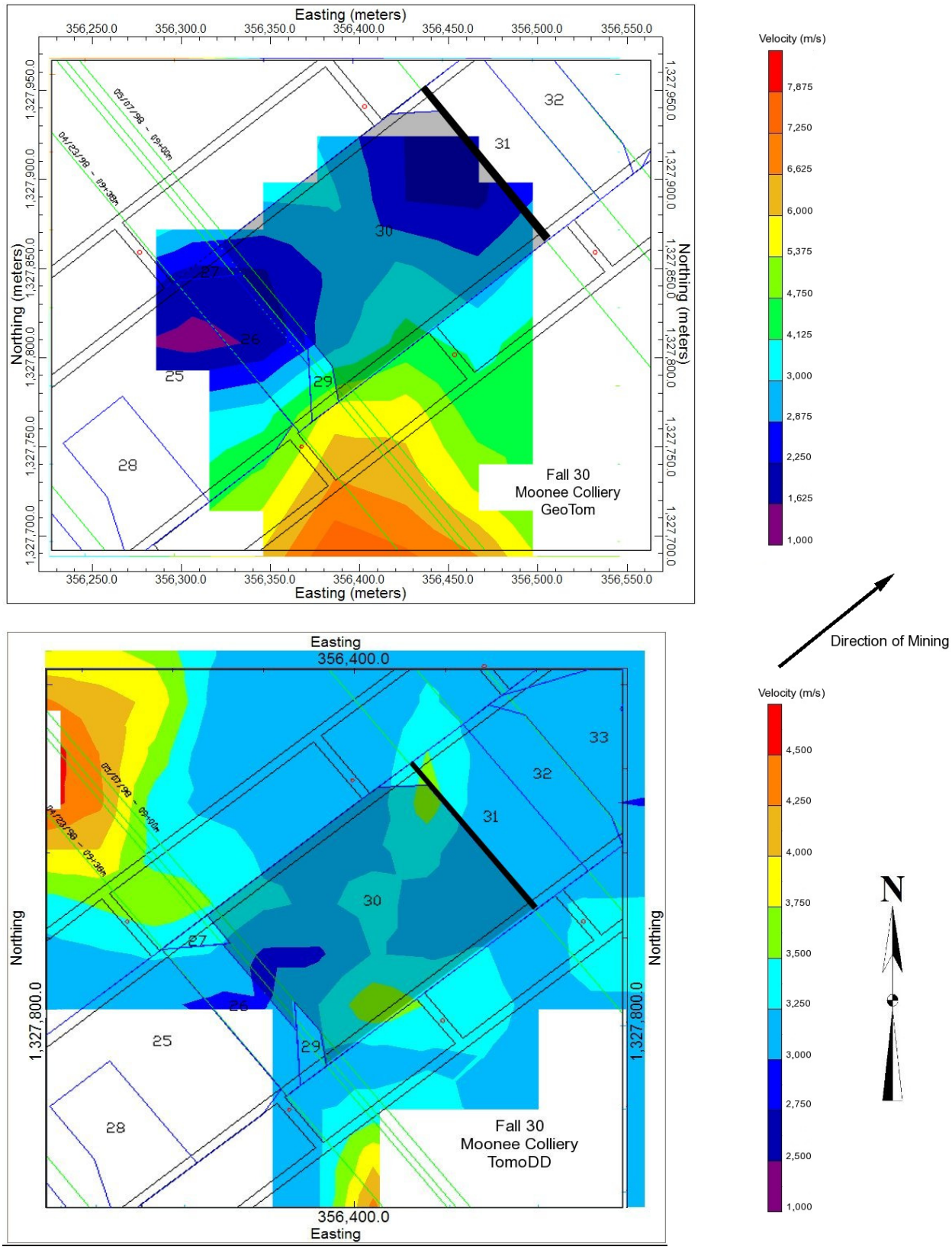

Figure D.8. Plan View Velocity Tomograms at seam level for Fall 30. Areas not traversed by rays are shown in white.

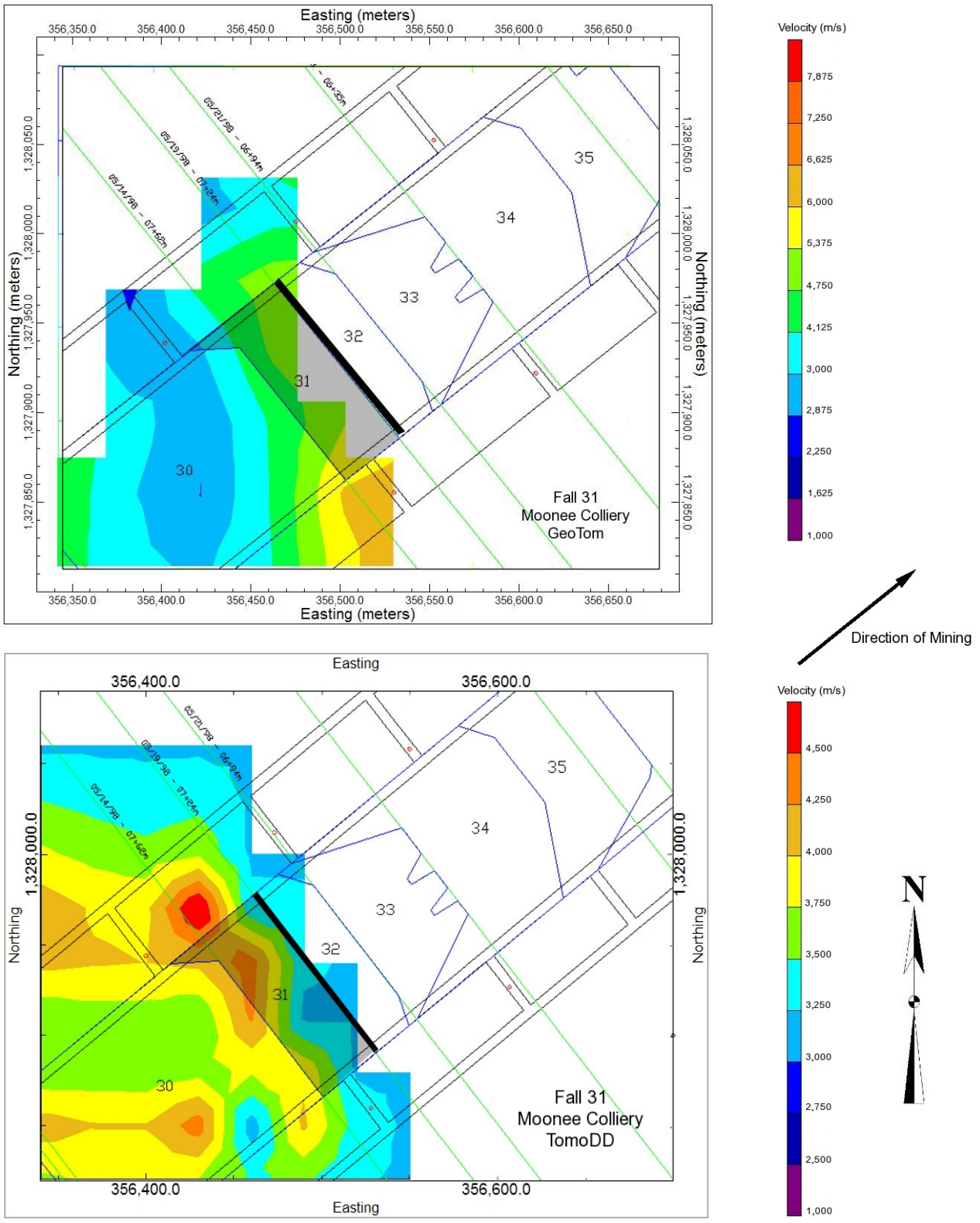

Figure D.9. Plan View Velocity Tomograms at seam level for Fall 31. Areas not traversed by rays are shown in white.

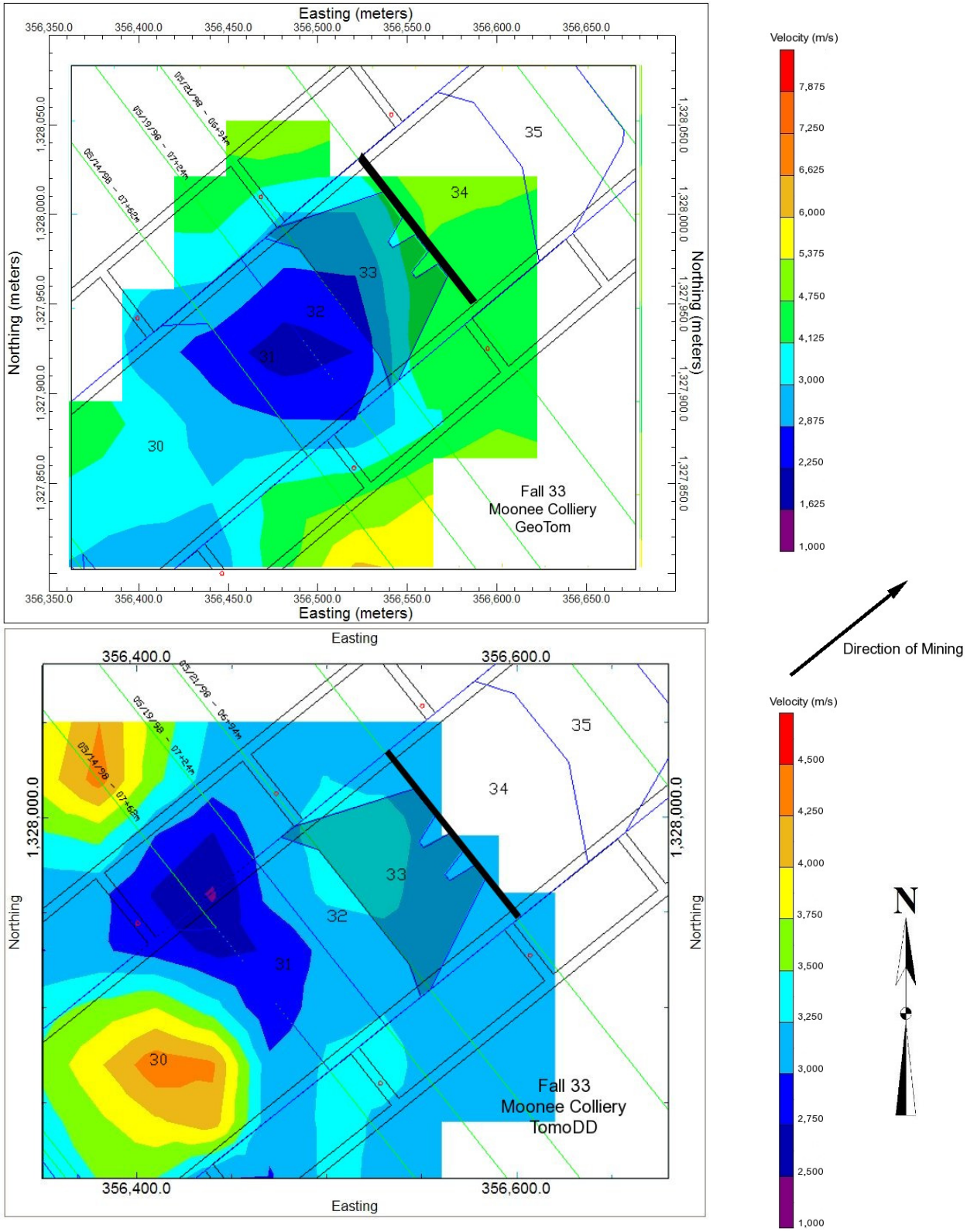

Figure D.10. Plan View Velocity Tomograms at seam level for Fall 33. Areas not traversed by rays are shown in white.

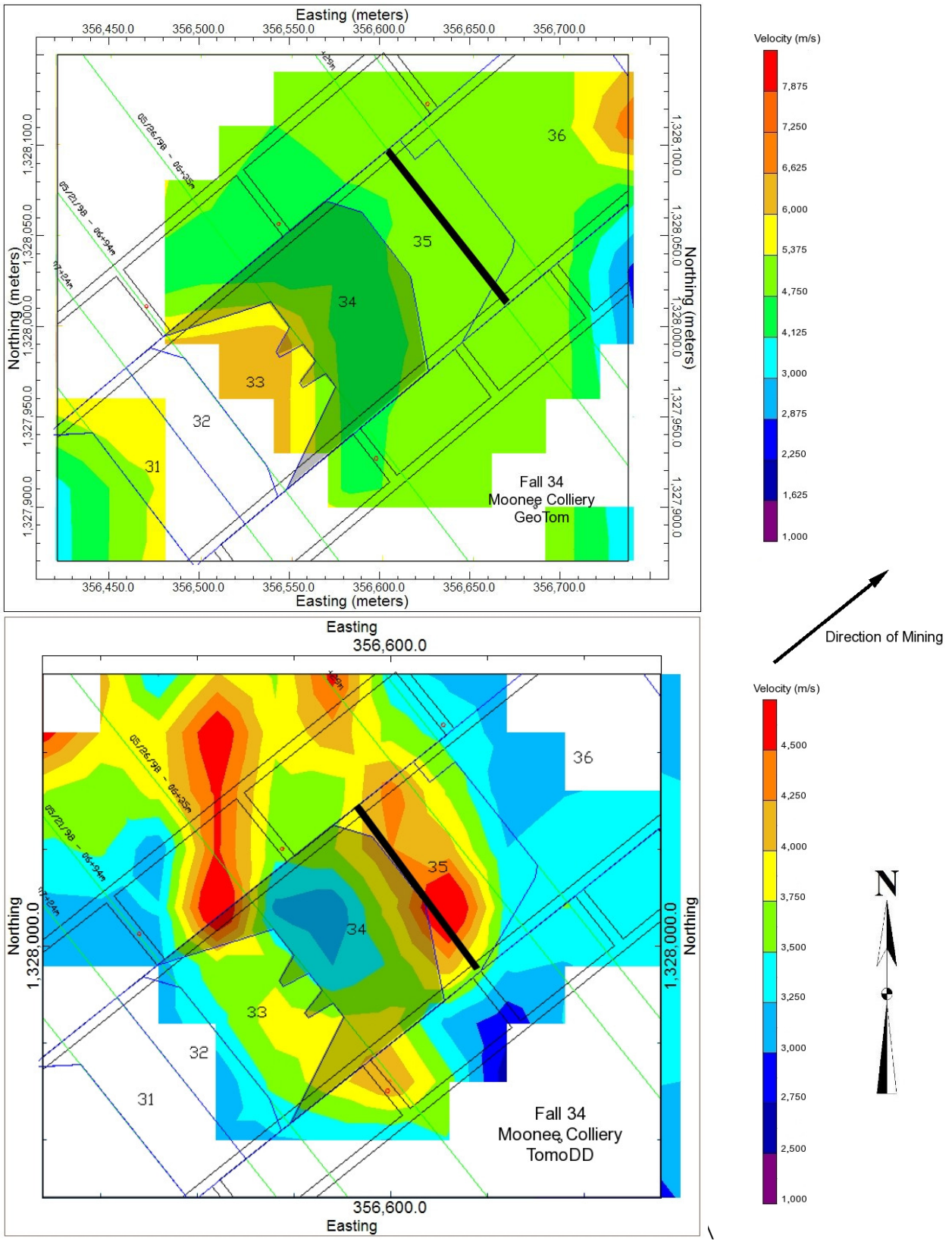

Figure D.11. Plan View Velocity Tomograms at seam level for Fall 34. Areas not traversed by rays are shown in white.

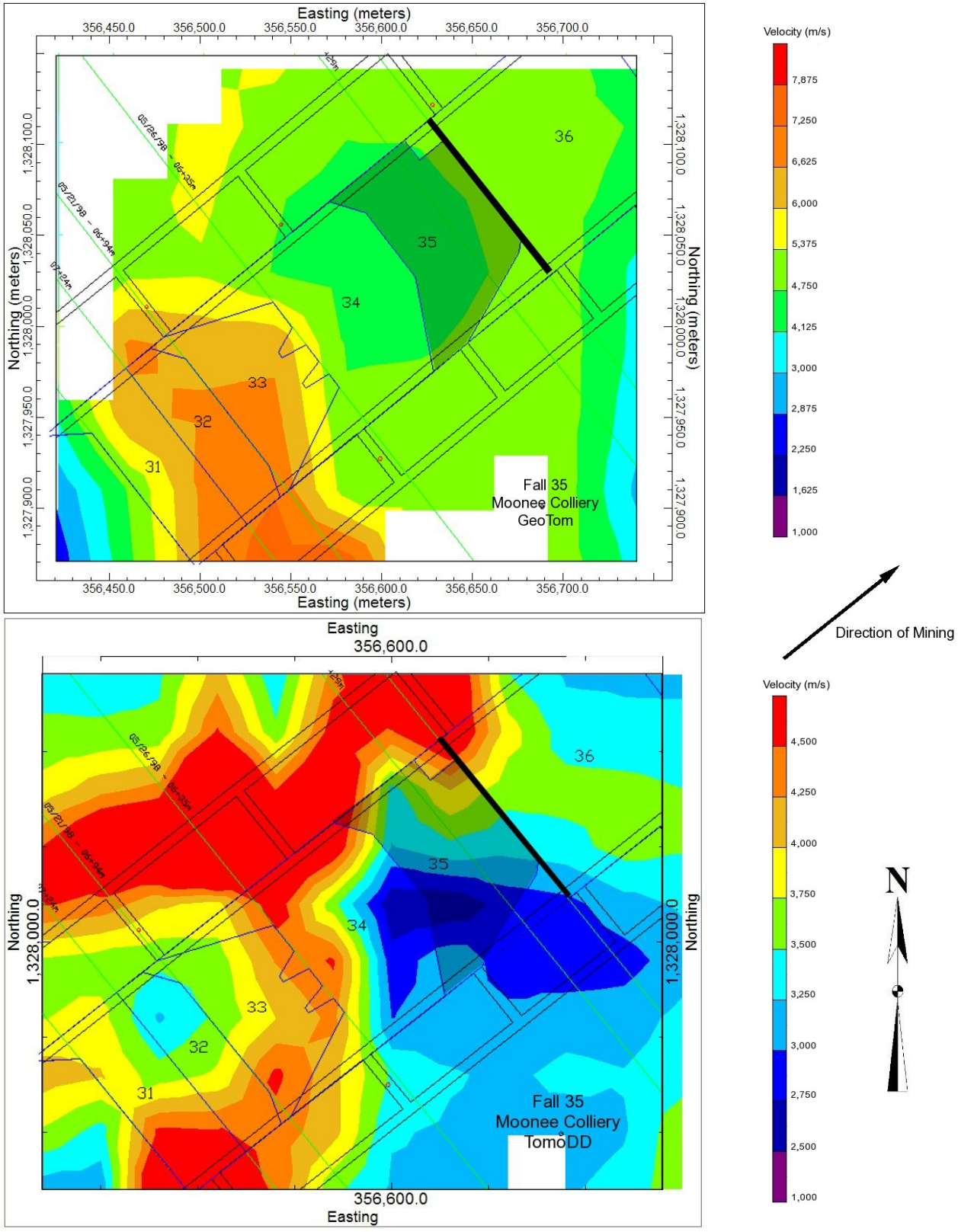

Figure D.12. Plan View Velocity Tomograms at seam level for Fall 35. Areas not traversed by rays are shown in white.

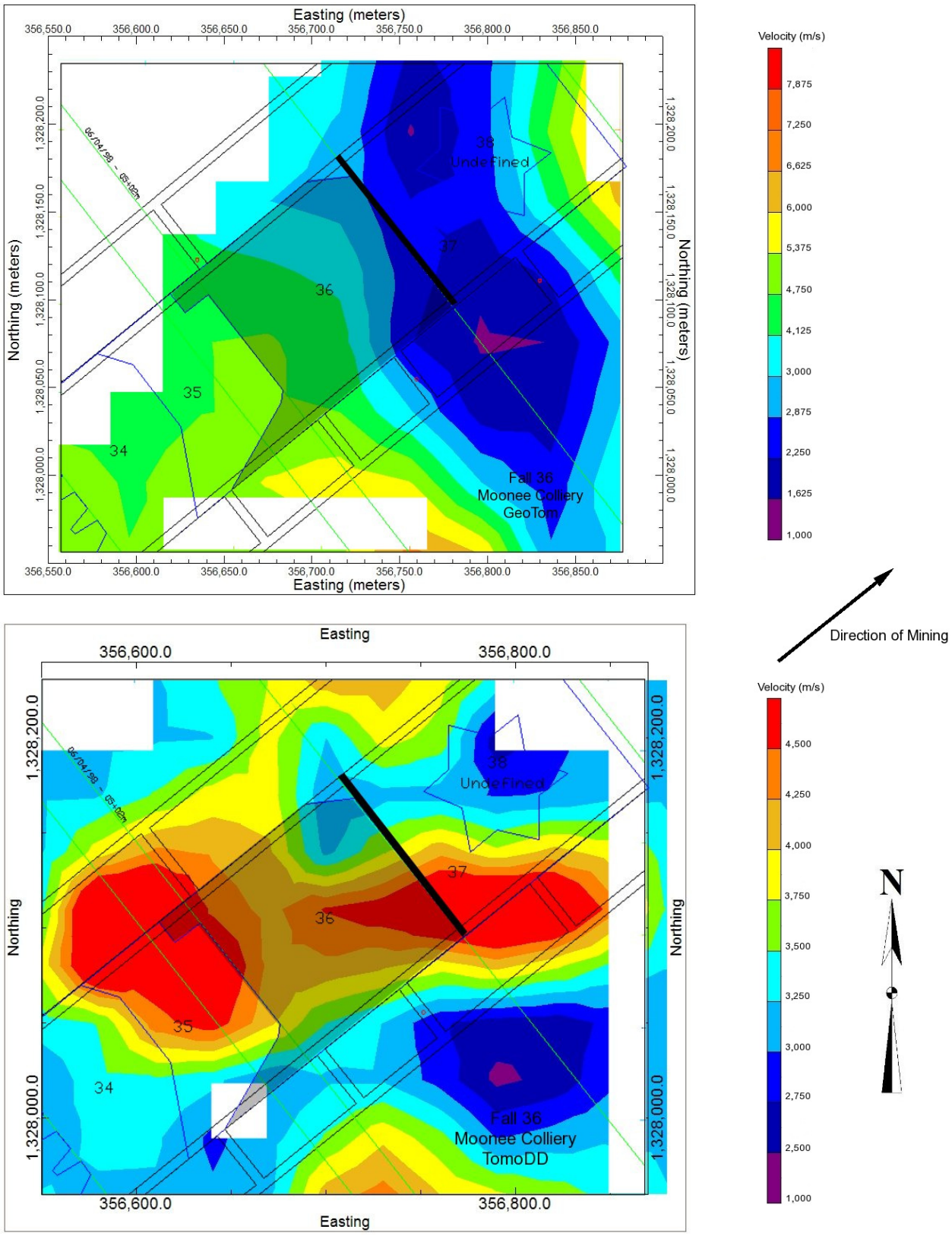

Figure D.13. Plan View Velocity Tomograms at seam level for Fall 36. Areas not traversed by rays are shown in white.

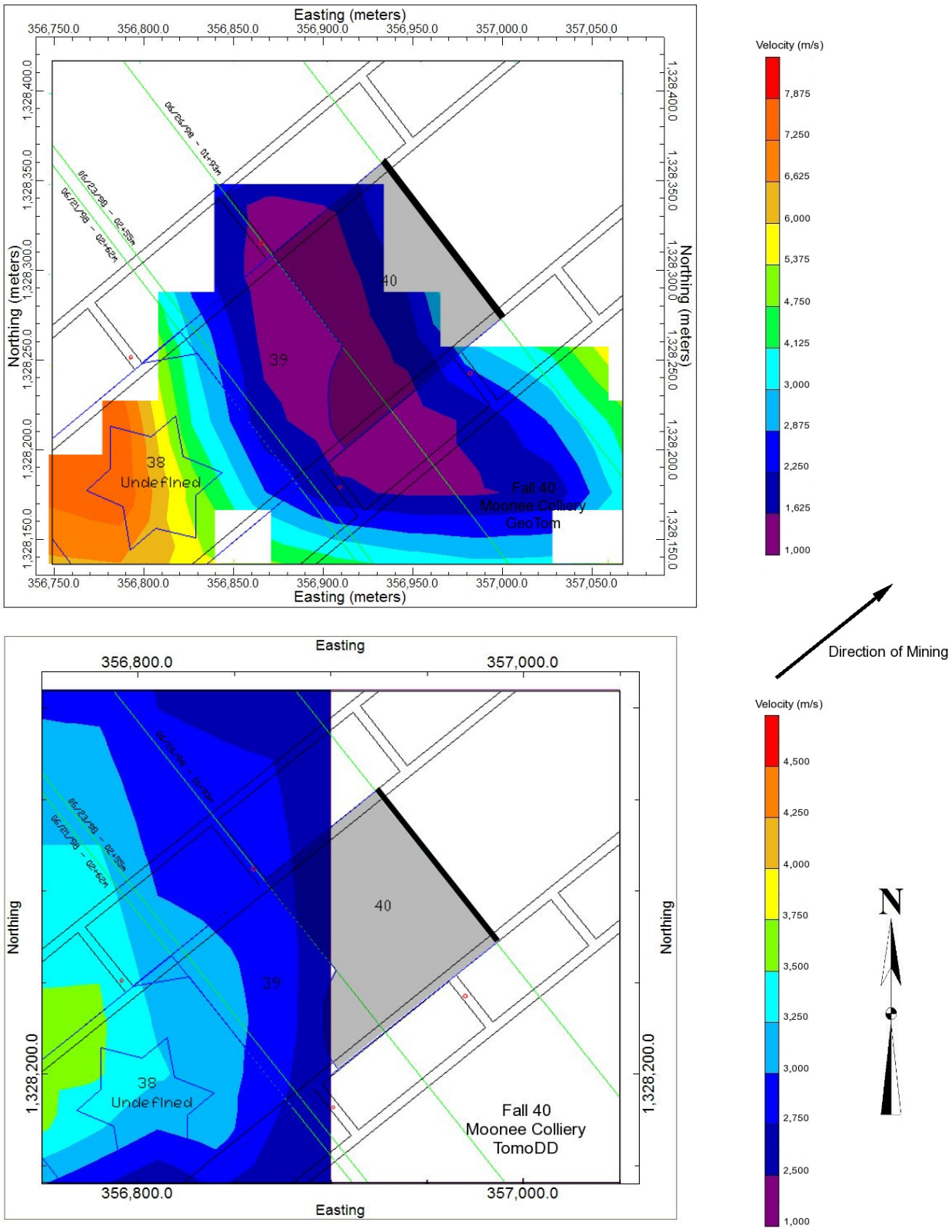

Figure D.14. Plan View Velocity Tomograms at seam level for Fall 40. Areas not traversed by rays are shown in white.